ABSTRACT

Title of dissertation: ENGINEERING PHYSIOLOGICALLY-RELEVANT MODEL SYSTEMS TO UNDERSTAND THE REQUIREMENTS OF RHINOVIRUS C INFECTION

Monty Eli Goldstein, Doctor of Philosophy, 2023

Dissertation directed by: Associate Professor, Margaret A. Scull,
Department of Cell Biology and Molecular Genetics

Rhinovirus (RV) is the most prevalent etiologic agent of the common cold, and infections by RV species C (RV-C) are often associated with more severe illness, and have been strongly correlated with childhood development of asthma. Due to lack of *in vitro* and *in vivo* model systems capable of supporting the RV-C life cycle, few details of RV-C biology are understood about this recently discovered, clinically-relevant respiratory pathogen. To reveal the nature of virus-host interactions and study viral pathogenesis, the application of physiologically-relevant model systems that capture relevant cell types, differentiation states, and microenvironmental cues is essential. Applying these principles to our investigations of RV-C, I engineered *in vitro* and *in vivo* model systems to better understand the requirement of specific host factors for RV-C replication in human and mouse cells. Specifically, I utilized a pseudostratified *in vitro* model of human airway epithelium (HAE) to study RV-C replication, and applied CRISPR/Cas9 technology in these cultures to assess the specific role for stimulator of interferon genes (STING) in promoting viral replication. Since RV-C species tropism is highly restricted, I then applied our knowledge of RV-C replication in HAE cultures towards building an improved RV-C

mouse model. Here, I first characterized RV-C replication in mouse lung cells *in vitro*, and demonstrated that human STING expression enhanced viral replication; second, I applied these findings *in vivo,* where I generated a transgenic mouse expressing the human ortholog of the RV-C receptor, cadherin-related family member 3 (CDHR3), along with human STING. While these mice lack overt symptoms typically associated with viral infection, they exhibited significantly increased viral replication 24 hours-post infection. Finally, to support ongoing efforts to further develop these mice as a robust small animal model of RV-C, I developed several novel cell lines which represent important tools to interrogate the impacts of other host factors on RV-C replication in mouse cells, which upon validation, can be re-engineered into these transgenic mice.

Engineering physiologically-relevant model systems to understand the requirements of rhinovirus C infection

by

Monty Eli Goldstein

Dissertation submitted to the Faculty of the Graduate School of the
University of Maryland, College Park in partial fulfillment
of the requirements for the degree of
Doctor of Philosophy
2023

Advisory Committee:

Associate Professor Margaret A. Scull, Chair
Professor Jeffrey DeStefano
Senior Investigator Alison McBride
Professor Andrew Pekosz
Professor James Culver, Dean's Representative

Dedication

This dissertation is dedicated to all those who helped me become the person and scientist I am today – from my parents and family, to my teachers and professors throughout the duration of my formal education – I have learned so much from you. Most importantly, none of this work would be possible without the dedicated guidance provided by my mentor, Dr. Margaret Scull, for whom I am beyond grateful.

Acknowledgements

I am extremely appreciative to have had so many memorable lab mates and colleagues throughout my time in the Scull lab, especially Talita Gagliardi, Ethan Iverson, Daniel Song, Kira Griswold, Eva Agostino, Maxinne Ignacio, Nia Razi, Leila Abdelhamid, Jeff Loube, Maria Rife, and Divya Swaminathan. You were always there lend a hand with an experiment, bounce an idea off of, or provide support when an experiment didn't turn out as I had hoped.

I would also like to acknowledge the members of my dissertation committee, namely Dr. Jeffery DeStefano, Dr. Alison McBride, Dr. Andrew Pekosz, and Dr. James Culver. Thank you for guiding me throughout.

I would like to acknowledge the funding sources which made all of this work feasible: Faculty-Student Research award from the University of Maryland, National Institute of Allergy and Infectious Diseases R21 AI149180, National Institutes of Health Institutional Training Grants T32 AI089621 and T32 AI125186, and AstraZeneca.

Table of Contents

Dedication ii
Acknowledgements iii
Table of Contents iv
List of Tables x
List of Figures xi
List of Abbreviations xii
Chapter 1 : Introduction 1
1.1 Rhinovirus Taxonomy and Relevance to Public Health 1
1.1.1 Classification 1
1.1.2 Clinical Relevance and Impact 3
1.1.3 Current Treatment Options 4
1.2 Rhinovirus Tropism 5
1.2.1 Species Tropism 5
1.2.2 Tissue Tropism 6
1.3 General Rhinovirus Lifecycle 6
1.3.1 Entry 6
1.3.2 Protein Production and Viral Genome Replication 7
1.3.3 Particle Assembly and Egress 9
1.4 The Impact of STING on RV Replication 9
1.5 Propagation of RVs In Vitro 10
1.5.1 Growth in Cell Lines 10
1.5.2 Initial Models for the Cultivation of RV-C 11
1.5.3 Discovery of CDHR3 as a Receptor for RV-C 13
1.5.4 CDHR3 SNP *rs6967330* and the Development of HeLa-E8 14
1.6 Using Mice to Model Rhinovirus Infection 16
1.6.1 Minor Group RV Mouse Models 16
1.6.2 Major Group RV Mouse Models 17
1.6.3 RV-C Mouse Models 18
1.7 Introduction to My Dissertation 18
Chapter 2 : Modeling Innate Antiviral Immunity in Physiological Context 21
2.1 Highlights 22
2.2 Abstract 22
2.3 Introduction 23

2.4 Key players in innate antiviral defense 25
2.5 Important considerations in modeling authentic antiviral responses 30
2.5.1 Variation in the expression and function of innate immune sensors and antiviral effectors 30
2.5.2 The impact of the microenvironment on innate antiviral responses 39
2.6 Utility of tissue-engineered and 3D cell culture systems in modeling innate antiviral responses 47
2.7 Additional applications and current challenges of assessing innate antiviral immunity in 3D model systems....52
Chapter 3 : Rhinovirus C replication is associated with the endoplasmic reticulum and triggers cytopathic effects in an in vitro model of human airway epithelium 56
3.1 Abstract....57
3.2 Author Summary 58
3.3 Introduction 59
3.4 Results....61
3.4.1 RV-C15 replicates in ciliated cells, yielding changes in CDHR3 expression...61
3.4.2 RV replication complex distribution is associated with vesicle formation 64
3.4.3 RV-C15 infection triggers fragmentation of Golgi stacks and induces PI4P ...66
3.4.4 Endoplasmic reticulum appears to be the RV-C15, but not RV-A16 or RV-A2, genome replication site....69
3.4.5 RV-C15 infection induces incomplete autophagy....71
3.4.6 STING expression promotes replication of RV-C15 in HAE 74
3.4.7 RV-C15 infection alters epithelial permeability, disposition of tight junction-associated proteins, and mucociliary clearance....77
3.5 Discussion 80
3.6 Materials and Methods....87
3.6.1 Primary and immortalized cell culture and viral stocks 87
3.6.2 CRISPR/Cas9-mediated knockout of STING in HAE 89
3.6.3 Titration of rhinoviruses by plaque assay and quantitative real-time PCR (qPCR) 90
3.6.4 RV infection in HAE and H1 HeLa cells 91
3.6.5 IF assays in HAE and H1 HeLa cells 92
3.6.6 Quantification of fluorescence levels and colocalization analysis 93
3.6.7 Transmission Electron Microscopy (TEM) in HAE....94
3.6.8 Immunoblotting assays 95
3.6.9 Lactate dehydrogenase (LDH) release cytotoxicity assay 96

3.6.10 Transepithelial Electrical Resistance (TEER) assay 96
3.6.11 Quantification of ZO-1 disposition using JAnaP 96
3.6.12 Measurement of Mucociliary Clearance (MCC)....97
3.7 Supporting information 98
3.7.1 Figure S3.1. RV-C15 replicates in ciliated epithelial cells leading to decreased CDHR3 levels. 98
3.7.2 Figure S3.2. Ring-like dsRNA localization in HAE is not specific to RV-C15 infection. 99
3.7.3 Figure S3.3. Golgi and PI4P-positive vesicles are not the main site for RV-C15 replication in HAE at 12hpi. 101
3.7.4 Figure S3.4. Global calnexin expression is not altered during RV-C15 infection in HAE. 102
3.7.5 Figure S3.5. RV-C15 replication induces incomplete autophagy in HAE at 12hpi. 103
3.7.6 Figure S3.6. Immunofluorescence of MCC experiment showing RV-C15 but not UV-RV-C15 infection in HAE at 12hpi. 104
Video S3.1. RV-C15-infected HAE showing perinuclear dsRNA (red) detection at 12hpi. 104
3.7.7 Supporting Tables 105
3.8 Author contributions 114
3.9 Acknowledgements 114
Chapter 4 : Human STING Promotes RV-C Replication in Mouse Cells *In Vitro* and *In Vivo* 116
4.1 Abstract 117
4.2 Introduction 118
4.3 Results 120
4.3.1 Murine and human CDHR3 orthologs exhibit similar tissue expression patterns, but lack complete homology 120
4.3.2 Murine cells are permissive for RV-C, and human STING expression significantly increases RV-C replication 123
4.3.3 Murine cells support the production of infectious particles 126
4.3.4 CDHR3 knockout is embryonically lethal in mice 129
4.3.5 Characterization of hCDHR3 expression in transgenic mice 130
4.3.6 Intranasal delivery of AAV 6.2-luciferase results in transgene expression in the lung. 132
4.3.7 AAV-mediated delivery of hSTING to hCDHR3 transgenic mice promotes RV-C15 replication *in vivo* 134

4.3.8 RV-A1A infection of WT mice with the addition of human STING does not significantly boost viral replication. 136
4.4 Discussion 137
4.5 Material and Methods 143
4.5.1 Plasmids 143
4.5.2 Tissue Culture 143
4.5.3 CRISPR/Cas9-mediated knockout of STING in HAE 143
4.5.4 *In vitro* transcription, rhinovirus rescue and amplification 145
4.5.5 Immortalized Cell Transfection and Infection 146
4.5.6 Plaque Assay 146
4.5.7 RV genome quantification by qPCR 147
4.5.8 Host gene expression quantification by qPCR 148
4.5.9 SDS-PAGE and Western Blot 148
4.5.10 Immunofluorescence 149
4.5.11 CellProfiler 150
4.5.12 In situ hybridization 150
4.5.13 Immunohistochemistry 152
4.5.14 Lentivirus Production 153
4.5.15 Generation of LET1-expressing mouse CDHR3 154
4.5.16 Homology modeling 154
4.5.17 Adeno-associated Virus 154
4.5.18 Generation of Transgenic Mice 154
4.5.19 Euthanasia 157
4.5.20 Tissue Collection for RNA and Protein 157
4.5.21 Lung Perfusion 157
4.5.22 IVIS 158
4.5.23 Lung Inflation 158
4.5.24 Ketamine-Xylazine Anesthetization 159
4.5.25 Intranasal Inoculation with AAV 160
4.5.26 Intranasal Inoculation with RV 160
4.5.27 Health Scoring 161
4.6 Supporting information 162
4.6.1 Figure S4.1: Transfection of LET1 cells in presence of hSTING with RV-C15 or RV-A1A does not affect cellular or released genome titers. 162

4.6.2 Figure S4.2: STING KO HAE cultures infected with RV-A16 result in earlier release of virus. 162
4.6.3 Figure S4.3: CDHR3 expression in Tg1. 163
4.6.4 Figure S4.4: CDHR3 expression in Tg2. 163
4.6.5 Figure S4.5: CDHR3 expression in Tg3. 164
4.6.6 Figure S4.6: Fluorescent immunohistochemistry localizes hCDHR3 in Tg mice to ciliated epithelium 164
4.6.7 Figure S4.7: Colorimetric immunohistochemistry localizes hCDHR3 in Tg mice to ciliated epithelium 165
4.6.8 Figure S4.8: RV-C infection of transgenic mice expressing CDHR3 with the addition of human STING 96hpi. 166
4.6.9 Figure S4.9: dsRNA is not detected in mice after infection with RV-C15 12 hpi. 166
4.6.10 Figure S4.10: The addition of human STING does not impact RV=A1A infection of WT mice. 167
4.6.11 Figure S4.11: LET1 and LET1-expressing hCDHR3 cells are not susceptible to RV-C15 infection. 167
4.6.12 Figure S4.12: MAVS amino acid homology by species, highlighting the predicted RV-C 3C cleavage site in humans at Q|A. 168
4.7 Author Contributions 168
4.8 Acknowledgements 168
Chapter 5 : Development of Novel Cell Lines to Support Further Study of the Molecular Determinants of RV-C Infection in Mice 170
5.1 Abstract 170
5.2 Introduction 171
5.3 Results 172
5.3.1 Establishment of LET1-hCDHR3 cells expressing hSTING: An *in vitro* platform to further interrogate the requirements of RV-C replication in a murine cell system 172
5.3.2 Establishment and characterization of mCDHR3-expressing cell lines 173
5.3.3 Infection of hCDHR3-expressing HeLa cells highlights the need for further optimization. 175
5.4 Discussion 178
5.5 Methods 179
5.5.1 Plasmids 179
5.5.2 Tissue Culture 180
5.5.3 *In vitro* transcription, rhinovirus rescue and amplification 181
5.5.4 Plaque Assay 181

5.5.5 RV genome quantification by qPCR....182
5.5.6 Immortalized Cell Infection....183
5.5.7 Host gene quantification by qPCR....183
5.5.8 Lentivirus Production....184
5.5.9 Generation of human and mouse CDHR3 cell lines....184
5.5.10 SDS-PAGE and Western Blot....185
5.5.11 Cell Surface Biotinylation and Immunoprecipitation Assay....186
5.5.12 Immunofluorescence....187
5.6 Acknowledgments....187
Chapter 6 : Discussion and Conclusion....189
References....196

List of Tables

Table 2.1 Comparison of primary and continuous cell lines.
Table 2.2 Current applications and description of ongoing advances in *in vitro* model technology that will enable further interrogation of antiviral responses in physiological context.
Table 3.1 Primary antibodies used in immunofluorescence assays.
Table 3.2 Secondary antibodies used in immunofluorescence assays.
Table 3.3 Primary and secondary antibodies used in immunoblotting assays.
Table 4.1 Genetic crosses of $Cre^{+/+}$ mice with $mCDHR3^{+/-}$ mice are unable to produce homozygous $mCDHR3^{-/-}$ offspring.
Table 4.2 Genetic crosses of $mCDHR3^{+/-}$ mice result in non-Mendelian offspring ratios, suggesting $mCDHR3^{-/-}$ mice are non-viable.
Table 4.3 Assessment of pre-wean mouse mortality suggests $mCDHR3^{/-}$ mice are embryonically lethal.
Table 4.4 Primers used to detect the hCDHR3 transgene.
Table 4.5 Primers used to confirm transgene homozygosity.

List of Figures

Figure 1.1 Circle phylogram of relationships for currently recognized genotypes of RV-A, RV-B, and RV-C.
Figure 1.2 RV genome organization.
Figure 1.3 RV-C15 infection in sinus mucosa.
Figure 1.4 HeLa cells expressing CDHR3 SNP *rs6967330* led to the establishment of HeLa-E8, a cell line capable of supporting the complete RV-C lifecycle.
Figure 1.5 CDHR3 SNP *rs6967330* results in subcellular localization difference
Figure 2.1 Diagram of pattern recognition receptor-initiated signaling events, interferon production, and subsequent interferon signaling leading to interferon-stimulated gene expression.
Figure 2.2 Variation in pattern recognition receptor expression profiles across cell types.
Figure 2.3: Impact of cell-cell and cell-extracellular matrix interactions on antiviral responses.
Figure 2.4: Polarized receptor expression and cytokine release impacts the dynamics of the host response to infection.
Figure 2.5: *In vitro* model systems with emergent properties.
Figure 3.1 RV-C15 replicates in ciliated epithelial cells, leading to decreased CDHR3 levels.
Figure 3.2 Detection of RV-C15 replication complexes in HAE.
Figure 3.3 Neither the Golgi nor PI4P-positive vesicles are the main site for RV-C15 replication in HAE.
Fig 3.4. ER is a site for RV-C15 genome replication in HAE.
Fig 3.5. RV-C15 replication induces incomplete autophagy in HAE at 12hpi.
Fig 3.6. STING expression promotes RV-C15 replication in HAE at 12hpi.
Fig 3.7. RV-C15 infection promotes translocation of tight junction proteins and impairs mucociliary clearance.
Fig 4.1 Murine CDHR3 is localized to similar tissues as human CDHR3, yet differs in several key aspects
Fig 4.2 Mouse cells replicate RV-C, and replication is significantly increased upon expression of human STING.
Fig 4.3 RV-C produced in mouse cells is infectious and capable of reinfection.
Fig 4.4 Selecting Tg1 as the transgenic mouse founder line.
Fig 4.5 Intranasal delivery of luciferase by AAV results in transgene expression in the lung.
Fig 4.6 RV-C infection of transgenic mice expressing CDHR3 with the addition of human STING results in sustained viral replication.
Fig 5.1 LET1 cells expressing hCDHR3 and inducible hSTING provide an *in vitro* alternative to transgenic mice.
Fig 5.2 Development and characterization of human and murine CDHR3-expressing cell lines.
Fig 5.3 RV-C15 stock is infectious, yet does not replicate to significant levels in HeLa-E8 cells.

List of Abbreviations

AAV	adeno-associated virus
ALI	air-liquid interface
AIM2	absent in melanoma 2
AMP	adenosine monophosphate
AP-1	activator protein 1
BAC	bacterial artificial chromosome
BSA	bovine serum albumin
CARD	caspase activation and recruitment domain
CDHR3	cadherin-related family member 3
cDNA	complementary DNA
cGAMP	cyclic GMP-AMP
cGAS	cyclic GMP-AMP synthase
CLR	C-type lectin receptor
CMV	cytomegalovirus
CO_2	carbon dioxide
COPD	chronic obstructive pulmonary disease
CPE	cytopathic effect
CTCF	corrected total cellular fluorescence
DAMP	damage-associated molecular pattern
DAB	3,3’-Diaminobenzene
DAPI	4’,6-diamidino-2-phenylindole
DC	dendritic cell
DENV	Dengue virus
DEPC	diethyl pyrocarbonate

dsRNA	double-stranded RNA
dpc	days post-conception
dpt	days post-transduction
EC	extracellular domain
ECM	extracellular matrix
eGFP	enhanced green fluorescent protein
ER	endoplasmic reticulum
ERGIC	endoplasmic reticulum-Golgi intermediate compartment
FBS	fetal bovine serum
Fluc	firefly luciferase
FoxJ1	forkhead box protein J1
GAPDH	glyceraldehyde3 3-phosphate dehydrogenase
GMP	guanosine monophosphate
HA	hemagglutinin
HAE	human airway epithelium
hCDHR3	human CDHR3
HCV	hepatitis C virus
HEK	human embryonic kidney
HIV	human immunodeficiency virus
hpi	hours post-infection
hpt	hours post-transfection
hSTING	human STING
hTERT	human telomerase reverse transcriptase
IAV	influenza virus
ICAM-1	intercellular adhesion molecule 1
IF	immunofluorescence

IFN	interferon
IFNAR2	interferon alpha and beta receptor subunit 2
IKK	IkB Kinase
IL	interleukin
IP	intraperitoneal
IRF	interferon regulatory factor
ISG	interferon-stimulated gene
ISH	*in situ* hybridization
ISRE	interferon-stimulated response elements
JACop	just another co-localization plug-in
JAK	Janus kinase
JAnaP	junction analyzer program
KO	knockout
LAMP-1	lysosome-associated membrane glycoprotein 1
LDH	lactate dehydrogenase
LDLR	low-density lipoprotein receptor
LGP2	laboratory of genetics and physiology 2
LPS	lipopolysaccharide
MAVS	mitochondrial antiviral signaling protein
MCC	mucociliary clearance
mCDHR3	murine CDHR3
MDA5	melanoma differentiation-associated protein
MMP-12	matrix metalloproteinase 12
mSTING	murine STING
NF-κB	nuclear factor kappa-light-chain-enhancer of activated B cells
NLR	nucleotide-binding oligomerization domain (NOD)-like receptor

NTC	non-targeting control
ORF	open-reading frame
PAMP	pathogen-associated molecular pattern
PNI	pronuclear injection
PFU	plaque forming unit
PI4P	phosphatidylinositol-4-phosphate
PI4K	phosphatidylinositol-4-kinase
PBS	phosphate-buffered saline
pDC	plasmacytoid dendritic cell
PRR	pattern recognition receptor
qPCR	quantitative polymerase chain reaction
RdRp	RNA-dependent RNA polymerase
RIPA	radio immuno-precipitation assay
RIG-I	retinoic acid-inducible gene I protein
RLR	RIG-like receptor
RSV	respiratory syncytial virus
RV	rhinovirus
SARS-CoV	severe acute respiratory syndrome coronavirus
SARS-CoV-2	severe acute respiratory syndrome coronavirus 2
sgRNA	single guide RNA
SNP	single nucleotide polymorphism
SOCS	suppressor of cytokine signaling
STAT	signal transducer and activator of transcription
STING	stimulator of interferon genes
TBK-1	TANK binding kinase 1
TBS	tris buffered saline

TBS-T	tris buffered saline tween
TEER	transepithelial electrical resistance
TEM	transmission electron microscopy
Tg	transgenic
TIR	Toll-Interleukin-1 resistance
TLR	Toll-like receptor
UTR	untranslated region
UV	ultraviolet
VP	viral protein
VPg	viral protein genome-linked
VSV	vesicular stomatitis virus
WB	western blot
WT	wild type
ZIKV	Zika Virus
ZO-1	zona occludens 1

Chapter 1 : Introduction

1.1 Rhinovirus Taxonomy and Relevance to Public Health

1.1.1 Classification

Rhinoviruses (RVs) form a clade within the *Enterovirus* genus of the *Picornaviridae* family, and comprise three species, RV-A, RV-B, and RV-C. Notably, while RV-A and -B have been described for decades [1], RV-C was identified more recently – in 2006 – as a result of improved molecular-based surveillance in the aftermath of the severe acute respiratory syndrome coronavirus (SARS-CoV) outbreak [2]. Each species can be further divided into genetically related subtypes denoted by a numbering system. RV-A is the largest group, where 80 different genotypes have been identified to date **[Figure 1.1]** [3].

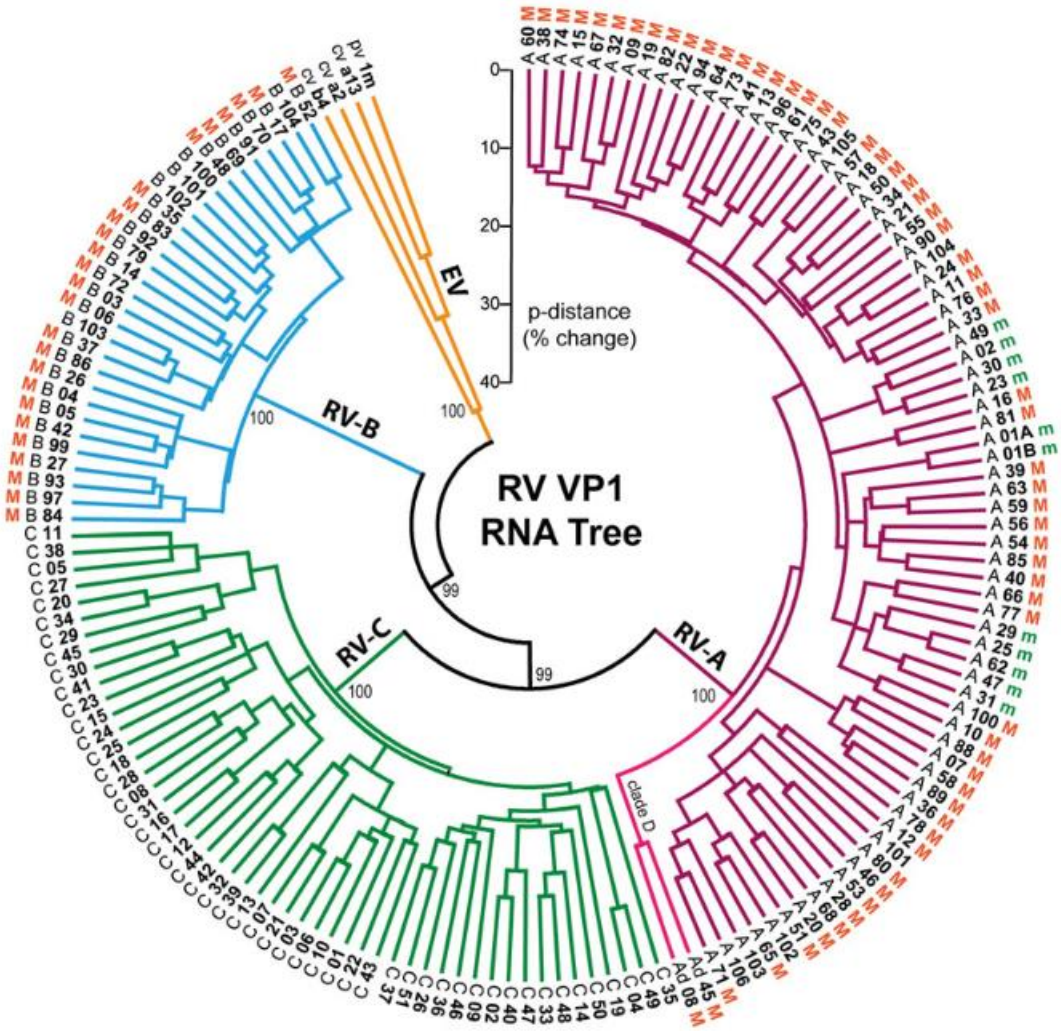

Figure 1.1: Circle phylogram of relationships for currently recognized genotypes [4] **of RV-A, RV-B, and RV-C.** Reproduced with permissions from [5]. The tree was calculated with neighbor-joining methods from aligned, VP1 RNA sequences, and rooted with data from four enteroviruses (EV) of the EV-A, EV-B, and EV-C species, similar to [6]. The Major ("M," ICAM-1) and minor ("m," LDLR) receptor groups are indicated if determined experimentally. The RV-C receptor is unknown. Bootstrap values (percent of 200 replicates) are indicated at key nodes.

RV-B contains the fewest, with 32 genotypes, and RV-C contains 57 genotypes [7,8]. For a RV strain to be assigned to a genotype, it typically requires greater than 86% nucleic acid sequence identity within key regions, while if it is more divergent, a new numerical

genotype is established [9]. Notably, phylogenic analyses cluster RV-C more closely with RV-A than with RV-B [10].

RVs can alternatively be classified by receptor usage into three distinct groups: RV-major, RV-minor and RV-C, with the “majority” of RVs using intercellular adhesion molecule 1 (ICAM-1) [11–13], a “minority” using low-density lipoprotein receptor (LDLR) family members [14], and all RV-C genotypes using cadherin-related family member 3 (CDHR3) [15]. Major-group RVs comprise the majority of RV-A and the entirety of RV-B, while the minor-group RVs consist of the remaining RV-A genotypes.

1.1.2 Clinical Relevance and Impact

RVs are a group of clinically-relevant respiratory viruses that are the etiologic agents of the common cold, with symptoms including cough, running nose, congestion, and sore throat [16–18]. While not all common colds are the result of a RV infection, RVs are responsible for the largest percentage of these typically mild respiratory infections, outranking coronaviruses, respiratory syncytial virus, parainfluenza viruses, and adenoviruses [19,20]. RV infections can also result in bronchiolitis or pneumonia in healthy individuals; however, severe outcomes are more frequently associated with infections in those suffering from underlying respiratory conditions, including asthma and chronic obstructive pulmonary disease (COPD) [21–24]. The tremendous diversity of co-circulating RVs further contributes to the frequency of recurrent infections, which ultimately drives the enormous impact of RVs – with some estimates as high as 20 billion dollars annually in the United States alone [25,26].

All RV species are capable of causing similar symptoms, and no single symptom is more likely to be associated with a particular species, group or genotype [27]. However, RV-B infections are typically linked with more mild and/or asymptomatic infections,

compared to RV-A and -C [28]. Conversely, RV-A and RV-C are not only more prevalent in the human population, but also have been more strongly linked with a heightened disease phenotype [28–30], with RV-C infections typically occurring during early childhood development, and RV-A infections being more prevalent in older children and adults. While RV-A infections do occur in young children, these infections often remain less severe and result in fewer hospitalizations, compared to an analogous RV-C infection [31–35]. Differences in clinical severity appear linked with the of co-evolution of RVs within the human population; whereby RV-B comprises the eldest lineage, followed by RV-A, and only in the last 3,000-5,000 years have RV-C emerged [36]. Clinical disease manifestations also correlate with lasting immunity as demonstrated from a cohort of children tracked longitudinally – where 8/12 patients who had been infected with RV-A lost all neutralizing antibodies after 4-8 years; while for those infected with RV-C, 19/20 retained high levels of neutralizing antibodies even after 14 years [37]. While these data suggest RV-C infections are primarily one-time events, the severity and propensity for asthma-induced hospitalizations in young children with not yet fully developed airways, makes RV-C of heightened focus for therapeutic development [38].

1.1.3 Current Treatment Options

To date, no approved vaccines or antivirals exist to combat RV infections. Despite some initial positive traction in the 1960s and 1970s [39–41], research into RV treatments slowed, primarily due to the great diversity among RVs, as well as the propensity for co-circulating RVs [42–44]. A lack of cross-reactive antibodies between genotypes further limits the efficacy and potential impact of a successful therapeutic [45]. Additionally, RVs bind their receptors deeply within the narrow 5-fold axis canyon, limiting access of potentially neutralizing antibodies, even within a single RV genotype [46]. Apropos with RV infections often solely resulting in common cold symptoms, they are seldom confirmed

clinically, and even more infrequently identified with genotype specificity. Therefore, without an accurate assessment of RV genotype circulation and seasonality patterns, it is impractical to develop genotype-specific treatments. Nonetheless, several antiviral compounds have been developed to targeting the RV capsid, such as Pleconaril, yet due to concerns of drug resistance, have ultimately proven ineffective [42,47,48]. Further, in order for antiviral treatments to be effective, they often need to be administered during early onset of symptoms, which is likely to occur prior to seeking medical treatment for RV infection. Thus, with a typically less severe disease presentation, the window for anti-RV therapeutics closes more rapidly. Antivirals targeting conserved proteins across RVs, including the RNA-dependent RNA polymerase (RdRp) and proteases have yet to be approved for clinical use [49].

1.2 Rhinovirus Tropism

1.2.1 Species Tropism

Unlike some other notable respiratory viruses, such as influenza A virus and coronaviruses, RVs have a very narrow host range that is restricted to higher primates. This is supported by data from several groups in the late 1960s and early 1970s, prior to the cessation of experimental studies using chimpanzees (*Pan troglodytes*), that demonstrated RV infection in this species with a genetically and biologically diverse panel of RVs including major group RV-B14 and -A43, and minor group RV-A30 and -A49 [50,51]. Beyond humans and chimpanzees, Pinto and Haff also demonstrated infection in experimentally inoculated gibbons (*Hylobatidae* family) with minor group RV-A1A and RV-A2 [52]. Further, Shipkowitz et al. successfully infected chimpanzees with another minor group RV, RV-30, during testing of a potential antiviral compound [51]. Recently, RV-C

was notably found to cause severe disease, including mortality, in chimpanzees in nature [53].

1.2.2 Tissue Tropism

During a typical RV infection, the upper respiratory tract, comprising the nasopharynx, is the primary site of viral replication. However, during more severe disease presentations, lower airway tissue can also become infected. Within the respiratory epithelium, RVs of all species have a preference for ciliated cells [30,54,55]. However, more work is needed to further elucidate any potential differences in cellular tropism between RV species and/or groups within the airway. RV-C replication efficiency in human airway epithelial (HAE) cultures varies by RV-C genotype with some demonstrating enhanced replication at cooler temperatures [56].

1.3 General Rhinovirus Lifecycle

1.3.1 Entry

RV particles are non-enveloped, and bind their target cells at the cell membrane via their cognate receptor, triggering particle uptake by receptor-mediated endocytosis. The mode of endocytosis for major-group RVs likely varies by cell-type where both dynamin- and clathrin-dependent, and clathrin-independent routes have been observed, and may ultimately be host species-specific, although further data is needed [57]. Within the endosome, ICAM-1 catalyzes uncoating of the viral capsid in a pH- and temperature-dependent manner for major-group RVs. While for minor-group RVs, LDLR is responsible for ligand internalization, but uncoating is induced solely by low pH, and thus occurs in a receptor-independent fashion. The entry mechanism for RV-C has yet to be elucidated, outside of binding CDHR3 as its receptor [57]. Like other picornaviruses, the RV genome

is thought to escape the endosome through pore formation, where the RNA can immediately be translated by host-cell machinery.

Notably, during the evolution of RVs, only a single amino acid change from either glutamine or glutamic acid to an arginine residue at position 234 in VP2 was necessary to alter receptor preference from ICAM-1 to CDHR3 [37]. Three other mutations likely co-evolved to aid in stabilizing the binding of CDHR3: asparagine at position 56 in viral protein (VP) VP3, isoleucine at position 276 in VP1, and a lysine residue at position 75. While the evolutionary timing of these mutations requires further study to place them in proper context, these mutations were likely advantageous and helped drive the divergence of the CDHR3-utilizing RVs. In support, the expression of ICAM-1 in the human airway is only elevated as a response to physical or chemical stress; such that major-group RV infections are most successful when the host has upregulated levels of ICAM-1. Whereas with a single mutation driving the switch in receptor to a constitutively expressed protein in the human airway epithelium, CDHR3, RVs gain a tremendous advantage of a constitutively susceptible host epithelial reservoir [37].

1.3.2 Protein Production and Viral Genome Replication

The viral genome is composed of a single-strand of positive-sense RNA, ~7.2kB in length, that has a 5'- viral protein genome-linked (VPg) cap, 3'- polyadenylated tail, and singular open-reading frame (ORF) [**Figure 1.2**] [58].

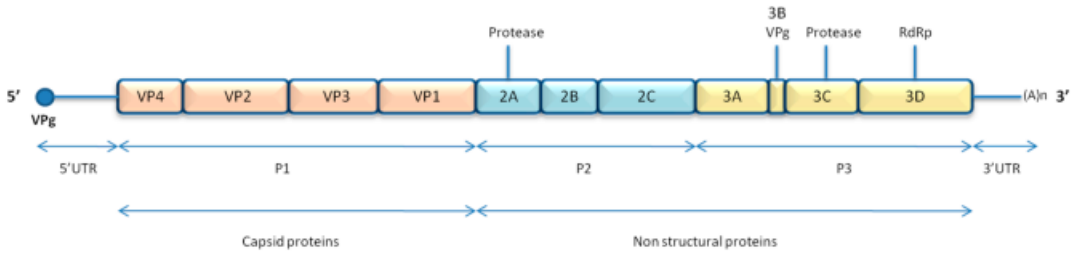

Figure 2.2: RV genome organization. Reproduced with permissions from [58]**.** From 5' to 3', the RV genome contains a 5'-UTR, followed by a single ORF containing structural

capsid proteins, VP4, VP2, VP3 and VP1, and nonstructural proteins, 2A, 2B, 2C, 3A, 3B, 3C and 3D. The 3' end of the genome contains a polyA-tail which is preceded by a 3'-UTR.

Immediately following uncoating, the singular ORF is translated into a polyprotein that is subsequently cleaved, yielding four structural and seven non-structural proteins. The structural proteins (VP1-VP4), which are encoded at the 5' end of the genome, form a pseudo-T=3 icosahedral capsid, where VP1-VP3 comprise the capsid subunits and VP4 serves as the supporting internal anchor. Sixty units of each structural protein self-assemble into the protective viral capsid. Non-structural proteins 2A and 3C are viral proteases responsible for proteolytic processing of the polypeptide into individual proteins, in addition to cleaving host factors such as transcription factors and antiviral effectors, triggering their degradation [59–65]. 2B and 3A are primarily responsible for membrane rearrangements associated with cytosolic viral replication, while also limiting the host cell's ability to traffic proteins [66–69]. 2C contains ATPase and helicase activities that are critical for unwinding RNA, necessary for replicating viral genomes [70,71], while 3B encodes for VPg critical for priming RNA synthesis [72–74], and 3D encodes the RdRp [75].

Replication of the viral genome requires a RdRp, while precursor proteins 2BC, 2C and 3A induce the assembly of cytoplasmic compartments where replication of viral genomes occurs [76]. Concurrently, RVs induce the overproduction of membranes and phospholipids to increase the available membrane surface area for viral replication [77,78]. Coined "replication organelles," these membrane-bound structures are multifunctional – providing protection to the viral RNA against degradative host enzymes and antiviral sensors, while also providing an environment for viral and host proteins to stage in close proximity [79,80]. While all positive-sense RNA viruses utilize replication organelles, their composition, including specific cellular factors, and originating subcellular

source often differ [81]. For enteroviruses, phosphatidylinositol-4-phosphate (PI4P) generated by phosphatidylinositol-4-kinase (PI4K) is critical for recruitment of viral and host proteins required for replication [81,82]. Further work is still needed to best understand the totality of host factors – both required and ancillary – for generating productive subcellular replication compartments.

1.3.3 Particle Assembly and Egress

Much has been inferred from related enteroviruses for how nascent RV proteins assemble and package. The structural proteins oligomerize to form the immature capsid, while the nonstructural proteins are thought to condense around a newly replicated positive-sense RNA genome to form the provirion [83]. During the final maturation step, the VP0 precursor protein is cleaved into VP2 and VP4 to complete the capsid formation [83]. While major- and minor-group RVs are most often associated with lytic release of new viral particles, RV-C infection largely lacks overt cytopathic effects (CPE), with the only observable phenotype being the slowing of cilia beating during peak viral replication [84]. Non-lytic viral release involves subverting cellular pathways including autophagy and necrosis. While many enteroviruses have been shown to utilize aspects of these pathways, the predominant cellular mechanism for non-lytic release of RVs is largely unknown [85,86].

1.4 The Impact of STING on RV Replication

In addition to the host factors noted above that are required for polyprotein translation and genome replication, stimulator of interferon genes (STING) was recently identified as an essential pro-viral factor for RV replication [87]. This was notable since STING is best known in the virology context as serving an antiviral role. Indeed, prior work has identified STING as a downstream effector molecule in detection of cytosolic dsDNA

[88]. Canonically, cytosolic dsDNA is sensed by cyclic GMP-AMP synthase (cGAS) which generates second messenger cyclic GMP-AMP (cGAMP). cGAMP then binds to STING which resides in the endoplasmic reticulum (ER). This event triggers the translocation of STING to the Golgi, where TANK-binding kinase 1 (TBK1) and IkB Kinase (IKK) are recruited, resulting in phosphorylation, and thus activation, of interferon regulatory factor 3 (IRF3). Phosphorylated IRF3 then undergoes dimerization and nuclear translocation leading to the transcription of antiviral genes, including interferon-β (IFNβ) [89,90].

Outside its role in antiviral defense, STING influences many other diverse cellular functions including autophagy, senescence, translation control, fatty-acid and glucose metabolism, and formation of cellular condensates [90]. Whether these non-canonical functions of STING are related to the mechanism underlying the pro-viral role for STING during RV replication is unknown, and there remains some debate over the requirement for STING during RV-B infections [87,91]. Importantly for this dissertation, human STING (hSTING) and mouse STING (mSTING) lack complete homology, and initial *in vitro* studies suggest mSTING cannot support RV replication [87]. Homology between human and murine STING orthologs is 69% conserved at the amino acid level, with much of this variation occurring within the transmembrane (56.3% conservation) and C-terminal tail (60.5% conservation) domains. Importantly, domain swapping between hSTING and mSTING has identified the cytoplasmic ligand-binding domain (79.1% conservation) as the key region impacting the proviral role of hSTING [87].

1.5 Propagation of RVs In Vitro

1.5.1 Growth in Cell Lines

Major- and minor-group RVs can be readily cultured using common laboratory epithelial and fibroblast cell lines including HeLa, A549 and WI-38 cells [84], as they

contain adequate endogenous receptor expression, and are permissive to RV replication. Of these, HeLa cells and their derivatives have become the standard for producing large quantities of virus after transfection of *in vitro*-transcribed viral genomes [92]. To recapitulate the cooler temperatures of the upper airway, RVs are regularly grown at 34^{o}C, rather than the typical core body temperature of 37^{o}C [18]. Beyond virus stock production, much of the scientific knowledge known about RVs stems from subsequent studies in these cell lines.

1.5.2 Initial Models for the Cultivation of RV-C

Despite the successful use of HeLa cells for the culture of RV-A and -B viruses, these cells were not susceptible to RV-C infection [84,93]. Utilizing *in vitro* transcribed RV-C15 RNA, Bochkov et. al determined that these cells remained permissive; however, serial passage experiments in cell lines failed to generate a cell-culture-adapted RV-C, which suggested an incompatibility of RV-C at the level of entry. As a result, initial characterization of RV-C15 was done in biopsied whole mounted primary sinus organ cultures [**Figure 1.3**] [84].

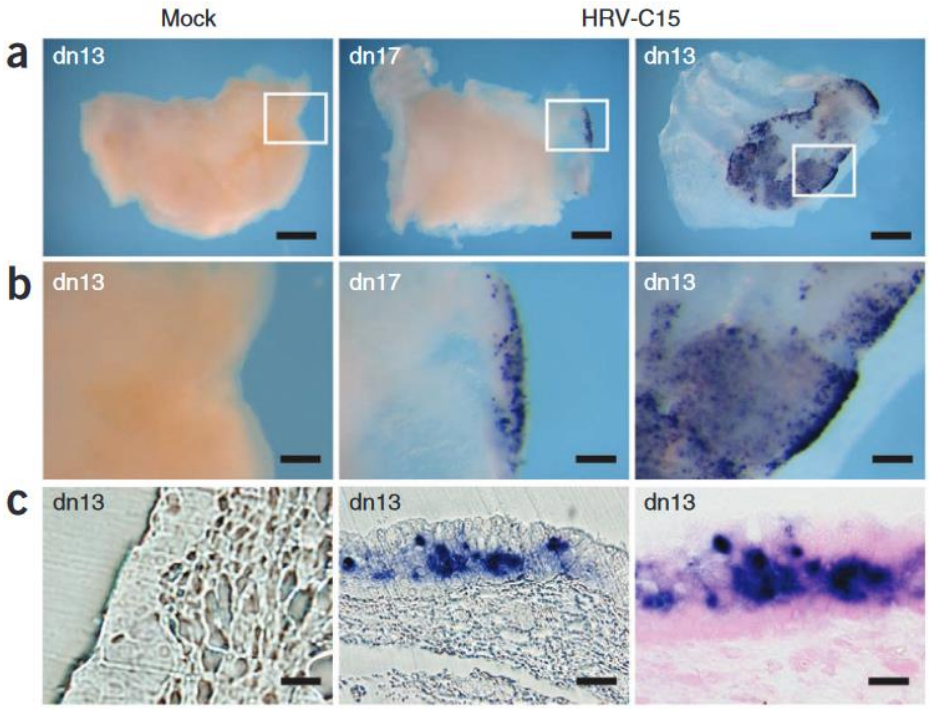

Figure 1.3: RV-C15 infection in sinus mucosa. Reproduced with permission from [84]**.** (**A**) Sinus cultures were inoculated with medium alone (left) or HRV-C15 (center and right), and whole mounts of the tissue were analyzed for HRV-C15 RNA by in situ hybridization (purple stain). Scale bars, 1 mm. (**B**) Higher magnification view of the areas boxed in panel a, showing uninfected cells (left) or cells containing viral RNA (center and right). Scale bars, 0.15mm. (**C**) Sections of mock- (left) or HRV-C–infected (center and right) sinus tissue. Right image is counterstained with eosin (pink). Scale bars, 15μm.

Although these tissues are difficult to obtain and long-term viability is poor, they provided the earliest platform for which to assay RV-C infection in a laboratory setting [93]. Bochkov et. al further confirmed the ability of nascent RV-C15 particles produced via transfection of *in vitro* transcribed RNA in HeLa cells to be fully infectious, and thereby capable of re-infection of primary sinus cultures [84], establishing the earliest protocol for rescuing RV-C. In an attempt to improve the utility of the RV-C culture system, Hao et. al, pioneered the culture of multiple genotypes of RV-C in human primary nasal and bronchial epithelial cell cultures, and importantly, identified the need to maintain a fully differentiated epithelium to achieve productive infection [93]. Unlike RV-A16 and RV-B14, which are competent for infection and replication in undifferentiated cells, RV-C11 and RV-C15 were

only capable of infection in fully-differentiated cultures grown under air-liquid interface (ALI) conditions [56,93]. Exposure to air on the apical surface, triggers differentiation of epithelial stem cells into a pseudostratified epithelium over the course of several weeks resulting in a culture consisting of multiple cell types including basal, secretory, ciliated, ionocyte and club. While these HAE cultures still require advanced cell culture practices compared to the cells lines used for growing major- and minor-group RVs, the HAE system allows for greater reproducibility compared to the *ex vivo* sinus biopsy cultures previously required. As HAE culture systems become more readily available, and economically worthwhile due to improved cell culture technologies and media preparations, a greater number of RV studies have begun to utilize these cultures when addressing questions of RV biology [94,95].

1.5.3 Discovery of CDHR3 as a Receptor for RV-C

Towards identifying the novel receptor for RV-C, Bochkov et. al compared gene expression between cells susceptible and non-susceptible for RV-C, and noted CDHR3 to be among the likeliest of potential candidates [15]. Ultimately, CDHR3 was then validated as a receptor for RV-C when CDHR3 was transfected into HeLa cells in the presence of RV-C, and increased binding and viral genomes were observed [**Figure 1.4**] [15].

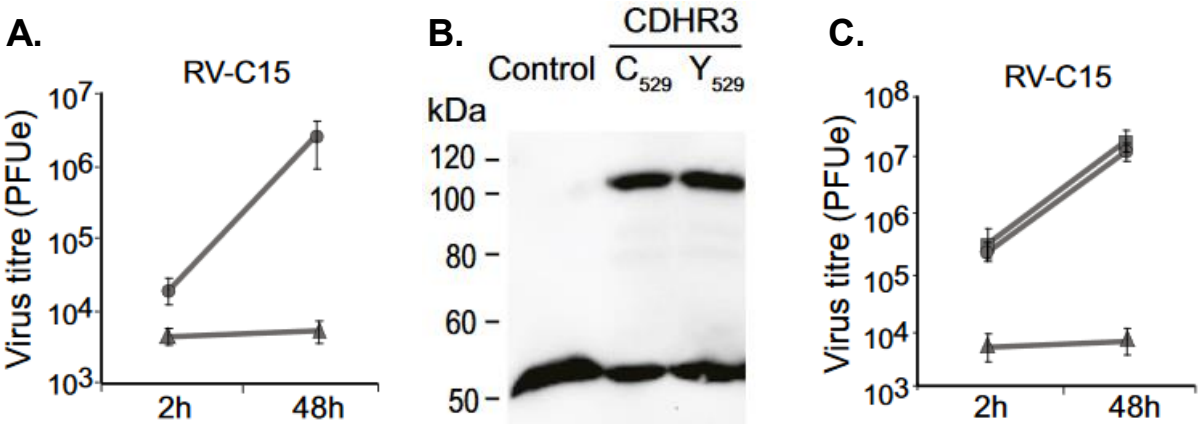

Figure 1.4: HeLa cells expressing CDHR3 SNP *rs6967330* led to the establishment of HeLa-E8, a cell line capable of supporting the complete RV-C lifecycle. Reproduced with permission from [15]**.** (**A**) RV-C15 binding (2 hpi) and replication (48 hpi) in HeLa cells transfected with wild-type CDHR3 (o), or Lipofectamine 2000 control (Δ) for 48 h (n = 5, data are means ± SD). (**B**) Western blot analysis of CDHR3 expression in HeLa cells transfected with wild-type (C529) or Cys529→Tyr variant (Y529) for 24 h and probed with α-CDHR3 polyclonal antibodies and α-tubulin antibodies (loading control). (**C**) RV-C15 binding (2 hpi) and replication (48 hpi) in HeLa cells transfected with CDHR3 Cys529→Tyr variant (□), FLAG-tagged CDHR3 Cys529→Tyr (o), or Lipofectamine 2000 control (Δ)for 48h (n = 5, data are means ± SD).

1.5.4 CDHR3 SNP *rs6967330* and the Development of HeLa-E8

Many studies have linked RV infection, and more specifically RV-C infection, to asthma exacerbations in young children. Concurrent with the identification of CDHR3 as the receptor for RV-C, Bonnelykke et al. described a potential basis for this connection – identifying a single nucleotide polymorphism (SNP) *rs6967330* within CDHR3, as a susceptibility locus for early childhood development of asthma [96]. This SNP yields a nonsynonymous coding mutation, swapping a cysteine to a tyrosine at position 529, located between domains 5 and 6. *In vitro* studies, attempting to understand the mechanism for this SNP's role in asthma development, linked the residue at position 529 with the subcellular localization pattern of the CDHR3 protein [**Figure 1.5**] [35,96], with CDHR3-C529Y stabilized on the cell surface, and CDHR3-C529 primarily localized intracellularly.

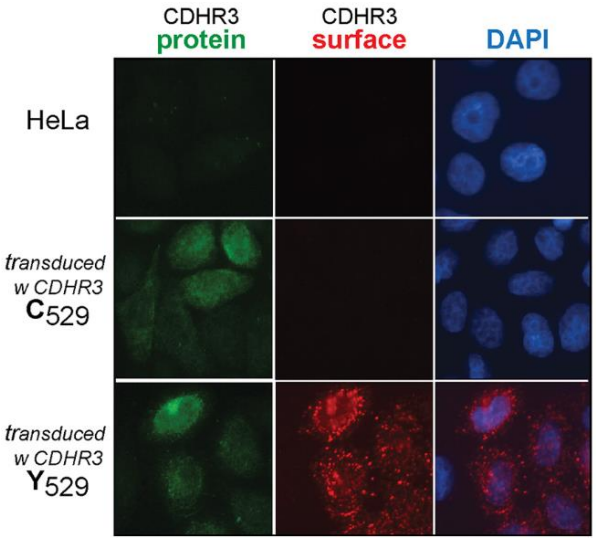

Figure 1.5: CDHR3 SNP *rs6967330* results in subcellular localization difference. Reproduced with permission from [31]**.** Fluorescence microscopy of CDHR3 expression. HeLa cells were transduced with lentiviral vectors for stable expression of N-terminal FLAG-tagged Cys529 or Tyr529 CDHR3 variants. Following cell fixation (4% paraformaldehyde) cells were stained (red) with anti-FLAG antibody (rabbit monoclonal; Sigma F2555) to visualize CDHR3 surface expression. They were then permeabilized (0.1% Tween 20 and 0.05% Triton X-100 in phosphate-buffered saline [PBS]) and stained with DAPI (4=,6-diamidino-2-phenylindole; blue) and with an anti-CDHR3 antibody (green; anti-FLJ23834 mouse monoclonal; Abcam ab56549). Native HeLa cells (cervical carcinoma origin) are homozygous A/A (data not shown) but do not express a CDHR3 protein unless transduced or transfected.

The difference in localization has been hypothesized to occur due to altered disulfide bond formation in the C529 variant, which disrupts the required disulfide bridge between C592 and C566. SNP *rs6967330* therefore causes the CDHR3-C529 protein to be misfolded, and thereby returned to the cytoplasm for degradation [96]. Intriguingly, the tyrosine-expressing, asthma-associated risk allele, is the ancestral allele within humans, and this residue is highly conserved across most mammals. Further, only in the past 8,000 years has the human population undergone a rapid evolution away from Y529 to expression of CDHR3-C529 [31,36]. The potential impact of the specific amino acid residue at position 529 has on RV-C infection, and the human population as a whole, will be further addressed in greater detail in later discussions sections.

Once it was determined that CDHR3 was a putative receptor for RV-C species, a modified HeLa cell line, named HeLa-E8, expressing the CDHR3-C529Y allele, was quickly established, allowing for the entire RV-C lifecycle to be completed in a non-differentiated cell culture system [15].

1.6 Using Mice to Model Rhinovirus Infection

1.6.1 Minor Group RV Mouse Models

To enable studies of RV-mediated disease, including spread, activation of immune defenses, and testing of therapeutics, animal models have been implemented. Mice in particular are relatively inexpensive, genetically tractable, and have a wide range of available reagents and resources. However, mice are not natural hosts for RVs, and therefore, in the development of mouse modes for particular RV groups, modifications to either virus or mouse have been necessary. For example, early observations noted that while minor group RVs were capable of utilizing the murine ortholog of LDLR to adsorb and gain entry into mouse cells, ensuing viral replication and release of progeny virus was precluded [97]. Therefore, to overcome the inability of minor group RV to replicate in mouse cells, Yin and Lomax [97] took advantage of the error-prone nature of the viral RdRp to select for variants capable of growing in murine L cells. Upon completion of 40 alternating passages in these murine fibroblasts and HeLa cells, a mouse-adapted RV-A2, termed RV-A2/L, was established [97]. Notably, the same group repeated this technique for an additional, minor-group RV, RV-A1A [98]. Greater efforts are needed to determine the extent of the mouse adaptations within the nonstructural proteins but alterations to 2B, 2C and 3A have been identified for RV-A2 and certain mouse adapted major-group viruses [79,97,99]. Interestingly, it was later demonstrated that RV-A1A was unique among RVs in its ability to infect mouse cells without prior adaptation [100]. As

more mouse cell lines have been developed, including tissue-specific cell types, further testing of RVs has been performed such as RV-A1B infection in murine lung-derived LA-4 and Mad/C3 cells, which confirmed the ability of these mouse cells to support the RV lifecycle [101].

Moving from the *in vitro* to the *in vivo,* Yin and Lomax further expanded the utility of mouse-adapted RV by growing RV-A2/L in primary mouse nasal turbinates for two passages prior to using this virus to inoculate BALB/c mice – marking the first documented example of a small-animal model for RVs [98]. Bartlett et al. demonstrated the ability to infect BALB/c mice with RV-A1B and observed viral-induced host responses compared with UV-inactivated RV-A1B, or major-group RV-A16-infected transgenic BALB/c mice expressing human ICAM-1. [102,103]. Similar RV-A1B infections have also categorized been in C57Bl/6 mouse backgrounds [104]. Taken together, mouse infections with minor group RV are possible, and can be improved through serial passaging of the virus prior to the infection.

1.6.2 Major Group RV Mouse Models

Like minor group RVs, major group RVs (*e.g.,* RV-A39 and RV-A16) are capable of replicating in mouse cells, however they are unable to adsorb, precluding infection [101,105] due to lack of ICAM-1 present on the murine cell surface [99]. Further, Bella and Rossmann reported that murine ICAM-1, even when expressed to sufficient levels in permissive murine cell lines, does not bind major group RV capsids [106]. Harris and Racaniello then demonstrated the ability of RV-A16 to infect L cells expressing the human ICAM-1 receptor [99]. A chimeric human-mouse ICAM-1 protein, containing domain 1 and 2 of human ICAM-1 with the remainder of the protein being of murine origin, stably expressed in the LA-4 cell background was sufficient to promote viral entry [101,107]. Bartlett et. al demonstrated the ability of RV-A16 to infect transgenic BALB/c mice

expressing this chimeric ICAM-1 receptor [102]. Notably, these mice showed evidence of replicating viral RNA, which is absent in UV-inactivated RV-A16 or non-transgenic mice, and induced a potent host immune response [102,108]. Any further replication defects in mouse cells can be overcome through serial passage [79], as done for minor group RVs [98]. Notably, replication defects were also observed upon infection of human ICAM-1-expressing baby hamster kidney cells with RV-B14, despite successful particle uptake [109].

1.6.3 RV-C Mouse Models

Non-minor group RV infection of mice without adaptations have yet to be reported, [15,84,110]. Further, given the difficulty of culturing RV-C *in vitro*, it was somewhat surprising when Rajput and Han et. al reported infection of wild-type (WT) BALB/c mice with RV-C15 [111]. Here the authors sought to solidify the connection between RV-C and asthma development, concluding that mice infected with RV-C15 preferentially drive the innate immune response towards a type 2 inflammatory response, including elevated bronchoalveolar eosinophils, mucin 5ac, IL-5, IL-13, IL-25, IL-33 and a greater expansion of type 2 innate lymphoid cells [111]. The resulting differential inflammatory response between a RV-C species and minor-group RV-A1B is an elegant finding, and connects RV-C infection, specifically, with early age asthma development. However, these data have not been replicated by other groups in the field to date.

1.7 Introduction to My Dissertation

Given the relatively recent identification of RV-C and its heightened impact on human health compared to other the RV species, it was important to better understand the biology of this important respiratory virus. Much of the understanding of RV-C-specific biology has been assumed from the other RVs and even more generally from other

enteroviruses. Specifically, knowledge gaps exist about the requirements for completing the RV-C lifecycle in human cells and whether replication is similarly efficient in murine cells. Together, aspects from these studies could be then applied toward developing mouse models for RV-C infection, enabling comparative studies between RV species in mice, as well as future development of vaccines and therapeutics.

Here, we define the molecular determinants of RV-C species tropism *in vitro*, and then apply them to mice, *in vivo.* Through this work we were able to better understand the biology of RV-C and compare it with major- and minor-group RVs. We note a preference for RV-C replication organelles formed from endoplasmic reticulum membranes, the requirement for hSTING in a RV species-specific manner, and the induction of incomplete autophagy which may facilitate non-lytic release.

We then assessed the ability of RV-C to function in mouse cells at the three primary stages of the viral lifecycle: entry, replication, and egress of infectious particles. To understand the requirement of RV-C to utilize CDHR3 as its putative receptor, we began our foray into RV-C tropism by assessing the ability for RV-C to potentially bind the murine ortholog of CDHR3 (mCDHR3). Notably, mice, *Mus musculus,* contain a histidine residue at position 529 (C529H), where the H529, like that of Y529, is presumed to stabilize disulfide bond formation and cell surface expression of mCDHR3 [31,96]. We then assess RV-C viral replication in mouse cells, and demonstrate the ability for *in vitro* transcribed RV-C RNA to replicate in murine lung epithelial cells. RV-C replication can be further increased with expression of human STING. We finally complete the viral lifecycle, by confirming the ability of nascent RV-C virions produced in the murine airway cells to be properly packaged and capable of reinfection of a permissive host. Applying our findings to the organismal level, we demonstrate the ability of RV-C to replicate in humanized,

hCDHR3- and hSTING-expressing mice; garnering significant increases in genome copy number, and thus validating our *in vitro* findings.

Taken together, our work provides the foundation for further development of the RV-C mouse model, where it can be utilized alongside the already existent mouse models for major and minor group RVs, and asthma, for understanding the impact of RV-C pathogenesis and testing of antiviral therapeutics.

Chapter 2 : Modeling Innate Antiviral Immunity in Physiological Context

Monty E. Goldstein[1] and Margaret A. Scull[1,#]

[1] Department of Cell Biology and Molecular Genetics, Maryland Pathogen Research Institute, 3134 Bioscience Research Building, University of Maryland, College Park, MD 20742, USA

[#] Corresponding author: 1-301-405-6846; scull@umd.edu

In order to develop the most applicable model for RV-C, it was first necessary to assess the criteria for what ultimately makes a model system relevant. In this review article, we aim to address this question by defining the antiviral signaling capabilities of commonly used model systems, from 2D cell culture, to 3D engineered tissues and organoids, to small animal models. Then, for each archetypal model system, we evaluate how well each model recapitulates the nature of the organism, and its overall utility for modeling the *in vivo* representation of a viral disease phenotype.

This chapter was previously published: Goldstein ME, Scull MA. Modeling Innate Antiviral Immunity in Physiological Context. J Mol Biol. 2022 Mar 30;434(6):167374. doi: 10.1016/j.jmb.2021.167374. Epub 2021 Dec 1. PMID: 34863779; PMCID: PMC8940657. [112]

this license, visit http://creativecommons.org/licenses/by/4.0/. My contribution to this work includes performing a comprehensive literature review, generating figures and tables, and writing and editing the manuscript.

2.1 Highlights

- The innate antiviral immune response is essential for controlling viral infection.
- Antiviral responses vary according to species, cell type, and microenvironment.
- 3D models allow interrogation of antiviral immunity in a physiological context.
- Further advancing 3D models will enable additional insight into the host response.

2.2 Abstract

An effective innate antiviral response is critical for the mitigation of severe disease and host survival following infection. *In vivo*, the innate antiviral response is triggered by cells that detect the invading pathogen and then communicate through autocrine and paracrine signaling to stimulate the expression of genes that inhibit viral replication, curtail cell proliferation, or modulate the immune response. In other words, the innate antiviral response is complex and dynamic. Notably, in the laboratory, culturing viruses and assaying viral life cycles frequently utilizes cells that are derived from tissues other than those that support viral replication during natural infection, while the study of viral pathogenesis often employs animal models. In recapitulating the human antiviral response, it is important to consider that variation in the expression and function of innate immune sensors and antiviral effectors exists across species, cell types, and cell differentiation states, as well as when cells are placed in different contexts. Thus, to gain novel insight into the dynamics of the host response and how specific sensors and effectors impact infection kinetics by a particular virus, the model system must be selected

carefully. In this review, we briefly introduce key signaling pathways involved in the innate antiviral response and highlight how these differ between systems. We then review the application of tissue-engineered or 3D models for studying the antiviral response, and suggest how these *in vitro* culture systems could be further utilized to assay physiologically-relevant host responses and reveal novel insight into virus-host interactions.

KEYWORDS

pattern recognition receptors; interferon; microenvironment; organoids; tissue engineering

2.3 Introduction

The innate immune system is an essential component of host defense against viral infection. An effective innate antiviral response requires successful pathogen detection followed by signal transduction and expression of interferons (IFNs), as well as an array of pro-inflammatory cytokines and chemokines. Together these molecules promote the establishment of a local antiviral state and help recruit immune cells to the site of infection. The innate immune response also facilitates cross-talk with the adaptive immune system to orchestrate resolution of the ongoing infection and ensure a more rapid response upon subsequent challenge. Without an intact innate antiviral response, viral replication proceeds unchecked, potentially leading to disseminated infection and life-threatening consequences for the infected individual (reviewed in [113]). This was recently evidenced in severe acute respiratory syndrome coronavirus 2 (SARS-CoV-2)-infected individuals that suffered severe outcomes as a result of genetic defects in the IFN pathway or autoantibody-mediated neutralization of IFN [114–116].

The discovery of key innate immune sensors and effectors – beginning with the description of interferon activity by Isaacs and Lindenmann in 1957 [117,118] – has led to

an increased understanding of the molecular basis for innate antiviral immunity. Subsequently, an immense amount of research has been conducted to define which innate immune sensors and effectors are critical for defense against specific viruses and their underlying mechanisms of action. Since standard cell lines in monolayer culture are readily scalable and generally amenable to overexpression or knockout approaches, they remain the 'go to' system for the identification of novel pro- and antiviral host factors and initial phenotyping of their impact on viral replication. However, antiviral signaling pathways are defective in some cell lines. Furthermore, viruses exhibit tropism for specific cell types *in vivo;* not only does sensor and effector expression vary between cell types, but the same cell may also respond differently (e.g., in type and magnitude) depending on cell differentiation state, cell-cell interactions, and other microenvironmental cues. The spatiotemporal patterns of the response will also depend on the location of infected and uninfected cells within the tissue and other physical dynamics within the system. Therefore, both cell type and its context are important factors when studying innate antiviral immune responses. In this regard, animal models are useful, as the complexity of these interactions is certainly captured *in vivo*; however, species-specific differences in immunity may not allow for direct extrapolation of results to infections in the human population, and human challenge studies are not always feasible.

Cell culture systems that capture relevant cell types, tissue architecture, and biomechanics to recapitulate the initiation, dissemination, and impact of antiviral signals have the potential to yield further insight. Tissue-engineered and 3D cell culture platforms are capable of meeting these requirements by incorporating relevant homo- and heterotypic cell-cell interactions, extracellular matrix (ECM) components, and multi-organ compartments. Additionally, these cultures can be derived from primary cells which have fewer defects in antiviral pathways that often result from mutations accumulated through

continuous passaging or immortalization methods. Here we provide a brief overview of pathogen detection and signaling pathways that are central to the interferon response, review how these sensors and effectors can vary between model systems, and highlight the application of more physiologically-relevant *in vitro* systems to probe novel concepts in intrinsic and innate antiviral immunity.

2.4 Key players in innate antiviral defense

Activation of the innate antiviral response is based on the ability of a cell to distinguish 'self' from 'non-self'. This is achieved, in part, through cellular expression of pattern recognition receptors (PRRs) that sense conserved structural features associated with bacterial, fungal, or viral pathogens, collectively termed pathogen-associated molecular patterns (PAMPs), as well as molecular signatures associated with damaged or dying cells referred to as damage-associated molecular patterns (DAMPs). Several classes of PRRs have been defined since Charles Janeway first hypothesized their [119], and individual receptors can be grouped by localization, ligand specificity, and function. Membrane-bound PRRs include the Toll-like receptors (TLRs) and C-type lectin receptors (CLRs), while cytosolic receptors include the RNA-sensing RIG-like receptors (RLRs), the absent in melanoma 2 (AIM2)-like receptors (ALRs), and nucleotide-binding oligomerization domain (NOD)-like receptors (NLRs). The importance of these receptors in the antiviral response is underscored by the vast array of viral strategies that have evolved to antagonize PRR activation and downstream signaling pathways (reviewed in [120–122]).

TLRs were the first PRRs described in humans [123–125], and to date, seven (TLR2, -3, -4, -7, -8, -9, and -10) of the ten TLRs identified in humans have been shown to play an important role in mediating host antiviral responses [reviewed in [126]]. TLRs

are found on cell-surface and intracellular (e.g., endosomal) membranes where they are well-positioned to detect viral glycoproteins (e.g., TLR2 [127]; TLR4 [128], also reviewed in [126]) or nucleic acid moieties (e.g., TLR3 [129], TLR7 [130]; TLR8 [131]; TLR9 [132]) during initial virus uptake into the cell (**Figure 2.1, left**). Indeed, virus-associated PAMPs are often linked to nucleic acid structures found in viral genomes, replication intermediates, or viral transcripts such as uncapped or double-stranded (ds) RNA as well as CpG-DNA that are either absent or sequestered in host cells. Activated TLRs signal via their Toll-Interleukin-1 resistance (TIR) domain through adapter molecules such as myeloid differentiation factor 88 (MyD88) and TIR domain-containing adaptor-inducing interferon-β (TRIF), ultimately leading to the nuclear translocation of nuclear factor kappa-light-chain-enhancer of activated B cells (NF-κB), activator protein 1 (AP-1), or interferon regulatory factors (IRF3, IRF7). Collectively, these transcription factors drive the production of both pro-inflammatory cytokines and interferons. Similar to TLRs, CLRs are also membrane-associated and found at the cell surface. CLRs, however, bind carbohydrates and are most well-known for their role in mediating fungal immunity. Activated CLRs may signal through immunoreceptor tyrosine-based activation motif (ITAM), hemi-ITAM, or immunoreceptor tyrosine-based inhibitory motifs (ITIM); alternatively, CLRs such as dendritic cell-specific intercellular adhesion molecule-3 grabbing non-integrin (DC-SIGN) and liver/lymph node-specific intercellular adhesion molecule-3 grabbing non-integrin (L-SIGN) mediate internalization of the receptor-ligand complex (reviewed in [133]). CLR-ligand endocytosis can promote antigen processing and major histocompatibility complex (MHC) presentation; however, in some cases, viruses such as human immunodeficiency virus (HIV) [134] and dengue virus (DENV) [135] have hijacked this interaction to promote trans-infection or virion uptake into target cells.

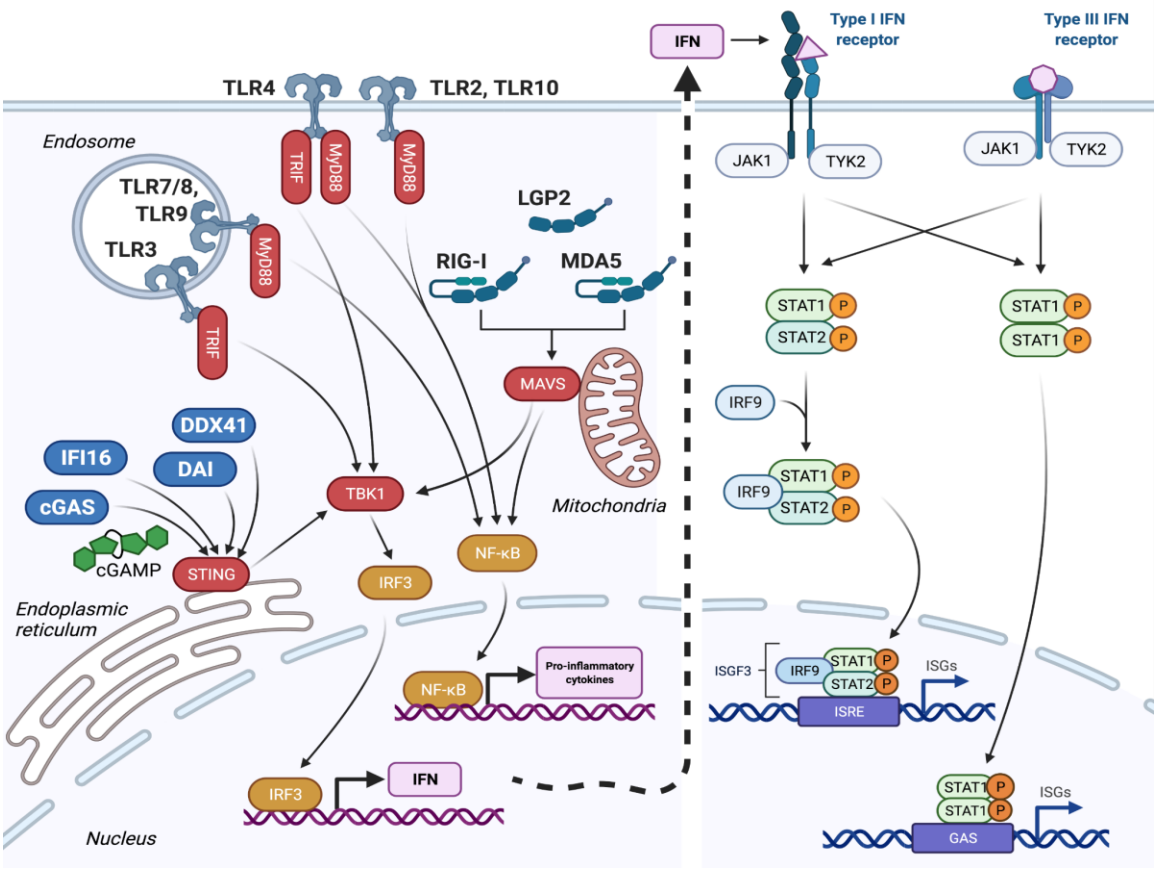

Figure 2.1: Diagram of pattern recognition receptor-initiated signaling events, interferon production, and subsequent interferon signaling leading to interferon-stimulated gene expression. Left) Pattern recognition receptors (blue), including membrane-associated TLRs, and cytosolic RNA (RIG-I, MDA5), and DNA sensors (cGAS, IFI16, DAI, DDX41), signal through adaptor proteins and downstream kinases (red), resulting in transcription factor activation (yellow; NF-κB, IRF3) and subsequent expression of IFN and pro-inflammatory cytokines. **Right)** Following secretion, IFN-I and IFN-III bind to their respective receptors on the cell surface. Receptor dimerization triggers the JAK/STAT pathway leading to phosphorylation and homo- or heterodimerization of STAT proteins. Both STAT1/STAT2 heterodimers (in association with IRF9 to form ISGF3) and STAT1 homodimers can drive ISG expression via interaction with ISRE and GAS elements, respectively, in target promoters. Created with BioRender.com.

RLRs include retinoic acid-inducible gene I protein (RIG-I), melanoma differentiation-associated protein 5 (MDA5), and laboratory of genetics and physiology 2 (LGP2). Both RIG-I and MDA5 sense dsRNA, although RIG-I associates preferentially with short 5′ di- and triphosphorylated short dsRNA [136,137] and MDA5, with long dsRNA ([138]; reviewed in [139]). Notably, although known for its role in defense against RNA

viral infections, RIG-I can also recognize DNA viral infections via RNA polymerase III-mediated conversion of AT-rich dsDNA into 5'-triphosphate (ppp) RNA [140,141]. Upon PAMP interaction, RIG-I and MDA5 interact with the downstream adaptor mitochondrial antiviral-signaling protein (MAVS) (also known as IFN-β promoter stimulator I (IPS-1), virus induced signaling adaptor (VISA), or caspase activation recruitment domain (CARD) adaptor inducing IFN-β (Cardif)) via their CARD domain to trigger interferon expression. LGP2, on the other hand, lacks a CARD domain, indicating LGP2 cannot initiate downstream signaling but may instead regulate RIG-I and MDA5 [142]. Cytosolic DNA receptors have also been identified and include DNA-dependent activator of IFN-regulatory factors (DAI) [143], DExD/H box helicases (e.g., DEAD-box helicase 41 (DDX41) [144]), interferon gamma inducible protein 16 (IFI16) [145], AIM2 [146], and cyclic GMP-AMP synthase (cGAS) [147], among others. Many of these receptors signal through stimulator of interferon genes (STING) and TANK-binding kinase 1 (TBK1) leading to IRF3 activation, although other pathways have also been reported (e.g., through β-catenin [148]) that also result in IFN gene transcription. In contrast, AIM2 engages apoptosis-associated speck-like protein containing a caspase recruitment domain (ASC) leading to inflammasome activation and caspase-1-mediated proteolytic processing of immature IL-1β and IL-18 [146], despite a lack of structural similarity to the NLR class of PRRs typically associated with inflammasome activation. While NLRs play an important role in host immunity, their role in antiviral defense is less well understood and both positive and negative effects on the interferon response have been described, often through intersection with the antiviral signaling pathways noted above (reviewed in [149]).

To date, three types of interferon have been defined according to shared structural features, receptor usage and biological effects: type I IFN (IFN-I; including 13 IFN-α subtypes, -β, -ε, κ, -ω) [117,150–153], type II (IFN-II; IFN-γ) [154], and type III (IFN-III;

comprising 4 IFN-λ subtypes) [155–157], with IFN-I and -III having well-established antiviral activity. This activity is mediated through autocrine and paracrine signaling where IFN-I and -III bind unique heterodimeric receptors – IFNα/β receptor subunit 1 (IFNAR1) / IFNα/β receptor subunit 2 (IFNAR2) in the case of IFN-I [158,159]; IFNLR1 / IL-10R2 in the case of IFN-III [155,156] (**Figure 2.1, right**). Receptor ligation by either IFN-I or -III leads to receptor dimerization and Janus kinase 1 (JAK1) phosphorylation which then triggers phosphorylation of the receptor and subsequent recruitment of signal transducer and activator of transcription (STAT) proteins (reviewed in [160]). Phosphorylated STAT1 and STAT2 heterodimerize and associate with IRF9 to form IFN-stimulated gene factor 3 (ISGF3) which can then translocate to the nucleus and stimulate antiviral gene transcription through binding of interferon-stimulated response elements (ISREs). Beyond this canonical signaling pathway, other kinases (e.g., JAK2, tyrosine kinase 2 (TYK2)) and STAT proteins can be phosphorylated, or STAT-independent pathways (e.g., mitogen-activated protein kinase (MAPK), phosphoinositide 3-kinase (PI3K)) activated after IFN treatment (reviewed in [161]). Notably, STAT1 homodimerization, or heterodimerization with other STATs (e.g., STAT3), can promote expression of additional interferon-stimulated genes (ISGs) through interaction with a gamma interferon activation site (GAS). Although hundreds of ISGs and non-coding RNAs have been identified ([162]; reviewed in [163]), the mechanism of action of relatively few have been described in detail. Nonetheless, it is clear from these studies, that ISGs antagonize the viral life cycle at each stage, helping to clear infection through elimination of viral components, induction of apoptosis, or by conferring resistance to uninfected cells. IFN-I can also have antiproliferative effects, modulate cell differentiation, and further sculpt the immune response through activation or suppression of specific immune cell subsets (e.g., T cells and regulatory T cells) [164,165]. These differential effects may be the result of IFN

concentration, variation in receptor expression levels, or time of IFN exposure (reviewed in [166]).

Finally, negative regulators of the IFN response play an essential role in resolving inflammation after viral clearance to avoid excessive toxicity and immunopathology associated with interferonopathies. Resolution of interferon expression and signaling occurs through a variety of mechanisms mediated by direct protein-protein interaction, post-translational modification, or non-coding RNAs that result in the degradation or inactivation of the PRRs, signaling intermediates, transcription factors, IFNs, and IFN receptors mentioned above. For example, JAK / STAT signaling is curtailed by IFN receptor endocytosis [167] as well as through the binding of ubiquitin-specific peptidase 18 (USP18) to IFNAR2, thereby blocking JAK1 interaction [168]. Similarly, suppressor of cytokine signaling (SOCS) proteins bind phosphorylated tyrosine residues to inhibit JAK activity and further target signaling components for ubiquitination and subsequent degradation via their Src homology 2 (SH2) and SOCS box domains, respectively (reviewed in [169]).

2.5 Important considerations in modeling authentic antiviral responses

2.5.1 Variation in the expression and function of innate immune sensors and antiviral effectors

Interspecies variation

Faithful recapitulation of human antiviral responses in a model system requires matched expression and functional conservation of relevant PRRs, signaling molecules, IFN receptors, and the full repertoire of ISGs. As noted above, cell lines from different species are often used as an *in vitro* "host," while animal models are a frequently-

employed tool for assessing viral pathogenesis. Mice in particular have been extensively utilized for analyzing various aspects of the host response to infection, and are therefore our focus in this section, although certainly additional variation exists across other model species (reviewed in [170–173]). While the overall architecture of the murine immune system is remarkably similar to humans given our drastically different lifestyles, key differences do exist [174–177], including in the phenotype and function of specific leukocyte populations (reviewed in [178]) and in a multitude of host factors that contribute to the innate antiviral response [179].

As species lineages radiated, each was subjected to their own set of diverse pathogens which drove variation in innate immune genes and led to significant changes in immune profiles over time [180]. For example, among the 84 rapidly-evolving, higher-primate, immunity-related genes as identified in Barreiro and Quintana-Murci [181], remarkably 30 of these have been linked to HIV. While this highlights the impact of just a single virus, the authors stipulate these virus-driven alterations in immunity are a product of selection not solely targeting HIV, but rather against a multitude of ancestral retroviral pathogens. Thus, species-specific aspects of innate antiviral immunity must be considered when using a non-human model system. This is true for both *in vitro* or *in vivo* systems since the level of conservation between humans and animals impacts the utility of both small animal models and cell lines from other species in dissecting the parameters of innate antiviral immunity for specific pathogens.

Not surprisingly, proteins involved in regulating the immune response, especially transcription factors and kinases have been shown to be more highly conserved between species, constrained by their multi-functional roles, whereas cytokines display strong specifies-specific diversity, attributed to maintaining a singular role in combating host-specific pathogens [179]. TLRs, for example, are incredibly well conserved and are

estimated to have originated with the diversification of vertebrates. Only TLR10, expressed in humans not mice, and TLR11-13 in mice and not humans, represent the main discrepancy to the overall TLR conservation [182]. Similarly, some NLRs have undergone expansion in mice (e.g., *Nlrp1*, *Nlrp4*, *Nlrp9*), while others have been lost (e.g., *NLRP8*, *NLRP13*) [183]. However, despite similar representation of highly-conserved orthologous proteins, the cellular expression pattern and tissue distribution of some PRRs is not uniform between species. For example, TLR4 in humans is highly expressed in spleen and peripheral blood lymphocytes (PBLs) [124,184]; while in mice, expression is most pronounced in the lung, heart, and spleen [185]. Expression profile differences are predicted to also exist in TLR2, TLR3, and TLR9 (reviewed in [186]). The molecular basis for these differences in basal TLR expression as well as differences in TLR upregulation in response to stimuli may be related to poorly conserved promoter sequences [187].

Evolution across species can also impact PRR ligand affinity and specificity, leading to differences at the functional level even in cases where expression profiles and the signal-transmitting domain (e.g., TIR, in the case of TLRs) is well-conserved. For example, the optimal CpG motif for human TLR9 activation (GTCGTT) differs from murine TLR9 (GACGTT) [188]. Further, there are species-specific differences in recognition of single-stranded RNA, with TLR7 and TLR8 acting as the primary sensors for this PAMP in humans, and TLR7 and TLR13 acting in mice [130,131,189,190]. Notably, murine TLR8 was originally thought to be non-functional, but subsequent work demonstrated activity after imidazoquinoline stimulation in the presence of DNA oligonucleotides [191] and a more recent study by Zhang and colleagues suggests a role for TLR8 outside of immunity [192]. Further, even in cases where human and mouse innate immune proteins function similarly in their respective hosts, relatively minor differences in sequence can have significant impacts on virus-host interactions and resulting antiviral response. For

example, viruses such as hepatitis A virus (HAV) and hepatitis C virus (HCV) are known to abrogate IFN production via cleavage of the upstream adaptor molecule, MAVS; however, a lack of sequence conservation at the HAV cleavage site in mice curtails the ability of HAV to block signaling via this mechanism, leading to an enhanced host response and failure of the virus to establish infection [193]. Similar barriers exist for other viruses such as DENV and Zika virus (ZIKV), both of which fail to cleave mouse STING [194,195] and degrade mouse STAT2 [196,197], restricting infection.

Differences in interferon gene composition also exist between species, illustrated by the expression of only two functional IFN-III genes, *Ifnl2* and *Ifnl3*, in mice, compared to the four expressed in humans. The implications of this in modeling the human antiviral response, however, remain unclear since the role of specific interferon subtypes in humans remains elusive despite purifying (in the case of IFN-α) or positive (as observed for IFN-λ) selection to suggest essential, unique functions [198]. Additionally, while IFN-I signaling is conserved across vertebrates, IFNAR1 and IFNAR2 proteins differ substantially, with only 50-51% sequence identity between humans and mice, making it difficult to relate IFN receptor activation and the precise nature of the interferon-stimulated response in murine models back to a human context [199]. Finally, many inbred mice used in laboratory experiments lack one or more interferon-stimulated genes (ISGs). CBA/J and BALB/c strains, for example, contain defective Mx1 genes [200]. While these defects may facilitate the use of otherwise non-permissive hosts to model pathogenesis, (e.g., influenza (IAV) [201]), researchers focusing on specific aspects of intrinsic antiviral immunity at the molecular level should carefully select the host background to ensure accurate modeling.

Intrahost variation

In addition to the differences in innate antiviral host factor expression patterns between species described above, variation exists within a host as a function of tissue and cell type [202–204]. This variation can impact the initiation, magnitude, and even primary mechanism of an antiviral defense; thus, even when using human cells to model antiviral responses, the tissue source and identity of the cells must be considered. For example, stem cells – a useful tool in a wide range of tissue engineering and regenerative medicine applications – are known to be resistant to viral infection (reviewed in [205]). This suggests they employ different antiviral defense mechanisms from their differentiated counterparts. Supporting this hypothesis, early observations noted that stem cells do not produce interferon and are insensitive to IFN treatment [206,207]. More recently, Maillard and colleagues demonstrated antiviral RNA interference (RNAi) in undifferentiated cells [208] and Wu et al. revealed that stem cells are characterized by intrinsic expression of canonical ISGs [209] providing additional insight into the underlying mechanistic basis for stem cell resistance to viral infection.

PRR expression profiles across fully differentiated cells are unique to individual receptors with RLRs being found in most cell types and NLRs, CLRs, and TLRs frequently detected in myeloid cells such as dendritic cells and macrophages in addition to endothelial and epithelial cells, suggesting a more restricted expression profile (reviewed in [210–214]). Furthermore, expression of specific TLRs across all epithelial cells is not uniform. Ioannidis et al. found that human tracheal epithelial cells lacked the TLR8 protein, and only expressed TLR6 and TLR2 in basal cells while other TLRs (TLR4, 5, 7, 9, 10) were confined to the luminal surface. In contrast, TLR1 and TLR3 were detected throughout the pseudostratified epithelium [204] (**Figure 2.2A**). Similar data have been reported in the gut, where Price et al. utilized TLR reporter mice to visualize TLR

expression in intestinal epithelial cells, revealing temporal differences and spatial compartmentalization that correlated with ligand-induced responses [203]. Most notably, TLR7 and TLR9 were not detected in epithelial cells, but found in the underlying lamina propria, and TLR5 expression in the small intestine was only found in Paneth cells in the crypt (**Figure 2.2B**). Huhta and colleagues took an immunohistochemical approach to similarly characterize TLR expression in human and mouse alimentary tracts, noting higher expression of TLRs in the small intestine [211] [99], while Faure-Dupuy et al. clearly show distinct TLR expression profiles in primary liver cell subsets [215].

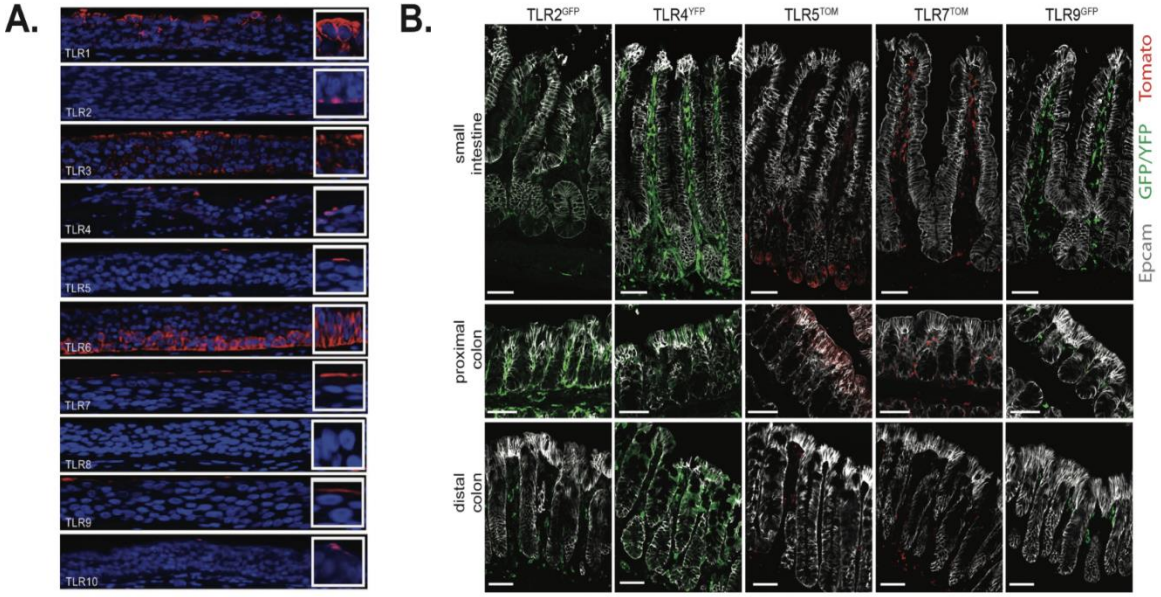

Figure 2.2: Variation in Pattern Recognition Receptor Expression Profiles Across Cell Types. A) Immunofluorescence staining using TLR-specific antibodies (red; nuclei, blue) in histological sections of human tracheal epithelium reveals differences in TLR expression and distribution across cell types. Images are oriented with basal cells along the bottom and the airway lumen on the top (reproduced from [204]). **B)** Green-fluorescent protein (GFP), yellow-fluorescent protein (YFP), or tdTomato (TOM) was inserted in the 3' end of the endogenous murine TLR gene of interest to create TLR reporter mice. Sections of TLR reporter mouse intestinal epithelium were then stained with antibodies targeting GFP/YFP (green) or tdTomato (red) to identify specific TLR expression across the small intestine, proximal and distal colon regions. Sections were also probed with anti-Epcam antibodies to identify epithelial cells (gray). Scale bars = 50 μm (reproduced from [203]).

In addition to PRRs, the basal level of downstream transcription factors, such as IRFs, also contribute to variation in IFN production. Plasmacytoid dendritic cells (pDCs), for example, have high constitutive levels of IRF7 [216] that enable them to produce very high levels of IFN-I, on the order of 200-1000 times more IFN-α than other blood cells, upon stimulation [217]. Differences in the type(s) of IFN a particular cell produces and the type(s) of IFN it can respond to are also critical. Nearly all cells can produce IFN-I, although subtype expression varies, with IFN-β being ubiquitous, IFN-α being produced primarily by leukocytes [218], and other IFN-Is (e.g., IFN-κ, IFN-ε) being expressed in a tissue-specific manner [151,219,220]. Similar to IFN-I, IFN-III is produced by many cell types; however, while essentially all nucleated cells can respond to IFN-I, IFN-III activity is observed primarily at epithelial surfaces as a result of receptor distribution [155,221]. Lastly, the pattern of ISG induction varies by cell type [222,223] – an observation that will likely be reinforced through the ongoing application of single cell technologies.

Primary cells vs. continuous cell lines

Cells from a given species, tissue, or of a certain type may be cultured as primary cells, or may be cancer-derived or immortalized, and thus propagated continuously. These cell lines have been essential for a multitude of seminal work in understanding the antiviral response to infection since they are amenable to genetic knockout and overexpression studies, and can be readily scalable to accommodate high-throughput screens. Continuous cell lines are chosen for their fast growth rates which, when combined with their inability to undergo senescence, make for an incredibly robust experimental pipeline. However, as IFN can drive anti-proliferative and pro-apoptotic responses, it is not surprising that antiviral signaling pathways intersect with those involved in tumor suppression. Cells lacking antiviral protein expression are more readily immortalized [224],

while conversely, cells lacking tumor suppressors (e.g., p53) or expressing oncogenes (e.g., SV40 large T-antigen, papillomavirus E6) are impaired in their ability to make and respond to IFN ([225,226]; reviewed in [227]) and are thus more susceptible to viral infection [228,229]. Further supporting the link between antiviral and antitumor immunity, Critchley-Thorne and colleagues [230] demonstrated that IFN signaling and subsequent ISG expression is impaired in breast cancer, and Hare et al. note that antiviral genes are often silenced or selected against during tumorigenesis [231]. Therefore, it is not surprising that many cancer-derived cell lines have defects in their antiviral components. For example, Huh7.5 cells contain a mutation in the RIG-I gene (T55I) that impairs IFN signaling and has been linked to enhanced permissiveness for HCV [232] and Vero cells have lost the ability to produce IFN due to spontaneous gene deletions [233,234]. While these defects have made them useful for cultivating certain difficult-to-grow viruses or for amplifying attenuated vaccine candidates, they are not optimal for assessing authentic antiviral responses.

While continuous cell lines are usually still capable of responding to IFN-I and potent IFN-I inducers, such as the dsRNA mimic polyinosinic-polycytidylic acid (Poly I:C) [235], implementing studies using primary cells allows for a more authentic recapitulation of the cell's progenitor tissue, including its innate immune response (**Table 2.1**). However, these cells are not without their own drawbacks. Passaging of primary cells rapidly approaches their senescent end-point, resulting in significant differences from earlier passages including cell enlargement, impeding apoptosis, and alterations to their normal cell cycle. Most significantly, older primary cells have heightened basal-level expression of IFN-β and mount an abnormally stronger interferon response ([236]; reviewed in [227,231]). Therefore, when performing innate immunity studies in primary cells it is critical

to carefully manage over-passaging and to match passages for all experiments to ensure reproducibility.

Table 2.1. Comparison of primary and continuous cell lines.

	Primary Cells	Continuous Cell Lines
Origin	Direct from Donor	Tumor-derived or immortalized
Ease of Use	Difficult	Easy
Genetic Manipulability	Low	High
Transfectability	Low	High
Growth Rate	Low	High
Passaging	Very Limited	Indefinite
Intact Signaling Pathways	Well preserved	Often defective
Representative of Progenitor Tissue	High	Low
Reproducibility	Inter-donor variation	Often clonal
Differentiable	High	Few cases
Preparation Time	Days to weeks	Immediate
Polarity	High	Low
Cost	High	Low

To overcome many of the challenges of primary cell culture studies, methods to immortalize these cells have been applied. Transduction of primary cells containing human telomerase reverse transcriptase (hTERT) instead of SV40 large T-antigen best preserves the complex innate immune framework of the non-immortalized primary cell, thus allowing for creation and implementation of immortal primary cell lines [237]. Through this method, cells are uniformly immortalized which lessens the bottleneck effect during spontaneous immortalization and also does not apply selective pressures which can silence antiviral pathways. Granted, even when primary cells are immortalized by hTERT, they too will eventually garner enough mutations to distinguish them from their primary progenitors and ultimately behave more like a cancerous cell line. Still, utilization of these cells can address the passaging difficulties of non-immortalized primary cell lines, thus allowing for more robust studies requiring cell modifications and selection, including overexpression and knockout using CRISPR technologies [231].

2.5.2 The impact of the microenvironment on innate antiviral responses

Cell-cell interactions

After identifying the appropriate cell type(s) in which to assay innate antiviral responses, consideration of the cellular context is critical since it can impact cellular phenotype, function, and ability to respond to stimuli. *In vivo*, cells are frequently in contact with one another and typically more than one cell type is present in the microenvironment. Thus, even in cases where cells are not in direct contact with one another, the inherent heterogeneity in antiviral response across component cell types can impact the system as a whole (**Figure 2.3**). This is especially relevant when striving to understand the effects of innate immune responses on a multicellular or tissue level.

For adjacent cells, intercellular contacts can contribute to virus spread and propagation of antiviral signals. For example, a variety of reports have described direct cell-cell transfer of viral components through cell protrusions such as tunneling nanotubes [238–240]. This mechanism of virus spread is not only more efficient than the assembly, release, and receptor-mediated uptake of nascent viral particles, but also shields the virus from antibody-mediated neutralization (reviewed in [241]). Furthermore, delivery of viral components (i.e., PAMPS) into neighboring cells via non-canonical pathways may lead to the activation of other cellular sensors or evasion of PRR-mediated detection altogether. While additional studies are needed to address this specific hypothesis, existing reports have shown that viruses being transmitted via cell-cell spread are less sensitive to the activity of intrinsic antiviral restriction factors. In particular, in the case of HIV, neither tetherin [242] nor rhesus TRIM5-α [243] is effective at restricting cell-cell transmission of virus between T cells at the virological synapse. Murrell and colleagues similarly described the ability of IFN-α treatment to efficiently block cell-free, but not cell-cell mediated

infection of dendritic cells (DCs) and Langerhans cells (LCs) by human cytomegalovirus (CMV) [244]. Furthermore, the direct transfer of viral proteins that act to antagonize antiviral responses, such as the IAV NS1 protein, is hypothesized to suppress innate antiviral pathways in recipient cells [238].

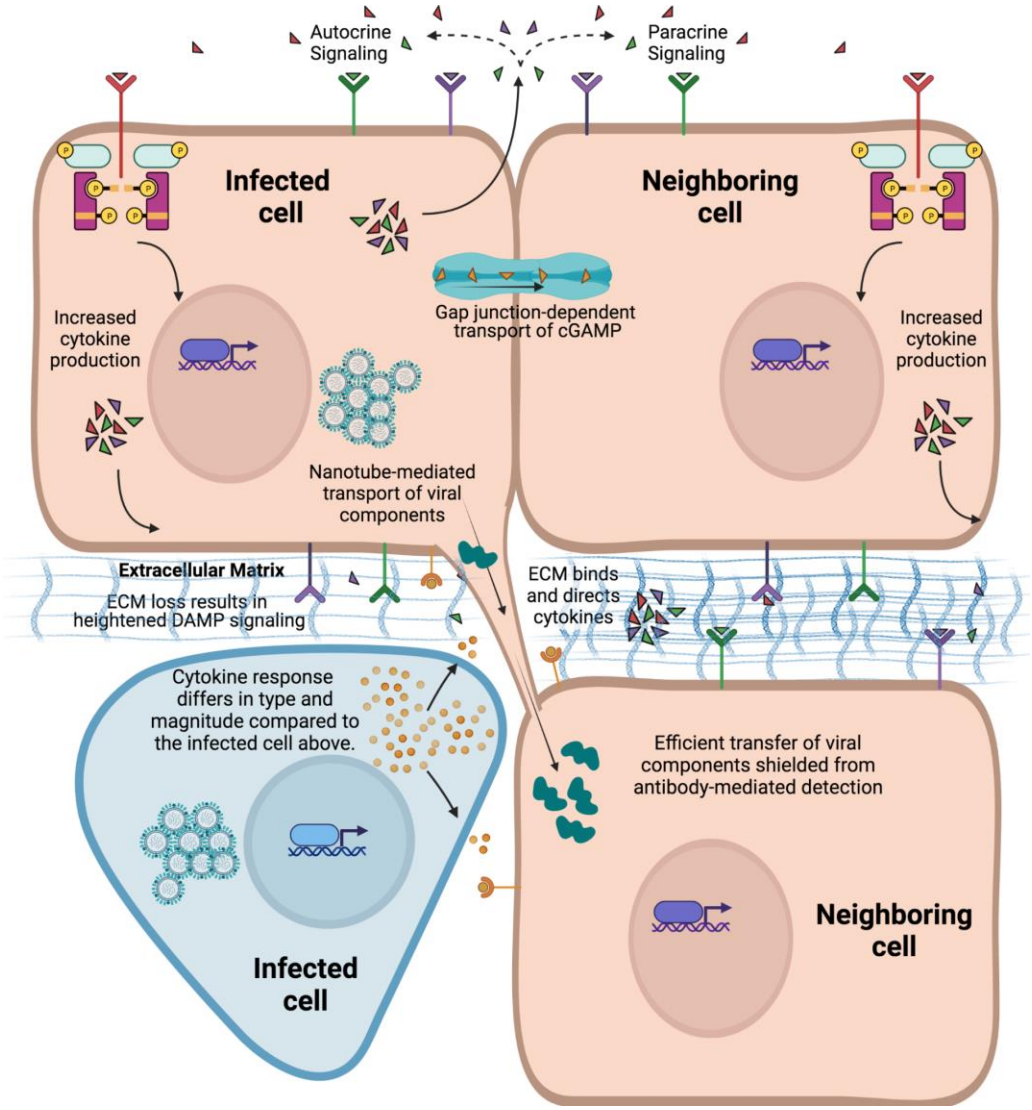

Figure 2.3: Impact of cell-cell and cell-extracellular matrix interactions on antiviral responses. Infected cells secrete cytokines (e.g., IFNs) that amplify antiviral and pro-inflammatory responses through autocrine and paracrine signaling. Notably, the type and magnitude of the host response can vary across different cell types (compare brown and blue cells), each of which contribute to the antiviral and inflammatory state at the culture-wide (i.e., tissue) level. Additionally, transport of the second messenger cGAMP across gap junctions can activate intrinsic immunity in neighboring cells, while viral components (e.g., nucleic acids, proteins, virions) can be transferred directly to other cells via

nanotubes, contributing to the spread of infection along with other modes of virus cell-to-cell spread [241,245]. In the extracellular space, ECM components can impact local cytokine concentration and activation, while ECM disruption following release of proteases during infection produces DAMPs that can further stimulate inflammation. Created with BioRender.com.

Antiviral signals can also be directly transferred between adjacent cells. Specifically, the second messenger cyclic GMP-AMP (cGAMP), which is produced following cGAS activation, can pass through gap junctions due to its small molecular weight [246,247]. Furthering these observations, Pepin et al. demonstrated that connexin-dependent cGAMP transfer from epithelial cells to phagocytes leads to STING-dependent transactivation and contributes to the propagation of antiviral responses, impacting IAV titers [248]. In some cases, cell-cell contact, or short-range exosomal transfer may even be required for activation of the antiviral response (reviewed in [249]). For example, Decembre and colleagues studied pDC responses during DENV infection, noting that pDCs only produced IFN-α when co-cultured with infected cells [250]. Thus, in sum, the component cell types comprising the model, as well as the direct cell-cell contacts influence the magnitude and dynamics of the antiviral response.

Cell-ECM interactions

Microenvironmental impacts on the host response are not limited to cell-cell interactions but are also influenced by extracellular matrix (ECM) components (**Figure 3**). The ECM comprises a diverse set of ~300 proteins arranged in a tissue-specific manner with varying concentrations and patterns [251]. Historically, the extracellular matrix was thought of as simply a scaffold to allow for cell adhesion and tissue development. However, more recent work has shown that the ECM is both a dynamic compartment – being degraded and remodeled during infection and subsequent tissue repair – and an

active player in modulating host immune responses. Specifically, ECM can regulate cell proliferation, differentiation, and migration through interaction with cell surface adhesion molecules and receptors, and influence cellular responses to soluble immunomodulatory factors by controlling their spatial distribution and activation state (reviewed in [252–254]). Indeed, the dissemination of cytokines that are secreted during infection *in vivo* is influenced by both surrounding cells and the structure and porosity of the ECM, which limits their simple diffusion ([255,256]; reviewed in [257]). As a result, local concentrations of cytokines can vary, yielding differential effects on cells throughout the microenvironment. Notably, this is in contrast to cytokine release *in vitro* in traditional monolayer cell culture models where gradients cannot be maintained in the liquid medium.

ECM components, such as proteoglycans and fibrillar proteins, can also directly bind growth factors and cytokines, including IFNs (reviewed in [258]). For example, Yoshida et al. [259] described the ability of fibronectin associated with the extracellular matrix to directly bind IFN-α and further demonstrated that ECM-bound IFN-α can induce STAT1 expression and cytotoxic effects in Panc-1 cells. Cellular exposure to different types of matrices can also impact their responsiveness to the same input signal. Kuwashiro et al. [260] demonstrated that fibrotic collagen associated with liver fibrosis can attenuate ISRE-driven luciferase activity in Huh7 cells after IFN-α treatment. This phenotype was linked to an increase in β1-integrin expression in cells cultured on type I collagen and was also shown to limit the effect of IFN on HCV replication [260].

Beyond ECM component interactions with host-derived soluble molecules, ECM components can also influence the antiviral response through direct pathogen interactions or stimulation of PRRs. The former can result in viral particle neutralization, as shown for tenascin-C – HIV interaction [261], or enhanced clearance, as described in the case of mindin and IAV [262]. Notably, the release of proteases and hydrolases such as matrix

metalloproteinases (MMPs), a disintegrin and metalloproteinases (ADAMs), and a disintegrin and metalloproteinases with thrombospondin motifs (ADAMTs) triggered during infection or released from dying cells can fragment the ECM. These degradation products (e.g., heparan sulphate; hyaluronic acid) can then act as DAMPs to trigger pro-inflammatory cytokine expression and leukocyte recruitment through TLRs or other cellular receptors (reviewed in [263]). Furthermore, ECM remodeling enzymes can also influence the antiviral response directly through other mechanisms. Here, Marchant et al. showed that MMP-12 is taken up by virus-infected cells where it drives transcription of *NFKB1A*, facilitating IFN-α secretion [264]. While these data define a direct role for MMP-12 in gene transcription, the authors also demonstrated MMP-12 can cleave IFN-α, preventing its ability to signal through its receptor, and thereby attenuating the antiviral response.

Cellular polarity

In vivo, individual cells adopt diverse morphologies through adhesive interactions with ECM and by the formation of junctions with neighboring cells, giving rise to distinct biological interfaces and in some cases, apical-basolateral polarity. It is well known that such cellular polarization can impact modes of viral entry; human parainfluenza virus 3, for example, can only infect the airway epithelium via the apical side [265] while measles virus preferentially enters through the basolateral surface [266]. However, in addition to viral entry factors, PRRs and IFN receptors also exhibit polarized expression which impacts how cells sense viral pathogens and respond to antiviral signals [267,268] (**Figure 2.4A and 2.4C**). For example, Muir et al. showed apical localization of TLR2 in human airway epithelial cultures at air-liquid interface (ALI) derived from individuals with cystic fibrosis, while TLR4 and TLR5 were predominantly basolateral [269]. Using primary

human airway epithelial cells, Ciencewicki et al. demonstrated that IFNAR2 localization changes as these cells undergo differentiation into a pseudostratified epithelium [267]. Notably, the predominantly basolateral detection of IFNAR2 in mature ALI airway cultures *in vitro* recapitulated the pattern of expression in human tissue *ex vivo* (**Figure 2.4C**), suggesting these cells are well-poised to respond to IFN-I produced by other cell types in the underlying tissue and may also limit receptor access when the epithelial barrier is intact. Similarly, in the GI tract, TLRs are concentrated on the basolateral surface of mucosal epithelial cells to minimize stimulation by commensal microbiota, but trigger host responses to more invasive pathogens [270]. Specifically, the asymmetrical distribution of TLR3 in the gut was linked to elevated IFN production following basolateral inoculation of intestinal organoids with mammalian reovirus, despite the fact that similar levels of infection were achieved after apical delivery of virus [268] (**Figure 2.4B**). Polarized cells may also release interferon and other cytokines asymmetrically following infection. This has been observed following infection by parainfluenza viruses and SARS-CoV-2 [271,272] (**Figure 2.4D**). The release of different amounts of cytokines to distinct extracellular compartments over different timescales may impact the cell types that receive the signal and the spatiotemporal dynamics of the response that follows which is discussed further in the section below.

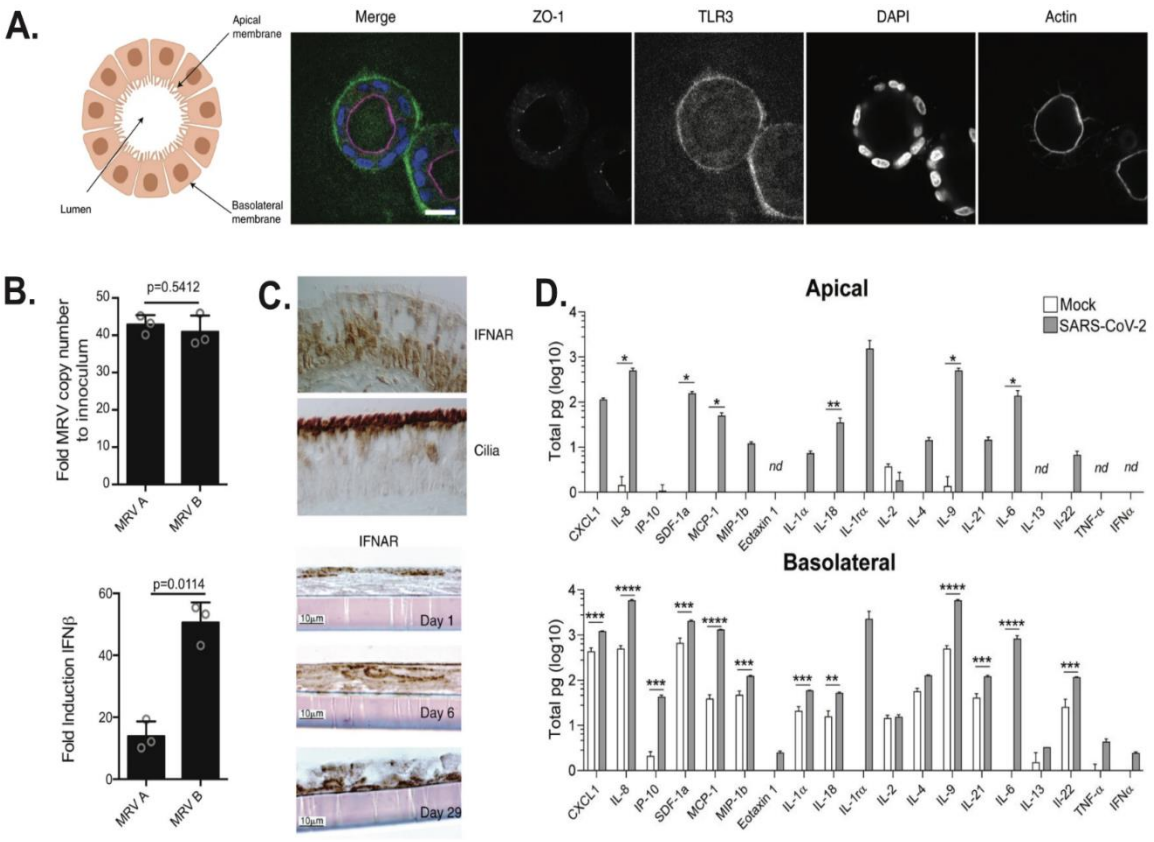

Figure 2.4: Polarized receptor expression and cytokine release impacts the dynamics of the host response to infection. A) Basolateral localization of TLR3 (green) in human colon organoids co-stained for the cellular tight junction protein ZO-1 (red), cytoskeletal protein actin (magenta), and nuclei (blue). Scale bar = 20 μm. **B)** Intestinal organoids shown in (A) were inoculated with mammalian reovirus via the apical (MRV A) or basolateral (MRV B) surface and expression level of both the MRV *μ2* genome segment and IFN-β was determined by quantitative reverse transcription PCR. The data show that despite similar levels of infection (top panel), basolateral inoculation resulted in significantly stronger induction of intrinsic antiviral immunity (bottom panel), likely due to the localization of TLR3. Mean +/- st dev; p values were calculated with two tailed unpaired t-test (reproduced from [268]). **C)** Immunohistochemical detection of IFNAR2 in ciliated human trachea *ex vivo* (top; staining shown in brown) and in human airway epithelial cultures over the course of differentiation *in vitro* (at day 1, 6, and 29; bottom). Scale bar = 10 μm. (reproduced from [267]). Airway lumen is positioned at the top in all images. **D)** Polarized cytokine release (apical vs. basolateral) following infection of an *in vitro* model of human airway epithelium with SARS-CoV-2 (MOI = 0.5; 72 hpi). Cytokines were quantified by Luminex assay and values below the limit of detection are designated *nd*. All data were analyzed using one-way or two-way ANOVA. *, $P < 0.05$; **, $P < 0.01$; ***, $P < 0.001$; ****, $P < 0.0001$ (reproduced from[272]).

Biomechanics

In addition to the impacts of cell-cell and cell-ECM interactions on cellular polarity and the antiviral response summarized above, cellular contacts and ECM rigidity further impact cellular responses as mechanical stimuli. Indeed, cells are subject to a variety of mechanical forces *in vivo* which can regulate intracellular signaling through the activation of mechanosensory ion channels, yielding effects on gene expression and overall cell phenotype.

In the lung, for example, airway cells (including epithelial, endothelial, and mesenchymal cells) are subjected to continuous cyclical stretch and compression during the respiratory cycle. While the impact of these forces on the IFN response specifically is unclear, it has been shown in alveolar cells to impact surfactant secretion and even contribute to a pro-inflammatory phenotype during mechanical ventilation (reviewed in [273]). Recently, Kilic et al. studied the effect of compression on normal airway epithelial cells, demonstrating changes in gene expression as early as 3 hours after mechanical stimulation and the induction of an asthma-like transcriptional profile [274]. Similarly, Solis et al. reported the expression of pro-inflammatory and chemoattractant mediators by macrophages and monocytes exposed to *in vitro* cyclical hydrostatic pressure was dependent on the ion channel, PIEZO1 [275]. PIEZO1 drives calcium-mediated activation of transcription factors AP-1 and endothelin 1 (EDN1) in response to mechanical stimuli - elegantly demonstrating how these types of extracellular cues can impact the innate immune response even in the absence of PRR activation [275]. Undoubtedly, immune cells sense and respond to a variety of mechanical stimuli during extravasation, transmigration, and eventual infiltration to specific tissues during the response to viral infection, and recent advances in technology facilitate further work in this area (reviewed in [276]).

In blood vessels, shear stress induced by non-laminar flow impacts NF-κB activity [277] and gene expression profiles in endothelial cells [277,278], while laminar flow was observed to suppress TLR2 levels [244] in addition to IFN-γ-mediated STAT1 activation and CXC chemokine expression [279]. Beyond the impact of biomechanics on gene expression, fluid flow within a tissue can impact the local concentration of soluble mediators and thus the spatiotemporal dynamics of the host response. Conversely, when flow is slowed, such as at arterial bifurcations, it can lead to high concentrations of cytokines due to a 'pooling effect' yielding to inflammation [280]. While the impact of flow on endothelial cell phenotypes has been investigated primarily through the lens of atherosclerosis, these findings have implications for modeling antiviral responses in endothelial cells under static vs. dynamic conditions *in vitro*.

2.6 Utility of tissue-engineered and 3D cell culture systems in modeling innate antiviral responses

Historically, traditional monolayer cell culture systems have provided the foundation for the discovery of many of the innate immune pathways discussed in section II. However, as detailed in section III, cellular context impacts antiviral responses. Notably, a variety of *in vitro* model systems, including precision-cut tissue slices, epithelial cultures at ALI, organoids, and 'on-chip' technologies, among others, can incorporate human primary cells, recapitulate aspects of tissue architecture and function, and integrate biological forces present *in vivo* such as cyclical stretch and fluidic shear (**Figure 2.5**). Since many of these systems are susceptible and permissive for viral infection, they provide a more robust platform to model physiologically-relevant antiviral responses. Detailed descriptions of these model systems, including organoids of the brain [281,282], airway [283,284], gut [285,286], placenta [287,288], and liver [289,290], have been

reviewed elsewhere [291–293]; thus, in this section, we limit our discussion to the application of these models to studying innate antiviral responses.

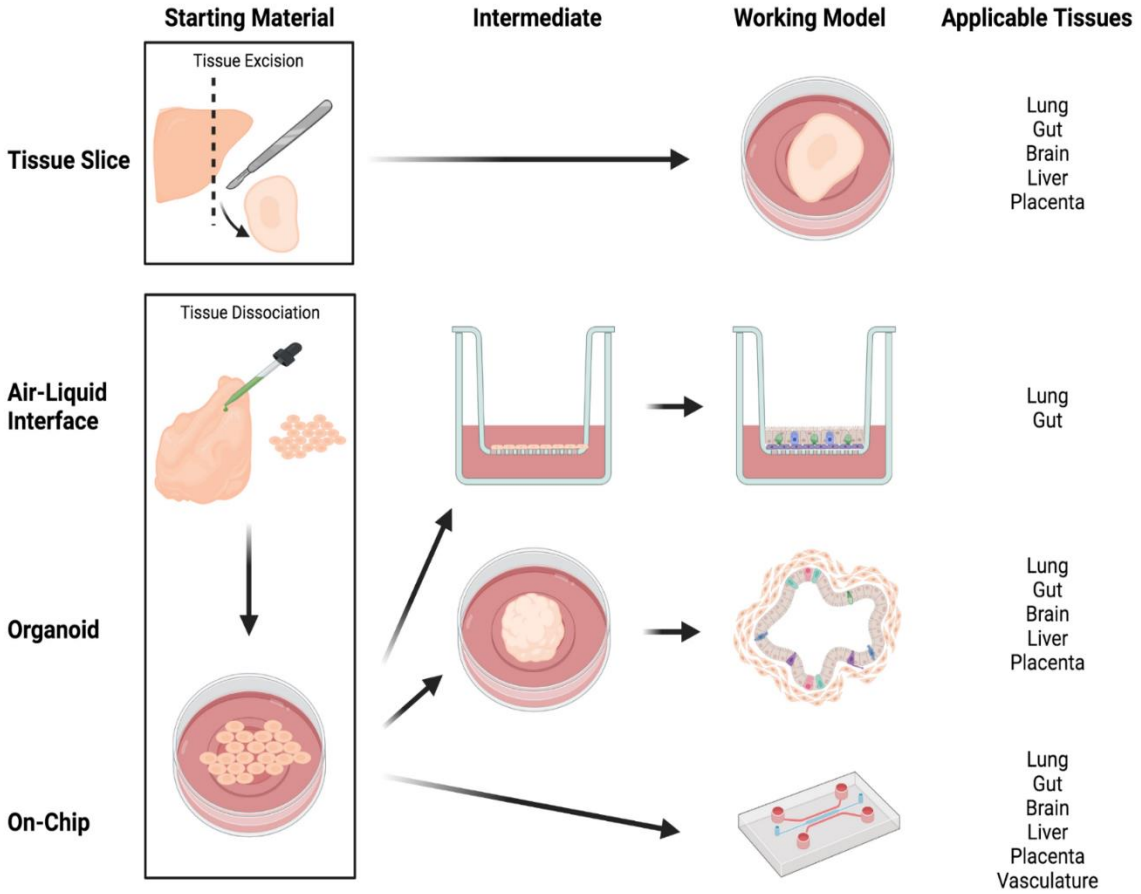

Figure 2.5: *In vitro* model systems with emergent properties. Schematics are shown for a variety of tissue culture platforms that recapitulate aspects of organ-specific, *in vivo* physiology. For tissue slice cultures, organotypic tissue is excised and cultured *ex vivo* for a short duration prior to infection. Air-liquid interface (ALI), organoid (also spheroid and enteroid), and on-chip cultures all are initiated from dissociated tissue before an expansion phase. For ALI cultures, cells are seeded on transwells for several days before media is removed from the apical chamber establishing the ALI system. Organoids, spheroid, and enteroid cultures all result in a recapitulation of the progenitor organ system, yet differ in how the culture is initiated. On-chip cultures have cells seeded into microfluidic chips specialized for a specific experimental goal. Created with BioRender.com.

As noted above, pseudostratified and organotypic models of the airway epithelium and intestinal mucosa recapitulate the cell type-specific expression and polarized distribution of PRRs and IFN receptors observed *in vivo* [203,204]. Thus, it is not surprising that these models, as well as other *in vitro* tissue culture systems with emergent

properties, have been shown to respond to immunomodulatory stimuli and mimic *in vivo* innate immune responses. For example, Henjakovic et al. characterized cytokine production in precision-cut *ex vivo* lung slices in response to LPS, IFNγ, and dexamethasone [294] while Temann et al. determined that these *ex vivo* cultures can respond to LPS stimulation even after long-term culture, indicating this *ex vivo* system is a robust platform that can predict inflammatory responses to various stimuli [295]. Similarly, *ex vivo* lung slices were shown to mount a pro-inflammatory response following exposure to a nanoparticle-based IAV vaccine candidate and were subsequently used to provide evidence of antigen-primed T cells in the lung after initial *in vivo* vaccine challenge in mice [296,297]. Regarding other airway models, microarray analysis of tracheal bronchial cells obtained through brush biopsies compared to unstimulated primary human airway epithelial (HAE) cells cultured at either ALI or in submerged conditions and Calu-3 cells, found that differentiated HAE cultures at ALI best mimic the gene expression profile of these cells *in vivo* [298]. Hui et al. later compared IAV replication kinetics and tissue tropism preferences between human airway organoid cultures and *ex vivo* bronchus cultures from the same donor and found airway organoids to be a suitable mimic that was also capable of eliciting potent immune responses [299]. More recently, Cheemarla and colleagues compared SARS-CoV-2-infected organoids with serially swabbed nasopharyngeal samples and demonstrated comparative viral kinetics and innate antiviral responses including high levels of CXCL10 [300]. Furthering this analysis, the authors utilized these cultures to assess the ability of a preceding rhinovirus 1A (RV-1A) infection to inhibit SARS-CoV-2 through the induction of protective ISGs culture-wide, including in bystander cells [300]. This was similar to previous work by the same group where RV-1A-induced immunity protected against 2009 pandemic H1N1 IAV in ALI HAE cultures [301].

Outside the airway, 3D models of brain microglia grown in the presence of a hydrogel matrix have also been shown by multiple groups [302–305] to respond to LPS stimulation, while Abreu et. al [306] established a differentiated stem cell-derived micro brain sphere capturing multiple cell types capable of phenocopying *in vivo* innate immune responses including production of CCL-2, TNF-α, IL-1β, IL-6, and IL-10. Importantly, Watanabe et al. were able to develop a cerebral organoid system, inclusive of cortical and basal ganglia regions, that improved upon previous models by mounting more reproducible innate antiviral signaling events following viral challenge by pathogens such as ZIKV [307]. Likewise in the liver, the development of a 3D microfluidic primary human hepatocyte model by Ortega-Prieto and colleagues that could garner hepatitis B virus (HBV) replication upon low MOI infection and produce an *in vivo*-like innate response including IL-8, macrophage-inflammatory protein-3α (MIP-3α), SerpinE1, and monocyte-chemoattractant protein-1 (MCP-1) has proven to be a major development for comparing HBV strains and their potentially differing activation of host immunity [308].

Beyond their utility in profiling *in vivo*-like host responses, cell culture models with emergent properties have also been employed to uncover novel aspects of pathogen detection and antiviral response that would otherwise be absent in conventional monolayer cultures or cell lines (**Table 2**). Some examples of this have been highlighted earlier in this review (e.g., the polarity of antiviral responses). Additionally, these models are useful in understanding antiviral defense in complex or maturing tissues, for instance, in ZIKV transmission to the developing fetus during pregnancy and subsequently, in the developing brain. Here, Bayer et al. [309] demonstrate the inability of ZIKV (and DENV) to infect full-term primary human trophoblasts due to constitutive release of IFN-III which – through autocrine and paracrine signaling – protect trophoblast and adjacent non-trophoblast tissue from viral invasion. To further understand the mechanism of antiviral

protection across the maternal-fetal barrier, Corry et al. were able to recapitulate the protective effects of IFN-λ1 and IFN-λ2 signaling in 3D primary trophoblast and organotypic chorionic villous explant models to highlight the antiviral properties of differentiated trophoblasts [310], and thus that maternal-fetal viral transmission is largely limited to early-stage, post-conception trophoblasts [311]. Through the use of human embryonic stem cell-derived cerebral organoids, Dang et al. were then able to confirm the activation of TLR3 upon ZIKV infection leading to a pro-apoptotic cascade, and ultimately a decrease in organoid volume characteristic of microcephaly [312]. Thus, without the use of these embryonic organoids, this connection between TLR3 signaling, apoptosis, and microcephaly would be unrealized. Likewise, additional studies utilizing brain organoids were able to link both neonatal herpes simplex virus I and CMV with microcephaly [313,314]. Moreover, while primary keratinocyte organoid models have become the gold-standard for studying and assessing the antiviral innate immune response against human papillomavirus (HPV), Jackson et. al recently reported an enhanced organoid model which incorporates Langerhans cells that can be utilized for studying early-stage infection and subsequent innate responses [315].

Table 2.2. Current applications and description of ongoing advances in *in vitro* model technology that will enable further interrogation of antiviral responses in physiological context.

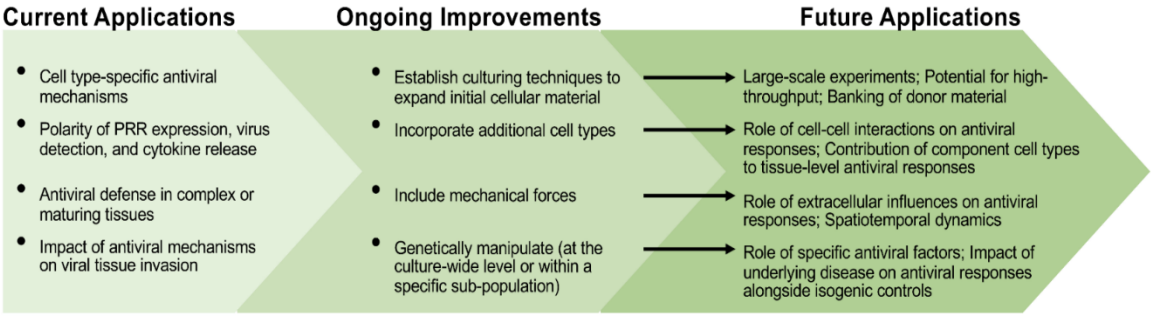

Furthermore, advanced culture techniques have yielded improved models of the blood-brain barrier, allowing for a better understanding of how antiviral defense impacts

the ability of viruses to invade the brain. These techniques include transwell and 'on-chip' technology [316], the latter of which have been designed to incorporate constant shear stress which promotes *in vivo* endothelial physiology [317]. Still, blood-brain barrier on-chip systems are often inadequate for investigating the antiviral response given the large volume of virus often needed in addition to the low cell density of these platforms. However, Bramley et. al [318] recently established a 3D model system recapitulating the blood-brain barrier after growing human brain microvascular endothelial cells within a bioreactor to provide constant shear force. Using this system, they determined that the physical vascular barrier provides greater antiviral defense compared to the ability of these 3D cultures to mount an antiviral innate immunological response through ISG-mediated signaling. They further demonstrate that disruption of the tight junctions as a result of stimulation with proinflammatory cytokines including TNF-α, lead to enhanced viral susceptibility.

2.7 Additional applications and current challenges of assessing innate antiviral immunity in 3D model systems.

Innate antiviral immunity is complex and multifaceted. Understanding the mechanisms that regulate the activation, propagation, and resolution of antiviral and pro-inflammatory responses requires a model system that recapitulates the *in vivo* setting where infection takes place. Traditional monolayer cell culture methods featuring cell lines have – and still provide – immense value, due to their simplicity, ease of use and genetic manipulability. However, where possible, efforts should be made to validate findings and further study innate antiviral immunity through the lens of more specialized cell culture systems with emergent properties. These systems allow for better representation of the natural host and therefore preserve more biologically relevant responses.

Current 3D and tissue-engineered models have been successfully employed to define the polarity of viral infection and host response, as well as cell type-specific responses, and the impact of infection on developing tissues, as reviewed above. However, while these model systems clearly represent more physiologically-relevant platforms in which to interrogate virus-host interactions, their utility in assessing the antiviral response has not been completely exploited. For example, organoids and 'on-chip' platforms could facilitate additional investigation into the role of extracellular influences (e.g., ECM; fluid flow) on ISG and cytokine expression, in addition to the spatiotemporal dynamics of IFN signaling. Notably, transgenic mice expressing IFN-sensitive, cell-based reporters have been developed to visualize and track the host response *in vivo* [319,320]; the translation of these approaches to 3D culture models *in vitro* will enable analysis in human systems with tunable parameters.

Improving existing cell culture systems with emergent properties will also further their application in understanding the antiviral response. For instance, polarized intestinal epithelial models have difficulty replicating the crypt-villus topography, with proliferating cells resident in the crypts and differentiated cells occupying the villi [287]; thus, utilizing intestinal organoids have been heavily relied upon for mimicking intestinal processes including comparisons across viruses [321]. Recently, Drummond and colleagues were able to grow enteroid cultures from isolated primary intestinal crypts which will be a useful tool for assessing cell type-specific antiviral responses due to their ability to induce differentiation into all four classic cell types of the gut: enterocytes, Paneth, goblet, and enteroendocrine [322]. Indeed, using a similar enteroid model and through the application of single-cell RNAseq, Triana et. al demonstrated a pro-inflammatory response in SARS-CoV-2-infected cells while bystander cells upregulated ISGs in a cell type-specific manner [323].

‘On chip’ systems are often specially designed to address a specific biological question and are thus incredibly focused in their utility, often making them less ideal for broad investigations into the innate response (reviewed in [324]). Nonetheless, Villenave, Wales, and Hamkins-Indik et. al developed a gut-on-a-chip capable of supporting coxsackievirus B1 infection and apical cytokine release [325], establishing a foundational on-chip device for investigating innate antiviral immune responses. Finally, recapitulating virus-induced hemorrhaging, caused by Ebola and Lassa fever viruses among others, are difficult to model *in vitro*, and thus nonhuman primate models have been heavily relied upon in understanding pathogenesis, antiviral responses, and therapeutic development. However recently, an on-chip method was developed where upon use of a phase-guide, two parallel channels can be produced which are sensitive to infection and vascular leakage [326]. While these methods remain in their infancy, certain on-chip technologies have provided the basis for *in vitro* interrogation of host-responses against these destructive pathogens.

Since viral infections often trigger more severe outcomes in those with underlying conditions, it is important to note that researchers have also made advancements in establishing ALI and organoid models derived from primary cells sourced from diseased donors, as well as through the manipulation of cells to either induce or correct the diseased phenotype. Inclusive among these models are ulcerative colitis, asthma, chronic obstructive pulmonary disease, cystic fibrosis, and other fibrotic lung syndromes [268,327–329]. Importantly, this latter technology now enables virus challenge experiments and analysis of antiviral host responses across healthy and diseased states in an isogenic setting.

Still, despite these advancements, challenges remain in order to fully implement studies interrogating the antiviral response in tissue culture systems with emergent

properties (**Table 2)**. For example, unlike their 2D counterparts, 3D or tissue-engineered model systems remain difficult to genetically modify or utilize in high-throughput platforms. Advancements in cell culture techniques and the establishment of stem cell-derived models have removed some of these constraints by enabling more extensive passaging of primary cells or providing a renewable source of cells, respectively. As a result, researchers have a larger window for cell manipulation and selection, as well as greater numbers for downstream applications [330,331]. However, while cultures lacking specific PRR or ISGs expression would be a powerful tool to determine their impact during infection in a relevant setting, examples of 3D systems in which *any* host factor has been genetically altered remain scarce [332–335]. Cell culture models with emergent properties could also be further improved through the routine incorporation of additional cell types, such as endothelial and immune cells, and tissue-relevant mechanical forces (reviewed in [284]) to better capture microenvironmental influences on cellular responses and immune modulation. In sum, through greater utilization and continued improvement of these 3D culture systems, a heightened understanding of the initial antiviral immune response can be achieved, while potentially discovering novel mechanisms which can only be observed in these more relevant, *in vivo-like* model systems.

Chapter 3 : Rhinovirus C replication is associated with the endoplasmic reticulum and triggers cytopathic effects in an in vitro model of human airway epithelium

Talita B. Gagliardi[1], Monty E. Goldstein[1], Daniel Song[2], Kelsey M. Gray[2], Jae W Jung[2], Maxinne A Ignacio[1], Kimberly M. Stroka[2,3,4,5], Gregg A. Duncan[2], and Margaret A. Scull[1]

1 Department of Cell Biology and Molecular Genetics, Maryland Pathogen Research Institute, 3134 Bioscience Research Building, University of Maryland, College Park, MD 20742, USA.

2 Fischell Department of Bioengineering, University of Maryland, College Park, MD 20742, USA.

3 Biophysics Program, University of Maryland, College Park, MD 20742, USA.

4 Center for Stem Cell Biology and Regenerative Medicine, University of Maryland, Baltimore, MD, 21201 USA.

5 Marlene and Stewart Greenebaum Comprehensive Cancer Center, University of Maryland, Baltimore, MD, 21201 USA.

Given the relatively recent discovery of RV-C, very little was known about how this virus replicates in the human respiratory airway epithelium, and much has simply been inferred from other RVs. Therefore, prior to trying to assess these requirements in a

foreign, murine airway, it was first paramount to understand some of its basic replication biology requirements in a physiologically-relevant human airway epithelial cell culture system. In this work, we performed direct comparisons between the three groups of RVs, major, minor, and -C to best understand the replication kinetics, dynamics, localization, required host factors, and ability to cause CPE.

This chapter features text and adaptions from a published article: Gagliardi TB, Goldstein ME, Song D, Gray KM, Jung JW, Ignacio MA, Stroka KM, Duncan GA, Scull MA. Rhinovirus C replication is associated with the endoplasmic reticulum and triggers cytopathic effects in an in vitro model of human airway epithelium. PLoS Pathog. 2022 Jan 7;18(1):e1010159. doi: 10.1371/journal.ppat.1010159. PMID: 34995322; PMCID: PMC8741012 [336] which is licensed under a Creative Commons Attribution 4.0 International License. To view a copy of this license, visit http://creativecommons.org/licenses/by/4.0/. My contribution to this work primarily focused on the role of STING expression on RV-C replication in HAE, including experimental design, performing analysis, and generating figures. Additionally, I was responsible for all western blots performed throughout the manuscript, addressing reviewer comments, as well as editing the manuscript.

3.1 Abstract

The clinical impact of rhinovirus C (RV-C) is well-documented; yet, the viral life cycle remains poorly defined. Thus, we characterized RV-C15 replication at the single-cell level and its impact on the human airway epithelium (HAE) using a physiologically-relevant in vitro model. RV-C15 replication was restricted to ciliated cells where viral RNA levels peaked at 12 hours post-infection (hpi), correlating with elevated titers in the apical

compartment at 24hpi. Notably, infection was associated with a loss of polarized expression of the RV-C receptor, cadherin-related family member 3. Visualization of double-stranded RNA (dsRNA) during RV-C15 replication revealed two distinct replication complex arrangements within the cell, likely corresponding to different time points in infection. To further define RVC15 replication sites, we analyzed the expression and colocalization of giantin, phosphatidylinositol-4-phosphate, and calnexin with dsRNA. Despite observing Golgi fragmentation by immunofluorescence during RV-C15 infection as previously reported for other RVs, a high ratio of calnexin-dsRNA colocalization implicated the endoplasmic reticulum as the primary site for RV-C15 replication in HAE. RV-C15 infection was also associated with elevated stimulator of interferon genes (STING) expression and the induction of incomplete autophagy, a mechanism used by other RVs to facilitate non-lytic release of progeny virions. Notably, genetic depletion of STING in HAE attenuated RV-C15 and -A16 (but not -B14) replication, corroborating a previously proposed proviral role for STING in some RV infections. Finally, RV-C15 infection resulted in a temporary loss in epithelial barrier integrity and the translocation of tight junction proteins while a reduction in mucociliary clearance indicated cytopathic effects on epithelial function. Together, our findings identify both shared and unique features of RV-C replication compared to related rhinoviruses and define the impact of RV-C on both epithelial cell organization and tissue functionality–aspects of infection that may contribute to pathogenesis in vivo.

3.2 Author Summary

Rhinovirus C has a global distribution and significant clinical impact–especially in those with underlying lung disease. Although RV-C is genetically, structurally, and biologically distinct from RV-A and -B viruses, our understanding of the RV-C life cycle has been largely inferred from these and other related viruses. Here, we performed a

detailed analysis of RV-C15 replication in a physiologically-relevant model of human airway epithelium. Our single-cell, microscopy-based approach revealed that–unlike other RVs–the endoplasmic reticulum is the primary site for RV-C15 replication. RV-C15 replication also stimulated STING expression, which was proviral, and triggered dramatic changes in cellular organization, including altered virus receptor distribution, fragmented Golgi stacks, and the induction of incomplete autophagy. Additionally, we observed a loss of epithelial barrier function and a decrease in mucociliary clearance, a major defense mechanism in the lung, during RV-C15 infection. Together, these data reveal novel insight into RV-C15 replication dynamics and resulting cytopathic effects in the primary target cells for infection, thereby furthering our understanding of the pathogenesis of RV-C. Our work highlights similar, as well as unique, aspects of RV-C15 replication compared to related pathogens, which will help guide future studies on the molecular mechanisms of RV-C infection.

3.3 Introduction

Rhinoviruses (RVs) are responsible for over 40% of respiratory virus infections in the human population [19,20,337,32]. Although well known as etiologic agents of the common cold, rhinoviruses can also infect the lower respiratory tract causing bronchiolitis or pneumonia and are a leading cause of virus-induced exacerbations in acute and chronic lung disease [21–24]. No vaccine or direct-acting antiviral is currently available due in part to the diversity of RVs in circulation, with over 160 genotypes identified [7,8]. These genotypes comprise three species (RV-A, RV-B, and RV-C) where RV-A and RV-C are the most prevalent and RV-C is associated with more severe clinical disease, especially in children [32–34]. Indeed, RV infection during the first year of life has been associated with wheezing episodes and is considered a risk factor for the development of asthma [24,338,339].

RV-C was discovered in 2006 [340] and compared to previously defined rhinovirus species, is unique at the genetic [341], structural [342], and biological level [343]. While all RVs (-A, -B, and -C) infect airway epithelial cells, RV-C uses a different host protein, cadherin-related family member 3 (CDHR3), to mediate particle uptake [344]. The restricted expression of CDHR3 to ciliated cells in the upper and lower airway epithelium [345–348] limits the cellular tropism of RV-C, compared to other RVs that utilize low-density lipoprotein receptor (LDLR) or intercellular adhesion molecule (ICAM)-1 as receptors [343] Notably, a non-synonymous single nucleotide polymorphism (SNP; rs6967330[A]) that yields stabilized CDHR3 protein expression at the cell surface is a causal variant for early childhood asthma with severe exacerbations [345]. Subsequent investigation has associated the CDHR3 asthma risk allele with heightened risk of respiratory tract illness with RV-C, but not other viruses [346]. More recently, stimulator of interferon genes (STING), a key adapter protein for cytosolic DNA-sensing pathways, was found to play a proviral role in RV-A and -C, but not -B, replication [349]. Thus, mechanisms of infection and replication are not always conserved between rhinovirus species.

Despite these advances, details of the RV-C life cycle and underlying mechanisms that contribute to pathogenesis remain scarce. While such studies remain hampered by the absence of immortalized cell lines or an *in vivo* mouse model that is naturally susceptible and highly permissive for RV-C replication, previous reports demonstrate that *ex vivo* tissue and primary airway cultures support infection [347,350]. Nonetheless, aside from receptor usage and cellular tropism, little is known about RV-C interactions with primary airway epithelial cells, the principal target for infection. Here we utilized both single-cell, microscopy-based analyses, and culture-wide measurements, to investigate the details of RV-C15 replication in an in vitro model of human airway epithelium (HAE).

Our data identify the endoplasmic reticulum (ER) as the primary site for RV-C15 replication and demonstrate the impact of infection on the structural integrity of ciliated cells and epithelial barrier function, thereby identifying both unique and shared features of RV-C amongst related viruses.

3.4 Results

3.4.1 RV-C15 replicates in ciliated cells, yielding changes in CDHR3 expression

Pseudostratified models of HAE at air-liquid interface are permissive for RV-C replication [350,351]. To detail the kinetics of RV-C15 replication in this model at higher-resolution, we inoculated HAE at 34˚C with 10^{10} RV-C15 RNA copies and quantified viral RNA intracellularly as well as in both the apical and basolateral compartments over time (**Figure 3.1A and 3.1B**). The dynamics of RV-C15 replication were similar in HAE from two different donors, where cell-associated RV-C15 RNA levels increased during the first 12 hours post-infection (hpi). This correlated with the detection of double-stranded (ds) RNA, a marker of viral replication, by immunofluorescence (IF; **Figure S3.1A**) and was in line with peak viral release into the apical chamber at 24hpi (**Figure 3.1A and 3.1B**). The lack of RV-C15 RNA in basolateral supernatants confirmed polarized release of RV-C15 to the airway lumen (**Figure 3.1A and 3.1B**), consistent with a previous report in nasal cells [56] and the clinical manifestation of RV-C-mediated disease.

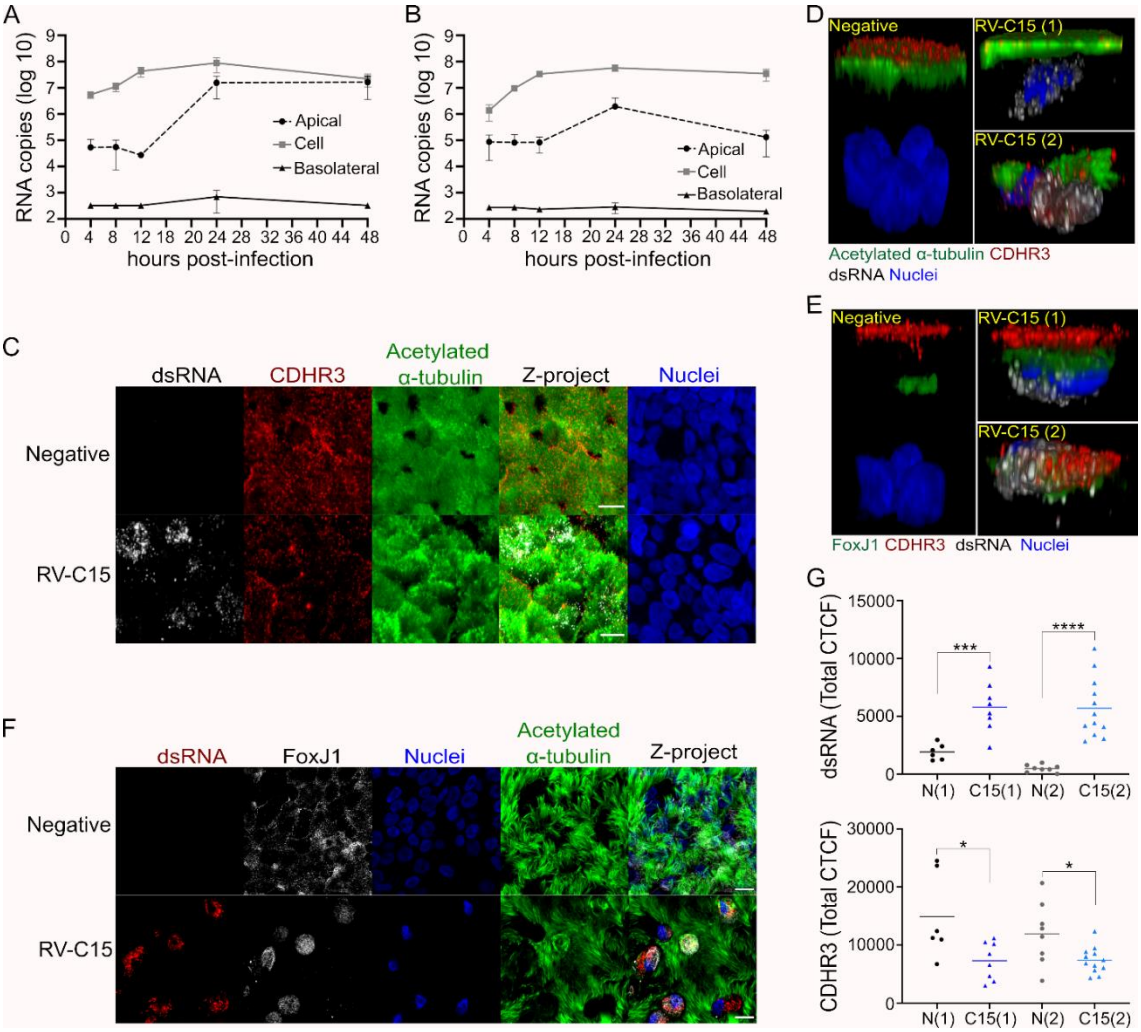

Figure 3.1. RV-C15 replicates in ciliated epithelial cells, leading to decreased CDHR3 levels. A and **B**: Multi-cycle RV-C15 growth delineated at 34˚C in HAE (**A**: donor 1; **B**: donor 2). Data shown are the mean +/- standard deviation across n = 3 cultures/time point. **C-E**: Immunofluorescence detection of CDHR3 (red) in non-infected or RV-C15-infected (dsRNA+, gray) ciliated cells identified by either acetylated α-tubulin (green; **C** and **D**) or FoxJ1 (green; **E**) at 12hpi. **C**: scale bar = 10μm. **D** and **E**: 3D visualization; z-stacks were at 1μm of thickness). **F**: Immunofluorescence detection of RV-C15 replication (dsRNA; red) in ciliated cells (FoxJ1, gray) with or without motile cilia (acetylated α-tubulin, green) at 12hpi (scale bar = 10μm). **G**: Quantification of dsRNA and CDHR3 fluorescence levels (CTCF) in non-infected (N) and RV-C15-infected (C15; dsRNA+) ciliated cells following immunofluorescence staining at 12hpi. Graphs show dsRNA and CDHR3 total CTCF (line = mean) quantified in HAE using FoxJ1 (N(1) and C15(1)) or acetylated α-tubulin (C15(2) and N(2)) as a marker of ciliated cells. Dots represent the sum of all fluorescence intensity (Total CTCF) quantified per cell. Statistical analysis was done using the Mann-Whitney U test (Two-tailed; 0.95% confidence interval; *p<0.05, ***p<0.001, ****p<0.0001).

Given that HAE cultures were permissive for RV-C15 replication, we next sought to investigate cell tropism in our system. Visualization of the RV-C receptor, CDHR3, in non-infected HAE by IF revealed expression at the apical surface in cells that were also positive for Forkhead box protein J1 (FoxJ1; known to promote ciliogenesis) or acetylated alpha-tubulin (a marker of mature ciliated cells; **Figure 3.1C, 3.1D and 3.1E**). Notably, the corrected total cellular fluorescence (CTCF) levels of CDHR3 had a limited relationship with FoxJ1 but were strongly correlated with acetylated alpha-tubulin levels, in line with increased expression of CDHR3 during differentiation (**Figure S3.1B and S3.1C**) [346]. Corroborating these data and previous research reporting ciliated cell tropism for RV-C [347,350], we detected dsRNA primarily in FoxJ1(+) cells, with some cells also staining positive for acetylated alpha-tubulin (**Figures 3.1F and S3.1D**). Notably, the loss of apical acetylated alpha-tubulin localization in dsRNA(+) cells (**Figures 3.1D and S3.1D**) may explain the lack of cilia visualized in these cells by en face IF (**Figure 3.1F**). The 3D views also suggested CDHR3 was internalized in some dsRNA(+) cells (**Figure 3.1D and 3.1E**).

To better understand the dynamics of FoxJ1, acetylated alpha-tubulin, and CDHR3 during infection, we analyzed global protein expression by Western blot (WB) and quantified fluorescence levels following immunostaining specifically in infected cells. Beyond the intrinsic variation expected across cultures in this model system, neither FoxJ1 nor acetylated alpha-tubulin protein levels were dramatically altered over the course of infection (**Figure S3.1E**). In contrast, CDHR3 protein expression decreased at 12 and 48hpi, coincident with robust detection of the viral capsid protein VP1 (**Figure S3.1F**). Subsequent single-cell analysis of acetylated alpha-tubulin and FoxJ1 fluorescence levels corroborated our WB data (**Figure S3.1G and S3.1H**). This was also true for CDHR3, in which fluorescence levels decreased significantly at 12hpi in cells with active viral replication (**Figure 3.1G**).

3.4.2 RV replication complex distribution is associated with vesicle formation

Picornaviruses, including RV-A and -B, replicate in association with cellular membranes, leading to the formation of double-membrane vesicles known as replicative complexes [82,352–354]. Thus, we investigated the distribution of replication complexes in RV-C15-infected HAE cultures by visualization of viral dsRNA and the impact of infection on intracellular membrane organization by transmission electron microscopy (TEM). While non-infected HAE were negative for dsRNA, as expected (**Figure 3.2A**), dsRNA in RV-C15-infected cultures was found in either a perinuclear (**Figure 3.2B and video S3.1**) or ring-like disposition closer to apical and basolateral membranes (**Figure 3.2C and video S3.2**). Neither phenotype was specific for RV-C15, however, as HAE infected with either RV-A16 or RV-A2 revealed similar dsRNA profiles (**Figure S3.2A–S3.2D**). Additionally, the ring-like distribution pattern was determined to be the minority profile across all dsRNA(+) cells visualized at 12hpi in cultures infected with RV-C15 (73 of 324; 22.53%), RV-A16 (20 of 148; 13.51%), or RV-A2 (12 of 34; 35.29%).

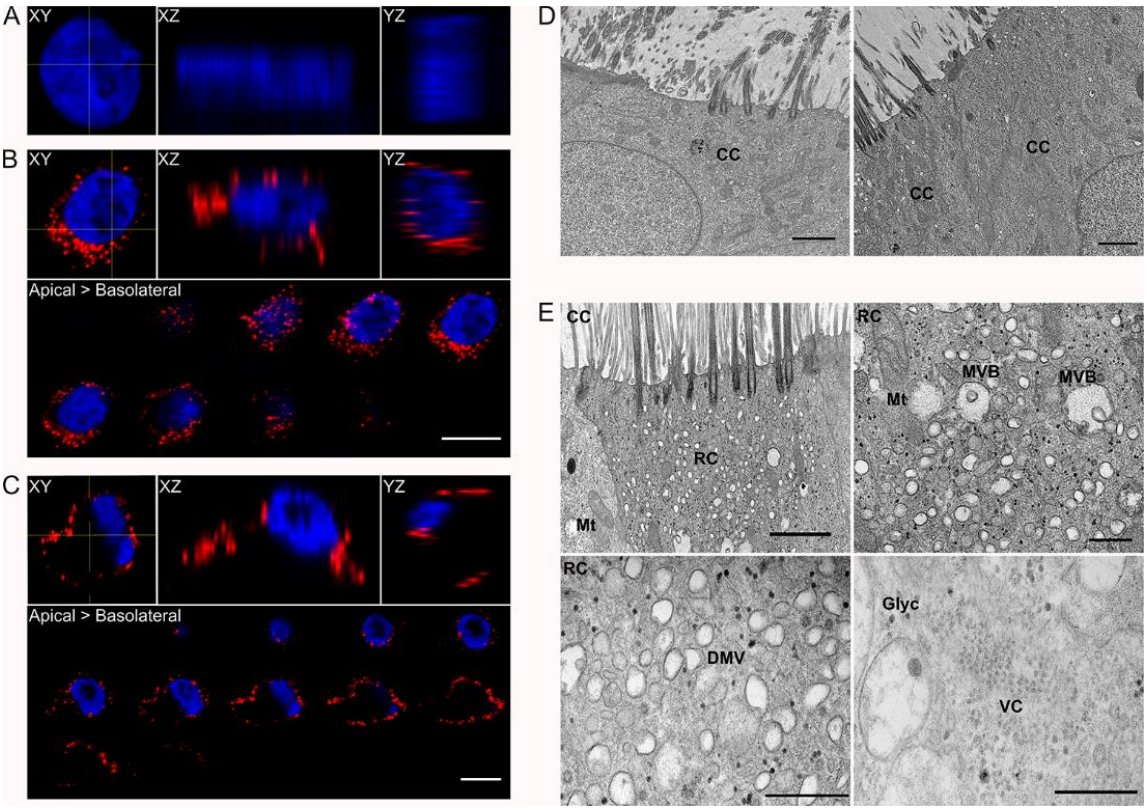

Figure 3.2. Detection of RV-C15 replication complexes in HAE. A-C: Orthogonal views (XY, XZ and YZ planes; yellow lines show the location of XZ and YZ views on the XY plane) from non-infected (**A**) and RV-C15-infected (**B-C**) cells immunostained for dsRNA (red) and nuclei (blue) at 12hpi (z-stacks at 1μm of thickness; scale bar = 10μm). **B-C**: Z-stacks (1μm of thickness) from RV-C15-infected HAE show dsRNA (red) detection by immunofluorescence with perinuclear (**B**) or ring-like disposition close to the plasma membrane (**C**). **D-E**: TEM of non-infected (**D**) and RV-C15-infected (**E**) HAE fixed at 12hpi. **D**: Visualization of ciliated cells (CC) in non-infected HAE (**D**–left panel) occasionally revealed small vesicles spread through the cytoplasm (**D**–right panel) (scale bar = 2μm). **E**: Larger vesicles were detected in ciliated cells (CC) from RV-C15-infected HAE that resembled replicative complexes (RC; **E**–upper-left panel; scale bar = 5μm) observed during RV-A and RV-B infection [354]. These vesicles were detected in close proximity to mitochondria (Mt) and multi-vesicular bodies (MVB; **E**–upper-right panel; scale bar = 2μm), and were found to have double-membranes (DMV; **E**–lower-left panel; scale bar = 0.5μm). Clusters of electron-dense structures in the cytoplasm of RV-C15-infected HAE were seen, reminiscent of viral crystals (VC; **E**–lower-right panel; scale bar = 0.5μm) described for other picornaviruses [355,356]. Glyc = glycogen.

Notably, the nuclei in cells with the ring-like dsRNA pattern were found near the apical cell surface instead of the usual basolateral location in polarized columnar cells (**Figure 3.2C, S3.2B and S3.2D**, possibly a result of large intracellular vesicle formation

(**Figure S3.2E and S3.2F**). Subsequent TEM analysis in non-infected HAE revealed a differentiated epithelium with no overt cytopathic effects (**Figure 3.2D**–left panel) and a limited number of vacuoles in the cytoplasm (**Figure 3.2D** right panel). In contrast, in RV-C15-infected HAE, we identified ciliated cells with many small vesicles clustered near multivesicular bodies, mitochondria, and electron-dense structures similar to β-particles of glycogen (**Figure 3.2E**–upper-left and upper-right panels, respectively). Under higher magnification, we were able to confirm these small vesicles had a double-membrane (**Figure 3.2E**–lower-left panel) similar to replicative complexes previously described for RV-A and RV-B [357]. Interestingly, some ciliated cells in RV-C15-infected HAE also contained electron-dense structures in their perinuclear region similar to the "viral crystals" observed in cells infected by other picornaviruses (**Figure 3.2E**–lower-right panel) [355,356].

3.4.3 RV-C15 infection triggers fragmentation of Golgi stacks and induces PI4P

Different cellular membranes can contribute to the formation of replication organelles during viral infection; however, the Golgi is the main source reported for many picornaviruses, including rhinoviruses [82,358]. Consequently, viral replication is associated with fragmentation of the Golgi stacks and changes in expression of phosphatidylinositol-4-phosphate (PI4P), a Golgi resident lipid [82,358,359]. To determine if RV-C replication induced similar effects, we inoculated HAE with RV-C15 –or RV-A16 and RV-A2 as positive controls [359,360] – and analyzed the Golgi by detection of giantin expression at 12hpi. While giantin visualization revealed a compact structure close to the nucleus in non-infected HAE (**Figure 3.3A**), giantin signal was spread throughout the cytoplasm in cells with evidence of active viral replication for all RVs tested (**Figure 3.3A**). The fragmentation of Golgi structures inferred from our IF data was further supported by

TEM, where, compared to the non-infected control, Golgi stacks were barely visible in cells from RV-C15-infected HAE cultures (**Figure 3.3B**).

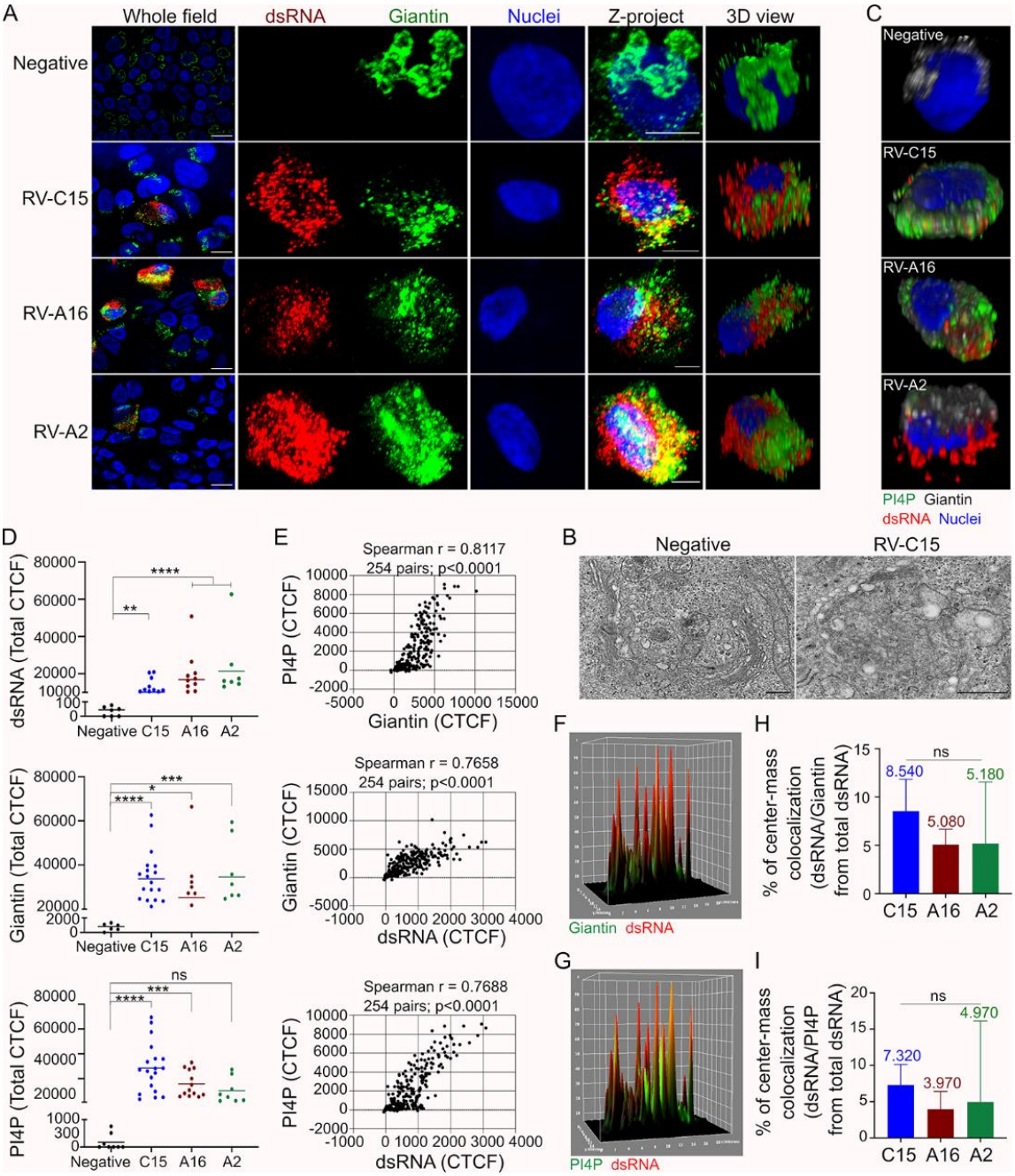

Figure 3.3. Neither the Golgi nor PI4P-positive vesicles are the main site for RV-C15 replication in HAE. A: Visualization of giantin (Golgi marker, green; nuclei, blue) in non-infected HAE and in HAE infected with RV-C15, RV-A16, or RV-A2 (dsRNA+, red) by immunofluorescence (z-stacks at 1µm of thickness; scale bar = 10µm) at 12hpi. **B**: Golgi stacks observed by TEM in ciliated cells from non-infected (left panel) and RV-C15-infected HAE (right panel) at 12hpi (scale bar = 2µm). **C**: 3D view of PI4P (green) and

giantin (gray) in non-infected or rhinovirus-infected (dsRNA+, red) HAE (nuclei, blue) detected by immunofluorescence at 12hpi (z-stacks at 1µm of thickness). **D**: Quantification of fluorescence levels (CTCF; line = mean) of dsRNA, giantin, and PI4P in non-infected HAE and HAE infected with RV-C15, RV-A16, or RV-A2 (dsRNA+ cells) at 12hpi. Dots represent the total CTCF per cell. Statistical analysis was done using the Kruskal-Wallis test following Dunn's multi-comparison test (*p<0.05, **p<0.01, ***p<0.001, ****p<0.0001; ns == non-significant). **E**: Spearman correlation analysis (two-tailed; 0.95% confidence interval) between PI4P and giantin fluorescence levels (CTCF) and also between each protein and dsRNA in RV-C15-infected HAE at 12hpi; each dot represents the fluorescence levels of PI4P and giantin quantified in the same Z-slice. **F** and **G**: 3D surface plot of RV-C15-infected HAE (at 12hpi) showing the immunodetection of dsRNA (red; **F** and **G**), giantin (green; **F**), PI4P (green; **G**); and colocalization (yellow) between dsRNA/giantin (**F**) or dsRNA/PI4P (**G**). **H** and **I**: Spatial colocalization analysis of dsRNA/giantin (**H**) and dsRNA/PI4P (**I**) in HAE infected with RV-C15, RV-A16, or RV-A2 at 12hpi. The median colocalization ratio is noted on top of each bar (bar = median with 95% confidence interval). Statistical analysis was done by Kruskal-Wallis test following Dunn's multi-comparison test.

In addition to a loss of Golgi integrity, we also observed enhanced detection of PI4P in cells with active RV replication compared to non-infected controls. Similar to giantin, PI4P was dispersed throughout the cytoplasm in infected cells, reflecting the same general distribution (perinuclear or ring-like) as observed for dsRNA (**Figures 3.3C, S3.3A and S3.3B**). To further assess the changes in giantin and PI4P levels, we compared the CTCF for these cellular targets in both non-infected and infected cells. Our data revealed both giantin and PI4P levels were elevated and strongly correlated in HAE infected with all RVs, though the change in PI4P was not significant for RV-A2 (**Figures 3.3D, 3.3E, S3.3C and S3.3D**). A direct relationship was also observed between giantin and dsRNA CTCF in RV-C15- and RV-A16-infected cells while PI4P and viral dsRNA CTCF were only correlated in RV-C15 HAE (**Figures 3.3E, S3.3C and S3.3D**).

The close association between Golgi membranes and picornavirus replication has been shown by the colocalization between viral dsRNA and different Golgi markers (e.g., giantin, TGN-46, GM130) [82,352,358]. Therefore, we next sought to evaluate the Golgi as a site for RV-C15 replication through colocalization analysis of dsRNA with giantin, and

PI4P. Despite the strong correlation between giantin and PI4P observed during RV-infection (**Figures 3.3E, S3.3C and S3.3D**), the ratio of colocalization between them was very low at pixel intensity and spatial levels (**Tables S3.1–S3.3**). Surprisingly, the ratios of viral dsRNA/giantin and dsRNA/PI4P colocalization were also low using pixel intensity-based methods (**Tables S3.4–S3.9**). The 3D surface plot from RV-C15-infected cells at 12hpi also demonstrated little evidence of colocalization between dsRNA and giantin (**Figure 3.3F**) or PI4P (**Figure 3.3G**). Spatial colocalization analysis confirmed these observations, with less than 9% of the total dsRNA detected at the same location as giantin or PI4P in RV-C15-infected cells (**Figure 3.3H and 3.3I**, and **Tables S3.4–S3.9**). Thus, despite the fragmentation of the Golgi stacks and increase of PI4P in airway epithelial cells with active RV-C15 replication, our data indicate the Golgi is not the main site for viral genome replication and PI4P is not a marker for sites of RV-C15 replication in HAE as observed for other RVs [82,358].

3.4.4 Endoplasmic reticulum appears to be the RV-C15, but not RV-A16 or RV-A2, genome replication site

Given the low ratio of colocalization between RV-C15 dsRNA and Golgi markers, we next evaluated ER membranes as a potential site for viral genome replication. WB analysis of the ER-associated protein calnexin in RV-C15-infected HAE did not indicate a dramatic change compared to non-infected cultures at 12, 24, or 48hpi (**Figure S3.4A**). However, at the single-cell level, calnexin fluorescence was not only elevated in cells infected with RV-C15, RV-A16, and RV-A2 compared to the negative control at 12hpi (**Figure 3.4A and 3.4B**) but also directly correlated with fluorescence levels of viral dsRNA (**Figure 3.4C**). Interestingly, the 3D view of HAE infected with RV-C15 at 12hpi showed calnexin spread throughout the cytoplasm, and there was a strong indication of calnexin and viral dsRNA colocalization (**Figure 3.4A and 3.4D**), which was further supported by 3D surface plot

data (**Figure 3.4E**). Adding to this, the perinuclear and ring-like distributions of dsRNA were also observed for calnexin in RV-infected cells (**Figure S3.4B**).

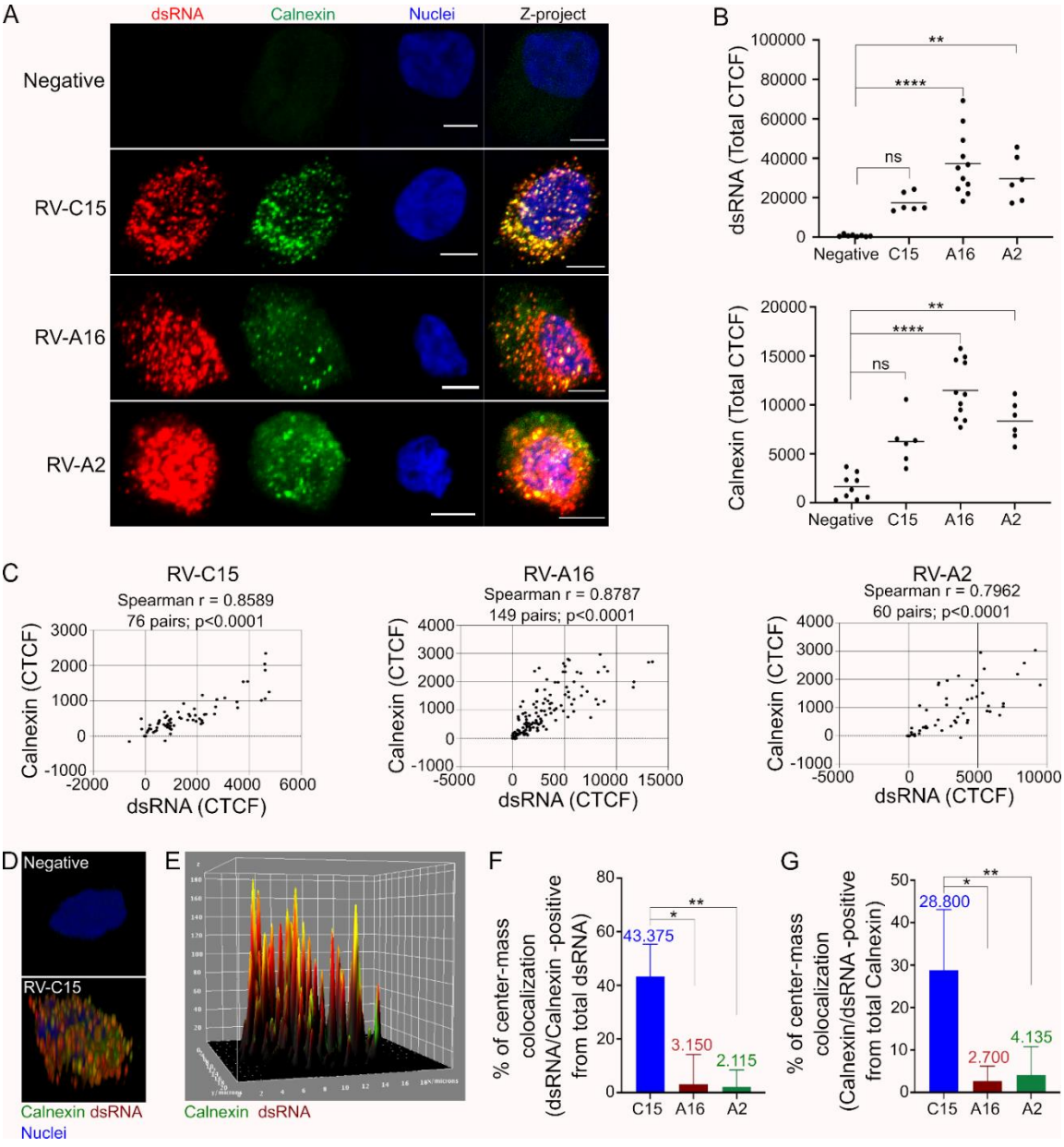

Figure 3.4. ER is a site for RV-C15 genome replication in HAE. A: Detection of calnexin (ER marker, green; nuclei, blue) in non-infected or rhinovirus-infected (dsRNA+, red) HAE at 12hpi (z-stacks at 1µm of thickness; scale bar = 5µm). **B**: Quantification of fluorescence levels (CTCF; line = mean) of dsRNA and calnexin in non-infected cells and RV-infected (dsRNA+) HAE detected by immunofluorescence at 12hpi. Dots represent the total CTCF per cell. Statistical analysis was done using Kruskal-Wallis test following Dunn's multi-comparison test (**p<0.01, ****p<0.0001). **C**: Spearman correlation analysis (two-tailed; 0.95% confidence interval) between calnexin and dsRNA fluorescence levels (CTCF) in

RV-C15, -A16, or -A2-infected HAE at 12hpi. Each dot represents the fluorescence levels of dsRNA and calnexin quantified in the same Z-slice. **D**: 3D view of RV-C15-infected HAE shows the immunodetection of calnexin (green), viral dsRNA (red), and calnexin/dsRNA colocalization (yellow) at 12hpi (z-stacks at 1µm of thickness). **E**: 3D surface plot of RV-C15-infected HAE shows the detection of calnexin (green), dsRNA (red), and calnexin/dsRNA colocalization (yellow) by immunofluorescence at 12hpi. **F-G**: Spatial colocalization analysis done in RV-C15, RV-A16, or RV-A2-infected HAE (dsRNA+) shows the ratio of dsRNA/calnexin (**F**) and calnexin/dsRNA (**G**) colocalization at 12hpi. The median colocalization ratio is plotted at the top of each bar (bar = median with 95% confidence interval); statistical analysis done by Kruskal-Wallis test following Dunn's multi-comparison test ($p<0.05$, $^{**}p<0.01$).

Pixel intensity-based analysis confirmed the high level of colocalization between viral dsRNA and calnexin in cells infected not only with RV-C15 (56.3%), but also RV-A16 (28%) and RV-A2 (49.1%) at 12hpi (**Tables S3.10–S3.12**). However, this high colocalization ratio was only confirmed for RV-C15-infected cells at the 3D level (spatial colocalization analysis; **Figure 3.4F and 3.4G**), suggesting that, unlike RV-A16 and RV-A2, the ER is the main site for RV-C15 genome replication.

3.4.5 RV-C15 infection induces incomplete autophagy

Previous studies have shown picornaviruses, including several rhinoviruses, manipulate the autophagy pathway to mediate non-lytic release of progeny following replication [361]. Since the induction of autophagy is rhinovirus genotype-specific [361–363], we sought to determine if RV-C15 triggered the induction of autophagy in HAE. Towards this goal, we inoculated cultures with RV-C15 alongside RV-A16 and RV-A2 as controls, and probed for Lysosome-associated membrane glycoprotein 1 (Lamp-1; a lysosome marker) and LC3b (an autophagosome marker) by WB. LC3b protein levels were minimal in non-infected HAE, suggesting a low basal rate of autophagy while Lamp-1, LC3b-I, and LC3b-II expression varied across donors and time points during RV-C15 infection. Still, LC3b-I and LC3b-II levels were clearly elevated at 12 and 48hpi in cultures with robust infection evidenced by RV-C15 VP1 protein levels (**Figure 3.5A**). Therefore,

we further evaluated levels of both Lamp-1 and LC3b in HAE by IF 12hpi. Lamp-1 and LC3b detection in HAE was significantly stronger in RV-C15- and RV-A2-infected cells while the level of detection in RV-A16-infected HAE was similar to the negative control (**Figure 3.5B and 3.5C**). Curiously, the 3D view of non-infected cells showed an apical localization of Lamp-1 while this protein was spread through the cytoplasm in RV-infected cells (**Figure 3.5B**). A high correlation ratio between Lamp-1 fluorescence levels and dsRNA was obtained in RV-infected cells; however, LC3b levels strongly correlated with dsRNA only in cultures infected with RV-C15 and RV-A2 (**Figures 3.5D and S3.5**). Together, these data suggest RV-C15 and RV-A2 (but not RV-A16) induce autophagy to significant levels over the baseline in HAE.

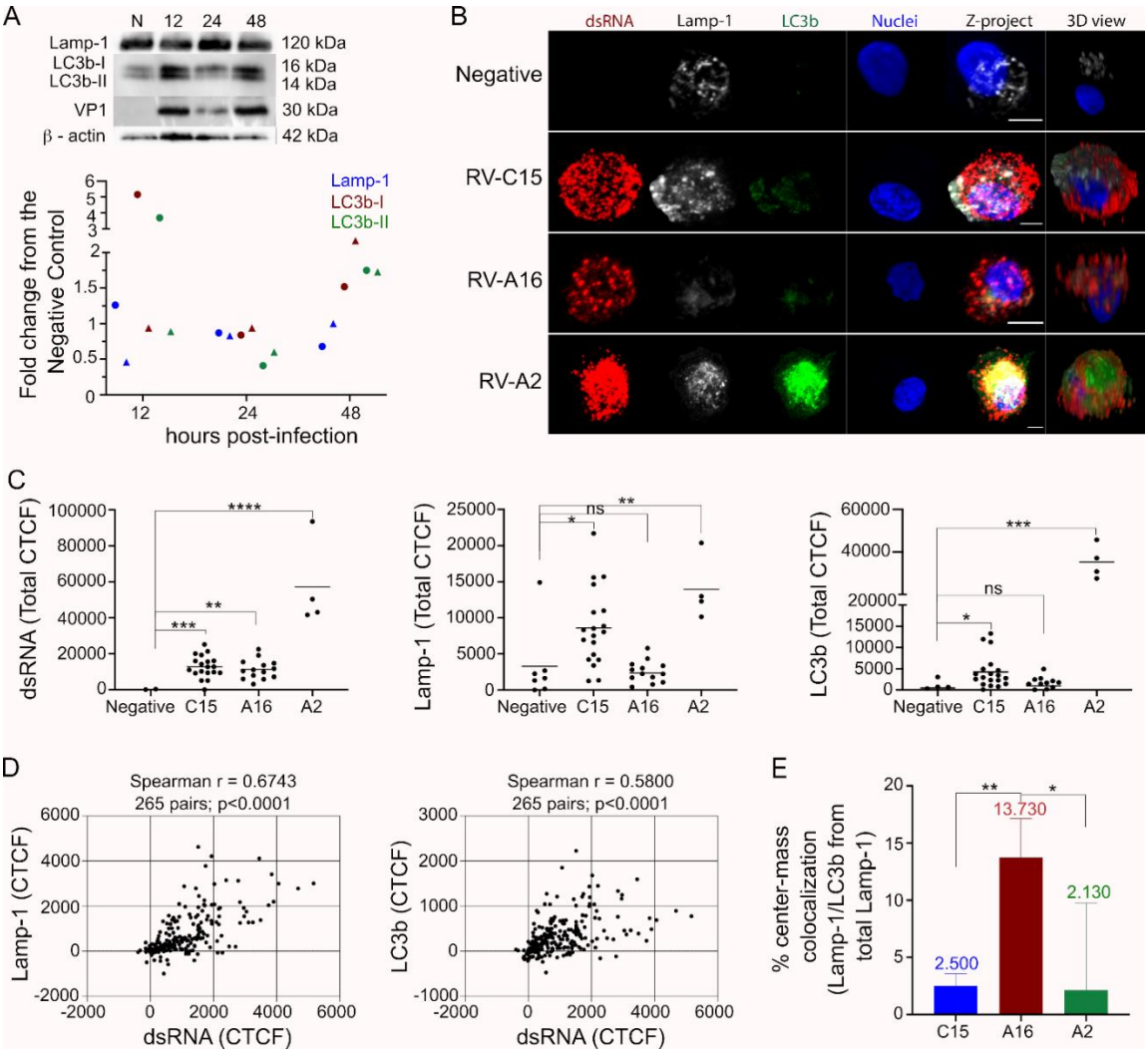

Figure 3.5. RV-C15 replication induces incomplete autophagy in HAE at 12hpi. A: Fold change graph represents Lamp-1, LC3b-I, and LC3b-II protein levels normalized to the endogenous control (actin) and compared to non-infected cultures. Data shown are from two independent donors, represented by circles and triangles. Blot above is from the donor represented by triangles, including the detection of VP1 protein of RV-C15. **B**: Detection of Lamp-1 (gray), LC3b (green) and dsRNA (red; nuclei, blue) in non-infected HAE and HAE infected with RV-C15, RV-A16, or RV-A2 by immunofluorescence at 12hpi (z-stacks at 1μm of thickness; scale bar = 5μm). **C**: Quantification of fluorescence levels (CTCF) for Lamp-1, LC3b, and dsRNA in non-infected and RV-infected (dsRNA+) HAE at 12hpi. Dots represent the total CTCF per cell and the line indicates the mean. Statistical analysis was done by Kruskal-Wallis test following Dunn's multicomparison test (*p<0.05, **p<0.01). **D**: Spearman correlation analysis (two-tailed; 0.95% confidence interval) between fluorescence levels for dsRNA and Lamp-1 or LC3b in RV-C15-infected HAE at 12hpi. Each dot represents the fluorescence levels of dsRNA and Lamp-1 or LC3b quantified in the same Z-slice. **E**: Spatial colocalization analysis of Lamp-1/LC3b colocalization in RV-C15, RV-A16, and RV-A2 -infected (dsRNA+) HAE at 12hpi. The median colocalization ratio value is plotted top of each bar (bar = median with 95%

confidence interval); statistical analysis done by Kruskal-Wallis test following Dunn's multi-comparison test (*p<0.05, **p<0.01).

Since the inhibition of autolysosome formation (the last step in the autophagy pathway) is characteristic of picornaviruses that induce this pathway to promote virus release [364], we further evaluated autolysosome formation defined by Lamp-1 and LC3b colocalization. Results from spatial colocalization analysis in cultures infected with RVs indicated greater detection of autolysosomes in RV-A16-infected cells compared to RV-C15- and RV-A2-infected cells (**Figure 3.5E and S3.13–S3.15 Tables**). Thus, these data suggest that, similar to RV-A2 but unlike RV-A16, RV-C15 induces incomplete autophagy in HAE.

3.4.6 STING expression promotes replication of RV-C15 in HAE

In this study, we observed RV-C15 genome replication in HAE to be associated with the ER (**Figure 3.4**) and the induction of incomplete autophagy at 12hpi (**Figure 3.5**). Interestingly, STING, which localizes to the ER, was recently shown to induce the autophagy pathway during RV-A16 infection [365] and was identified as a proviral factor for RV-A and RV-C, but not RV-B, where STING overexpression facilitated viral genome replication in Huh-7 cells [349]. Based on these data, we investigated the expression of STING in HAE infected with RV-C15. Interestingly, we detected an increase in STING expression overtime, in line with increasing viral VP1 levels (**Figure 3.6A**) as well as robust detection of STING by IF in dsRNA(+) ciliated cells at 12hpi (**Figure 3.6B**). Notably, 3D view analysis revealed that dsRNA/STING-double positive cells also exhibited dispersed distribution of acetylated alpha-tubulin, suggesting STING levels increase as replication progresses (**Figure 3.6C**). Indeed, the CTCF of STING not only increased significantly in HAE infected with RV-C15 (**Figure 3.6D**), but also strongly correlated with dsRNA levels at 12hpi (**Figure 3.6E**). However, despite the maximum Z-projection, 3D surface plot, and

pixel intensity colocalization analysis suggesting high level of dsRNA/STING colocalization in RV-C15-infected HAE (**Figure 3.6F and 3.6G, and S3.16 Table**), spatial colocalization analysis indicated the median colocalization ratio between both targets was lower than 5% (**Figure 3.6H**).

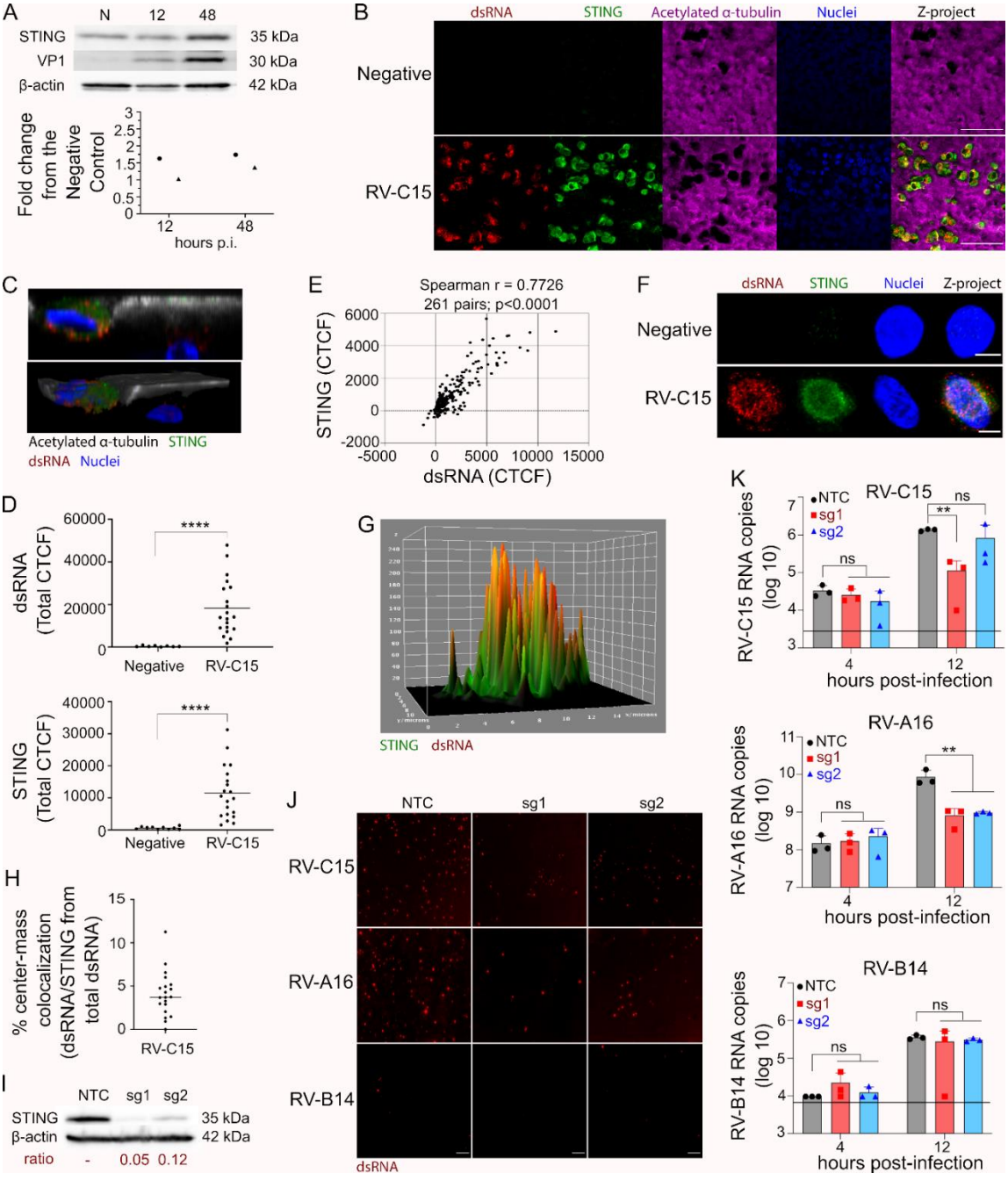

Figure 3.6. STING expression promotes RV-C15 replication in HAE at 12hpi. A: Western blot showing STING and VP1 expression at 12 and 48hpi in non-infected or RV-

C15-infected HAE. Fold change graph represents STING protein levels normalized to the endogenous control (actin) and compared to non-infected cultures. Data shown are from two independent donors, represented by circles and triangles. Blot above is from the donor represented by triangles. **B**: Immunofluorescence detection of STING (green) in non-infected or RV-C15-infected (dsRNA+; red) ciliated cells (acetylated α-tubulin, magenta) at 12hpi (scale bar = 50μm). **C**: XZ orthogonal view (upper) and 3D view (below) of RV-C15-infected HAE shows the detection of STING (green) and viral dsRNA (red) in ciliated cells (acetylated αtubulin, gray) at 12hpi (z-stacks at 1μm of thickness). **D**: Quantification of dsRNA and STING fluorescence levels (CTCF) in non-infected and RV-C15-infected (dsRNA+) HAE at 12hpi. Dots represent the total CTCF per cell and the line indicates the mean. Statistical analyses were done by Mann-Whitney test (two-tailed; 0.95% confidence interval; **p<0.01). **E**: Spearman correlation analysis (two-tailed; 0.95% confidence interval) between fluorescence levels for dsRNA and STING in RV-C15-infected HAE at 12hpi. Each dot represents the fluorescence levels of dsRNA and STING quantified in the same Z-slice. **F**: 2D split channel views of RV-C15-infected HAE showing the detection of STING (green), dsRNA (red), and STING/dsRNA colocalization (yellow) by immunofluorescence at 12hpi (scale bar = 5μm). **G**: 3D surface plot of RV-C15-infected HAE shows the detection of STING (green), dsRNA (red), and STING/dsRNA colocalization (yellow) by immunofluorescence at 12hpi. **H**: Spatial colocalization analysis shows the ratio of dsRNA/STING colocalization in RV-C15-infected HAE at 12hpi (bar = median). **I**: Western blot showing STING expression, quantified below, in HAE derived from BCi-NS1.1 cells transduced with non-targeting control (NTC), sgRNA1 (sg1), or sgRNA2 (sg2). **J**: Immunofluorescence detection of dsRNA (red) in HAE derived from BCi-NS1.1 cells transduced with NTC, sgRNA1 (sg1), or sgRNA2 (sg2) infected with RV-C15, RV-A16, or RV-B14 at 12hpi (scale bar = 100μm). **K**: qPCR to detect RV RNA in HAE derived from BCi-NS1.1 cells transduced with NTC, sgRNA1 (sg1), or sgRNA2 (sg2) and infected with RV-C15, RV-A16, or RV-B14 at 4 and 12hpi. Each bar represents the mean value obtained across n = 3 cultures/condition (individual dots); the black line represents the limit of detection (RV-C15 = $10^{3.5}$; RV-A16 = $10^{5.9}$(not visible on the graph); RV-B14 = $10^{4.8}$); statistical analysis was done by Ordinary One-way ANOVA and Tukey's multiple comparisons test (**p<0.01).

To better understand the importance of STING to RV-C15 genome replication, we genetically knocked-out STING using a CRISPR/Cas9 approach in immortalized human airway epithelial cells (BCi-NS1.1 cells [366]), differentiated them into HAE cultures (**Figure 3.6I**), and infected them with RV-C15, RV-A16, or RV-B14. Immunofluorescence detection of dsRNA at 12hpi confirmed the susceptibility of control cultures expressing a non-targeting guide RNA to RV-C15, RV-A16, and RV-B14 infection (**Figure 3.6J**). However, the frequency of dsRNA(+) cells was lower in STING-depleted HAE infected with RV-C15 or RV-A16 (**Figure 3.6J**). While infection with RV-B14 was less efficient

overall, a similar frequency of dsRNA(+) cells were observed in both control and knockout HAE (**Figure 3.6J**). STING-knockout cultures also had significantly lower intracellular viral RNA copy numbers for RV-C15 and RV-A16 but not RV-B14, further validating our results (**Figure 3.6K**) and suggesting that the increase of STING expression in RV-C15-infected HAE has an advantageous impact on viral genome replication.

3.4.7 RV-C15 infection alters epithelial permeability, disposition of tight junction-associated proteins, and mucociliary clearance

Our results to this point highlight RV-C15-induced cytopathic effects at the single-cell level in HAE (**Figures 3.1–3.5**). To extend these observations, we quantified extracellular lactate dehydrogenase (LDH) at the culture-level as an indication of plasma membrane leakage. LDH release was restricted to the apical compartment and did not exceed 20% of the maximum levels obtained from lysed control cultures; however, LDH levels increased over time (**Figure 3.7A**) in line with RV-C15 replication kinetics (**Figure 3.1A and 3.1B**). Thus, we sought to further evaluate the global impact of RV-C15 infection on epithelial integrity. Interrogation of HAE permeability during RV-C15 infection revealed a significant, albeit transient, decrease in transepithelial electrical resistance (TEER) at 12hpi (**Figure 3.7B**). Since the transepithelial transport of ions is mediated by pores formed by integral membrane proteins termed claudins [367], we next investigated the expression and localization of claudin-1 during RV-C15 infection in HAE. While claudin-1 protein levels in cultures infected with RV-C15 did not vary (**Figure 3.7C**), we observed a change in claudin-1 distribution in RV-C15-infected cells at 12hpi by IF (**Figure 3.7D**). To determine if this translocation was specific to claudin-1, we characterized Zona occludens 1 (ZO-1), a cytoplasmic tight junction-associated protein. Similar to claudin-1, with the exception of one donor at 48hpi, ZO-1 protein levels for both subunits (ZO-1 +α and ZO-1 -α) did not vary in RV-C15-infected HAE compared to the negative control (**Figure 3.7C**),

while ZO-1 disposition was more widespread in dsRNA(+) cells (**Figure 3.7E**). To quantify the effect of RV-C15 infection on ZO-1 disposition over time, we utilized the Junction Analyzer Program (JAnaP) [368–370], which allowed us to assess the profile of ZO-1 detected in non-infected and RV-C15-infected cells (**Figure 3.7F**). The increase of discontinuous ZO-1 quantified in this assay (**Figure 3.7G**) indicates the ZO-1 translocation in HAE (**Figure 3.7E**) parallels the progression of RV-C15-infection. Additionally, two profiles of discontinuous ZO-1 were evaluated, and ZO-1 was found in a more perpendicular than punctual disposition in RV-C15- infected HAE (**Figure 3.7H and 3.7I**).

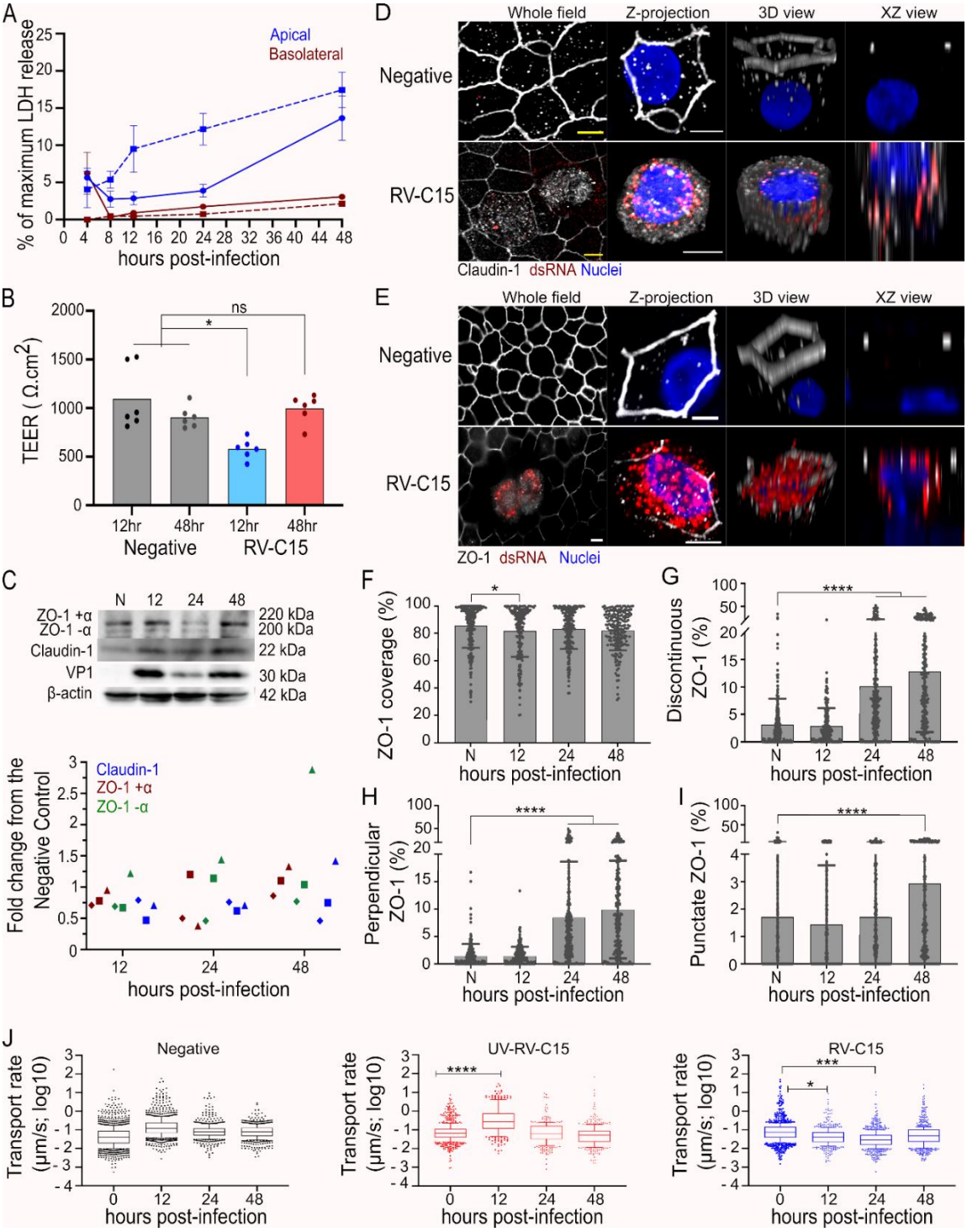

Figure 3.7. RV-C15 infection promotes translocation of tight junction proteins and impairs mucociliary clearance (MCC). A: Percentage of maximum LDH release graph shows the cytotoxicity of RV-C15 infection in HAE from two donors (continuous and dash lines). Mean and standard error of the mean values were obtained across n = 3 cultures/time-point. **B**: Quantification of transepithelial electrical resistance (TEER) in non-infected and RV-C15-infected HAE (two donors; each performed in triplicate). Each bar

represents the mean value obtained across n = 3 cultures/condition (individual dots); statistical analysis was done by Ordinary one-way ANOVA following Tukey's multiple comparisons test (*p<0.05, ns= non-significant). **C**: Fold change graph represents claudin-1 and zona occludens-1 (ZO-1) α+ and α- protein levels normalized to the endogenous control (actin) and compared to non-infected cultures. Data shown are from three independent donors, represented by diamonds, triangles, and squares. Blot above is from the donor represented by triangles, which includes the detection of VP1 of RV-C15. **D-E**: Visualization of claudin-1 (**D**, gray) and ZO-1 (**E**, gray) in non-infected and RV-C15-infected (dsRNA+, red) HAE (nuclei, blue) detected by immunofluorescence at 12hpi (z-stacks at 1μm of thickness; scale bar = 5μm). **F-I**: Quantification of ZO-1, detected by immunofluorescence, in non-infected and RV-C15-infected using the JAnaP software [368–370]. Total ZO-1 detected per cell perimeter (percentage of coverage; **F**); detection of discontinuous ZO-1 (disrupted; **G**)—perpendicular (**H**) and punctate (**I**) profiles. Each bar represents the mean ZO-1 value obtained across different fields per culture/time-point (individual dots). Statistical analysis was done by Ordinary one-way ANOVA following Dunnett's multiple-comparison test (*p<0.05, ***p<0.001, ****p<0.0001).

Given the ciliated cell tropism RV-C15 and the important role of these cells in promoting mucociliary clearance (MCC), we also assessed the global impact of RV-C15 infection on mucus transport. HAE cultures were equilibrated at 34˚C and the transport rate of red-fluorescent microspheres in the extracellular mucus gel was calculated immediately prior to inoculation, and up to 48hpi. IF confirmed viral replication at 12hpi in HAE inoculated with viable, but not UV-inactivated, RV-C15 (**Figure S3.6**). The transport of microspheres indicated a slight increase in MCC in HAE inoculated with PBS and a similar, albeit significant, elevation in microsphere transport rate in UV-inactivated RV-C15-inoculated cultures at 12hpi (**Figure 3.7J**), likely attributable to the addition of fluid on the apical surface after the T = 0 time point. Despite this, RV-C15 infection resulted in a significant decrease in MCC at both 12 and 24hpi (**Figures 3.7J and S3.6B**) indicating viral replication impairs this innate host defense mechanism.

3.5 Discussion

RV is becoming increasingly recognized as a cause of both upper and lower respiratory tract infection [21–24,32]. Furthermore, the risk for development of asthma in

children after infection by RV, especially RV-C [24,338,339], highlights the clinical relevance of these viruses. Due to restricted receptor expression in traditional immortalized cell culture systems [351], we investigated RV-C15 replication using an in vitro model of HAE that supports the entire RV-C life cycle. Previous studies in similar systems have shown the impact of temperature and cell differentiation stage on RV-C replication [56,347,350]. Here, we detail a multi-step replication curve for RV-C15 (**Figure 3.1A and 3.1B**), indicating the peak of intracellular viral load at 12hpi by qPCR and IF (**Figures 3.1A, 3.1B and S3.1A**) and peak viral release at 24hpi (**Figure 3.1A and 3.1B**) in agreement with a previous report characterizing RV-C11 and RV-C15 infection in bronchial cells [351].

In well-differentiated HAE, we detected CDHR3 on the apical surface of ciliated cells (**Figure 3.1C–3.1E**). Interestingly, we did not observe any evidence of cytosolic CDHR3 in non-infected cells, differing from previous immunofluorescence data [346,348] but in agreement with CDHR3 detection on cilia by TEM [346]. However, CDHR3 distribution changed and protein levels decreased in RV-C15-infected cells (**Figures 3.1C–3.1E, 3.1G and S3.1F**) without altering levels of acetylated alpha-tubulin or FoxJ1 (**Figure S3.1E, S3.1G and S3.1H**). Unlike ICAM-1 (the receptor for major-group RVs) and LDLR (the receptor for minor-group RVs), the dynamics of CHDR3 during infection and associated pathway(s) of RV-C entry remain unknown. After endocytosis of RV-A and RV-B particles, ICAM-1 and LDLR are either degraded in the lysosome with empty capsids, or LDLR is trafficked from the endosome to be recycled [371]. The intracellular distribution of CDHR3 and the loss of protein expression after RV-C15 infection in HAE suggests CDHR3 follows the same path as other RV receptors.

After confirming the susceptibility of our HAE models to RV-C15 infection, we further investigated the localization and association of replication complexes with various

organelle markers at the single-cell level. Using dsRNA as a marker for virus replication, we observed both perinuclear and ring-like distribution of replication centers closer to the basolateral membrane during RV-C15, RV-A16, and RV-A2 replication (**Figures 3.2A–3.2C and S3.2A–S3.2D**). To our knowledge, the latter profile has not been described during RV or any other picornavirus infection, and our TEM data indicates the formation of large intracellular vesicles filled with unknown electron-dense content may be the underlying cause of altered dsRNA disposition. Interestingly, other cellular markers such as giantin, PI4P, and calnexin (**Figures S3.3D and S3.4B**) showed a similar ring-like distribution in these cells, further suggesting the presence of a large vesicle that precipitates global changes in intracellular organization. Whether these large vesicles play a specific role in RV replication or if they are simply indicative of cellular changes that precede cell death is unknown. Indeed, we hypothesize that the perinuclear and ring-like patterns of dsRNA may be indicative of different stages of infection, with the ring-like formation occurring later during the viral life cycle, coincident with more advanced cytopathic effects.

Notably, our TEM analysis also identified smaller, double-membraned vesicles, similar to those identified during replication of other RVs and related picornaviruses [82,352–354] that likely represent sites of RV-C15 genome replication (**Figure 3.2D and 3.2E**). Prior reports identified the induction of replicative complexes derived from the ER by the poliovirus 2BC and 3A proteins [372,373] and the same proteins in RV-A16 were associated with the ER at an early stage of viral infection [359]. Still, work to date suggests the Golgi is the primary site for picornavirus genome replication [82,352,358]. Further, the formation of replicative complexes has been associated with cholesterol exchange driven by OSBP1 [82], accumulation of ER-vesicles resulting from the inhibition of ERGIC-to-Golgi transport [360], and fragmentation of Golgi stacks induced by the viral 3A protein

[358,359]. In this study, we observed an increase of giantin and PI4P levels, dissolution of Golgi stacks, and spread of PI4P-positive vesicles in RV-C15-infected cells (**Figures 3.3A-3.3D and S3.3A**) suggesting RV-C impacts Golgi membranes similar to other picornaviruses. However, despite the strong correlation between dsRNA and fluorescence levels of both giantin and PI4P (**Figure 3.3E**), colocalization analysis indicated neither giantin- nor PI4P-positive vesicles are the main site for RV-C15 genome replication (**Figure 3.3H and 3.3I**). Similar observations were made in RV-A16-infected HAE (**Figure 3.3**) although dsRNA fluorescence levels only strongly correlated with giantin and not PI4P (**Figure S3.3B**). These data were unexpected, as prior work in HeLa and nasal epithelial cells noted PI4P enrichment of Golgi membranes during RV-A16 genome replication [82]. Different from the literature [82], Golgi and PI4P-positive vesicles were not the main site for RV-A2 genome replication in HAE either (**Figure 3.3H and 3.3I**), and neither the significant increase in levels of giantin nor insignificant increase in PI4P correlated strongly with viral dsRNA (**Figures 3.3D and S3.3C**). It is important to highlight that our study evaluated rhinovirus replication in HAE at a later time point than other reports (3-8hpi) [82,352,354]; thus, our data do not exclude the possibility that Golgi and PI4P-positive membranes support RV replication earlier in infection.

Most notably, our results demonstrated elevated levels of calnexin in RV-infected HAE (**Figure 3.4A and 3.4B**) and a high ratio of dsRNA/calnexin colocalization in cells infected with RV-C15, but not RV-A2 and RV-A16 (**Figure 3.4E–3.4G**), identifying the ER as the main site for RV-C15 replication. The increase in calnexin levels observed in this study could be the result of ER stress in infected cells, as reported for RV-A1B and RV-A16 [374,375]. The RV-A16 2B protein [375] forms pores on ER membranes, promoting calcium ion efflux, which increases membrane permeability and triggers stress. These effects on ER membranes have been associated with more efficient release of vesicles

that may represent additional sites for picornavirus replication [376]. Notably, inhibition of ER stress resulted in a decrease in RV-A1B replication [374] corroborating the hypothesis that ER-derived vesicles are a site for viral replication [376] and supporting our conclusion that RV-C15 replication is associated with the ER in HAE (**Figure 3.4E–3.4G**).

In the final stages of the viral life cycle, progeny picornavirus virions are released through cell lysis or by usurping the autophagy pathway [361–363]. Exploitation of the autophagy pathway was originally shown for poliovirus [364] and is characterized by virus-mediated inhibition of autolysosome formation and release of autophagosomes full of nascent virions that likely protects particles from the immune response [362]. RV-A2 induced incomplete autophagy in HAE in contrast to RV-A16 (**Figure 3.5B and 3.5C**), as expected [363]. This conclusion was based on elevated Lamp-1 and LC3b levels, but a very low ratio of Lamp-1/LC3b colocalization indicating a failure to form autolysosomes (**Figure 3.5E**). The results obtained in RV-C15-infected HAE were similar to RV-A2, indicating the induction and manipulation of the autophagy pathway (**Figure 3.5B, 3.5C and 3.5E**). Use of the autophagy pathway to release progeny would explain the absence of cytopathic effects visible under light microscopy in HAE cultures infected with RV-C15. To our knowledge, this is the first time the autophagy pathway has been analyzed during RV-C infection.

The identification of ER as a site for genome replication and induction of autophagy during RV-C15 infection of HAE led us to investigate STING, which has been associated with the induction of ER stress and autophagy [365,377]. In this study, we detected an increase in STING expression in RV-C15-infected HAE (**Figure 3.6A, 3.6B, 3.6D and 3.6F**) which correlated with levels of dsRNA (**Figure 3.6E**) and VP1 protein (**Figure 3.6A**). This correlation, however, was not related to a close interaction between STING and dsRNA, as the median colocalization ratio at the spatial level was lower than 5% (**Figure**

3.6H). Additionally, viral genome replication was impacted in the absence of STING, resulting in significantly lower intracellular viral RNA levels at 12hpi for RV-C15 and RV-A16, but not RV-B14 (**Figure 3.6J and 3.6K**). These data, which assayed endogenous STING expression in RV-infected HAE, corroborate published data in undifferentiated cells indicating STING expression is important for RV-A and RV-C genome replication [349]. STING is an ER-resident transmembrane protein which can be phosphorylated by TANK binding Kinase I (TBK1) or translocated to the ER-Golgi intermediate compartment (ERGIC) before phosphorylation [378]. The phosphorylation of STING in the ER is necessary for autophagy induction during RV-A16 infection [365], while the translocation to the ERGIC is required for ER stress [377]. The low ratio of dsRNA/STING spatial colocalization at 12hpi (**Figure 3.6H**) is surprising and indicates that either genome replication of RV-C15 occurs at different sites on ER membranes (STING-negative) or most of STING had already been translocated to ERGIC. RV-C15 replication also induced autophagy in HAE, though more experiments are needed to relate this phenomenon to STING activation.

Given the observed impacts of RV-C15 replication in infected cells, we further probed the effects of viral infection on the epithelium functionality, including barrier permeability and mucociliary clearance. The level of cytotoxicity of RV-C15 infection in HAE, measured by LDH release, increased overtime in the apical compartment only (**Figure 3.7A**), in agreement with viral cellular tropism for ciliated epithelial cells that face the luminal surface of the airway (**Figure 3.1**) [347,350]. The dissociation of tight junctions during viral infection, including RV-A and RV-B, has been associated with the loss of epithelial-selective permeability and an increase in bacteria translocation across the epithelium [379]. A previous analysis of RV-A16, RV-A1B, and RV-A39 found the reduction of TEER and increase in epithelium permeability for inulin were associated with

both claudin-1 and ZO-1 dissociation [376]. Similar to these reports, RV-C15 temporarily increased epithelial permeability to small particles and ions (as indicated by a temporary loss in TEER, **Figure 3.7B**) which may be due, at least in part, to claudin-1 translocation (**Figure 3.7D**). Additional claudins (e.g., claudin-3, -4 and -5) that are also expressed in the airway epithelium and known to impact transcellular transport were not assayed here [380,381]. Still, the altered expression of tight junction proteins was not restricted to claudin-1 as we also detected ZO-1 throughout the cytoplasm in dsRNA(+) cells without any change in overall protein levels during infection (**Figure 3.7C and 3.7E**). Despite being a tight junction protein, ZO-1 interactions are more important to cell polarization and paracellular permeability [382]. Although we did not check paracellular transport of large particles, the observed disrupted states for ZO-1 indicated progressive translocation with ongoing viral infection (**Figure 3.7F–3.7I**), possibly impacting cellular organization. Nonetheless, the loss of TEER and changes in claudin-1 and ZO-1 observed in this study for RV-C15 were less dramatic than previous reports for RV-A and RV-B [361,363,379]. The lesser impact on epithelium permeability caused by RV-C15 infection may be associated with an earlier induction of the mechanism of repair, which could result from the shift in cell metabolism to a glycolysis state followed by lipid biosynthesis [383].

Beyond epithelial barrier integrity, we also identified an impact of RV-C15 on mucociliary clearance functionality. MCC decreased significantly after 12hpi in HAE infected with RV-C15 but not UV-inactivated virus, similar to a previous study that reported an impact on MCC 5 days post-infection [95], and indicating that active viral replication interferes with this cellular mechanism of pathogen removal (**Figure 3.7J**). We speculate that the temporary increase in MCC observed in cultures inoculated with UV-inactivated virus is due to the addition of fluid on the apical surface. However, as this increase was not significant for the negative control, it may also indicate that the host response to

incoming viral particles stimulates MCC. The coordinated beating of ciliated cells drives the basal MCC rate of ~5.5 mm/min, which can be altered by mucus composition, temperature, and humidity [384–386]. Indeed, mucus hypersecretion is a known symptom during RV infections [387], which has also been associated with changes in mucus composition [388]. In this study, we noted altered distribution of acetylated alpha-tubulin in cells with active viral replication (**Figure 3.1D and 3.1F**) which likely indicates impaired cilium structure and function in these cells. Whether the progressive loss of cilia function and eventual death of infected cells contributes to our observed change in MCC during RV-C15 infection is not clear.

In conclusion, our present study expands our current understanding of RV replication in a physiologically-relevant setting, substantiating previous observations related to virus-induced membrane reorganization, and demonstrating that RV-C15 displays many typical features of picornavirus infection. In addition, we identify RV-C15 replication in association with ER membranes unlike previously characterized RVs. While we speculate that these data identify a unique feature of RV-C replication, our study is limited by the use of only one RV-C genotype; thus, further analysis to confirm these observations using additional RV-C isolates is important. Notwithstanding, our findings underscore the fact that virus-host interactions critical for rhinovirus replication are not always conserved, possibly contributing to their different clinical profiles, and supporting further investigation into this group of pathogens.

3.6 Materials and Methods

3.6.1 Primary and immortalized cell culture and viral stocks

Human airway tracheobronchial epithelial cells isolated from airway specimens from four unique donors without underlying lung disease were provided by Lonza, Inc.

Primary cells derived from single patient sources were expanded on plastic and subsequently plated (5 x 10^4 cells/well) on rat-tail collagen type 1-coated permeable transwell membrane supports (6.5mm, #3470; Corning, Inc., Corning, NY). HAE cultures were grown in Pneumacult-Ex basal medium (#05008, StemCell Technologies, Seattle, WA), or Pneumacult-ALI medium (#05001, StemCell Technologies, Seattle, WA) with provision of an air-liquid interface for approximately 6 weeks to form differentiated, polarized cultures that resemble *in vivo* pseudostratified mucociliary epithelium. CDHR rs6967330 genotyping was achieved by sequencing using the following primers: 5'-GAAAGAAGGCCCGCCAGAACCC-3' (forward) and 5'-TGGGGCTGGAATCAAGGTCGGT-3' (reverse; this study): donor 1 –heterozygous G/A (used in **Figures 3.1A, 3.1C, 3.2, 3.3A, 3.3B, 3.4, 3.5A, 3.6A, 3.7, 3.S1A, S3.1D–S3.1G, S3.2, S3.4, and S3.6**); donor 2 –homozygous G/G (used in **Figures 3.1B, 3.7A, 3.7C and 3.7D**); donor 3 –undetermined (used in **Figures 3.1D–3.1G, 3.3C–3.3I, 3.5A, 3.6B–3.6G, 3.7C, S3.1B, S3.1C, S3.1F–S3.1I, S3.3 and S3.4B**); and donor 4 –homozygous A/A (used in **Figures 3.5B–3.5E, 3.7B, and S3.5**). The two CDHR3 alleles, G and A, yield amino acids C529 and Y529, respectively.

H1 HeLa (#CRL-1988; ATCC, Manassas, VA) and HEK-293T (#CRL-11268; ATCC) cells were cultivated in Dulbecco's Modified Eagle Medium (DMEM; #11965118; Gibco–Thermo Scientific, Waltham, MA) supplemented with fetal bovine serum (FBS; GenClone FBS; Genesee Scientific, San Diego, CA) and 1% penicillin/streptomycin (#15140122; Gibco). All cell cultures were maintained at 37˚C with 5% CO2 and tested regularly for mycoplasma.

RV-C15, RV-A2, RV-B14, and RV-A16 were rescued from infectious clones kindly donated by Drs. James Gern and Yuri A. Bochkov, (pRV-C15), Dr. Wai-Ming Lee (pRV-A2) and Dr. Ann Palmenberg (pRV-B14 and pRV-A16) from the University of Wisconsin–

Madison. Rescue of infectious RV was done according to published protocols [92,389] in H1 HeLa cells, with one modification: viral RNA transfection was performed using jetPRIME reagent (#114–07; Polyplus transfection, Illkirch, France).

3.6.2 CRISPR/Cas9-mediated knockout of STING in HAE

Single guide RNAs (sgRNA) targeting STING or no known target (NTC) and flanked by restriction sites for cloning into the pLentiCRISPRv2 backbone [390] with eGFP replacing puromycin selection were as follows: sgRNA1- 5'-CACCGCATATTACATCGGATATCTG-3' and 5'-AAACCAGATATCCGATGTAATATGC-3'; sgRNA2- 5'-CACCGACTCTTCTGCCG GACACTTG-3' and 5'-AAACCAAGTGTCCGGCAGAAGAGTC-3'; NTC- 5'-CACCGGCA CTACCAGAGCTAACTCA-3' and 5'-AAACTGAGTTAGCTCTGGTAGTGCC-3'. Lentiviral stocks were generated by co-transfection of 1µg pLentiCRISPRv2 (Addgene plasmid #52961 donated by Dr. Feng Zhang) [390], 0.2µg pCMV-VSV G (Addgene plasmid #8454 donated by Dr. Bob Weinberg) [391]), and 0.7µg psPAX2 (Addgene plasmid #12260 donated by Dr. Didier Trono) into HEK-293T cells with jetPRIME reagent (Polyplus transfection). Lentivirus-laden supernatant was collected and replaced at 24 hour intervals up to 72 hours, pooled, and filtered to remove viable cells and debris. For target cell transduction, lentivirus-containing supernatants were applied to BCi-NS1.1 cells (kindly provided by Drs. Matthew Walters and Ronald Crystal [366]), maintained as HAE at 40–60% confluence with a final concentration of 20mM HEPES (Gibco) and 4µg/mL Polybrene (#TR10003G, Fisher Scientific). Cells were then centrifuged (1,000 x g for one hour at 37˚C) and incubated at 37˚C with 5% CO2 for 6hr. The inoculum was removed and replaced with fresh Pneumacult-Ex Plus media (StemCell Technologies). At 60–80% confluence, eGFP-positive cells were enriched by fluorescence-activated cell sorting on a BD FACSAria-II Cell Sorter (BD Bioscience). These sorted BCi-NS1.1 cells were then

expanded, seeded at $3.3x10^4$ cells/well on 6.5mm rat-tail collagen type I-coated transwell membranes, and cultured at air-liquid interface as previously described for HAE.

3.6.3 Titration of rhinoviruses by plaque assay and quantitative real-time PCR (qPCR)

RV-A2, RV-B14, and RV-A16 stocks were titrated by plaque assay method using H1 HeLa cells plated in 24-well dishes and a published protocol with modifications [392]. Briefly, 90% confluent H1 HeLa monolayers were inoculated with ten-fold serial dilutions of the viral stock in McCoy's medium with 2% FBS and 30mM $MgCl_2$. After 1 hour incubation at room temperature (RT), the inoculum was exchanged for a semi-solid overlay composed of 0.6% of bacteriological agar (#A5306; Sigma-Aldrich, Saint Louis, MO) in DMEM-F12 (#12500062; Gibco), supplemented with 1% FBS (Genesee), 1% penicillin/streptomycin (Gibco), 1% L-glutamine (#25030081; Gibco), and 30mM $MgCl_2$ (Sigma-Aldrich). The plate was incubated at 34˚C for 72 hours and the cells were fixed with 4% formaldehyde (#47608; Sigma-Aldrich; diluted in a 0.15M saline solution). The fixing solution was removed together with the overlay after a 24-hour incubation at RT and plaques visualized by staining the monolayer with 0.1% Crystal Violet (#C0775; Sigma-Aldrich) diluted in a 20% ethanol (200 proof) solution. RV-C15 was titrated by qPCR, which was also used to quantify RV-A16 and RV-B14 in experiments done in CRISPR/Cas9-modified HAE. To quantify viable viral particles, 10µl of RV-C15 stock or 100µL of experimental sample was first treated with 1u RNase A (#EN053; Thermo) and 1u DNase I (#18047019; Invitrogen–Thermo Scientific) for 1hr at 37˚C. Viral RNA was then extracted using a QIAamp Viral RNA Mini Kit (#52904; Qiagen, Hilden, Germany); total RNA was extracted from cells using a RNeasy Mini Kit (#74104; Qiagen). Next, up to 1µg of RNA was used in a reverse transcription reaction (High Capacity cDNA Reverse Transcriptase Kit; #4368814; Applied Biosystem–Thermo), with random hexamer primers, as per the

manufacturer's protocol. qPCR was done using 3µl of cDNA, 10pM HRVTF63 forward (5'–ACMGTGTYCTAGCCTGCGTGGC–3') and HRVTR reverse (5'–GAAACACGGACAC CCAAAGT GT–3') primers, 10pM HRVTF probe (5'–FAM/TCCTCCGGCCCCTGAAT/ BHQ1–3'), and LuminoCT Taqman Master Mix (#L6669; Sigma-Aldrich) according to the manufacturer's protocol. For absolute quantification, a standard curve was delineated using cDNA generated from ten-fold serial dilutions of in vitro-transcribed pRV-C15, pRV-A16, and pRV-B14.

3.6.4 RV infection in HAE and H1 HeLa cells

One week before the experiment in HAE, cells were washed 3 x 30 minutes with 100µl of phosphate buffered saline (PBS; #P5119; Gibco) at 37˚C to remove excessive mucus. In CRISPR/ Cas9-modified BCi-NS1.1-derived HAE an additional wash was performed immediately before inoculation. HAE cultures were inoculated on the apical surface with 10µl of PBS (negative control), sucrose-purified RV-C15 (10^{10} copies of RNA), RV-A16 ($5x10^5$ PFU), RV-B14 ($5x10^5$ PFU), or RV-A2 ($5x10^5$ PFU) and incubated at 34˚C with 5% CO2 until sample collection. In the replication curve and cytotoxicity assays, the inoculum was removed, and the apical surface rinsed with PBS, at 4hpi. For HAE culture sample collection, 100µl of PBS (Gibco) was added to the apical chamber and harvested after a 30-minute incubation at 34˚C; basolateral samples (500µl ALI media) were collected directly from underneath the culture. Cells were harvested from the transwell membranes using 350µl RLT buffer (#74104; Qiagen) for downstream RNA extraction, or 75µl of Radio Immuno-Precipitation Assay (RIPA) buffer (#89900S; Thermo) plus protease inhibitors (#88666; Thermo Scientific) for subsequent Western blot (WB) assays. The aliquots for RNA extraction and WB were stored at -80˚C and -20˚C, respectively. Alternatively, cultures were fixed with 4% (w/v) freshly-prepared paraformaldehyde (#157-8-100; Electron Microscopy Sciences) for immunofluorescence

(IF) assays or 2% (w/v) glutaraldehyde in 0.1M cacodylate buffer for downstream transmission electron microscopy analysis.

3.6.5 IF assays in HAE and H1 HeLa cells

HAE cultures were fixed with 100µl (apical) and 500µl (basolateral) 4% (w/v) freshly prepared paraformaldehyde (#157-8-100; EMS). After a 15-minute incubation at RT, cultures were washed once for 3 minutes with PBS and then incubated for 10 minutes at RT with a quenching solution (25mM NH_4Cl diluted in PBS) before being washed twice for 3 minutes each with PBS. Permeabilization of cell membranes was done using 0.2% Triton-X diluted in PBS; after a 15-minute incubation at RT, the cells were washed 3 x 3 minutes with PBS. A blocking solution: 10% normal donkey (#017-000-121, Jackson Labs) or normal goat serum (#005-000-121, Jackson Labs) diluted in PBS with 0.2% Tween-20 was added and only removed from the apical side after a 10-minute incubation at RT. The apical surface of the culture was washed 3 x 3 minutes with PBS. Primary antibody diluted in PBS with 0.2% Tween-20 and 1% Bovine Serum Albumin (BSA; #BP9700100; Fisher Scientific) was added to the apical chamber and incubated overnight at 4˚C, protected from light. The apical surface was washed 3 x 5 minutes with PBS and incubated with the secondary antibody diluted in PBS with 1% BSA. After a 2-hour incubation at RT, protected from light, the secondary antibody solution was removed and the apical surface of HAE was washed 3 x 5 minutes with PBS. If necessary, additional stains were done by repeating this protocol; reducing the secondary antibody incubation to 20 minutes when the next primary antibody applied was generated in the same species as another primary antibody used in the same experiment. Fluorescent-conjugated primary antibodies were applied during the final round of staining, where applicable. Nuclei were visualized in the final step by adding 1ng/ml of Hoechst 33342 (#H3570; Invitrogen) diluted in PBS with 0.2% Tween-20 to the apical surface. After a 5-minute incubation at RT, the cultures were

washed 3 x 5 minutes with PBS, after which the transwell membrane was separated from the plastic holder and mounted on a glass slide using VectaShield Antifade mounting medium (#H-1000-10; Vector Laboratories) and 1.5mm-thick cover glass. Images were acquired with a Zeiss Axio Observer 3 Inverted fluorescence microscope (Cell Observer HS image system, Zeiss Axiocam 503 mono camera, optimal acquisition mode, AIM-Zen 2007 software) equipped with EC-Plan-NEOFLUOR 20x/0.5NA Ph2 and 40x/ 0.75NA Ph2 air objectives. Higher resolution images and z-series optical sections (at 1μM intervals) were acquired with a LSM710 Zeiss confocal microscope (Argon laser, pinhole of 1 airy unit (AU), zoom factor of two, optimal acquisition mode, AIM-Zen 2009 software) equipped with a 63x/1.4NA Oil DIC Plan Apo objective at the Imaging Core, University of Maryland, College Park. All images were analyzed using Fiji–ImageJ v.2.1.0/1.53c software [393]. Z-series from a pre-selected region of interest (ROI) are displayed as maximum intensity z-projection, orthogonal views (XY, XZ and YZ planes), and 3D surface plots; they were also used for 3D volume reconstruction (3D view) using Fiji [393]. The IF protocol described above was used in all assays with the following exception: for PI4P detection, permeabilization was done using a 20mM Digitonin solution (diluted in PBS). Antibodies used in this study are listed below (**Tables 1 and 2**).

3.6.6 Quantification of fluorescence levels and colocalization analysis

The CZI files from z-stacks collected with a step-size at 1μM were analyzed at region and single-cell levels using Fiji—ImageJ v.2.1.0/1.53c software [393]. For single-cell analysis, the selection of the region of interest (ROI) was based on positivity for dsRNA(+) in RV-infected HAE. At least 5 cells per region were selected to increase rigor. Quantification of fluorescence levels was done in ROI single-cell images following the Corrected Total Cell Fluorescence (CTCF) method [394]. Total CTCF (equal to the sum of CTCF per slice/sample) was calculated per channel and statistically significant

differences determined by Mann-Whitney U (Two-tailed; $p<0.05$ significance; 0.95% confidence interval) using Prism GraphPad v.9 (GraphPad Software).

Table 3.1. Primary antibodies used in Immunofluorescence assays.

Primary Antibody	Dilution	Catalog #	Source
Mouse IgG2a anti-dsRNA (J2) mAb	1:1000	#10010200	SCICONS, Budapest, Hungary
Mouse IgG2b anti-acetylated alpha-tubulin (6-11B-1) mAb A647- conjugated	1:50	#sc-23950-AF647	Santa Cruz Biotechnology Incorporation, Dallas, Texas
Mouse IgG1 anti-FoxJ1 mAb (2A5)	1:200	#14-9965-82	Invitrogen–Thermo
Rabbit IgG anti-claudin-1 mAb [EPRR18871]	1:500	#ab211737	Abcam, Cambridge, UK
Goat IgG anti-calnexin polyclonal antibody	1:500	#PA5-19169	Thermo
Rabbit IgG anti-giantin pAb—Golgi Marker	1:500	#ab80864	Abcam
Rabbit IgG anti-cadherin-28 (CDHR3) pAb	1:500	#orb182906	Biorbyt, Cambridge, UK
Rabbit IgG anti-Lamp-1 (D3D11) mAb	1:500	#9091	Cell Signaling, Danvers, MA
Rabbit IgG anti-LC3b (EPR18709) mAb A647-conjugated	1:100	#ab225383	Abcam
Mouse IgM anti-PI(4)P (clone PI4-2) mAb	1:200	#Z-P004	Echelon Bioscience, Salt Lake City, Utah
Rabbit IgG anti-TM173/STING polyclonal antibody	1:100	#19851-1AP	Proteintech, Rosemont, IL

https://doi.org/10.1371/journal.ppat.1010159.t001

Table 3.2. Secondary antibodies used in Immunofluorescence assays.

Secondary Antibody	Dilution	Catalog #	Source
Donkey anti-mouse IgG H&L 2°Ab A594-conjugated	1:500	#ab150108	Abcam
Donkey anti-goat IgG H&L 2°Ab A488-conjugated	1:500	#a150129	Abcam
Donkey anti-rabbit IgG H&L 2°Ab A647-conjugated	1:500	#ab150075	Abcam
Donkey anti-rabbit IgG H&L 2°Ab A555-conjugated	1:500	#ab150074	Abcam
Goat anti-mouse IgG2a 2°Ab A555-conjugated	1:200	#A21137	Thermo
Goat anti-mouse IgG1 2°Ab A488-conjugated	1:200	#A21121	Thermo
Goat anti-mouse IgM (heavy chain) 2°Ab A647-conjugated	1:200	#A21238	Thermo

https://doi.org/10.1371/journal.ppat.1010159.t002

To evaluate the ratio of colocalization between two markers, the background was subtracted from ROI single-cell images following application of a threshold model and watershed filter to better identify the centroids. The final images were first used in colocalization analysis by pixel intensity-based methods (Pearson, threshold Manders, and Van Steensel's methods), followed by spatial analysis based on the distance between centers of mass [395]. All colocalization analysis was done using the Just Another Co-localization Plug-in (JACoP) plugin from Fiji [393].

3.6.7 Transmission Electron Microscopy (TEM) in HAE

The TEM protocol used in this study was based on published methods [353] with modifications, as follows: Cultures were fixed with 2% (w/v) glutaraldehyde in 0.1M cacodylate buffer (100ml on top and 500ml on the bottom) for 60 minutes at RT. The

transwell membranes were then separated from the plastic holder and transferred to a new 24-well plate where a second fixation step was carried out with 1% osmium tetroxide (OsO4) in 0.1M cacodylate buffer plus 1% potassium ferricyanide ($K_3Fe(CN)_6$). Two percent uranyl acetate (diluted in distilled H2O) was used as post-fixative. The membrane was then incubated in propylene oxide before being embedded in Spurr's Resin. The samples were sectioned to 60–90nm with a diamond knife (DiATOME) and ultra microtome (Reichart-Jung) and two slices were placed per copper grid (EMS). The images were obtained using a Hitachi S-4700 Field Emission Scanning Electron Microscope with transmitted electron detector in the Laboratory for Biological Ultrastructure, University of Maryland, College Park.

3.6.8 Immunoblotting assays

Total protein in cell lysates (stored at -20˚C in RIPA buffer) were quantified by BCA Protein Assay (#23225; Pierce). A total of 20µg per sample (or 25µg and 30µg for STING and ZO-1 blots, respectively) was then separated on a NovexWedgeWell 4–20% Tris-Glycine gel (#XP04202BOX; Invitrogen-Thermo) and transferred to a PVDF membrane. Membranes were blocked with 5% non-fat milk solution (diluted in 0.1% Tween-20 in Tris-buffered saline (TBS-T)) or 3% BSA (diluted in TBS-T) for the detection of the tight junction proteins and incubated overnight at 4˚C with the primary antibody (**Table 3**). Following a series of washes in TBS-T, membranes were incubated for 1hr at RT with the appropriate peroxidase-conjugated secondary antibody. All antibodies were diluted in 5% non-fat milk TBS-T solution. Blots were visualized using SuperSignal West Femto Maximum Sensitivity Substrate (#34094; Thermo) or SuperSignal West Dura Extended Duration Substrate (#34075; Thermo). Western blot imaging was performed on an iBright 1500 (Thermo Fisher) and densitometry carried out with ImageJ software.

Table 3.3. Primary and secondary antibodies used in immunoblotting assays.

Primary Antibody	Dilution	Catalog #	Source
Mouse IgG2b anti-acetylated alpha-tubulin (acetyl K40) monoclonal antibody	1:5000	#ab24610	Abcam
Mouse IgG1 anti-FoxJ1 monoclonal antibody (2A5)	1:1000	#14-9965-82	Invitrogen–Thermo
Rabbit IgG anti-CDHR3 polyclonal antibody	1:1000	#HPA011218	Atlas—Sigma-Aldrich
Goat IgG anti-calnexin polyclonal antibody	1:1000	#PA5-19169	Thermo
Rabbit IgG anti-Lamp-1 (D3D11) monoclonal antibody	1:1000	#9091	Cell Signaling
Mouse IgG2b anti-LC3b monoclonal antibody	1:1000	#83506	Cell Signaling
Mouse IgG2b anti-claudin-1 monoclonal antibody	1:1000	#sc-166338	Santa Cruz
Rabbit IgG anti-ZO-1 polyclonal antibody	1:200	#61–7300	Invitrogen
Mouse anti-β-Actin (clone AC-15) monoclonal antibody, peroxidase-conjugated	1:15000	#A3854	Sigma-Aldrich
Rabbit IgG anti-TM173/STING monoclonal antibody	1:1000	#66680-1-Ig	Proteintech
Mouse anti-VP1 RV-C15 monoclonal antibody	1:100 (from 0.1mg/mL)	Clone 30C12	Gift from Ann Palmenberg [77]
Secondary Antibody	**Dilution**	**Catalog #**	**Source**
Recombinant mouse IgGk light chain binding protein conjugated to Horseradish Peroxidase (HRP)	1:10000	#sc516102	Santa Cruz
Donkey anti-Goat IgG HRP- conjugated	1:10000	#A15999	Thermo
Goat anti-rabbit IgG HRP- conjugated	1:10000	#32460	Thermo

https://doi.org/10.1371/journal.ppat.1010159.t003

3.6.9 Lactate dehydrogenase (LDH) release cytotoxicity assay

Apical and basolateral samples were used to quantify LDH release in RV-C15-infected HAE with the CytoTox 96 Non-Radioactive Cytotoxicity Assay kit (#G1780; Promega, Madison, WI) following the manufacturer's protocol.

3.6.10 Transepithelial Electrical Resistance (TEER) assay

TEER was quantified in HAE using the Millicell Electrical Resistance System (ERS)-2 (Sigma) after adding 100μl of Pneumacult-ALI medium to the apical surface and incubating cultures for 30 minutes at 34˚C. Statistical analysis of resulting data was done by ordinary one-way ANOVA and Tukey's multiple comparison test methods using Prism GraphPad v.9 software (GraphPad).

3.6.11 Quantification of ZO-1 disposition using JAnaP

Junction coverage and characterization were quantified using the Junction Analyzer Program (JAnaP) as previously described [368–370]. In short, the perimeter of each cell was identified via waypoints in immunofluorescent images of ZO-1. The junctions

were isolated from the background using a threshold value of 5–8. Threshold identification is described in the supplement of [368] and in the JAnaP User-Guide available at https://github.com/StrokaLab/JAnaP along with the JAnaP program in its entirety. Junction characterization was performed by calculating the length of each individual junction piece that coincides with the perimeter as well as the relative aspect ratio (RAR) with respect to the cell perimeter. A junction was classified as continuous if its length was greater than 15 pixels, otherwise it was deemed discontinuous and further separated into perpendicular or punctate if the RAR was greater or less than 1.2, respectively. Statistical analysis was done by one-way ANOVA and Dunnett's multiple comparison test using Prism GraphPad v.9 software (GraphPad).

3.6.12 Measurement of Mucociliary Clearance (MCC)

Mucociliary transport was measured based on the transport of 2μm red-fluorescent polystyrene microspheres (Sigma-Aldrich). Five microliters of microsphere suspension (1:500 dilution in PBS; Sigma-Aldrich) was added on top of the native mucus; after a 24-hour incubation at 34˚C, videos of three regions were recorded using a Zeiss Axio Observer 3 Inverted fluorescence microscope (Cell Observer HS image system, Zeiss Axiocam 503 mono camera, optimal acquisition mode, Zen 2007 software) equipped with a 10x/0.25NA Ph1 air objective. Images were collected at a frame rate of 0.5 Hz for 10 seconds on the plane of the mucus gel. Images were acquired centrally within cultures and away from the edges, where mucus tends to accumulate. The microsphere tracking data analysis was based on an image processing algorithm that was custom written in MATLAB (The MathWorks). Briefly, the analysis software computes the XY-plane trajectories of each fluorescent microsphere in each frame. Using the trajectory data, displacement of microspheres was computed, and transport rate was calculated by dividing the displacement of microsphere by total time elapsed.

3.7 Supporting information

3.7.1 Figure S3.1. RV-C15 replicates in ciliated epithelial cells leading to decreased CDHR3 levels.

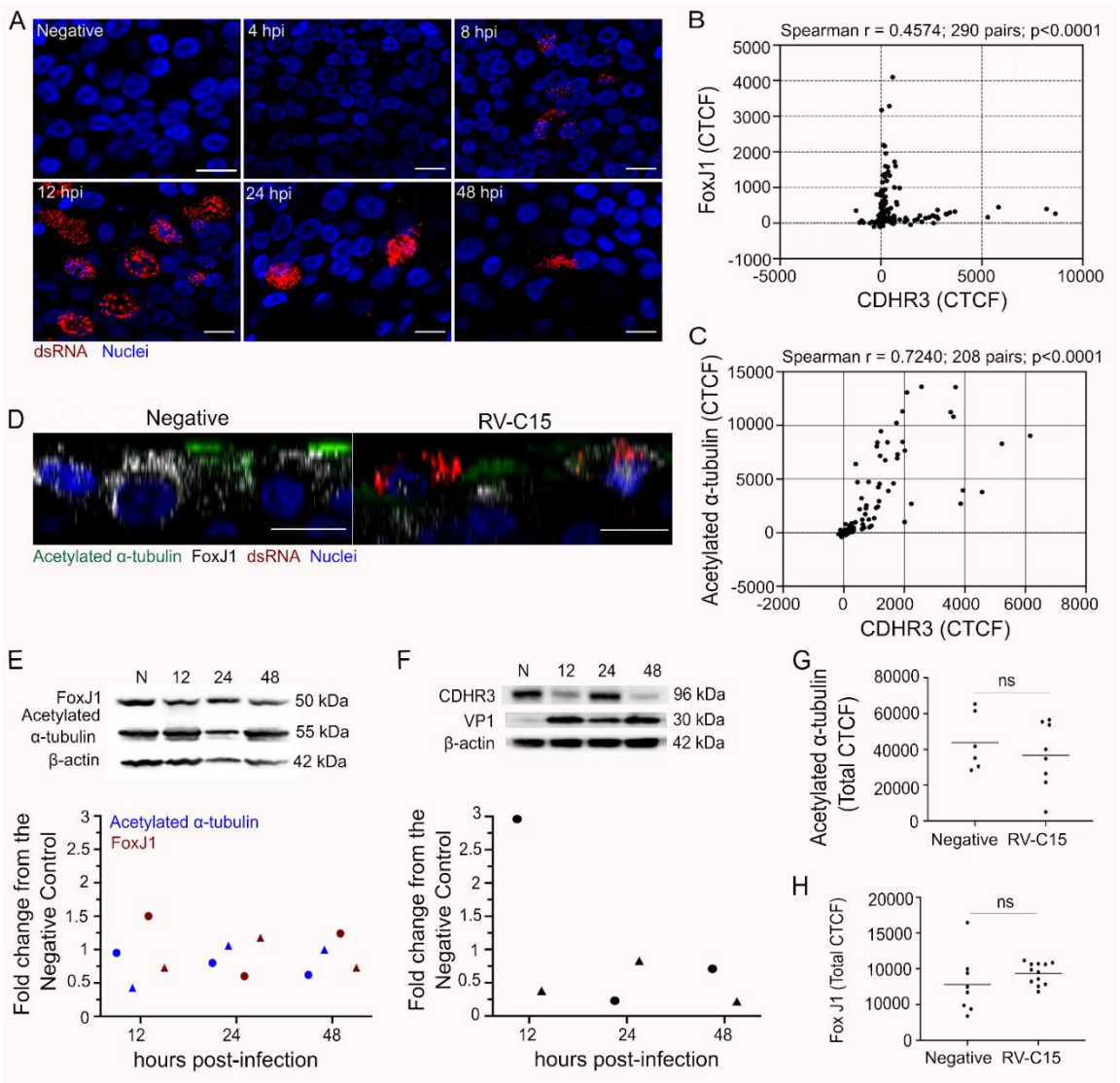

A: Immunofluorescence to detect dsRNA (red) in RV-C15 (10^{10} RNA)- infected HAE (nuclei, blue; scale bar = 10μm). **B-C**: Spearman correlation analysis (two-tailed; 0.95% confidence interval) between fluorescence levels of CDHR3 and FoxJ1 (**B**) or acetylated α-tubulin (**C**) in non-infected HAE at 12hpi. Each dot represents the fluorescence levels of CDHR3 and FoxJ1 or acetylated α-tubulin quantified in the same Z-slice. **D**: Orthogonal XY view from noninfected and RV-C15-infected (dsRNA+, red) HAE (nuclei, blue) stained by immunofluorescence for FoxJ1 (gray) and acetylated α-tubulin (green) at 12hpi (z-stacks at 1μm of thickness; scale bar = 10μm). **E** and **F**: Fold change graph represents FoxJ1 (**E**), acetylated α-tubulin (**E**), and CDHR3 (**F**) protein levels normalized to the endogenous control (actin) and compared to non-infected cultures. Data shown are from

two independent donors, represented by circles and triangles. Blot above is from the donor represented by circles (**E**) and triangles (**F**); VP1 protein of RV-C15 [396] was detected in cultures from the donor "triangle" used for both assays (**E**, **F**). **G-H**: Quantification of fluorescence levels (CTCF) for acetylated α-tubulin (**G** and FoxJ1 (**H**) in non-infected and RV-C15-infected (dsRNA+) HAE at 12hpi. Dots represent the total CTCF per cell and the line represents the mean. Statistical analysis was done using MannWhitney U test (Two-tailed; 0.95% confidence interval). (TIF)

3.7.2 Figure S3.2. Ring-like dsRNA localization in HAE is not specific to RV-C15 infection.

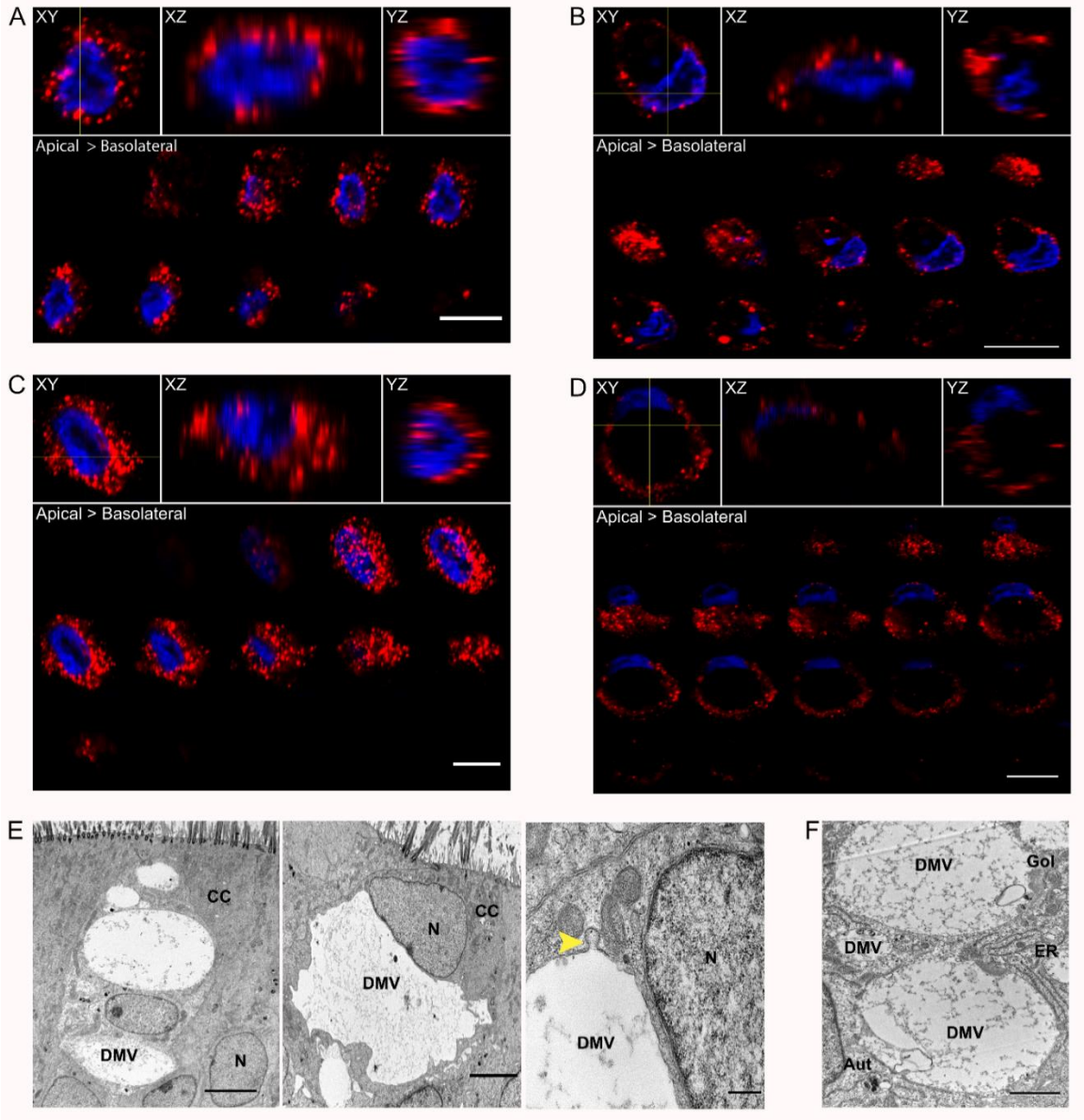

A-D: Orthogonal views (XY, XZ and YZ planes; yellow lines show the location of XZ and YZ views on the XY plane) from the RV-A16 (**A-B**) and RV-A2 (**C-D**) -infected HAE immunostained for dsRNA (red; nuclei, blue) at 12hpi (z-stacks at 1μm of thickness). Z-stacks at 1μm of thickness shows two profiles for dsRNA (red) detection by immunofluorescence at perinuclear (**A**, **C**) or close to the plasma membrane in a ring-like disposition (**B**, **D**) at 12hpi (scale bar = 10μm). **E-F**: Transmission electron microscopy of HAE infected with RV-A16 (**E**; scale bars = 5, 2, and 2μm respectively) or RV-A2 (**F**; scale bar = 2μm) at 12hpi. Visualization of ciliated cells (CC) with large, double-membrane vesicles (DMV; **E** and **F**) located above (**E**–left panel) or below the nucleus (**E**–middle panel); and the fusion of small vesicles to a larger vesicle (**E**–right panel; yellow arrow). N = nucleus; GoI = golgi; ER = endoplasmic reticulum; Aut = autophagosome. (TIF)

3.7.3 Figure S3.3. Golgi and PI4P-positive vesicles are not the main site for RV-C15 replication in HAE at 12hpi.

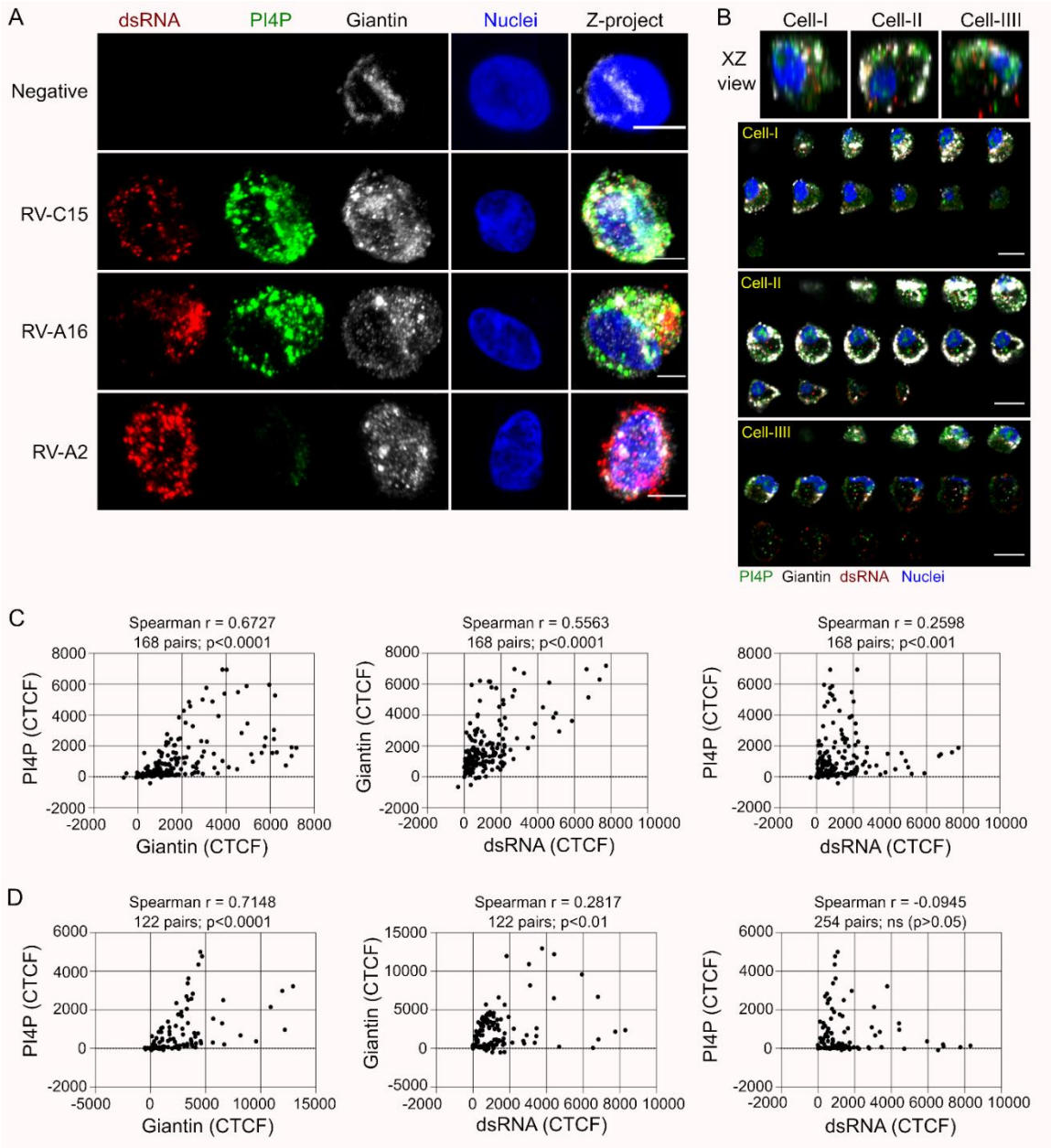

Maximum Z-projection for dsRNA (red), PI4P (green), and Giantin (gray) detection by immunofluorescence in non-infected and RV-infected HAE (scale bar = 5µm) (**A**). **B**: XZ orthogonal views (individual and montage of z-series) showing the differences in giantin (gray) and PI4P (green) distribution in RV-C15-infected cells with dsRNA (red) with either a perinuclear (cell I) or ring-like profile (cells II and III) (scale bar = 5µm). **C-D**: Spearman correlation analysis (two-tailed; 0.95% confidence interval) between giantin and PI4Pfluorescentlevels (CTCF) in RV-A16 (**C**) or RV-A2 (**D**) -infected HAE at 12hpi. Each dot represents the fluorescence levels of giantin and PI4P quantified in the same Z-slice. (TIF)

3.7.4 Figure S3.4. Global calnexin expression is not altered during RV-C15 infection in HAE.

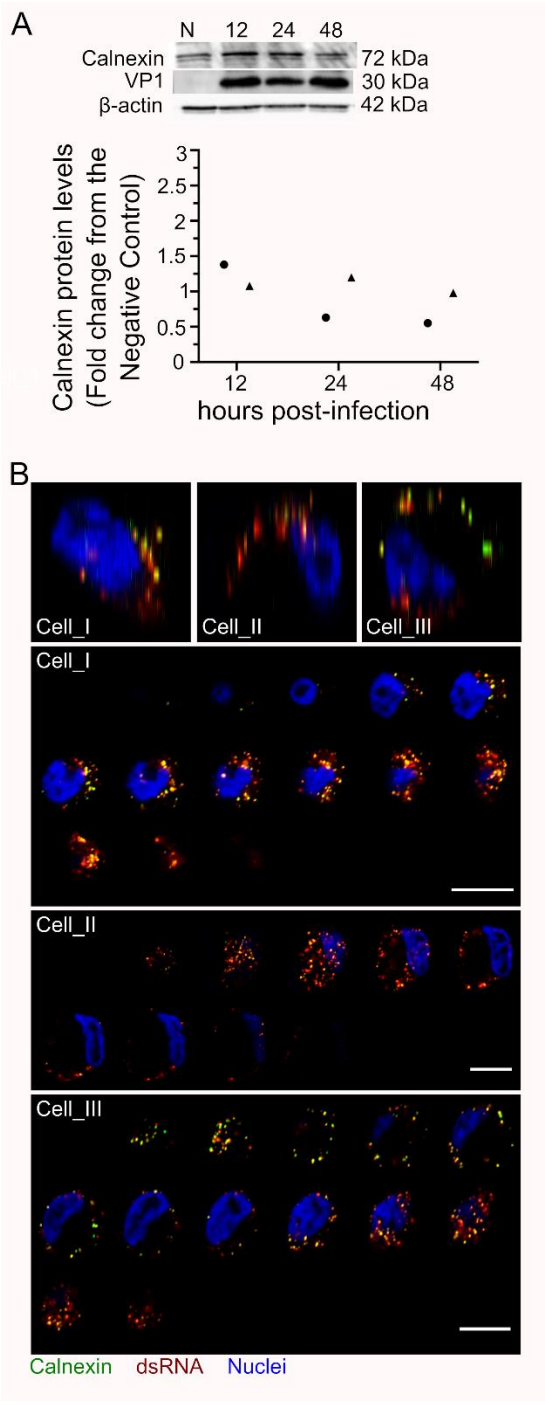

A: Fold change graph represents calnexin protein levels normalized to the endogenous control (actin) and compared to non-infected cultures. Data shown are from two independent donors, represented by circles and triangles. Blot above is from the donor

represented by triangles, which includes the detection of VP1 of RV-C15. **B**: Orthogonal XZ views show the perinuclear (cellI) and ring-like (cell-II and cell-III) pattern of dsRNA (red) and calnexin (green) in RV-C15 infected HAE (scale bar = 5µm). (TIF)

3.7.5 Figure S3.5. RV-C15 replication induces incomplete autophagy in HAE at 12hpi.

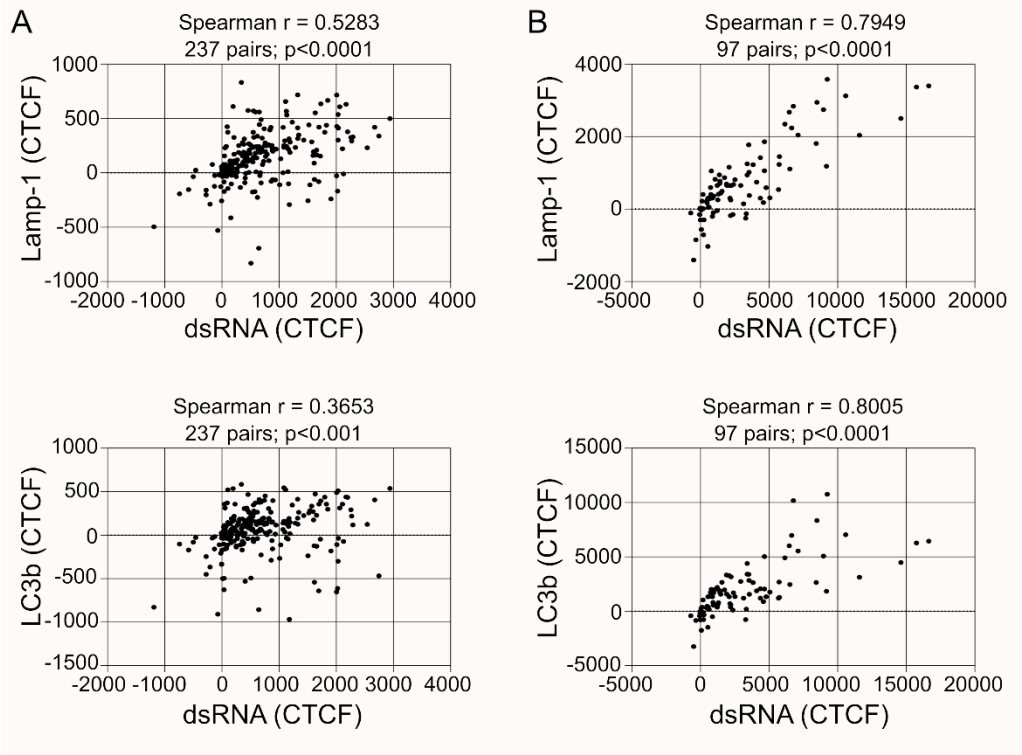

A-B: Spearman correlation analysis (two-tailed; 0.95% confidence interval) between dsRNA and Lamp-1 or LC3b fluorescence levels (CTCF) in RV-A16 (**A**) or RV-A2 (**B**) - infected HAE at 12hpi. Each dot represents the fluorescence levels of dsRNA and Lamp-1 or LC3b quantified in the same Z-slice. (TIF)

3.7.6 Figure S3.6. Immunofluorescence of MCC experiment showing RV-C15 but not UV-RV-C15 infection in HAE at 12hpi.

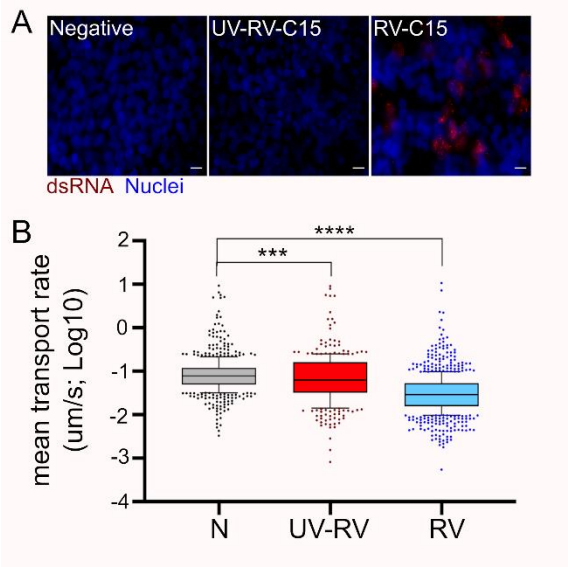

A: Immunofluorescence detection of dsRNA (red; nuclei, blue) in non-infected HAE or HAE inoculated with UV-RV-C15 or RV-C15 at 12hpi (scale bar = 10µm). **B**: Mean transport rate of mucus in non-infected HAE compared to HAE inoculated with UV-RV-C15 or RV-C15 at 24hpi. Box represents the 10–90 percentile values of MCC quantified in the same culture/condition at different time-points. Statistical analysis was done using Kruskal-Wallis followed by Dunn' multi-comparison test (***p<0.001; ****p<0.0001). (TIF)

Supporting Videos:

Video S3.1. RV-C15-infected HAE showing perinuclear dsRNA (red) detection at 12hpi. (AVI)

Video S3.2. RV-C15-infected HAE showing ring-like dsRNA (red) detection at 12hpi. (AVI)

3.7.7 Supporting Tables

Table S3.1. Pixel intensity-based and spatial (distance between center-mass) colocalization analysis between giantin and PI4P in RV-C15-infected HAE. (DOCX)

Sample	PCC	thM1	thM2	Van Steensel's dx (pixel)	Giantin centroids (n)	PI4P centroids (n)	% center-mass colocalization (giantin/PI4P from total giantin)
RV-C15 1A	0.190	0.136	0.319	-1	145	90	3.45%
RV-C15 1B	0.106	0.071	0.264	1	193	90	3.63%
RV-C15 2A	0.188	0.148	0.206	2	217	107	7.37%
RV-C15 2B	0.251	0.299	0.265	2	56	95	8.93%
RV-C15 2C	0.080	0.105	0.085	0	95	75	4.21%
RV-C15 3A	0.305	0.226	0.459	0	157	133	11.46%
RV-C15 3B	0.228	0.233	0.267	-1	115	92	6.96%
RV-C15 4A	0.187	0.129	0.367	2	275	69	2.91%
RV-C15 4B	0.168	0.158	0.219	2	51	98	3.92%
RV-C15 4C	0.209	0.212	0.258	2	47	62	12.77%
RV-C15 4D	0.167	0.129	0.269	5	162	117	6.17%
RV-C15 4E	0.023	0.036	0.025	1	25	67	4.00%
RV-C15 4F	0.093	0.107	0.106	4	51	88	15.69%
RV-C15 5A	0.074	0.066	0.106	3	56	88	7.14%
RV-C15 5B	0.083	0.068	0.140	-5	73	68	5.48%
RV-C15 5C	0.092	0.122	0.082	1	42	60	9.52%
RV-C15 6A	0.232	0.190	0.316	0	61	87	9.84%
RV-C15 6B	0.099	0.131	0.087	3	48	71	8.33%
RV-C15 6C	0.150	0.152	0.161	-1	57	64	8.77%
Median	**0.167**	**0.131**	**0.219**	**1**	**61**	**88**	**7.14%**

Table S3.2. Pixel intensity-based and spatial (distance between center-mass) colocalization analysis between giantin and PI4P in RV-A16-infected HAE. (DOCX)

Sample	PCC	thM1	thM2	Van Steensel's dx (pixel)	Giantin centroids (n)	PI4P centroids (n)	% center-mass colocalization (giantin/PI4P from total giantin)
RV-A16 1A	0.053	0.066	0.068	-15	116	96	3.45%
RV-A16 1B	0.133	0.083	0.266	-4	40	83	2.50%
RV-A16 1C	0.081	0.073	0.135	2	53	109	9.43%
RV-A16 2A	0.051	0.076	0.093	-17	80	139	3.75%
RV-A16 2B	0.102	0.095	0.150	9	49	66	0.00%
RV-A16 2C	0.062	0.049	0.109	1	45	46	2.22%
RV-A16 3A	0.206	0.166	0.328	-2	65	93	7.69%
RV-A16 3B	0.035	0.028	0.110	17	26	52	0.00%
RV-A16 3C	0.210	0.133	0.421	3	80	47	6.25%
RV-A16 3D	0.192	0.151	0.271	1	36	49	0.00%
RV-A16 4A	0.086	0.063	0.189	20	63	82	3.17%
RV-A16 4B	0.081	0.046	0.187	6	77	108	2.60%
RV-A16 4C	0.122	0.054	0.319	-2	73	56	4.11%
Median	**0.086**	**0.073**	**0.187**	**1**	**63**	**82**	**3.17%**

Table S3.3. Pixel intensity-based and spatial (distance between center-mass) colocalization analysis between giantin and PI4P in RV-A2-infected HAE. (DOCX)

Sample	PCC	thM1	thM2	Van Steensel's dx (pixel)	Giantin centroids (n)	PI4P centroids (n)	% center-mass colocalization (giantin/PI4P from total giantin)
RV-A2 1A	0.141	0.165	0.136	2	12	2	16.67%
RV-A2 1B	0.116	0.125	0.122	4	50	3	6.00%
RV-A2 2A	0.066	0.059	0.113	2	137	3	2.19%
RV-A2 2B	0.206	0.216	0.231	-3	80	2	2.50%
RV-A2 3A	0.039	0.056	0.035	1	26	2	3.85%
RV-A2 4A	0.028	0.032	0.041	5	81	3	3.70%
RV-A2 5A	0.095	0.092	0.122	-1	56	4	7.14%
RV-A2 6A	0.180	0.279	0.158	0	114	6	5.26%
Median	**0.106**	**0.109**	**0.122**	**2**	**68**	**3**	**4.55%**

Table S3.4. Pixel intensity-based and spatial (distance between center-mass) colocalization analysis between dsRNA and giantin in RV-C15-infected HAE. (DOCX)

Sample	PCC	thM1	thM2	Van Steensel's dx (pixel)	dsRNA centroids (n)	Giantin centroids (n)	% center-mass colocalization (dsRNA/giantin from total dsRNA)
RV-C15 1A	0.174	0.157	0.228	-1	137	6	3.65%
RV-C15 1B	0.175	0.153	0.248	1	79	9	11.39%
RV-C15 2A	0.168	0.158	0.227	2	69	10	13.04%
RV-C15 2B	0.237	0.354	0.191	2	93	11	11.83%
RV-C15 2C	0.176	0.223	0.158	0	51	13	23.53%
RV-C15 3A	0.117	0.120	0.149	-1	101	15	14.85%
RV-C15 3B	0.133	0.167	0.142	2	89	5	5.62%
RV-C15 4A	0.094	0.125	0.102	1	83	7	8.43%
RV-C15 4B	0.142	0.122	0.215	1	90	10	11.11%
RV-C15 4C	0.150	0.165	0.187	8	62	9	12.90%
RV-C15 4D	0.106	0.124	0.117	1	112	6	5.36%
RV-C15 4E	0.105	0.080	0.168	0	99	2	2.02%
RV-C15 4F	0.056	0.069	0.071	2	96	12	11.46%
RV-C15 5A	0.062	0.044	0.128	-3	82	8	8.54%
RV-C15 5B	0.079	0.071	0.121	-7	81	2	2.47%
RV-C15 5C	0.102	0.083	0.162	-1	104	5	4.81%
RV-C15 6A	0.162	0.163	0.185	0	101	7	6.93%
RV-C15 6B	0.060	0.056	0.094	3	91	6	6.59%
RV-C15 6C	0.085	0.056	0.163	1	92	11	10.87%
Median	**0.117**	**0.124**	**0.162**	**1**	**91**	**8**	**8.54%**

Table S3.5. Pixel intensity-based and spatial (distance between center-mass) colocalization analysis between dsRNA and giantin in RV-A16-infected HAE. (DOCX)

Sample	PCC	thM1	thM2	Van Steensel's dx (pixel)	dsRNA centroids (n)	Giantin centroids (n)	% center-mass colocalization (dsRNA/giantin from total dsRNA)
RV-A16 1A	0.069	0.056	0.146	-12	135	96	6.67%
RV-A16 1B	0.133	0.092	0.235	0	128	83	5.47%
RV-A16 1C	0.069	0.055	0.147	2	101	109	3.96%
RV-A16 2A	0.140	0.128	0.241	0	88	139	3.41%
RV-A16 2B	0.050	0.049	0.104	1	86	66	4.65%
RV-A16 2C	0.032	0.023	0.097	0	59	46	5.08%
RV-A16 3A	0.161	0.173	0.194	-14	49	93	10.20%
RV-A16 3B	0.138	0.079	0.308	1	39	52	15.38%
RV-A16 3C	0.007	0.024	0.043	20	49	47	2.04%
RV-A16 3D	0.060	0.056	0.091	-9	78	49	5.13%
RV-A16 4A	0.105	0.122	0.116	4	108	82	6.48%
RV-A16 4B	0.004	0.010	0.018	15	90	108	2.22%
RV-A16 4C	0.074	0.045	0.149	-19	68	56	2.94%
Median	**0.069**	**0.056**	**0.146**	**0**	**86**	**82**	**5.08%**

Table S3.6. Pixel intensity-based and spatial (distance between center-mass) colocalization analysis between dsRNA and giantin in RV-A2-infected HAE. (DOCX)

Sample	PCC	thM1	thM2	Van Steensel's dx (pixel)	dsRNA centroids (n)	Giantin centroids (n)	% center-mass colocalization (dsRNA/giantin from total dsRNA)
RV-A2 1A	0.032	0.036	0.058	2	113	4	3.54%
RV-A2 1B	0.045	0.038	0.088	14	94	4	4.26%
RV-A2 2A	0.053	0.058	0.077	1	78	9	11.54%
RV-A2 2B	0.046	0.074	0.054	-19	97	5	5.15%
RV-A2 3A	0.044	0.029	0.108	1	77	1	1.30%
RV-A2 4A	0.087	0.066	0.140	0	116	10	8.62%
RV-A2 5A	0.075	0.046	0.190	19	160	12	7.50%
RV-A2 6A	0.106	0.179	0.110	10	96	5	5.21%
Median	**0.050**	**0.052**	**0.098**	**2**	**97**	**5**	**5.18%**

Table S3.7. Pixel intensity-based and spatial (distance between center-mass) colocalization analysis between dsRNA and PI4P in RV-C15-infected HAE. (DOCX)

Sample	PCC	thM1	thM2	Van Steensel's dx (pixel)	dsRNA centroids (n)	PI4P centroids (n)	% center-mass colocalization (dsRNA/PI4P from total dsRNA)
RV-C15 1A	0.259	0.357	0.220	0	137	6	4.38%
RV-C15 1B	0.108	0.224	0.098	-2	79	3	3.80%
RV-C15 2A	0.281	0.371	0.256	0	69	6	10.14%
RV-C15 2B	0.280	0.385	0.235	-1	93	4	4.30%
RV-C15 2C	0.051	0.068	0.060	-1	51	5	9.80%
RV-C15 3A	0.212	0.298	0.182	0	101	8	7.92%
RV-C15 3B	0.230	0.290	0.215	-1	89	4	4.49%
RV-C15 4A	0.253	0.519	0.148	0	83	18	19.28%
RV-C15 4B	0.227	0.220	0.280	-1	90	10	11.11%
RV-C15 4C	0.292	0.327	0.305	-1	62	12	19.35%
RV-C15 4D	0.244	0.388	0.176	0	118	3	2.54%
RV-C15 4E	0.040	0.029	0.087	-2	99	2	2.02%
RV-C15 4F	0.052	0.065	0.067	0	96	3	3.13%
RV-C15 5A	0.211	0.168	0.302	-2	82	7	7.32%
RV-C15 5B	0.092	0.122	0.101	-1	81	2	2.47%
RV-C15 5C	0.082	0.055	0.161	-1	104	4	3.85%
RV-C15 6A	0.295	0.371	0.254	0	101	8	7.92%
RV-C15 6B	0.144	0.097	0.243	0	91	8	8.79%
RV-C15 6C	0.130	0.085	0.233	6	92	12	10.87%
Median	**0.212**	**0.224**	**0.215**	**-1**	**91**	**6**	**7.32%**

Table S3.8. Pixel intensity-based and spatial (distance between center-mass) colocalization analysis between dsRNA and PI4P in RV-A16-infected HAE. (DOCX)

Sample	PCC	thM1	thM2	Van Steensel's dx (pixel)	dsRNA centroids (n)	PI4P centroids (n)	% center-mass colocalization (dsRNA/PI4P from total dsRNA)
RV-A16 1A	0.068	0.056	0.142	-1	135	116	6.67%
RV-A16 1B	0.105	0.146	0.117	1	126	40	3.97%
RV-A16 1C	0.194	0.184	0.262	-1	101	53	2.97%
RV-A16 2A	0.095	0.111	0.170	-1	88	80	0.00%
RV-A16 2B	0.099	0.108	0.144	0	86	49	4.65%
RV-A16 2C	0.048	0.052	0.098	0	59	45	3.39%
RV-A16 3A	0.243	0.359	0.204	2	49	65	6.12%
RV-A16 3B	0.116	0.154	0.154	-13	39	26	7.69%
RV-A16 3C	0.184	0.296	0.165	0	49	80	2.04%
RV-A16 3D	0.193	0.218	0.195	-1	78	36	6.41%
RV-A16 4A	0.196	0.382	0.122	0	108	63	2.78%
RV-A16 4B	0.112	0.192	0.084	0	90	77	2.22%
RV-A16 4C	0.201	0.290	0.163	2	68	73	5.88%
Median	**0.116**	**0.184**	**0.154**	**0**	**86**	**63**	**3.97%**

Table S3.9. Pixel intensity-based and spatial (distance between center-mass) colocalization analysis between dsRNA and PI4P in RV-A2-infected HAE. (DOCX)

Sample	PCC	thM1	thM2	Van Steensel's dx (pixel)	dsRNA centroids (n)	PI4P centroids (n)	% center-mass colocalization (dsRNA/PI4P from total dsRNA)
RV-A2 1A	0.072	0.060	0.118	-1	113	12	1.77%
RV-A2 1B	0.077	0.058	0.137	-2	94	50	3.19%
RV-A2 2A	0.110	0.152	0.106	-1	78	137	12.82%
RV-A2 2B	0.118	0.163	0.111	-1	97	80	6.19%
RV-A2 3A	0.049	0.024	0.141	-1	77	26	2.60%
RV-A2 4A	0.079	0.069	0.115	-2	116	81	4.31%
RV-A2 5A	0.081	0.058	0.182	0	160	56	5.63%
RV-A2 6A	0.211	0.224	0.243	-1	93	114	16.13%
Median	**0.080**	**0.065**	**0.128**	**-1**	**96**	**68**	**4.97%**

Table S3.10. Pixel intensity-based and spatial (distance between center-mass) colocalization analysis between dsRNA and calnexin in RV-C15-infected HAE. (DOCX)

Sample	PCC	thM1	thM2	Van Steensel's dx (pixel)	dsRNA centroids (n)	Calnexin centroids (n)	% center-mass colocalization (dsRNA/calnexin from total dsRNA)
RV-C15 1A	0.53	0.63	0.47	2	142	188	54.93%
RV-C15 1B	0.49	0.51	0.49	2	120	150	41.67%
RV-C15 2C	0.19	0.13	0.34	1	1233	208	4.38%
RV-C15 2D	0.41	0.6	0.29	2	73	184	28.77%
RV-C15 3E	0.29	0.55	0.16	1	122	271	45.08%
RV-C15 4F	0.35	0.57	0.22	1	112	212	55.36%
Median	**0.381**	**0.563**	**0.317**	**1.5**	**121**	**198**	**43.37%**

Table S3.11. Pixel intensity-based and spatial (distance between center-mass) colocalization analysis between dsRNA and calnexin in RV-A16-infected HAE. (DOCX)

Sample	PCC	thM1	thM2	Van Steensel's dx (pixel)	dsRNA centroids (n)	Calnexin centroids (n)	% center-mass colocalization (dsRNA/calnexin from total dsRNA)
RV-A16 1A	0.366	0.407	0.387	1	141	385	14.18%
RV-A16 1B	0.289	0.372	0.292	3	128	274	10.16%
RV-A16 1C	0.265	0.328	0.271	2	101	161	2.97%
RV-A16 1D	0.340	0.231	0.607	3	410	289	2.68%
RV-A16 1E	0.287	0.276	0.374	2	184	365	3.26%
RV-A16 2F	0.352	0.263	0.618	2	286	217	3.15%
RV-A16 2G	0.320	0.236	0.584	4	241	180	0.83%
RV-A16 2H	0.358	0.255	0.637	3	362	235	0.55%
RV-A16 3I	0.339	0.389	0.359	2	85	142	22.35%
RV-A16 3J	0.272	0.315	0.312	2	285	139	1.05%
RV-A16 3K	0.364	0.280	0.633	0	99	185	4.04%
Median	**0.339**	**0.280**	**0.387**	**2**	**184**	**217**	**3.15%**

Table S3.12. Pixel intensity-based and spatial (distance between center-mass) colocalization analysis between dsRNA and calnexin in RV-A2-infected HAE. (DOCX)

Sample	PCC	thM1	thM2	Van Steensel's dx (pixel)	dsRNA centroids (n)	Calnexin centroids (n)	% center-mass colocalization (dsRNA/calnexin from total dsRNA)
RV-A2 1A	0.3	0.5	0.22	2	224	292	1.79%
RV-A2 2B	0.37	0.58	0.29	-1	95	175	8.42%
RV-A2 3C	0.43	0.51	0.44	2	128	82	1.56%
RV-A2 4D	0.45	0.48	0.52	2	173	32	1.73%
RV-A2 6E	0.33	0.47	0.29	2	246	74	2.44%
RV-A2 7A	0.28	0.48	0.22	1	155	108	2.58%
Median	**0.353**	**0.491**	**0.288**	**2**	**164**	**95**	**2.11%**

Table S3.13. Pixel intensity-based and spatial (distance between center-mass) colocalization analysis between dsRNA and giantin in RV-C15-infected HAE. (DOCX)

Sample	PCC	thM1	thM2	Van Steensel's dx (pixel)	dsRNA centroids (n)	Giantin centroids (n)	% center-mass colocalization (dsRNA/giantin from total dsRNA)
RV-C15 1A	0.14	0.15	0.15	-1	142	269	18.31%
RV-C15 1B	0.19	0.2	0.2	-3	120	221	12.50%
RV-C15 2C	0.07	0.06	0.15	1	1233	326	2.51%
RV-C15 2D	0.13	0.2	0.1	0	73	270	10.96%
RV-C15 3E	0.09	0.17	0.06	-2	122	281	24.59%
RV-C15 4F	0.15	0.23	0.11	-1	111	161	25.23%
Median	**0.136**	**0.183**	**0.130**	**-1**	**121**	**269.5**	**15.40%**

Table S3.14. Pixel intensity-based and spatial (distance between center-mass) colocalization analysis between dsRNA and giantin in RV-A16-infected HAE. (DOCX)

Sample	PCC	thM1	thM2	Van Steensel's dx (pixel)	dsRNA centroids (n)	Giantin centroids (n)	% center-mass colocalization (dsRNA/giantin from total dsRNA)
RV-A16 1A	0.372	0.501	0.333	-3	141	14	10.64%
RV-A16 1B	0.331	0.441	0.313	2	128	2	1.56%
RV-A16 1C	0.363	0.607	0.264	-1	101	7	6.93%
RV-A16 1D	0.241	0.306	0.311	1	410	1	0.24%
RV-A16 1E	0.269	0.480	0.223	-1	184	26	14.67%
RV-A16 2F	0.319	0.346	0.450	-1	286	5	2.45%
RV-A16 2G	0.376	0.378	0.515	5	241	8	3.32%
RV-A16 2H	0.241	0.318	0.337	0	362	0	0.00%
RV-A16 3I	0.115	0.172	0.153	0	85	7	8.24%
RV-A16 3J	0.215	0.311	0.228	5	285	69	21.05%
RV-A16 3K	0.259	0.260	0.440	-18	99	1	1.01%
Median	**0.269**	**0.346**	**0.313**	**0**	**184**	**7**	**3.32%**

Table S3.15. Pixel intensity-based and spatial (distance between center-mass) colocalization analysis between dsRNA and giantin in RV-A2-infected HAE. (DOCX)

Sample	PCC	thM1	thM2	Van Steensel's dx (pixel)	dsRNA centroids (n)	Giantin centroids (n)	% center-mass colocalization (dsRNA/giantin from total dsRNA)
RV-A2 1A	0.19	0.27	0.21	0	608	628	4.11%
RV-A2 2B	0.33	0.52	0.27	-3	95	120	2.11%
RV-A2 3C	0.27	0.3	0.33	2	128	253	1.56%
RV-A2 4D	0.34	0.36	0.44	0	173	104	8.67%
RV-A2 6E	0.26	0.39	0.23	-1	246	140	7.32%
RV-A2 7A	0.22	0.39	0.18	1	155	132	2.58%
Median	**0.266**	**0.378**	**0.249**	**0**	**164**	**136**	**3.35%**

Table S3.16. Pixel intensity-based and spatial (distance between center-mass) colocalization analysis between dsRNA and STING in RV-C15-infected HAE. (DOCX)

Sample	PCC	thM1	thM2	Van Steensel's dx (pixel)	dsRNA centroids (n)	STING centroids (n)	% center-mass colocalization (dsRNA/STING from total dsRNA)
RV-C15 1A	0.241	0.256	0.288	0	107	91	3.74%
RV-C15 1B	0.363	0.492	0.326	2	109	54	0.92%
RV-C15 1C	0.297	0.207	0.597	-4	80	74	11.25%
RV-C15 1D	0.025	0.029	0.054	2	150	77	6.00%
RV-C15 1E	0.055	0.055	0.090	3	136	92	3.68%
RV-C15 1F	0.041	0.044	0.087	0	101	55	2.97%
RV-C15 1G	0.060	0.030	0.163	-2	151	59	1.32%
RV-C15 1H	0.005	0.023	0.021	-1	137	98	1.46%
RV-C15 2A	0.321	0.406	0.319	-1	53	46	7.55%
RV-C15 2B	0.367	0.395	0.455	-1	61	37	6.56%
RV-C15 2C	0.239	0.197	0.333	2	138	51	2.90%
RV-C15 2D	0.212	0.232	0.300	-7	54	80	3.70%
RV-C15 2E	0.005	0.021	0.049	-3	116	78	5.17%
RV-C15 2F	0.127	0.096	0.213	-1	86	103	4.65%
RV-C15 3A	0.402	0.471	0.400	2	42	33	4.76%
RV-C15 3B	0.314	0.268	0.466	-3	49	62	2.04%
RV-C15 3C	0.265	0.266	0.325	0	61	36	3.28%
RV-C15 3D	0.198	0.152	0.300	1	81	55	4.94%
RV-C15 3E	0.455	0.631	0.371	1	51	16	0.00%
RV-C15 3F	0.149	0.292	0.101	1	70	52	4.29%
Median	**0.226**	**0.220**	**0.300**	**0**	**83.5**	**57**	**3.72%**

Table S3.17. Pixel intensity-based and spatial (distance between center-mass) colocalization analysis between Lamp1 and LC3b in RV-C15-infected HAE. (DOCX)

Sample	PCC	thM1	thM2	Van Steensel's dx (pixel)	Lamp-1 centroids (n)	LC3b centroids (n)	% center-mass colocalization (Lamp-1/LC3b from total Lamp-1)
RV-C15 1A	0.262	0.129	0.570	-1	58	49	5.17%
RV-C15 1B	0.040	0.032	0.098	-1	70	98	1.43%
RV-C15 1C	0.159	0.114	0.300	0	56	134	3.57%
RV-C15 1D	0.048	0.016	0.240	0	9	20	0.00%
RV-C15 2A	0.058	0.034	0.183	-2	22	154	4.55%
RV-C15 2B	0.256	0.120	0.631	-1	18	48	16.67%
RV-C15 2C	0.027	0.016	0.107	-1	50	44	0.00%
RV-C15 3A	0.148	0.037	0.684	-1	24	27	0.00%
RV-C15 3B	0.157	0.047	0.620	-1	98	33	3.06%
RV-C15 3C	0.107	0.023	0.596	-2	40	27	12.50%
RV-C15 3D	0.186	0.071	0.577	-2	32	35	3.13%
RV-C15 4A	0.128	0.030	0.677	-2	40	37	2.50%
RV-C15 4B	0.142	0.040	0.597	-2	29	40	0.00%
RV-C15 4C	0.186	0.061	0.690	-3	40	41	2.50%
RV-C15 5A	0.249	0.082	0.792	-1	77	26	2.60%
RV-C15 5B	0.067	0.010	0.534	-1	45	7	0.00%
RV-C15 6A	0.321	0.153	0.723	-1	32	30	3.13%
RV-C15 6B	0.054	0.012	0.323	0	23	10	0.00%
RV-C15 6C	0.024	0.007	0.129	-1	62	0	0.00%
Median	**0.142**	**0.037**	**0.577**	**-1**	**40**	**35**	**2.50%**

Table S3.18. Pixel intensity-based and spatial (distance between center-mass) colocalization analysis between Lamp1 and LC3b in RV-A16-infected HAE. (DOCX)

Sample	PCC	thM1	thM2	Van Steensel's dx (pixel)	Lamp-1 centroids (n)	LC3b centroids (n)	% center-mass colocalization (Lamp-1/LC3b from total Lamp-1)
RV-A16 1A	0.604	0.670	0.569	-1	42	60	16.67%
RV-A16 1B	0.388	0.585	0.296	-1	32	124	9.38%
RV-A16 1C	0.399	0.635	0.290	-2	18	92	0.00%
RV-A16 3A	0.510	0.610	0.488	-1	29	46	24.14%
RV-A16 3B	0.435	0.584	0.356	-1	41	116	17.07%
RV-A16 3C	0.409	0.557	0.338	-2	48	55	8.33%
RV-A16 3D	0.583	0.665	0.538	-2	22	44	27.27%
RV-A16 4A	0.568	0.647	0.530	-1	60	49	16.67%
RV-A16 4C	0.535	0.618	0.493	-1	27	32	7.41%
RV-A16 5A	0.395	0.590	0.308	-2	51	160	13.73%
RV-A16 5B	0.418	0.605	0.318	-2	35	40	2.86%
RV-A16 5C	0.392	0.599	0.304	-2	35	96	17.14%
RV-A16 5D	0.456	0.639	0.376	-2	41	103	7.32%
Median	**0.435**	**0.610**	**0.356**	**-2**	**35**	**60**	**13.73%**

Table S3.19. Pixel intensity-based and spatial (distance between center-mass) colocalization analysis between Lamp 1 and LC3b in RV-A2-infected HAE. (DOCX)

Sample	PCC	thM1	thM2	Van Steensel's dx (pixel)	Lamp-1 centroids (n)	LC3b centroids (n)	% center-mass colocalization (Lamp-1/LC3b from total Lamp-1)
RV-A2 1A	0.361	0.372	0.388	0	123	56	9.76%
RV-A2 2A	0.370	0.175	0.869	-1	47	50	2.13%
RV-A2 3A	0.393	0.281	0.601	-1	79	98	3.80%
RV-A2 3B	0.228	0.225	0.299	0	64	41	0.00%
RV-A2 4A	0.166	0.096	0.367	-2	31	84	0.00%
RV-A2 4b	0.141	0.119	0.231	-2	18	55	0.00%
RV-A2 4C	0.135	0.120	0.242	-3	49	67	4.08%
Median	**0.228**	**0.175**	**0.367**	**-1**	**49**	**56**	**2.13%**

3.8 *Author contributions*

Conceptualization: Talita B. Gagliardi, Margaret A. Scull.

Data curation: Talita B. Gagliardi, Monty E. Goldstein, Daniel Song, Maxinne A. Ignacio.

Formal analysis: Talita B. Gagliardi, Monty E. Goldstein, Daniel Song, Kelsey M. Gray, Jae W. Jung.

Funding acquisition: Margaret A. Scull.

Supervision: Kimberly M. Stroka, Gregg A. Duncan, Margaret A. Scull.

Validation: Kimberly M. Stroka, Gregg A. Duncan.

Writing – original draft: Talita B. Gagliardi.

Writing – review & editing: Talita B. Gagliardi, Margaret A. Scull.

3.9 *Acknowledgements*

We thank Drs. James Gern, Yuri A. Bochkov, Wai-Ming Lee, and Ann Palmenberg from University of Wisconsin–Madison (UW, Madison, WI) for providing the rhinovirus plasmids. In addition, we thank Ann Palmenberg (UW) for donating an aliquot of the anti-VP1 antibody. We would also like to thank the Addgene depositors Drs. Feng Zhang, Bob

Weinberg, and Didier Trono for their contributions in making reagents broadly accessible and Drs. Matthew Walters and Ronald Crystal (Weill Cornell Medical College) for donating the BCi-NS1.1 cells. We are also grateful to the directors and teams at the MPRI Flow Cytometry and Cell Sorting Facility, Imaging Core, and the Laboratory for Biological Ultrastructure at the University of Maryland, College Park, for their assistance. Finally, we acknowledge Eva Agostino for critical reading of the manuscript.

Chapter 4 : Human STING Promotes RV-C Replication in Mouse Cells *In Vitro* and *In Vivo*

Monty E. Goldstein[1], Maxinne A Ignacio[1], Jeffrey M. Loube[1], Matthew R. Whorton[2], Yueh-Ming Loo[3], and Margaret A. Scull[1]

1 Department of Cell Biology and Molecular Genetics, Maryland Pathogen Research Institute, 3134 Bioscience Research Building, University of Maryland, College Park, MD 20742, USA.

2 Vollum Institue, Oregon Health and Science University, Portland, OR, 97239, USA.

3 Vaccines and Immune Therapies, BioPharmaceuticals R&D, AstraZeneca, Gaithersburg, MD, 20878, USA.

Building on our work characterizing RV-C replication in the human airway epithelium, we explored the ability of RV-C to infect and replicate in mouse cells *in vitro*, and then ultimately, *in vivo* in mice. While mice are not natural hosts for RV infection, they represent a tractable, inexpensive, and widely-available animal model that has been used extensively to understand viral pathogenesis and respiratory disease. Mouse models have been established for major- and minor- group RVs; however, no animal models for RV-C have yet to be validated.

This chapter, with slight adaption will be submitted for publication: Goldstein ME, Ignacio MA, Loube JM, Whorton MR, Loo, YM, Scull MA. Human STING promotes RV-C replication in mouse cell *in vitro* and *in vivo*. My contribution to this work includes

performing all experiments with the exception of the initial generation of the transgenic human-CDHR3-expressing mouse lines and the homology modeling of the RV-C capsid together with human or murine CDHR3. I was responsible for experimental design, performing analysis, generating figures and writing of this chapter.

4.1 Abstract

Rhinovirus C (RV-C) infects ciliated cells within the airway epithelium, and work by our group and others have demonstrated that host factors cadherin-related family member 3 (CDHR3) and stimulator of interferon genes (STING) support viral replication using well-differentiated *in-vitro* models of human airway epithelium. However, interrogation of RV-C-induced disease mechanisms necessitates an animal model. Previously, mice have been utilized to study major and minor RVs after adaptation of either host or virus. Recently, RV-C infection was reported in wild type mice; however, titers were not sustained and these data have not been reproduced by other groups. Thus, the requirements for RV-C infection in mice remain unclear. Here we report that human (h) and murine (m) CDHR3 orthologs have similar tissue distribution; however, homology is limited, and several substitutions in mCDHR3 may impact RV-C interactions. Bypassing entry, we demonstrate RV-C can replicate in mouse lung epithelial type 1 (LET1) cells following RV-C15 transfection, and produce infectious virus capable of re-infecting susceptible HeLa-E8 cells, suggesting the later stages of the viral life cycle are supported. Still, we observed a significant increase in frequency of dsRNA-positive cells and intensity of dsRNA staining following expression of hSTING. Taken together, we hypothesized both hCDHR3 and hSTING would be required for RV-C infection in mice *in vivo*. Thus, we developed and characterized a transgenic mouse expressing hCDHR3, and further utilized adeno-associated virus to deliver hSTING to the murine airway. Importantly, we

achieved significantly higher RV-C15 titers 24 hours-post infection in mice expressing both hCDHR3 and hSTING compared to either wild-type mice, or mice with only hCDHR3 or hSTING alone. To our knowledge, these data represent the first RV-C infection in mice with increasing replication 24 hours post-infection (hpi). As the field better understands the totality of host factors required for RV-C infection, this mouse model can serve as a platform for further modification – ultimately establishing an *in vivo* model, fully recapitulating human viral dynamics and host disease.

4.2 Introduction

Responsible for over 40% of respiratory virus infections in the human population, rhinoviruses (RVs) are highly prevalent respiratory viral pathogens [19,20,32,337]. While most often regarded as etiologic agents of the common cold, RVs can infect the lower airways resulting in bronchiolitis or pneumonia, and are often associated with virus-induced exacerbations in acute and chronic lung disease, such as asthma and chronic obstructive pulmonary disease (COPD) [21–24]. RVs comprise three species: RV-A, -B, and -C. While RV-A and -B infections have been described for decades [397], RV-C was only identified in 2006 [2], and has since been associated with more severe disease phenotypes and more frequent hospitalizations within the pediatric population [28–35]. Currently, no therapeutics have been approved to prevent or treat infections by any species of RV.

To understand RV-C mediated disease and to support the development of antivirals and vaccines against RVs, animal models are critical. However, all RV species have a very narrow host range, primarily limited to humans, and entirely restricted outside of higher primates. Both major-group and minor-group RVs have been documented to infect chimpanzees in a laboratory setting, and certain minor-group RV infections were

also recorded in gibbons [50–52]. More recently, a lethal outbreak of RV-C in Uganda, provided the first evidence of any naturally occurring RV infections in non-human hosts [53].

While mice represent an inexpensive, genetically-tractable model that are often excellent models of viral disease, they are not natural reservoirs for RV. Therefore, not surprisingly, development of RV mouse models for major-group and minor-group required expression of intercellular adhesion molecule 1 (ICAM-1) or virus adaptation, respectively [97,99,101,102,105]. As RV-C utilizes cadherin-related family member 3 (CDHR3) to mediate host cell entry, prior RV mouse models are not predicted to be useful. Further, murine CDHR3 (mCDHR3) lacks complete homology with the human (h) ortholog, suggesting modifications to mediate entry in a murine host would be necessary. Recently, Rajput and Han et. al reported infection of wild-type (WT) BALB/c mice with RV-C15 [111]. However, RV-C15 titers never rise above the initial inoculum and decrease rapidly after 16 hpi. Thus, these results suggest a need for an alternative mouse model.

Here, we define the ability of RV-C to replicate and produce infectious virus in mouse lung epithelial type I (LET1) cells [398], and utilize human stimulator of interferon genes (hSTING) [87] – which was recently identified as a proviral factor for RV replication – to significantly increase viral replication *in vitro*. Applying these findings *in vivo*, we developed a transgenic mouse expressing hCDHR3 and hSTING, and demonstrate that these mice support RV-C replication, but also highlight the need for additional optimization.

4.3 Results

4.3.1 Murine and human CDHR3 orthologs exhibit similar tissue expression patterns, but lack complete homology

RV-C is difficult to culture in standard cell lines [84,93] and CDHR3 expression in HeLa cells was subsequently shown to enable RV-C particle uptake, indicating CDHR3 acts as a receptor for this virus [15]. Thus, we initially sought to identify differences between human and murine orthologs of CDHR3. We obtained total RNA from C57Bl/6 mouse tissues, and assayed relative expression of CDHR3 by qPCR. In line with prior profiling of CDHR3 in human bronchial and murine tracheal epithelial tissues [399,400], we observed elevated CDHR3 expression in the mouse lung and trachea, in addition to the ovaries of female mice as compared to other organs and tissues (**Figure 4.1A**).

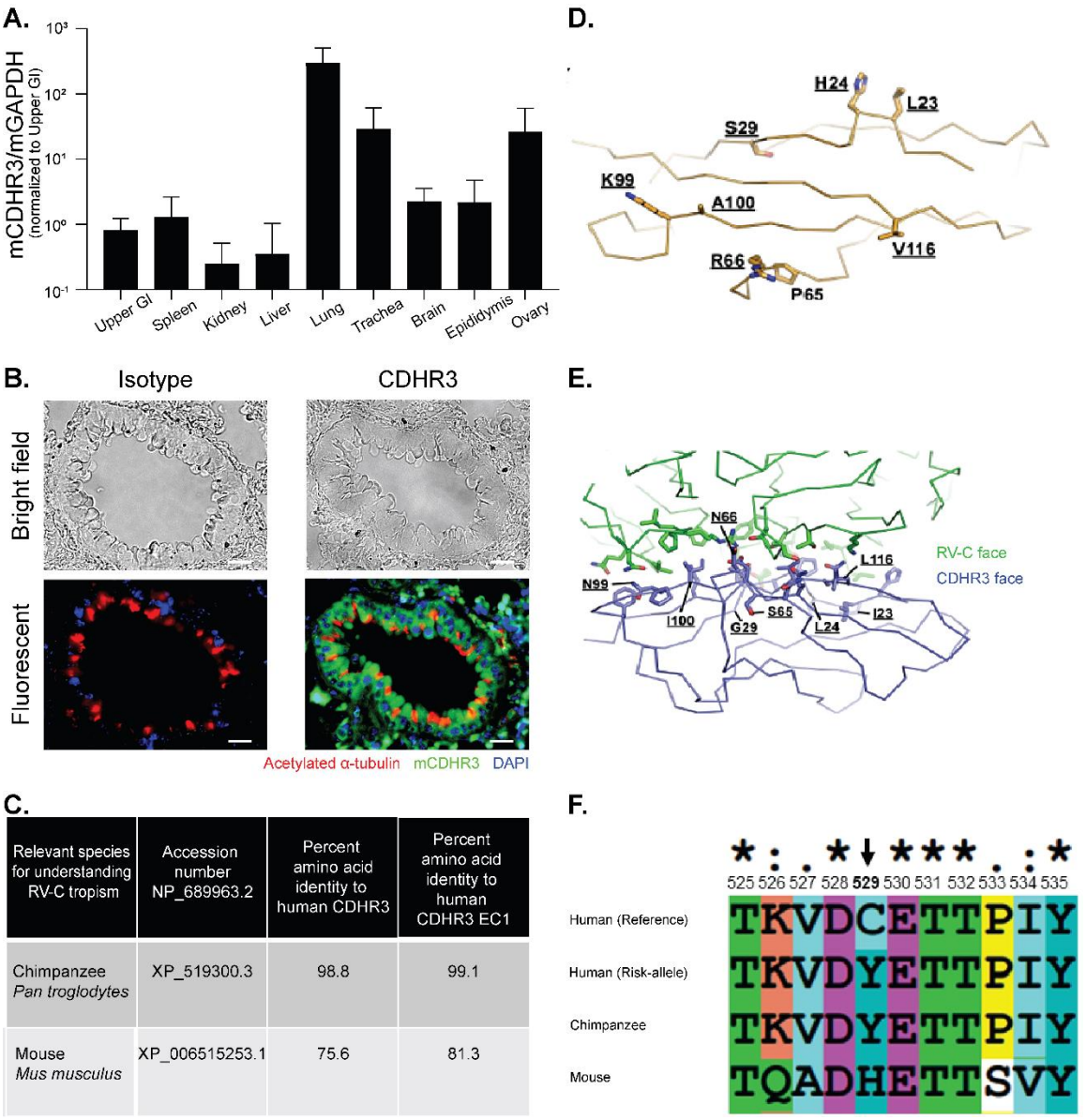

Relevant species for understanding RV-C tropism	Accession number NP_689963.2	Percent amino acid identity to human CDHR3	Percent amino acid identity to human CDHR3 EC1
Chimpanzee *Pan troglodytes*	XP_519300.3	98.8	99.1
Mouse *Mus musculus*	XP_006515253.1	75.6	81.3

Figure 4.1: Murine CDHR3 is localized to similar tissues as human CDHR3, yet differs in several key aspects. (**A**) qPCR of murine CDHR3 expression relative to murine GAPDH by tissue across n=4 male and n=4 female mice. (**B**) Immunohistochemical detection of CDHR3 in BALB/c mouse lung tissue. Nuclei (DAPI; blue) and cilia (acetylated-alpha tubulin; red). Scale bar = 20μm. (**C**) Table detailing CDHR3 amino acid conservation in chimpanzees and mice. (**D**) A side view of the cryo-EM structure of RV-C15 (green) in complex with the human CDHR3. EC1 (blue) is shown as a Ca trace. The side chains that comprise the RV-C15-EC1 interface are represented as sticks. Residues that differ from the mouse ortholog are labeled. (**E**) A structural homology model of the mouse CDHR3 EC1 domain, which was generated using the human CDHR3 EC1 as a template, is shown. Only residues that differ from the human CDHR3 EC1 domain are shown and labeled. (**F**) Homology of CDHR3 at position 529, performed using ClustalX2.

Further, within the murine airway, we were able to localize mCDHR3 to the ciliated epithelium, as determined by co-staining with acetylated α-tubulin (**Figure 4.1B**). These data indicate that the CDHR3 orthologs are expressed in similar tissues and cell types; however, protein alignments revealed they are not entirely conserved (**Figure 4.1C**). Specifically, mCDHR3 is only 75.6% similar to hCDHR3 on the amino acid level, and furthermore, 81.3% conserved within extracellular domain 1 (EC1), the putative RV-C - CDHR3 interacting region. This is in contrast to the near complete sequence homology of chimpanzee (*Pan troglodytes*) CDHR3, where natural RV-C infection has been documented [53].

Given the lack of conservation in CDHR3 EC1 between humans and mice, we mapped the cryogenic electron microscopy (cryo-EM) structure of RV-C15 in complex with hCDHR3 EC1 to determine the critical interacting residues between the viral capsid and this cellular receptor, noted graphically as sticks (**Figure 4.1D**). As the cryo-EM structure of mCDHR3 has not yet been solved, we performed homology modeling to identify residues of mCDHR3 EC1 which differ from the human ortholog (**Figure 4.1E**). These results identified nine residues which individually and together were predicted to negatively impact virus receptor binding.

Beyond binding, residue 529 is known to influence the surface expression of hCDHR3 [31,96], and could therefore impact entry into mouse cells. Notably, mCDHR3 position 529 contains a histidine residue which is distinct from RV-C susceptible species, and may further impact cell surface expression and availability (**Figure 4.1F**). While further mutagenesis efforts are needed to measure the contributions of each mutation individually and in combination, these data suggest differences in cell surface expression from changes at position 529 and within the RV-C – EC1 interface may have deleterious effects on viral particle uptake into mouse cells.

4.3.2 Murine cells are permissive for RV-C, and human STING expression significantly increases RV-C replication

We next sought to directly assess whether mouse cells are permissive for RV-C15 replication. To do so, we utilized murine lung epithelial type 1 (LET1) cells and transfected *in vitro*-transcribed viral RNA to bypass the initial stages of infection. RV-A1A is rare in its ability to replicate in mice without prior adaptation, thus, we utilized this RV as a positive control [98]. We then visualized ongoing viral replication following mock-transfection, or transfection of RV-A1A or RV-C15 genomic RNA, using either a probe specific for a conserved region within the RV 5'-UTR of the anti-genome, or an antibody that detects dsRNA (**Figure 4.2A**).

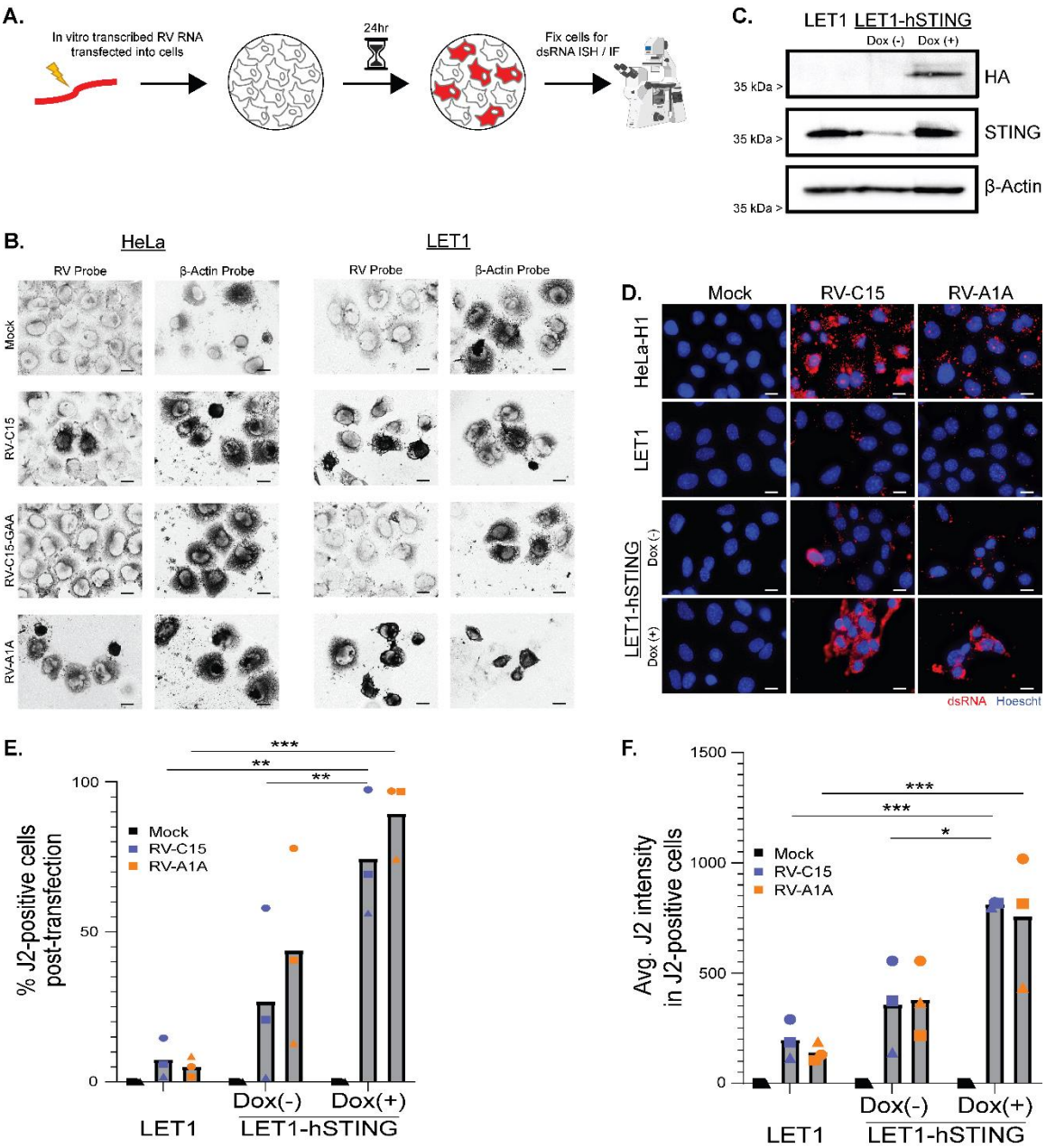

Figure 4.2: Mouse replicate RV-C, and replication is significantly increased upon expression of human STING. (A) cartoon describing experimental design. HeLa-H1 cells or LET1 cells were transfected in parallel with *in vitro* transcribed RV RNA or mock-transfected. (**B**) *In situ* hybridization (ISH) probes (dark) identify the presence of negative-sense RV RNA, indicative of replicating RV for RV-C15-transfected LET1 (right) and HeLa cells (positive-control, left), but not in mock or replication-deficient (RV-C15-GAA) genome transfected cells at 24 hours post-transfection. (**C**) Western blot showing inducible expression hSTING in modified LET1 cells. (**D**) Immunofluorescence-mediated detection of dsRNA (red) in HeLa cells (positive-control), LET1, LET1-hSTING with or without induction after transfection with either RV-C15 or RV-A1A RNA (positive-control) but not in mock-transfected wells, confirms RV-C15 replication in a mouse cell background. Staining was performed 24hpt. Nuclei (hoescht; blue). Scale bar = 20µm**.** (**E**) CellProfiler

quantification of % dsRNA-positive cells as from panel **D**. Each individual point (square, circle or triangle) represents the mean from an independent experiment. In each experiment, >30 cells were assayed across n=4 immunofluorescence images taken at predetermined locations within the culture. Statistical analysis was performed using a Mann-Whitney U test (two-tailed; 0.95% confidence interval; "**p<0.01, ***p<0.001). (**F**) CellProfiler quantification of average dsRNA intensity in dsRNA-positive cells. Statistical analysis was performed using a Mann-Whitney U test (two-tailed; 0.95% confidence interval; "*p<0.05, ***p<0.001).

HeLa-H1 cells were transfected in parallel as an additional control, and all cells were fixed 24 hours later. Subsequent staining demonstrated *in situ* hybridization (ISH) of the RV anti-genome probe in HeLa-H1 cells transfected with either RV-A1A or -C15 RNA, indicating replication of both RVs tested, with RV-A1A exhibiting robust signal (**Figure 4.2B**). RV-A1A- and RV-C15-, but not mock-, transfected LET1 cells also reacted with the RV 5'UTR probe, indicating that indeed, these murine cells can replicate RV-C15. The addition of a replication-deficient RV-C15 virus (RV-C15-GAA) harboring mutations at the conserved GDD motif within the RNA-dependent RNA polymerase [401] further validated these findings, while hybridization of a control probe targeting the cellular-expressed β-actin transcripts in both cell types and under all conditions confirmed RNA integrity in the samples.

Recently, McKnight et. al identified hSTING as a proviral factor which was able to augment RV-C replication [87]. Importantly, murine STING was unable to convey the same proviral effect, unless a murine-adapted RV-A16 (RV-A16L) was used [87]. Therefore, we assayed whether expression of hSTING in mouse cells would enhance replication of WT, non-mouse adapted, RV-C. Towards this, we generated a LET1 cell line expressing an HA-tagged, tetracycline-inducible hSTING construct by stable-transfection and subsequent puromycin selection. Upon induction with doxycycline, we observed an increase in hSTING expression as identified by the HA-tag (**Figure 4.2C**). Then, to assess the impact of hSTING in these cells in the context of RV replication, we followed the

workflow detailed in **Figure 4.2A**, probing for replication using an antibody specific for dsRNA (J2; **Figure 4.2D**). As anticipated, HeLa-H1 cells supported replication of both RV-C15 and RV-A1A, as indicated by visualization of dsRNA-positive puncta in RV- but not mock-transfected conditions. Similarly, we observed the presence of dsRNA in LET1 cells and LET1 cells expressing hSTING with or without doxycycline induction after transfection with RV-C15 or RV-A1A, but not in mock-transfected cells. To quantify these data, we designed a custom CellProfiler [402] pipeline to assign dsRNA signal to a specific cell, and determined the percentage of dsRNA-positive cells (**Figure 4.2E**). We noted a statistically significant increase in dsRNA in LET1-hSTING-expressing cells upon transfection with RV-C15 or RV-A1A, in which a vast-majority of RV-C15-transfected, and nearly all RV-A1A-transfected cells were replicating virus. While differences in transfection efficiency between cell lines preclude a direct comparison of replication levels between HeLa-H1 and LET1 cells, we did observe a similar staining pattern between RV-A1A and RV-C15 in LET1 cells, suggesting comparable replication efficiency for these two rhinoviruses in a mouse cell background without further adaptation. The increased frequency of dsRNA+ cells in the LET1-hSTING condition could be attributed to differences in transfection efficiency, or the extent of viral replication in these cells which may facilitate detection of dsRNA. Thus, we quantified the intensity of dsRNA signal in dsRNA+ cells and observed that, on a per-cell basis, the fluorescence intensity in RV-C15-transfected cells was higher in LET1-hSTING expressing cell compared to uninduced LET1-hSTING cells, or the parental LET1 cell line (**Figure 4.2F**).

4.3.3 Murine cells support the production of infectious particles

In the final stages of the viral life cycle, nascent virions are assembled and released from the infected cell. Since we found that LET1 cells are permissive for RV-C15

replication, we next designed an experiment, depicted in **Figure 4.3A**, to assess the production of infectious progeny. HeLa-H1 and LET1 cells were transfected in parallel as done in Figure 1A, however here, the supernatants were collected 24 hours-post transfection (hpt) and then filtered to remove any potentially infected cells or virus-containing cellular debris. These supernatants were then transferred to naive HeLa-E8 cells that have been previously modified to express hCDHR3, and shown to support the entire RV-C lifecycle [15].

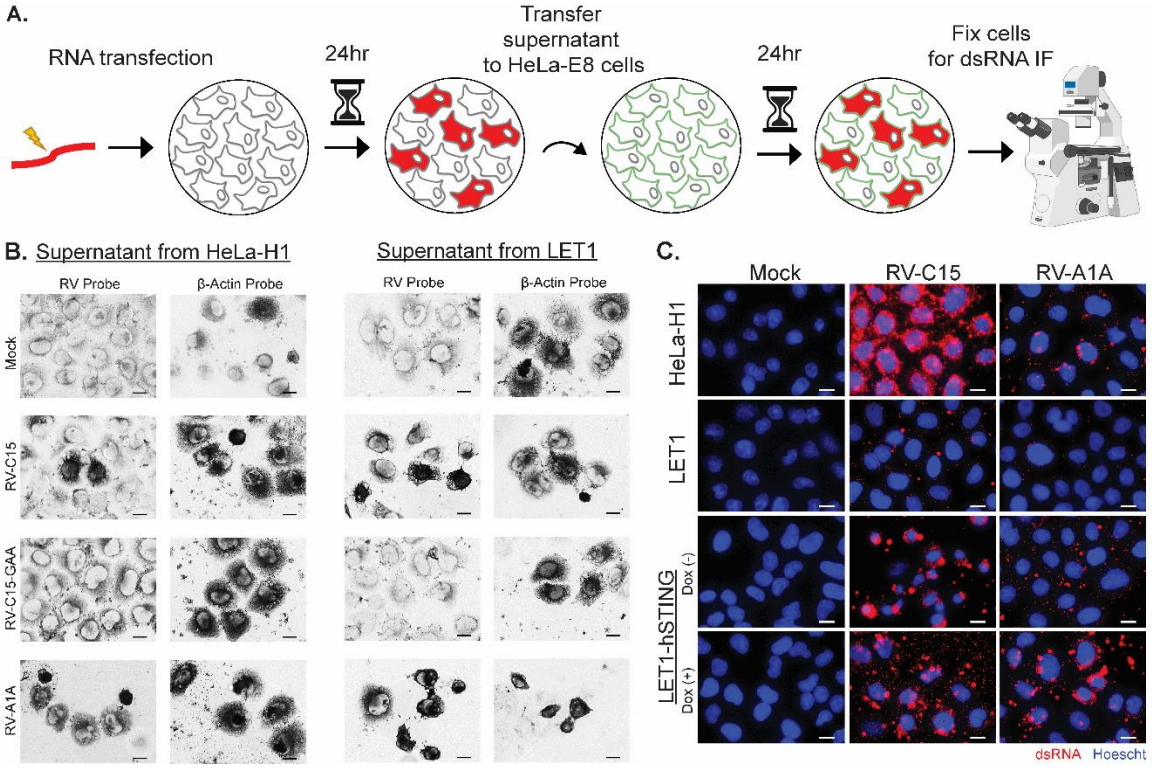

Figure 4.3: RV-C produced in mouse cells is infectious and capable of reinfection. (**A**) Cartoon describing experimental design. HeLa-H1, LET1, or LET1-hSTING cells with or without induction of hSTING were transfected in parallel with *in vitro* transcribed RV RNA or mock-transfected. 24 hpt supernatants were collected, filtered to remove any cellular material, and passaged to naïve HeLa-E8 cells. (**B**) *In situ* hybridization (ISH) probes (dark) identify the presence of negative-sense RV RNA, indicative of replicating RV of dsRNA in HeLa-E8 after reinfection with supernatants described in A, confirming infectious particle formation in LET1 cells. β-Actin ISH probes validate proper preservation of total RNA. Scale bar = 20μm. (**C**) Immunofluorescence-mediated detection of dsRNA (red) in HeLa-E8 cells after infection 24hpi with RV-C15 from HeLa-H1 (positive-control), LET1, LET1-hSTING with or without induction producer cells after transfection with either RV-C15 or RV-A1A RNA (positive-control) but not in mock-transfected wells. Nuclei (hoescht; blue). Scale bar = 20μm**.**

ISH probes, **Figure 4.3B**, targeting the RV anti-genome were used to identify infected HeLa-E8 cells. Our results show that infectious particles were produced in HeLa cells after transfection with RV-C15 or RV-A1A RNA, but not in mock or replication-deficient RV-C15 conditions, as expected. Importantly, we also detected RV probe reactivity in HeLa-E8 cells after inoculation with LET1 cell-derived supernatants originating from RV-A1A or RV-C15-transfected cultures, confirming mouse cells support the production of infectious RV particles.

To assess the impact of exogenous hSTING expression on infectious particle production, we also transfected RV genomes into HeLa-H1, LET1, and LET1-hSTING cells in the presence or absence of doxycycline. We then quantified viral genomes in the supernatants collected from these cultures 24 hpt, and also filtered and passaged additional supernatant to naïve HeLa-E8 cells. Surprisingly, we did not observe any significant differences in the number of RV genome copies in supernatants from LET1 cells or LET1 cells expressing hSTING (**Supplemental Figure 4.1A and 4.1B**). However, additional experiments in human airway epithelial (HAE) cultures suggest a potential role of STING in modulating the timing of RV particle release (**Supplemental Figure 4.2)** – thus, the impact of STING on various stages of the RV life cycle remains to be fully elucidated. Nonetheless, the presence of infectious extracellular viral particles in the conditioned media from HeLa and LET1 cells was confirmed by staining HeLa-E8 cells inoculated with these mediums for replicating virus, by J2-mediated immunofluorescence (**Figure 4.3C**). We observed dsRNA signal in HeLa-E8 cells resulting from infection by virus produced in the HeLa-H1 control cells, but also from virus produced in LET1 cell alone and in the presence or absence of hSTING.

4.3.4 CDHR3 knockout is embryonically lethal in mice

Our work above suggests a potential incompatibility between RV-C and mCDHR3, and indicates hSTING expression in mouse cells can increase replication. Therefore, we sought to generate mice expressing both of these human proteins to assess the impact on RV-C replication *in vivo*. Initially, we attempted to replace mCDHR3 entirely with the human ortholog. Towards this goal, mice heterozygous for constitutive knockout (KO) of mCDHR3 were generated by crossing animals containing loxP sites flanking exons 2 and 4 of mCDHR3 (C57BL/6NTac-Cdhr3-<tm6330Tac_A-C05>) with the ubiquitous Cre deleter model 12524 (experimental cross 1) from Taconic Biosciences. Resulting animals that were mCDHR3$^{+/-}$ were then crossed, to determine if homozygous mCDHR3$^{-/-}$ animals could be produced (experimental cross 2). However, the genotyping results (**Table 4.1**) of the 71 offspring revealed none of the mice were mCDHR3$^{-/-}$, thereby indicating that homozygous KO of CDHR3 is lethal.

Table 4.1: Genetic crosses of Cre$^{+/+}$ mice with mCDHR3$^{+/-}$ mice are unable to produce homozygous mCDHR3$^{-/-}$ offspring.

Cre genotype	mCDHR3 genotype	Total number of offspring
Cre$^{+/+}$	mCDHR3$^{-/-}$	0
Cre$^{+/+}$	mCDHR3$^{+/-}$,	48
Cre$^{+/+}$	mCDHR3$^{+/+}$,	23

The production of mCDHR3$^{+/-}$ and mCDHR3$^{+/+}$ offspring also support the conclusion of complete penetrance in homozygous lethality (**Table 4.2)**. Given the expected 1:2:1 monohybrid genotypic ratio, we calculated a χ^2 value of 8.34002E-06 for the resulting genotypes of observed mouse pups.

Table 4.2. Genetic crosses of mCDHR3$^{+/-}$ mice result in non-Mendelian offspring ratios, suggesting mCDHR3$^{-/-}$ mice are non-viable.

Genotype	Expected number of offspring	Observed number of offspring	% of total offspring
mCDHR3$^{-/-}$	18	0	0%
mCDHR3$^{+/-}$	36	48	67.61%
mCDHR3$^{+/+-}$	18	23	32.39%

Additionally, to understand the inability to generate homozygous mCDHR3$^{-/-}$ mice, we tracked pre-wean mortality over the course of a year (**Table 4.3**). Genotypic analysis revealed the number of pups found dead or missing was very similar between experimental crosses 1 and 2 indicating that the lethality from CDHR3 KO is most likely embryonic. Notably, litter size was slightly lower in experimental 2 compared to experimental cross 1.

Table 4.3. Assessment of pre-wean mouse mortality suggests mCDHR3$^{-/-}$ mice are embryonically lethal.

Experiment	Missing + Found Dead	Weaned Pups	Pre-Wean Mortality %	Average Litter Size at Weaning
Experimental Cross 1	24	121	16.55%	4.5
Experimental Cross 2	18	94	16.07%	3.9

4.3.5 Characterization of hCDHR3 expression in transgenic mice

Since homozygous mCDHR3 KO was embryonically lethal, we instead developed a transgenic C57Bl/6 mouse which expressed hCDHR3 in addition to the endogenous mCDHR3 by random transgene integration. Because hCDHR3 was integrated at random using the endogenous promotor, it was necessary to assess these mice for their hCDHR3 expression profiles. Thus, we performed qPCR in the lungs and trachea from three hCDHR3 transgenic (Tg) lines created in parallel (Tg1, Tg2, and Tg3), including both male

and female mice in our analysis to confirm transgene integration did not occur in a sex-linked manner. Specifically, we assayed expression of mCDHR3, murine glyceraldehyde3 3-phosphate dehydrogenase (GAPDH), and hCDHR3 and then plotted the ratios of the fold-change differences in expression of hCDHR3 to mGAPDH to mCDHR3 to mGAPDH (**Figure 4.4A**).

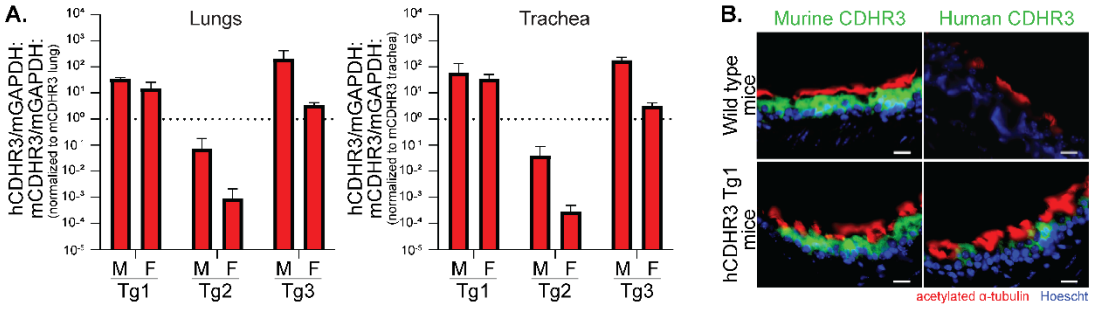

Figure 4.4: Selecting Tg1 as the transgenic mouse founder line. (**A**) Ratio of relative human CDHR3 expression to murine CDHR3 expression as compared to murine GAPDH in lungs and trachea of transgenic founder lines, Tg1, Tg2 and Tg3 by qPCR across n=4 male and n=4 female mice. (**B**) Immunohistochemical detection of human and murine CDHR3 (green) in Tg1 mouse lung tissue compared to WT mice. Nuclei (Hoescht; blue) and cilia (acetylated-alpha tubulin; red). Scale bar = 20µm.

We further compared relative expression in the upper gastrointestinal tract, spleen, kidney, liver, brain, and reproductive tissues (epididymis or ovaries) to yield a more complete understanding of the transgene expression profile in these mice (**Supplemental Figures 4.3, 4.4, 4.5)**. Notably, while hCDHR3 was not detected in Tg2, we found robust transgene expression in the lungs and trachea both Tg1 and Tg3. Based on these results, we then performed immunohistochemical staining for CDHR3 orthologs in lung tissue sections from the Tg1 and Tg3 lines. As expected, we detected mCDHR3 in both wild type and transgenic mice, while hCDHR3 was only observed in Tg1 and Tg3, where it localized to the ciliated airway epithelium (**Figure 4B, Supplemental Figure 6, 7**). While both Tg1 and Tg3 demonstrated robust hCDHR3 expression in the airway which localized to the

epithelium, Tg1 had a more comparable expression profile between sexes, therefore we selected Tg1 for subsequent RV-C mouse challenge studies.

4.3.6 Intranasal delivery of AAV 6.2-luciferase results in transgene expression in the lung.

Having demonstrated the benefit of hSTING expression for RV-C replication in mouse cells *in vitro*, we wanted to determine if it had similar effects on RV-C replication in mice *in vivo*. Thus, we used an adeno-associated virus 6.2 (AAV) vector to mediate delivery of hSTING to the mouse airway. Initial experiments were aimed at determining the optimal temporal window for observing transgene expression in our model. Here, mice were intranasally inoculated with either AAV6.2-expressing firefly luciferase (AAV-Fluc) or PBS as a control, and subsequently sacrificed on days 3, 6, 11, 18, 25 and 32 post-AAV transduction (dpt; **Figure 4.5A**).

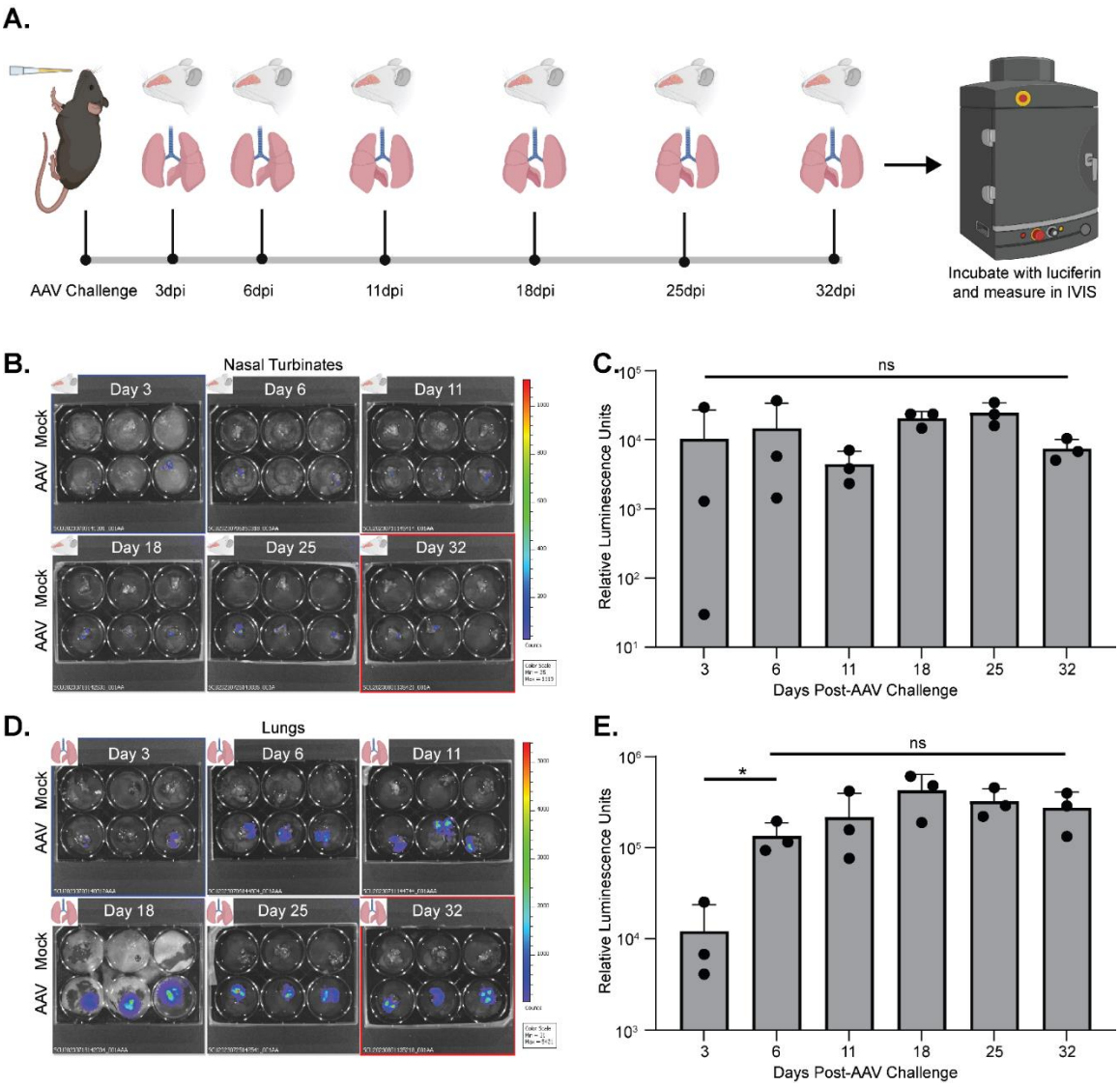

Figure 4.5: Intranasal delivery of luciferase by AAV results in transgene expression in the lung. (**A**) Cartoon describing experimental design. N=36 mice were intranasally inoculated with either AAV-Fluc or PBS and lungs and nasal turbinates were assayed for luciferase activity using an IVIS 3, 6, 11, 18, 25 and 32 dpt. (**B**) IVIS images across timepoints of nasal turbinates. (**C**) Quantification of luciferase activity in nasal turbinates across timepoints. (**D**) IVIS images across timepoints of the lungs. (**E**) Quantification of luciferase activity in the lungs across timepoints.

Nasal turbinates (**Figure 4.5B**) and lungs (**Figure 4.5D**) were collected, and flushed or inflated, respectively, with luciferin immediately prior to measuring luciferase activity using an IVIS imager. Quantification of the luminescence signal in the nasal turbinates and lungs over the duration of this 32-day study revealed very low and consistent luciferase signal

in the murine nasal turbinates across all time points (**Figure 4.5C**) and a significant increase in luciferase signal in the murine lungs between day 3 and 6 post-AAV transduction (**Figure 4.5E**). Since transgene expression in the lungs plateaued after day 6, we selected a time point after this (day 10) for RV challenge in subsequent experiments.

4.3.7 AAV-mediated delivery of hSTING to hCDHR3 transgenic mice promotes RV-C15 replication *in vivo*

To next assess the impacts of hCDHR3 and hSTING expression alone, and in combination, on RV-C infection in mice, we inoculated WT and hCDHR3 transgenic (Tg1) mice intranasally with AAV expressing either hSTING (AAV-hSTING) or AAV-Fluc. We then challenged these mice on day 10 post-transduction with RV-C15, or UV-inactivated-RV-C15, and harvested lungs at 12 and 24 hpi (**Figure 4.6A**).

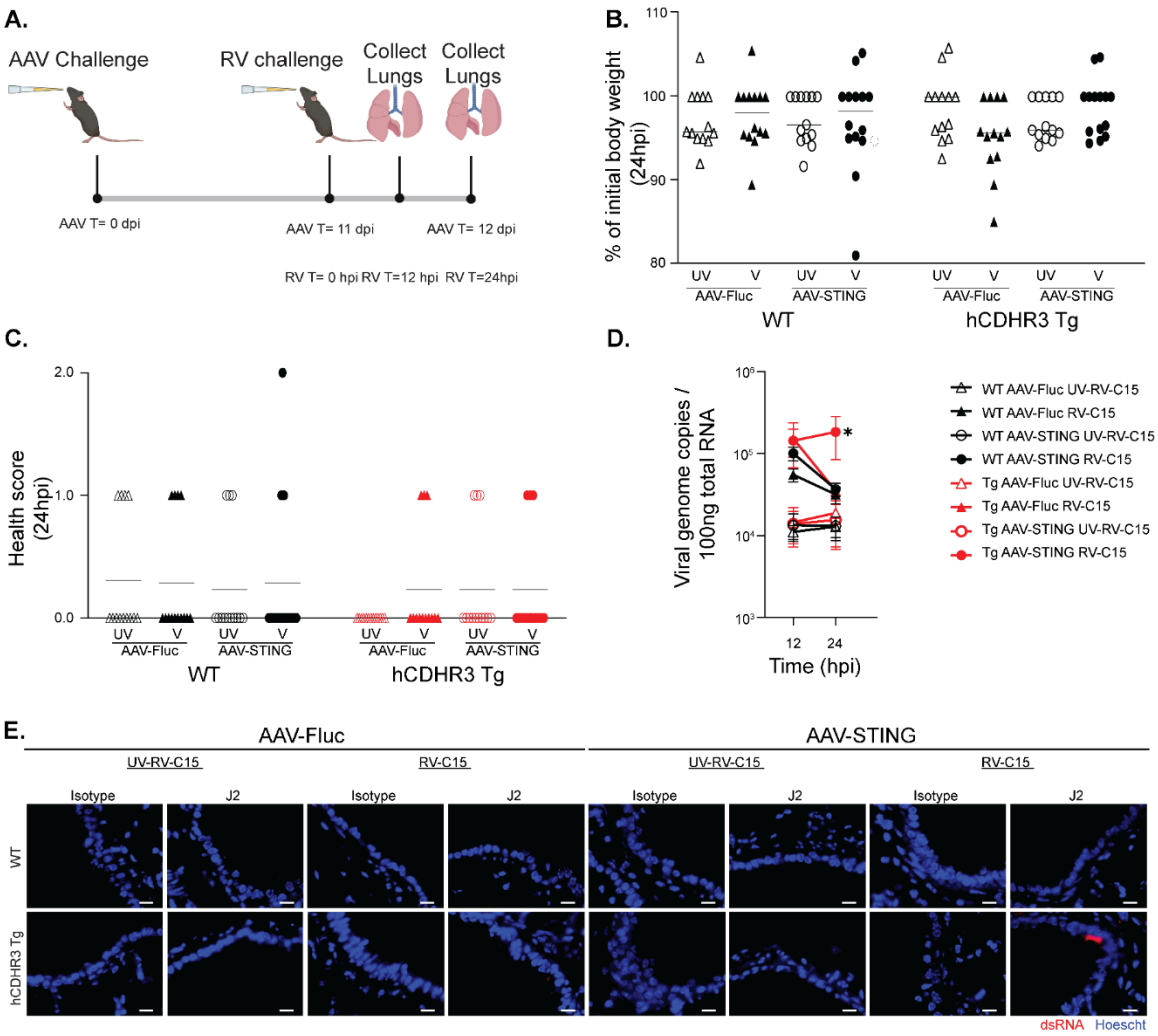

Figure 4.6: RV-C infection of transgenic mice expressing CDHR3 with the addition of human STING results in sustained viral replication. (**A**) Cartoon depicting experimental design. Transgenic mice (Tg) expressing human CDHR3 (hCDHR3), or WT mice were transduced with either human STING, or firefly luciferase (Fluc) via adeno-associated virus (AAV) by intranasal inoculation. On day 10 post-AAV transduction, mice were then intransally inoculated with RV-C15 or UV-inactivated RV-C15. Mice were then sacrificed and total lungs were collected at 12 and 24 hpi. (**B**) Body weights of the mice were tracked over the course the RV-C15 infection. Each dot represents the percent change in weight at 24hpi compared to the initial weight. (**C**) Health scores of the mice were tracked over the duration of the RV-C15 infection. The lower the score the healthier the mouse, such that a score of zero is a fully healthy mouse and a score of 5 is the highest score allowed prior to euthanasia. (**D**) qPCR detection of RV genome copy numbers at 12 and 24hpi. Each point represents mean genome copy numbers from n= 11-14 mice assayed across n= 3 independent experiments. Black shapes represent WT mice and red shapes represent hCDHR3 Tg mice. Triangles represent mice receiving AAV-Fluc and circles represent mice receiving AAV-STING. Empty shapes represent UV-inactivated RV-C15 conditions while filled in shapes represent mice receiving infectious RV-C15. Statistical analysis was performed using a Mann-Whitney U test (two-tailed; 0.95% confidence interval; *p<0.05). (**E**) Immunohistochemical detection of J2 (red) in RV-C15 infected paraffin-embedded mouse lung sections 24hpi. Nuclei (DAPI; blue). Scale bar =

20μm. (**F**) H&E staining of mouse lung slides. Scale bar = 20μm. (G) AB-PAS staining of mouse lung slides. Scale bar = 20μm.

As anticipated, there were no significant changes in either weight (**Figure 4.6B)** or health status (**Figure 4.6C**) between experimental groups within this 24 hr-time frame. We then extracted total RNA from the mouse lungs, and determined viral titers by quantifying genome copy numbers by qPCR (**Figure 4.6D, Supplemental Figure 4.8**). In alignment with a prior report [403], RV-C15 titers decreased between time points in wild type mice. In fact, we observed a loss in RV-C15 genome copies between 12 and 24hpi in all conditions except in mice expressing both hCDHR3 and hSTING, where the mean RV-C titer was elevated in 10 out 13 mice, and were found to be significantly higher than those in all control conditions at the 24-hr time point. Thus, only Tg1 mice transduced with hSTING were able to sustain RV-C replication. To further validate this finding, we probed fixed mouse lung sections from this study for dsRNA using standard immunohistochemical protocols (**Figure 4.6E, Supplemental Figure 4.9**). While the frequency of dsRNA-positive cells was low, we were able to identify the presence of replicating RV-C15 in mouse lungs from hCDHR3 transgenic mice that received AAV-hSTING at 24hpi, but not in any other mouse lung tissues.

4.3.8 RV-A1A infection of WT mice with the addition of human STING does not significantly boost viral replication.

Given the proviral impact of STING on both RV-A and RV-C *in vitro* [87], and our ability to garner RV-C15 infection of hCDHR3-expressing mice in the presence of hSTING, we next sought to determine if AAV-mediated expression of hSTING could enhance RV-A1A replication in WT mice. Unlike most minor-group RVs, RV-A1A can infect WT mice without any adaptive mutations [98]. Therefore, we utilized our AAV-mediated lung

delivery strategy as we had employed for RV-C, to assess whether the presence of hSTING could enhance viral replication. After intranasal inoculation of RV-A1A or UV-RV-A1A on Day 10 post-AAV transduction, we monitored the mice and collected lungs at 12, 24, and 96hpi for PCR-based quantification of genome copy number (**Supplemental Figure 4.10**). However, surprisingly, there was no significant difference in replication between PBS, AAV-Fluc and AAV-STING groups across all timepoints.

4.4 Discussion

RV is a leading cause of both upper and lower respiratory tract infection [21–24,32]. Furthermore, the heightened risk for development of asthma in children after infection by RV, and especially RV-C [24,338,339], highlights the importance of studying these pathogens. Differentiated 3D airway epithelial cultures provide a platform to interrogate viral replication requirements and innate host responses in physiological context [56,84,93,336]. However, they do not encompass the totality of an organism, including lacking the ability to exhibit global symptoms of virus-induced illness and any adaptive immune response. RV tropism is limited to higher primates, and outside of a recent example of zoonotic spillover into chimpanzees, no natural RV infections have been documented in other species [53]. Therefore, given the limited utility of *in vitro* models for pathogenesis studies, the restricted host range of RVs, and the potential value of an *in vivo* mouse model of RV infection, we sought to understand the natural barriers to infection of mice. Examples of RV adaptations to allow for infection of mice or mouse cells have been previously described for major- and minor-group RVs [79,97–99,101–104,108,404–408]. Notably, RV-C infection was recently reported in 8-12 week old female BALB/c mice and six-day-old C57BL/6J mice without any prior adaptation of virus or host [403,409]. While these data are challenging to explain in light our own results, there are differences

in inoculum dose, age, and animal sub-strain that could potentially contribute. It is also noteworthy that RV-C titers in these previously reported models progressively decline overtime. Furthermore, the lack of a UV control in some experiments and use of a “high inoculum” in these initial reports make it challenging to understand if the RNA detected and host responses reported are a reflection of active replication, or merely related to the input virus. Additional studies, ideally involving parallel inoculation of these RV-C mouse models alongside our model with the same virus stock would be useful to resolve these discrepancies.

Prior research into RV-C has primarily focused on CDHR3 which promotes viral entry into the airway epithelium, and has demonstrated that CDHR3 is expressed in ciliated cells across multiple tissues [399,400,410]. While we demonstrate a similar tissue expression profile for mCDHR3, including localization to the ciliated airway epithelium, a lack of homology at the amino acid level, including across EC1 and at residue 529, starkly contrasts the strong conservation between hCDHR3 and chimpanzee CDHR3, a species where natural RV-C infection has occurred [53].

In modeling the interaction of RV-C with the EC1 of CDHR3, we note nine differing residues which result in altered shape and charge at the RV-C - mCDHR3 EC1 interface. Among these differences, the N66R, N99K, and I100A substitutions are the most extreme, and would significantly alter the shape and charge distribution of this particular region. Additionally, substitutions of two residues that do not directly interact with RV-C, G29S and S65P, are relatively severe and may have an impact on the structure of neighboring residues. While the I23L and L116V substitutions are relatively conserved, they may also have an impact on the conformation of the RV-C15 - EC1 interface. The L24H substitution is notable; however, Sun et al. showed that a similarly-extreme L24D mutation had minimal effect on the ability of hCDHR3 EC1 to either bind RV-C15 or support infection

[411]. Therefore, it is possible that the L24H substitution may not negatively impact the RV-C15 - EC1 interaction. In sum, when taken together, the totality of substitutions at and surrounding the predicted RV-C15 - mCDHR3 EC1 interface are predicted to destabilize any RV-C - mCDHR3 interactions.

In humans, a non-synonymous single nucleotide polymorphism (SNP; rs6967330[A]) in CDHR3 results in an amino acid change from cysteine to tyrosine at position 529 [96] that is thought to enhance protein stability. The mutation is a known risk-allele for childhood development of asthma [96], and correlates with increased CDHR3 expression at the cell surface [31,96]. Further, SNP rs6967330 is associated with increased RV-C binding in HeLa cells [412,413], as well as heightened risk of respiratory tract illness with RV-C, but not other viruses [414]. Chimpanzees similarly harbor a tyrosine at this position, correlating with their natural susceptibility to RV-C infection. Mice, however, are one of only a few mammalian lineages to express neither cysteine, nor tyrosine, but rather a histidine residue. The impact of CDHR3-H529 on surface expression and stability has yet to be experimentally detailed. Given CDHR3 surface expression has been hypothesized to result from the lack of an extraneous cysteine (C529) disrupting the disulfide bridge between C592 and C566, it is probable that CDHR3-H529 is surface stable.

In probing the later stages of the viral life cycle, after entry and uncoating, we found that mouse cells support RV-C15 replication and the production of infectious progeny. These data closely mirror prior work that shows major-group, but not minor-group, RVs were capable of replicating in mouse cells without viral adaptation [102]. Notably, hSTING, but not mSTING was shown to support RV replication in human cells *in vitro* [87]. These results are not unexpected given that mSTING is only 69% conserved on the amino acid level compared to hSTING. Further, two mutations in viral protein 2C were previously

sufficient to exchange the requirement for hSTING with mSTING, and thereby confer mouse-adaptation of RV-A16 [87,99]. Together this suggests an interaction of 2C with STING, yet co-immunoprecipitation studies have thus far failed to detect any direct interaction between hSTING and RV proteins [85]. Our work demonstrates that expression of hSTING in mouse cells enhances RV-C15 and RV-A1A replication. While our western blot data indicates HA-tagged hSTING is undetectable in LET1-hSTING in the absence of doxycycline induction, we did note an increased percentage of dsRNA positive cells and increased dsRNA intensity within this cell population compared to unmodified LET1 cells. These data suggest that either the inducible hSTING construct is leaky, or that through the process of selecting cells containing the hSTING construct we simultaneously isolated a sub-population of LET1 cells that are naturally more permissive for RV replication. Nonetheless, induction of hSTING further increased levels of intracellular RV replication. The inability to correlate enhanced intracellular replication with significantly higher extracellular titers was surprising. Still, the mechanism underlying STING's proviral function remains unknown, and these data further emphasize the need for additional research to ascertain the role of STING during RV replication. Nonetheless, these data together indicate that once RV-C15 genomes successfully reach the cytoplasm, the entirety of the RV-C lifecycle can be completed, and that STING enhances the formation of double-stranded RNA during replication. Ultimately, these data provided a strong indication that an *in vivo* RV-C infection in a mouse was possible, should the proper entry conditions be achieved.

Towards our goal of generating a robust mouse model for RV-C, we initially attempted to develop a CDHR3 KO mouse line such that hCDHR3 could fully replace all endogenous mCDHR3. Our discovery that KO of mCDHR3 in mice is embryonically lethal was unanticipated, as there is very little data regarding CDHR3's canonical functionality

or contribution to adverse phenotypes. In late 2019, CRISPR-Cas9 technology was used to knockout CDHR3 in primary human airway epithelial cells, yet here, CDHR3 KO cells proliferated normally, had increased basal cell marker gene expression, and most importantly complete genetic depletion of this gene did not negatively impact the development of ciliated cells [415].

Using mice expressing hCDHR3 in addition to the endogenous mCDHR3, we were able to detect a significant increase in RV-C replication and detect dsRNA-positive epithelial cells at 24hpi, but only in mice that also received AAV6.2 expressing hSTING. This finding was noteworthy as it represents the first recorded example of RV-C infection in a non-primate host, where mean viral titers increased above that of the initial inoculum. Interestingly, we did not detect similarly increased viral titers when these mice were assayed at earlier, 12hpi, or later 96hpi timepoints. These data suggest that RV-C15 infection in mice – even in the presence of hCDHR3 and hSTING – is transient in nature, with RV-C15 only replicating for a short duration prior to clearance by innate defense mechanisms. These data are reflected *in vitro*, where hCDHR3 alone was not sufficient to detect active replication of RV-C15 in LET1 cells (**Supplemental Figure 4.11**). Indeed, it is possible that other host factors must be supplied or humanized, in order to achieve a more robust infection. Alternatively, it is possible that RV-C15 is not able to adequately control the murine innate immune response. In human cells, RV prevents global host translation by 2A protease-mediated cleavage of eIF4G [416], while antiviral innate immune sensors of RV infections (e.g., RIG-I, MDA-5 and MAVS) are also targets of viral protease activity [417–420]. Notably, there are numerous examples of positive sense RNA viruses (e.g., alphaviruses [421,422]; flaviviruses [423,424]; coronaviruses [425–427]) that fail to antagonize host immunity in mice and are thereby restricted for replication in this host. Further, we specifically note that the MAVS cleavage site targeted by RV-C is not

conserved in mice (**Supplemental Figure 12**) [420]. Therefore, we hypothesize that these transgenic mice depleted for innate immune sensors or downstream effector molecules would result in prolonged RV-C15 infection.

Interestingly, our findings with RV-C15 did not extend to RV-A1A, as we did not observe any enhanced viral titers in the presence of hSTING. Since RV-A1A requires hSTING for replication *in vitro* [87], and our infection conditions match what had been performed previously for RV-A1A infection of WT mice [98], more efforts are needed to understand the function of hSTING during RV infection to better understand why hSTING was only able to boost RV-C15 but not for RV-A1A genome replication *in vivo*. It is possible, that since RV-A1A was able to replicate efficiently in mice without adaptations, that this virus can already utilize mSTING and therefore we observe no proviral effects upon expression of hSTING. However, this conflicts with our *in vitro* data which suggests that LET1 cells express mSTING, and RV-A1A replication is significantly increased upon overexpression of hSTING. Thus, perhaps, to observe the proviral phenotype for RV-A1A *in vivo*, we need to increase the expression of hSTING in the mouse airway.

Ultimately, this study characterizes the role of hSTING during RV-C15 infection in mouse cells *in vitro* and *in vivo*. Our data represent the initial blueprint toward generating a mouse model of RV-C infection, utilizing transgenic mice expressing hCDHR3 and AAV-mediated delivery of hSTING. We speculate that hSTING expression enables faster replication that thus allows RV-C to temporarily overcome the murine immune system, or alternatively, that hSTING expression impedes normal immune signaling in the mouse – thereby explaining the observed significant increase in RV-C15 titer 24 hpi. While these mice likely do not encompass the totality of factors and conditions needed, they suggest that a RV-C15 mouse model is ultimately achievable.

4.5 Material and Methods

4.5.1 Plasmids

RV-A1A, RV-A16 and RV-C15 cDNAs were previously described [84], and kindly provided by Drs. Anne Palmenberg and James Gern, respectively. The replication-defective (GAA) mutant was generated by overlapping PCR insertion around BsrGI-AflII restriction enzymes from the WT RV-C15 plasmid. The following four primers were used: BsrGI reverse: 5'-CTCCTTACTCATTGTTGTACAGGC-3', GAA forward: 5'-GCATATGGTGCTGCTGTAGTAGTGTC-3', GAA reverse: 5'-GACACGACGACATCATCACCATATGC-3', AflII forward: 5'-GCAGCCTTAAGCAATGGAGAC-3'. Final plasmid was sequenced to confirm GDD to GAA mutagenesis.

The tetracycline inducible hSTING construct was previously described [87], and kindly provided by Dr. Stanley Lemon.

4.5.2 Tissue Culture

All HEK-293T cells (CRL-3216, ATTC), HeLa-H1 (CRL-1958, ATCC), HeLa-E8 [15] (Gern Lab), LET1 cells (NR-42941, BEI Resources), LET1-hSTING, LET1-hCDHR3 cells were grown in DMEM with 10% heat-inactivated fetal bovine serum (FBS), and maintained at 37^{o}C with 5% CO_2. LET1-hSTING media was further supplemented with 0.8ug/mL puromycin. To induce hSTING expression in LET1-hSTING cells, 10ug/mL doxycycline was added three days prior to transfection.

4.5.3 CRISPR/Cas9-mediated knockout of STING in HAE

Single guide RNAs (sgRNA) targeting STING or no known target (NTC) and flanked by restriction sites for cloning into the pLentiCRISPRv2 backbone [390] with eGFP

replacing puromycin selection were as follows: sgRNA1- 5'-CACCGCATATTACATCGGATATCTG-3' and 5'-AAACCAGATATCCGATGTAATATGC-3'; sgRNA2- 5'-CACCGACTCTTCTGCCG GACACTTG-3' and 5'-AAACCAAGTGTCCGGCAGAAGAGTC-3'; NTC- 5'-CACCGGCA CTACCAGAGCTAACTCA-3' and 5'-AAACTGAGTTAGCTCTGGTAGTGCC-3'. Lentiviral stocks were generated by co-transfection of 1µg pLentiCRISPRv2 (Addgene plasmid #52961 donated by Dr. Feng Zhang) [390], 0.2µg pCMV-VSV G (Addgene plasmid #8454 donated by Dr. Bob Weinberg) [391]), and 0.7µg psPAX2 (Addgene plasmid #12260 donated by Dr. Didier Trono) into HEK-293T cells with jetPRIME reagent (#114-017, Polyplus). Lentivirus-laden supernatant was collected and replaced at 24hour intervals up to 72 hours, pooled, and filtered to remove viable cells and debris. For target cell transduction, lentivirus-containing supernatants were applied to BCi-NS1.1 cells (kindly provided by Drs. Matthew Walters and Ronald Crystal [366]), maintained as HAE at 40–60% confluence with a final concentration of 20mM HEPES (#15630080, Thermo Scientific) and 4µg/mL Polybrene (#TR1003G, Fisher Scientific). Cells were then centrifuged (1,000 x g for one hour at 37^{o}C) and incubated at 37^{o}C with 5% CO2 for 6hr. The inoculum was removed and replaced with fresh Pneumacult-Ex Plus media (#05040, StemCell Technologies). At 60–80% confluence, eGFP-positive cells were enriched by fluorescence-activated cell sorting on a BD FACSAria-II Cell Sorter (BD Bioscience). These sorted BCi-NS1.1 cells were then expanded, seeded at 3.3x10^{4} cells/well on 6.5mm rat-tail collagen type I-coated transwell membranes, and cultured at air-liquid interface. HAE cultures were grown in Pneumacult-Ex Plus basal medium, or Pneumacult-ALI medium (#05001, StemCell Technologies) with provision of an air-liquid interface for approximately 6 weeks to form differentiated, polarized cultures that resemble *in vivo* pseudostratified mucociliary epithelium.

4.5.4 *In vitro* transcription, rhinovirus rescue and amplification

RV-A1A was linearized using the XhoI restriction enzyme (#R0146S, New England Biolabs), RV-A16 was linearized using the SacI restriction enzyme (#R0156S, New England Biolabs; Ipswich, MA), and both RV-C15 and RV-C15-GAA were linearized using ClaI (#R0197S, New England Biolabs). The linear plasmid was purified using either Monarch DNA Cleanup Kit (#T1030S, New England Biolabs) or QiaQuick Gel Extraction Kit (#28704, Qiagen) using the MinElute columns (#28004, Qiagen). *In vitro*-transcribed RV RNAs were synthesized using the MEGAscript T7 Kit (#AM1337, Invitrogen) following the manufacturer's protocol. Infectious virus stocks were then produced in HeLa-H1 cells by transfection of *in vitro*-transcribed RNA. For RV-A1A and RV-A16, $7.0x10^5$ HeLa-H1 cells were seeded per well into a 24-well plate, while for RV-C15, HeLa-H1 were grown in a T75 until 90% confluence before transfecting using JetPrime (Polyplus), following the manufacturer's protocol. For RV-C15 rescue, double the amount of RNA and JetPrime reagent were used. Four hours post-transfection the media containing the transfection mix was removed and replenished with McCoy's media containing 2% FBS, 1% penicillin-streptomycin, 1% L-glutamine and 30 mM $MgCl_2$ and incubated at 34^{o}C. RV-C15 was collected 24 hpt, while RV-A1A and RV-A16 were collected after observing robust cell death. For amplification, RV-A1A and RV-A16 supernatants were then transferred to a T75 containing confluent HeLa-H1 monolayers. RV-A1A and RV-A16 supernatants were collected upon observing cytopathic effects, typically 48-72 hpi, and RV-C15 supernatants were collected at 24hpt. These supernatants were then clarified by centrifugation at 1,000 x g for 10min. RV-A1A and RV-A16 supernatants were titered by plaque assay, and the genome copy number of RV-C15 stocks were quantified by qPCR.

4.5.5 Immortalized Cell Transfection and Infection

LET1, LET1-hSTING uninduced, LET1-hSTING doxycycline induced (all $4.0x10^4$/well), and HeLa-H1 cells ($6.5x10^4$/well) were seeded in an 8-well cell culture slide (#CCS-8, MatTek Corporation) in DMEM (#25-500, Genesee Scientific) with 10% FBS and incubated overnight at 37°C and 5% CO_2. To assess viral replication, 500ng of viral genomic RNA was transfected alongside 1uL of JetPrime reagent using the JetPrime protocol. 4hpt, media was removed and replaced with McCoy 5a Media (#16000082, Gibco Laboratories) supplemented with 2% FBS, 1% Pen/Strep (#15140-122, Gibco Laboratories), and 30mM Mg^{2+} and returned to a 34°C incubator with 5% CO_2. 24hpt supernatants were collected and filtered with a 0.45μm filter by centrifugation. All LET1 and LET1-hSTING cells were then fixed with paraformaldehyde and HeLa cells were fixed with ice cold methanol. For reinfection assays, filtered supernatants were directly added to $7.5x10^4$ HeLa-E8 cells seeded the day prior in an 8-well cell culture slide and incubated for 24 hours in at 37°C.

4.5.6 Plaque Assay

RV-A1A and RV-A16 stocks were titrated by plaque assay method using H1 HeLa cells plated in 24-well dishes and a published protocol with modifications [392]. Briefly, 90% confluent H1 HeLa monolayers were inoculated with ten-fold serial dilutions of the viral stock in McCoy's medium with 2% FBS and 30mM $MgCl_2$. After a 1hr incubation at room temperature, the inoculum was exchanged for a semi-solid overlay composed of 0.6% of bacteriological agar (#A5306; Sigma-Aldrich) in DMEM-F12 (#12500062; Gibco), supplemented with 1% FBS, 1% penicillin/streptomycin, 1% L-glutamine (#25030081; Gibco), and 30mM $MgCl_2$. The plate was incubated at 34°C for 72 hours and the cells were fixed with 4% formaldehyde (#47608; Sigma-Aldrich; diluted in a 0.15 M saline solution).

The fixing solution was removed together with the overlay after a 24-hour incubation at room-temperature and plaques visualized by staining the monolayer with 0.1% Crystal Violet (#C0775; Sigma-Aldrich) diluted in a 20% ethanol solution.

4.5.7 RV genome quantification by qPCR

Total RNA was extracted from cells using an RNeasy Mini Kit (#74104; Qiagen). To quantify viable RV genomes from an RV stock or experimental supernatant, 100µl sample was first treated with 1u RNase A (#EN053; Thermo) and 1u DNase I (#18047019; Invitrogen–Thermo Scientific) for 1hr at 37˚C and then inactivated at 70˚C for 15min. Viral RNA was then extracted using a QIAamp Viral RNA Mini Kit (#52904; Qiagen). For RNA extraction from whole tissues, tissues were homogenized using a TissueLyser (Qiagen) using 5mm stainless steel beads (#69989; Qiagen) for 15min at 50 oscillations/sec. Total RNA was then extracted from tissue using an RNeasy Universal Kit (#73404; Qiagen).

To reverse transcribe extracted RNA into cDNA, 100 ng of total cellular RNA was used in a reverse transcription reaction (High Capacity cDNA Reverse Transcriptase Kit; #4368814; Applied Biosystems), with random hexamer primers, as per the manufacturer's protocol. For cDNA synthesis after viral RNA extraction from supernatants, a fixed 10uL volume was used.

qPCR was done using 3µl of cDNA, 10pM HRVTF63 forward (5'–ACMGTGTYCTAGCCTGCGTGGC–3') and HRVTR reverse (5'–GAAACACGGACAC CCAAAGT GT–3') primers, 10pM HRVTF probe (5'–FAM/TCCTCCGGCCCCTGAAT/ BHQ1–3'), and LuminoCT Taqman Master Mix (#L6669; Sigma-Aldrich) according to the manufacturer's protocol. For absolute quantification, a standard curve was delineated using cDNA generated from ten-fold serial dilutions of *in vitro*-transcribed pRV-C15, pRV-A1A. This standard curve of RNA was used to calculate an exponential regression line

based on the corresponding standard curve when plotted on a semi-log scale. This formula could then be used to input the cycle threshold (CT) value of interest to calculate the genome copy number from a particular well of a qPCR run.

A 50µL pre-amplification supermix (#1725160; Bio-Rad) reaction was performed prior to running a Taqman Probe qPCR reaction to amplify RV signal from mouse lung tissue. Following manufacturer's protocol, 2.5µL of forward and reverse primers at 100µM were diluted with 495 µL of water. Then 25µL of supermix was combined with 5.0µL of the diluted forward and reverse primer mixture, 19µL of water and 1µL of the specific cDNA to reach a 50µL total volume reaction.

4.5.8 Host gene expression quantification by qPCR

Total RNA was extracted and cDNA was prepared as detailed above. Relative gene expression was quantified using the two-step QuantiFast SYBR Green Kit (#204054; Qiagen) using a Roche LC480 thermocycler (Roche Life Sciences) according to the manufacturer's protocol. Primers were as follows: mCDHR3: 5'-AGGACCGAAAGCATTCGATTT-3' and 5'-AGGCTCGTTCACATCTGTCAC-3'; mGAPDH (endogenous control): 5'-AGGTCGGTGTGAACGGATTTG-3' and 5'-GGGGTCGTTGATGGCAACA-3'. For transduced cell line validation, total RNA was extracted using the RNeasy Kit (#74104, Qiagen) prior to qRT-PCR analysis, as above. Human CDHR3 primers used were: 5'-TTACCTGCTACAGGCAATGTG-3' and 5'-CCTGACAGCCAATTCACCCTAA-3'.

4.5.9 SDS-PAGE and Western Blot

Cell lysates were collected in RIPA buffer containing protease inhibitors (#N653-500mL, VWR) and total protein was quantified using a Pierce BCA assay (#23227,

Thermo Fisher Scientific; Waltham, MA). Protein lysates (25µg) were denatured by heating (98ºC, 2min) and separated on a Novex™ WedgeWell 4–20% Tris-Glycine gel (#XP04202BOX; Invitrogen-Thermo) under reducing conditions. Proteins were transferred to PVDF membranes (GE Healthcare Life Sciences; Marlborough, MA or using eBlot L1 (GenScript).

Membranes were blocked in 5% milk diluted in tris-buffered saline with 0.1% Tween-20 (TBS-T; #BP337-100, Fisher Scientific) for 1 hour at room temperature with rocking. Human and murine CDHR3 proteins were then detected using primary antibodies (#HPA011218, 1:2000; Sigma-Aldrich; #orb182906, 1:1000; Biorbyt) diluted in blocking buffer. STING was detected endogenously (66680-1-Ig, 1:1000; Proteintech) or by HA-tag (26183 1:1000, Invitrogen). Following incubation overnight at 4ºC membranes were washed 3X for 15 minutes each with TBS-T before incubation with HRP-conjugated donkey anti-Rabbit IgG (1:10,000; #A16035, Invitrogen). Anti-β-Actin-HRP conjugated antibody (#A3854, Sigma-Aldrich) was diluted 1:35000 in 5% TBS-T and incubated at room temperature for one hour. Western blots were visualized with SuperSignal West dura (#34075, Thermo Scientific), or femto (#35095, Thermo Scientific) reagent and imaged on either FujiFilm LAS-3000 or iBright FL15000 imagers.

4.5.10 Immunofluorescence

Following fixation at 24hpt in either 4% PFA (LET1 cells) or ice cold methanol (HeLa cells), as above, cells were washed 2X with PBS and 3X with PBS with 1 mM $CaCl_2$ and 1 mM $MgCl_2$ (PBS++), then permeabilized with 0.2% Triton X-100 / PBS++ (Thermo Fisher Scientific) in for 15 minutes. Once permeabilized, cells were blocked in 3% BSA /PBS++ for 1 hour in a humidified chamber at room temperature. The J2 antibody (#10010200, Scicons) was diluted in 1% BSA / PBS++ 1:1000. Following overnight

incubation in a humidified chamber at 4°C, cells were washed with PBS++ prior to secondary antibody staining. Secondary antibody Goat anti-mouse IgG2a AlexaFluor555 (#A-21137, Thermo Scientific) was applied for 1 hour at room temperature in a humidified chamber. Cells were washed with PBS++ and incubated with Hoescht (1:1000, 10 min; #33342, Thermo Scientific) and mounted using VectaShield (#H-1000, Vector Laboratories) as done for immunohistochemistry, detailed below.

4.5.11 CellProfiler

We used CellProfiler [402] to quantify percentage of infected LET1 cells, as well as intensity within infected cells. Individual channels of nuclei, J2, and long exposure 488 auto-fluorescent images were loaded into the CellProfiler pipeline. These images were taken at 63X magnification from four predetermined locations within the transfected culture. CellProfiler defined the cell borders of the cells using the auto-fluorescent signal. Next, nuclei were isolated by CellProfiler and were superimposed on the defined cell boundaries. Only those cells which contained nuclei were deemed proper cells and subsequently analyzed. Next, J2 signal was isolated to individual objects or units of similarly intense regions of signal, and overlaid onto proper nucleated cells. Integrated J2 intensity within a cell was calculated as the summation of all J2 object intensities. Cells were scored as infected when the integrated J2 intensity within a cell was over 100.

4.5.12 In situ hybridization

24 hpt, cells were fixed with 4% paraformaldehyde for 15 minutes. Following fixation, cells were washed with PBS and quenched with 25mM NH_4Cl (A9434-500G Sigma Aldrich) for 10 minutes. Slides were washed 3X with PBS before permeabilization with 0.25% Triton X-100 in PBS. Slides were incubated with prehybridization mix containing 3% BSA and 4X sodium citrate buffer (#C8532-100g, Thermo Scientific) for 20

minutes at 55ºC. ISH Probe, 5'-DigN/GGA+YGG+RACC+RACTACTTTGG+RTGTCC-3'DigN RV or β-Actin, was diluted to 2.5nM in 1mL of pre-warmed hybridization buffer of 10% dextran sulfate in 4X sodium citrate buffer. ISH probes were hybridized at 55ºC for 1 hour. A series of washes using buffers pre-warmed to 55ºC was performed on a rocker: 3 washes with 4X sodium citrate buffer with 0.1% Tween-20 for 5 minutes each, 2 washes with 2X sodium citrate buffer for 5 minutes each, 1 wash with 1X sodium citrate buffer for 5 minutes. Lastly, a room temperature wash with diethyl pyrocarbonate (DEPC; #D5758, Sigma-Aldrich) PBS was performed. Endogenous peroxides were quenched with 30% hydrogen peroxide (#216763, Sigma-Aldrich) for 20 minutes in a light protected environment. Slides were washed with DEPC PBS for 5 minutes before blocking with 4% BSA, 3% donkey serum (#017-000-121, Jackson Laboratories), 3% goat serum (#005-000-121, Jackson Laboratories), 0.1% Triton X-100 in DEPC PBS for 30 minutes. Goat anti-digoxigenin antibody (#MB-7000, Vector Laboratories) was diluted 1:500 in a dilution buffer of 4% BSA. 0.1% Triton X-100 in DEPC PBS and applied to the slides overnight at 4ºC. Slides were washed twice with DEPC PBS with 0.1% Tween-20 (DEPC PBS-T) for 10 minutes each and twice again with DEPC PBS-T for 5 minutes each. Rabbit anti-goat biotinylated secondary antibody (#BA-1000, Vector Laboratories) was diluted 1:500 in dilution buffer and incubated at room temperature for 30 minutes. Slides were again washed 4X with DEPC PBS for 5 minutes on a rocker. Signal was amplified using Streptavidin-conjugated horseradish peroxidase (#RABHRP3, Sigma-Aldrich) diluted 1:300 in dilution buffer for 30 minutes. Slides were washed 3X with DEPC PBS for 5 minutes each on a rocker. Color was revealed using NovaRed Substrate Kit (#SK-4800, Vector Laboratories) for 5 minutes in a light protected environment. The color reaction was stopped by washing twice with DEPC PBS for 5 minutes. Slides were washed 6X for 3 minutes each with DEPC H_2O. To prepare for imaging, slides were dehydrated using the following series of washes: 95% ethanol with 1% acetic acid (#A38-212, Fisher Scientific),

95% ethanol, 100% ethanol, 100% ethanol, 50% ethanol with 50% xylenes (#X3P-1GAL, Fisher Scientific), 100% xylenes, 100% xylenes and a final 100% xylene wash for 5 minutes. VectaShield and coverslip addition were performed in the same manner as was done for IHC.

4.5.13 Immunohistochemistry

Paraffin-embedded, BALB/c mouse lung tissue sections (Zyagen; San Diego, CA) or C57Bl/6 (Experimental Pathology Research Laboratory at New York University) on glass slides were used in immunohistochemistry assays to detect mCDHR3. Deparaffinization was performed using the following series of washes: 2X 100% xylene for 5 minutes each, 2X 100% ethanol for 3 minutes each, 2X 90% ethanol for 3 minutes each, 1X 70% ethanol for 3 minutes and 1X H_2O for 10 minutes. For dsRNA detection, prior to the blocking step, heat-induced epitope retrieval was performed by heating the tissue-containing slides in sodium citrate buffer (10mM sodium citrate, 0.05% Tween-20 in dH_2O) at 95^oC for 15min. Slides were then incubated with 3% bovine serum albumin in PBS with 1mM $CaCl_2$ and 1mM $MgCl_2$ (PBS++) for 1 hour at room temperature in a humidified chamber to prevent nonspecific binding. For colorimetric immunohistochemical detection, slides were incubated in hydrogen peroxide solution for 15min prior to blocking. Blocking solution was removed and antibodies were freshly diluted in 1% BSA as follows: rabbit anti-mouse CDHR3 (; #orb182906, Biorbyt), 1:3200; isotype control IgG (#GTX35009, GeneTex), 1:32000; mouse anti-acetylated alpha tubulin (#Ab24610, Abcam), 1:2000. J2 (#100010200, Scicons) or IgG2a isotype control was diluted 1:500 in 1% BSA. Antibodies were added to the lung tissue sections and incubated at room temperature in a humidified chamber overnight. The slides were then washed 3X for 5 minutes with PBS++ prior to the addition of secondary antibodies, AlexaFluor647 anti-rabbit IgG and AlexaFluor555 anti-mouse IgG diluted 1:500 in 1% BSA, for 1 hour at room

temperature in a humidified chamber. For dsRNA detection, AlexaFluor555 anti-mouse IgG2a was diluted 1:200 in 1% BSA. Slides were washed once for 5 minutes with PBS++ before DAPI (#62248, Thermo Scientific) diluted to final concentration of 1:1000, or Hoescht 1:1000 was added to the slides for 10 minutes. Slides were washed two additional times with PBS++ and tissue sections were mounted with VectaShield mounting media prior to imaging on an Axio Observer 3 inverted fluorescence microscope (Zeiss) equipped with an AxioCam 503 mono camera and Zeiss Zen software for image acquisition and processing. For dsRNA staining, a VectaShield containing DAPI (#H-1200, Vector Labs) was used and therefore no additional nuclear staining was required. For colorimetric staining, anti-rabbit-HRP 1:500 used and then colorimetric development was performed using the Pierce (3,3'-Diaminobenzene) DAB substrate kit per manufacturer's guidelines (#64238, Abcam).

4.5.14 Lentivirus Production

6-well plates were coated with Poly-L-lysine (3P8920, Sigma-Aldrich), washed with cell-grade H_2O (#A1287301, Gibco Laboratories), and allowed to dry prior to seeding HEK-293T cells ($4x10^5$ cells/well). Cells were grown overnight at 37°C / 5% CO_2 in Dulbecco's Modified Eagle Medium (DMEM; #25-500, Genesee Scientific) containing 10% FBS (GenClone) to achieve 80% confluency the next day. Cells were then washed with PBS and transfected with psPAX2 (a gift from Dr. Didier Trono (Addgene plasmid #12260), pCMV-VSV-G (a gift from Dr. Bob Weinberg (Addgene plasmid #8454) and human CDHR3 expression plasmids (a gift from Dr. James Gern) using JetPrime (Polyplus) according to the manufacturer's protocol. 6 hours post-transfection (hpt), media was replaced with DMEM / 3% FBS and lentivirus-containing supernatant was collected at 48 and 72 hpt. Harvested supernatants were pooled, clarified by centrifugation (2000 *x* g, 10 min, 4°C) and filtered (0.2 micron). HEPES (#15630-080, Gibco Laboratories) and

polybrene (#TR1003G, Fisher Scientific) were added to achieve final concentrations of 20mM and 4µg/mL, respectively, and lentiviral stocks were stored at -80°C prior to use.

4.5.15 Generation of LET1-expressing mouse CDHR3

LET1 cells were seeded into 12 well plates at $7x10^4$ cells/well and incubated overnight at 37°C. The next day, cells were transduced with 400µL of hCDHR3 lentivirus stock in a final volume of 2ml DMEM / 10% FBS containing 20mM HEPES and 4µg/mL polybrene via centrifugation (1000 *x* g) for 1 hr at 37°C). Following spinoculation, cells were returned to the incubator for 6-18hrs at which point the media was replaced with 1mL DMEM / 2% FBS until the transduced phenotype was observed and / or cells were required to be split. hCDHR3-containing cells were selected using 2.5ug/mL Blasticidin S HCl.

4.5.16 Homology modeling

A structural homology model of the mouse CDHR3 EC1 domain was generated using the SWISS-MODEL web server [428], with the human CDHR3 EC1 domain structure used as a template [429].

4.5.17 Adeno-associated Virus

Adeno-associated viruses expressing human STING (AAV-hSTING) and firefly luciferase (AAV-Fluc) were purchased from VectorBuilder Incorportated.

4.5.18 Generation of Transgenic Mice

A bacterial artificial chromosome (BAC) containing CDHR3 with point mutation C529Y (*rs6967330*, TGT->TAT), CTD-2262G10 was obtained from human RPCI-11 BAC library. The appropriate modification was introduced into the BAC using bacterial recombination procedures. The C529Y variant was inserted seamlessly using annealed

oligos and negative selection via an rpsL-kanaR cassette. After purification of the modified BAC, its quality was checked using pulsed-field gel electrophoresis. Important regions of the gene of interest (such as exons) as well as the introduced modification were confirmed by sequencing. This strategy allows the generation of a transgenic mouse line expressing the human CDHR3 gene carrying the C529Y variant under the control of the human CDHR3 promoter. CDHR3 exon 1 contains the translation initiation codon. The engineered CTD-2262G10 BAC can then be used for pronuclear injection (PNI) into fertilized C57BL/6NTac oocytes.

Generation of hCDHR3 transgenic founder mice were made by PNI with random genome integration. After administration of hormones, superovulated C57Bl/6NTac females were mated with C57Bl/6NTac males. One cell stage embryos were isolated from the oviducts at 0.5 days post-conception (dpc). For microinjection, the one cell stage embryos were placed in a drop of hCZB medium under mineral oil. A microinjection pipette with an approximate internal diameter of 0.5um at the tip was used to inject the DNA solution into each embryo. After recovery, 25-35 injected one cell stage embryos were transferred to one of the ovidcuts of 0.5 dpc pseudopregnant NMRI females.

The integration of the transgene was evaluated by PCR assays using oligo sequences specific for the transgene. The primer sets (**Table 4**) were used to confirm presence of the transgene at the 5'-end, human exon 1, human exon 6, human exon 12, 3'-UTR and 3'-end. Each reaction contained 5µL 0X PCR Buffer (Invitrogen), 2µL $MgCl_2$ (50mM), 1µL dNTPs (10mM), 1µL forward primer (5µM), 1µL reverse primer (5uM), 1µL control forward primer (5µM), 1uL control reverse primer (5uM), 0.2µL Taq Polymerase (5 U/µL, Invitrogen), 38.50µL H_2O and 2µL DNA. PCR was performed using the following steps: 1) 95^{o}C for 5 min, 2) 35 cycles of 95^{o}C for 30 s, 60 ^{o}C for 30 s and 72^{o}C for 1min, 3) 72^{o}C for 10min.

Table 4.4: Primers used in determining presence of hCDHR3 transgene

Primer Name	Sequence	Expected Fragment Size (base pairs)
Control FWD	5'-GAGACTCTGGCTACTCATCC-3'	585
Control REV	5'-CCTTCAGCAAGAGCTGGGGAC-3'	
5'-end FWD	5'-CCTTGTTCATGCAGCACTTG-3'	307
5'-end REV	5'-CCCAAACCCGACAGTTGTC-3'	
Exon 1 FWD	5'-TACCGCCAAAGCCTCTGT-3'	306
Exon 1 REV	5'-CTCAATTGAACAAGCCTCCC-3'	
Exon 12 FWD	5'-CCATGGCAGTTAGGACATCTG-3'	369
Exon 12 REV	5'-AGAGACCCTAAGTCAACCAGTTG-3'	
3'-UTR FWD	5'-CTGGGGTTCTCATTGTTTGC-3'	310
3'-UTR REV	5'-CAGCTGGAACTAGAACTCTGTGG-3'	
3'-end FWD	5'-GCGCCTCACTTTGTCACC-3'	322
3'-end REV	5'-GGCCTAGAATTCTCTGTGGG-3'	

A total of 6 founder mice were produced but only 4 founder animals were fully validated to express the full length transgene. 1 additional founder was found to be sterile, yielding 3 hCDHR3 transgenic founder lines to evaluate. Founder mice were then bred with C57Bl/6NTac mice for one generation to achieve offspring heterozygous for hCDHR3 transgene expression. Mice were then interbred and mice homozygous for the transgene were identified by Taqman qPCR (**Table 4.5**) after one generation. All transgenic mice were sequenced and confirmed by Transnetyx, Inc.

Table 4.5: Primers used in confirming transgene homozygosity

Primer Name	Sequence
CDHR3-Z.28721-FWD	5'-GATGATGACAGTGAGGCACCAA-3'
CDHR3-Z.28721-REV	5'-CGCTCCCCACTCCAGATG-3'
CDHR3-Z.28721-Probe	5'-6FAM-CAACAGATTCAACTTCAC-MGBNFQ-3'
BETA-ACTIN33-FWD	5'-CATGCAAGGAGTGCAAGAACA-3'

BETA-ACTIN95R-REV	5'-GGAGCCCCTGTCCTGAGACT-3'
VIC-BETA-ACTINZ2-Probe	5'-VIC-AGCTAAGTTCAGTGTGCTGG-MGBNFQ-3'

4.5.19 Euthanasia

All mice were euthanized with a fill rate of 4.4 L/min of CO_2 until the animal(s) had completely stopped breathing, approximately 10 min. Mice were euthanized in their home cages, where possible, but if not were transferred to clean cages immediately prior.

4.5.20 Tissue Collection for RNA and Protein

During necropsy, the spleen, upper portion of the gastrointestinal tract, kidney, liver, lungs, trachea and brain were collected from all animals. For females, the ovary was collected while for males the epididymis was additionally harvested for subsequent assessment of their total mCDHR3 and hCDHR3 expression levels. Additionally, for *in vivo* imaging system (IVIS) measurements, nasal turbinates were collected. Only lungs were harvested as part of any infection studies. Each collected tissue was placed in 500µL of RNAlater and stored at 4^{o}C. During infection studies involving AAV treatments, a lung lobe from a single animal per condition per sex per time point was not collected for RNA processing but instead flash-frozen using a mixture of dry ice and 100% ethanol for protein analysis to confirm transgene expression.

4.5.21 Lung Perfusion

During necropsy and prior using an IVIS, an 18-gauge needle was inserted into the right ventricle and flushed with 20mL of PBS to flush blood from the lungs and aid in imaging using an IVIS.

4.5.22 IVIS

To prepare tissues for the IVIS, lungs were prepared in a similar manner as described above for formalin fixation, but instead of filling with formalin, lungs are filled with 750µL of 30 mg/mL luciferin (#122799, PerkinElmer) and set in a well of a black 6-well plate (#07-202-461, Corning). Additionally, during necropsy, nasal turbinates were collected and placed in a separate black 6-well plate. Both lungs and nasal turbinates were soaked in 2 mL of 30 mg/mL luciferin for 15min prior to measuring on the IVIS. Quantification of luminescence signal was performed using Living Image 4.7.4.

4.5.23 Lung Inflation

In order to fix the mouse lungs for histological assays, the mouse was placed in a supine position and held in place using adhesive tape over its nose. The chest and throat area was sprayed with isopropanol and a vertical incision was made parallel to the airway. Using forceps, the salivary glands and hyoid muscles on either side of the airway were retracted exposing the underlying trachea. A piece of 3-0 silk suture, approximately 15 cm in length was folded in half and pulled underneath the trachea. The suture was then cut dividing it into two 7.5 cm pieces. Using a spring scissor, a small, 45-degree, angled incision was made into the trachea between the 3rd and 4th cartilaginous tracheal ring. A blunt, 18-gauge, 1.0 in needle was inserted into the trachea and forceps were used to gently pull the trachea over the needle, allowing the needle to be inserted approximately 0.5in. The proximal suture was tied, using a double-knot, keeping the needle in-place within the trachea. Next, the animal was pinned down by its limbs and sprayed with isopropanol. An incision was made to open body cavity just below the ribcage, and perpendicular incisions were made to expose the diaphragm. The diaphragm was then carefully punctured and removed, to care to avoid damaging the lungs. The ribcage was

then removed, and angled cuts – deep along the proximal end and shallower along the distal end – were made to aid in ease of extraction of the lungs, while additionally protecting the lungs from accidental puncture through contact with the severed ribs. A needle was subsequently attached, using the luer end of a needle, to a piece of 0.25 in outer-diameter, 0.125 in inner diameter Tygon tubing. The tubing was connected to a 60 mL syringe filled to 25cm above the mouse with 10% formalin to insure equal levels of inflation regardless of lung capacity. The stop-cock controlling Formalin flow was opened the lungs were allowed to inflate for 10min. The distal suture was secured around the trachea, via double-knot, just as the needle is removed and the Formalin flow stopped. With the lungs inflated and secured, the trachea was severed completely, above where it was tied off. The lungs (and heart) were now carefully cut of the chest cavity and placed in ample volume of 10% Formalin. The top to the formalin jar was then sealed, while holding the overhanging suture thread to prevent the lungs from sinking. The lungs were left in fixative overnight at room temperature. The next day, the heart was separated from the lungs and then transferred to PBS before weighing the lungs and shipping to NYU Histology Core for preparation of paraffin-embedded lung sections.

4.5.24 Ketamine-Xylazine Anesthetization

For anesthetization, mice were given a cocktail of ketamine and xylazine. The allowed dose of ketamine was 80-100 mg/kg and 5.0-12.5 mg/kg of xylazine. All drugs were diluted to proper concentration in sterile water prior to intraperitoneal (IP) injection. For all studies, the lowest possible dose, 80mg/kg of ketamine and 5.0mg/kg xylazine was given to minimize the time under anesthesia. The stock concentration of ketamine is 100 mg/mL and 20 mg/mL for the xylazine stock. Thus anesthesia was diluted in the followed ratio of 2.4 parts ketamine : 0.75 parts xylazine : 8.85 parts sterile water. This allowed for

each mouse to receive a dose of 4µL of diluting anesthesia cocktail per gram of body weight, i.e. a 25g mouse would receive 100µL of anesthesia cocktail.

Each mouse was weighed immediately prior to delivery of anesthesia and the exact, µL, volume was pipetted into a 0.5mL 28-gauge insulin syringe. The mouse was then scruffed, and tilted cranially, allowing the internal organs to shift, and opening extra space for the IP injection given to the lower abdomen to either side of the midline. The animal was the returned to its cage which was placed on a warming pad, allowing the animal to properly maintain its body temperature. Within several minutes, the animal fell unconscious and a toe pinch was performed to confirm complete sedation. Animals were subsequently monitored until awake, and a checkup performed 3 hours post-anesthetization, confirming recovery.

4.5.25 Intranasal Inoculation with AAV

Once sedated, the mouse was scruffed and 10^{11} genome copies of Adeno-associated virus (AAV) was delivered by intranasal inoculation. A maximum volume of 50µL was permitted to be delivered, evenly distributed across the nares, dropwise by pipette. To achieve a 10^{11} genome copy dose, the AAV was diluted in sterile phosphate-buffered saline (PBS). The AAV was designed to deliver and subsequently express either hSTING or Firefly luciferase (FLuc) as a positive control. AAV-infected mice were returned to their cages, are left untouched for 10 days, allowing for adequate expression of the delivered transgene.

4.5.26 Intranasal Inoculation with RV

Once anesthetized, the mouse was scruffed and a maximum of 1.4E+10 copies of RV-C15, or 5.0E+6 PFU of RV-A1A were delivered to the mouse airway by intranasal inoculation. A maximum volume of 50µL was permitted to be delivered, evenly distributed

across the nares, dropwise by pipette. Either infectious RV-C15 or ultraviolet (UV)-inactivated RV-C15 was delivered. For UV-inactivation, RV-C15 was stored on ice, while a UV light was turned on for two-hours inside the biological safety cabinet.

4.5.27 Health Scoring

After RV-C15 inoculation, throughout the duration of experimentation, all mice were monitored once daily and assessed for its ability to groom, respond to stimuli (behavior) and maintain body weight. Each mouse was examined and scored from 0-2 for the three categories. A score of 0 represents an unaffected symptom, score of 1 represents moderate symptoms, a score of 2 describes a severe symptom, and a score of 3 describes the most severe symptom (only possible to achieve in the behavior and weight categories). For grooming scores, a score of 0 describes a mouse with a smooth coat and bright eyes, while a score of 1 describes a mouse with a slight lack of grooming, i.e. looking slightly scruffy or hunched at rest, and a score of 2 describes a mouse with a rough coat, hunched at rest and/or crusty or closed eyes. For behavior scores, a score of 0 describes a completely normal mouse, while a score of 1 was used for a mouse with minor changes to its normal behavior such as slight lethargy, a score of 2 describes a mouse with reduced mobility, inactivity, labored breathing and complete lethargy, while a score of 3 describes an immobile mouse even after stimulation. Each animal was then weighed and a percent of original (T=0) weight is calculated. A weight score of 0 was used for a mouse which has not lost any body weight or has gained weight, a score of 1 was used for a mouse which has lost <10% of its weight, a score of 2 was used for mouse which has dropped between 10-20% of its original weight and a score of 3 was used for a mouse which has dropped >20% of its weight. The summation of its daily scores across all three categories was then calculated, and if an animal had a total score of 3-5 it was monitored twice daily. If a mouse reached a score of 6 or greater, it was immediately

euthanized. Additionally, if a mouse lost >20% of its body weight, regardless of other scores, it was also euthanized.

4.6 Supporting information

4.6.1 Figure S4.1: Transfection of LET1 cells in presence of hSTING with RV-C15 or RV-A1A does not affect cellular or released genome titers.

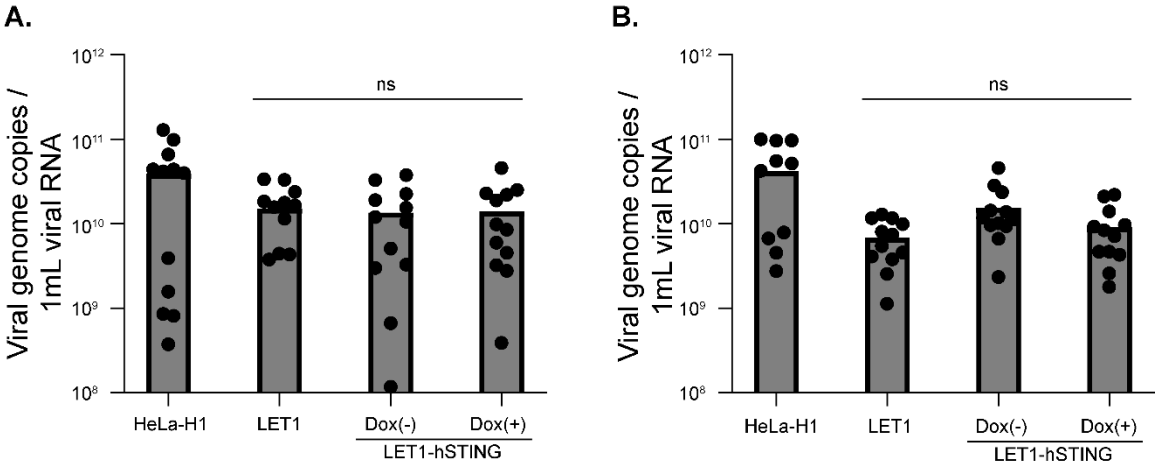

(**A**) qPCR detection of supernatant-containing RV-C15 genome copies 24 hpt. (**B**) qPCR detection of supernatant-containing RV-A1A genome copies 24 hpt.

4.6.2 Figure S4.2: STING KO HAE cultures infected with RV-A16 result in earlier release of virus.

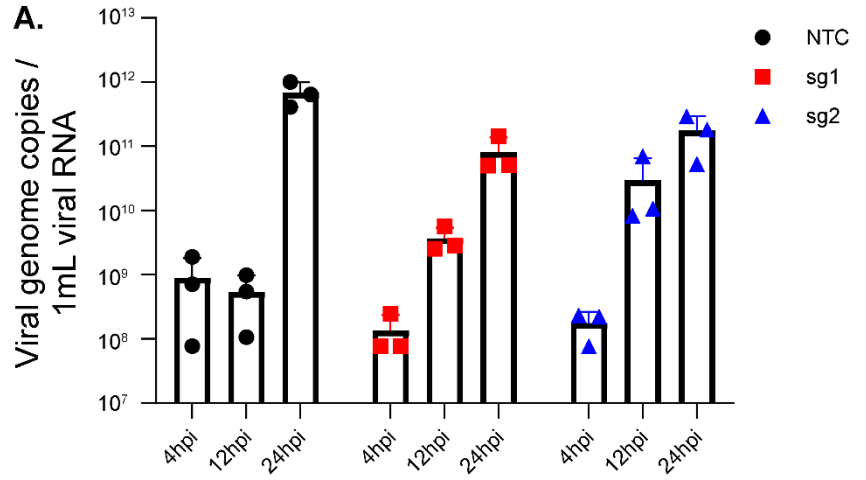

(**A**) qPCR detection of apically released RV-A16 infected HAE derived from BCi-NS1.1 cells transduced with NTC (black), STING KO sgRNA1 (sg1; red), or STING KO sgRNA2 (sg2; blue) at 4, 12, and 24hpi.

4.6.3 Figure S4.3: CDHR3 expression in Tg1.

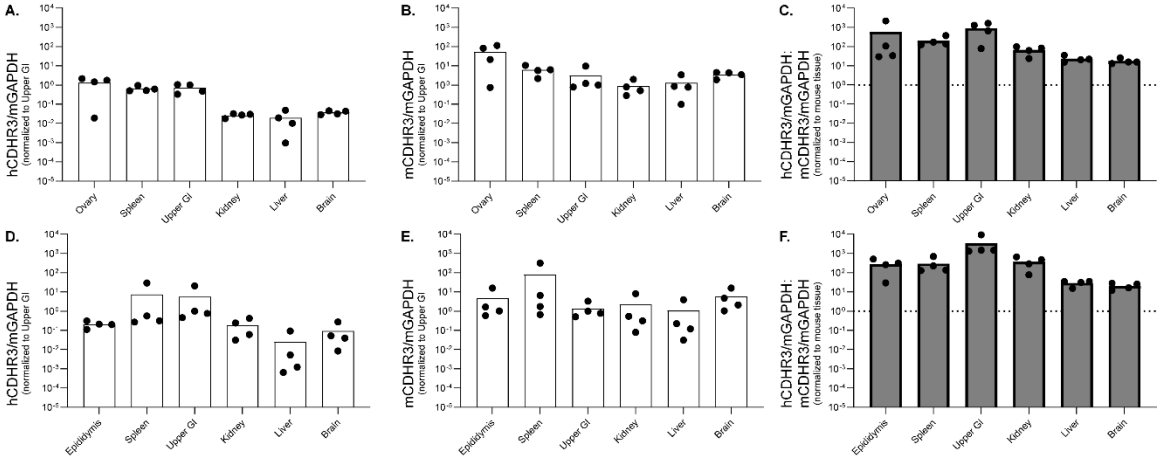

(**A**) Relative expression of hCDHR3 to murine GAPDH in female Tg1 mice. (**B**) Relative expression of mCDHR3 to murine GAPDH in female Tg1 mice (**C**) Ratio of relative human CDHR3 expression to murine CDHR3 expression of Tg1 by qPCR across n=4 female mice. (**D**) Relative expression of hCDHR3 to murine GAPDH in male Tg1 mice. (**E**) Relative expression of mCDHR3 to murine GAPDH in male Tg1 mice **(F)** Ratio of relative human CDHR3 expression to murine CDHR3 expression of Tg1 by qPCR across n=4 male mice.

4.6.4 Figure S4.4: CDHR3 expression in Tg2.

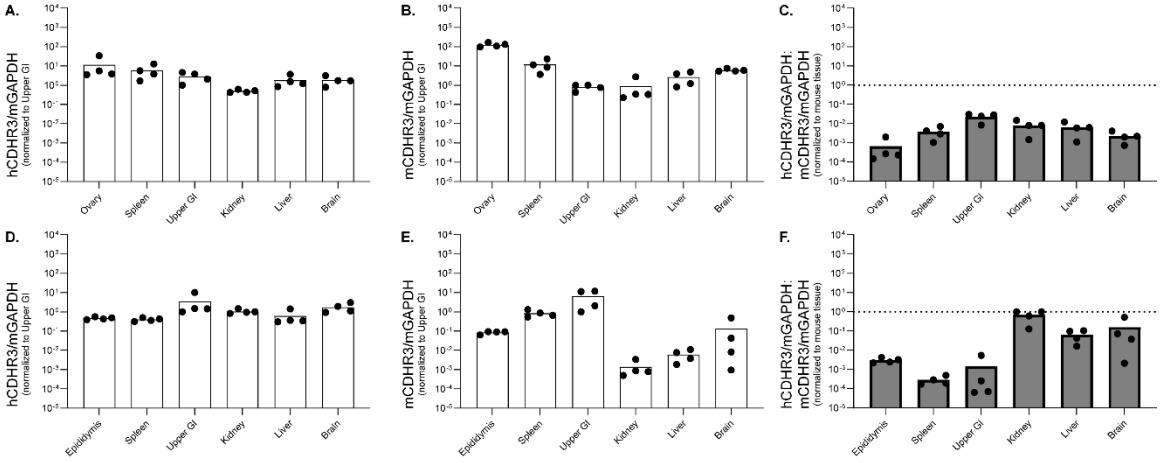

(**A**) Relative expression of hCDHR3 to murine GAPDH in female Tg2 mice. (**B**) Relative expression of mCDHR3 to murine GAPDH in female Tg2 mice (**C**) Ratio of relative human CDHR3 expression to murine CDHR3 expression of Tg2 by qPCR across n=4 female mice. (**D**) Relative expression of hCDHR3 to murine GAPDH in male Tg2 mice. (**E**) Relative expression of mCDHR3 to murine GAPDH in male Tg2 mice **(F)** Ratio of relative human CDHR3 expression to murine CDHR3 expression of Tg2 by qPCR across n=4 male mice.

4.6.5 Figure S4.5: CDHR3 expression in Tg3.

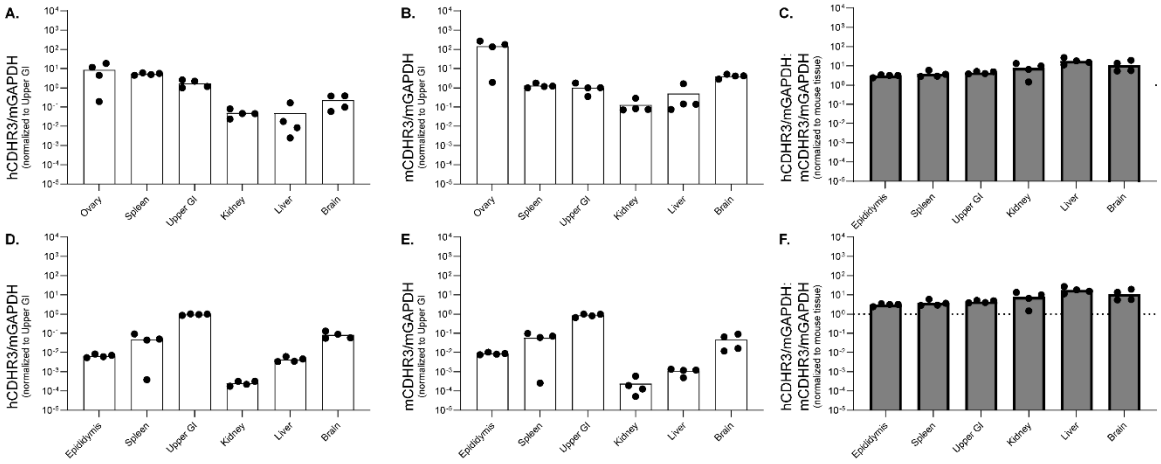

(**A**) Relative expression of hCDHR3 to murine GAPDH in female Tg3 mice. (**B**) Relative expression of mCDHR3 to murine GAPDH in female Tg3 mice (**C**) Ratio of relative human CDHR3 expression to murine CDHR3 expression of Tg3 by qPCR across n=4 female mice. (**D**) Relative expression of hCDHR3 to murine GAPDH in male Tg3 mice. (**E**) Relative expression of mCDHR3 to murine GAPDH in male Tg3 mice **(F)** Ratio of relative human CDHR3 expression to murine CDHR3 expression of Tg3 by qPCR across n=4 male mice.

4.6.6 Figure S4.6: Fluorescent immunohistochemistry localizes hCDHR3 in Tg mice to ciliated epithelium

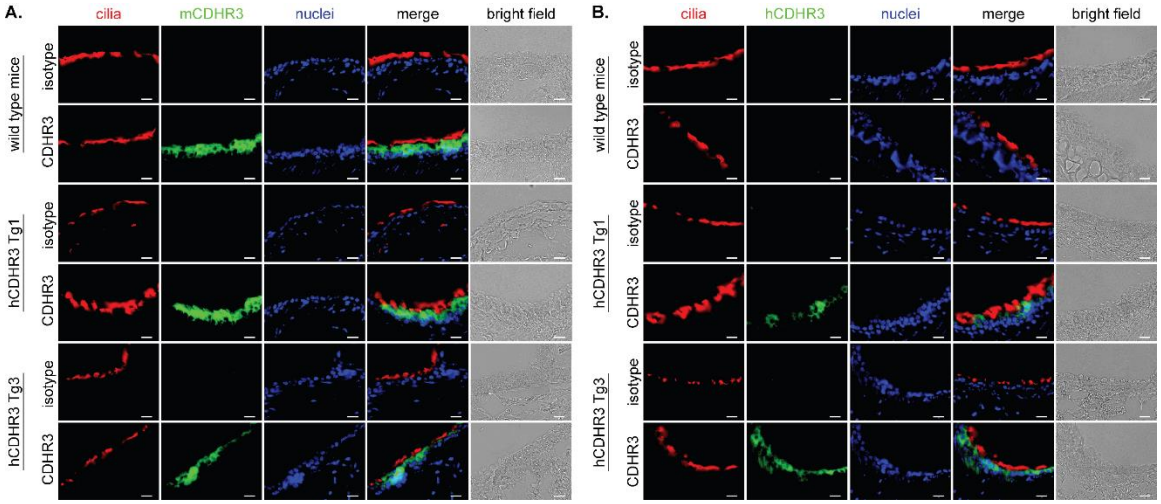

Fluorescent immunohistochemical detection of murine (**A**) and human (**B**) CDHR3 (green) in Tg1, Tg3 mouse lung tissue compared to WT mice. Nuclei (Hoescht; blue) and cilia (acetylated-alpha tubulin; red). Scale bar = 20µm.

4.6.7 Figure S4.7: Colorimetric immunohistochemistry localizes hCDHR3 in Tg mice to ciliated epithelium

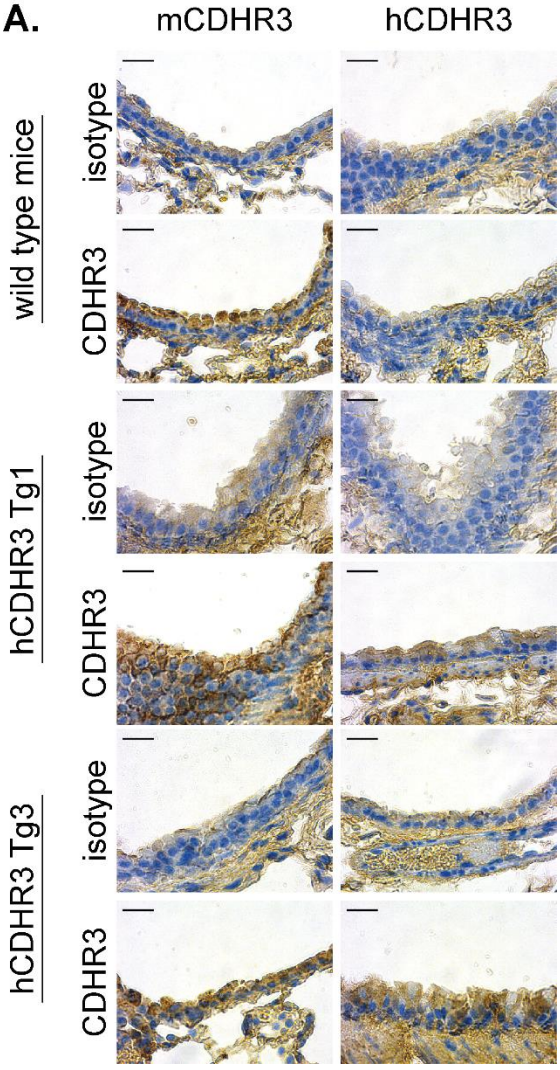

(**A**) Immunohistochemical detection of human and murine CDHR3 (brown) in Tg1, Tg3 mouse lung tissue compared to WT mice. Nuclei (hematoxylin; blue). Scale bar = 20µm.

4.6.8 Figure S4.8: RV-C infection of transgenic mice expressing CDHR3 with the addition of human STING 96hpi.

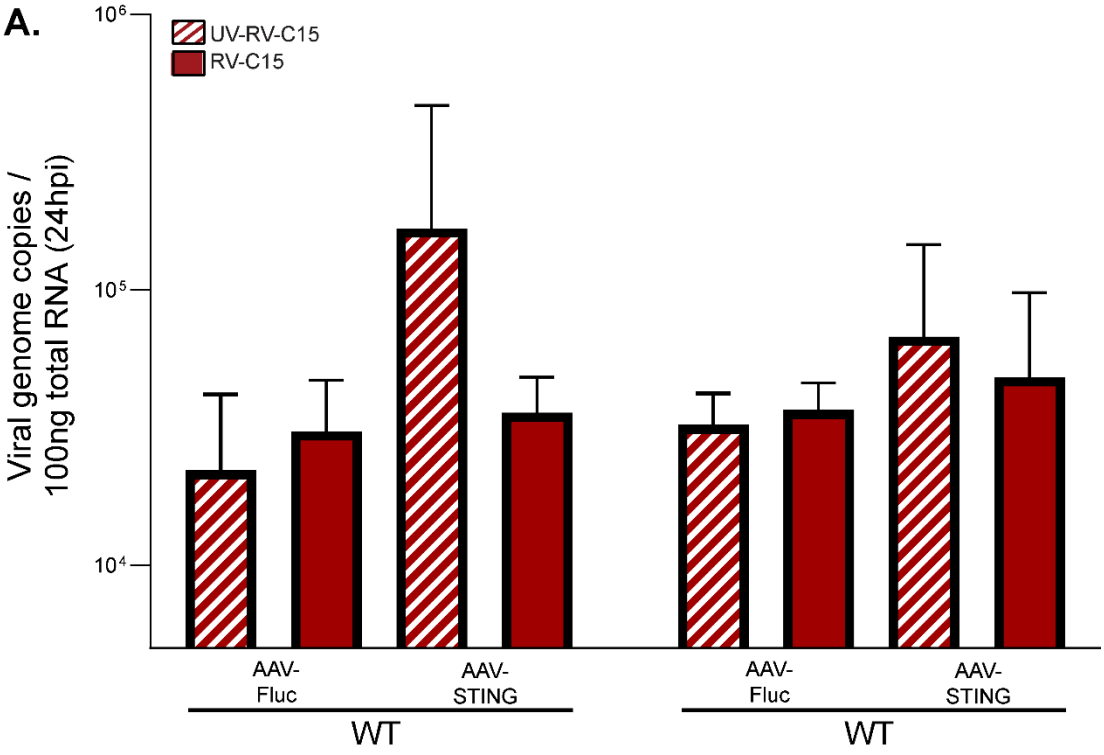

(**A**) qPCR detection of RV genome copy numbers at 96h hpi in WT (left) and Tg (right).

4.6.9 Figure S4.9: dsRNA is not detected in mice after infection with RV-C15 12 hpi.

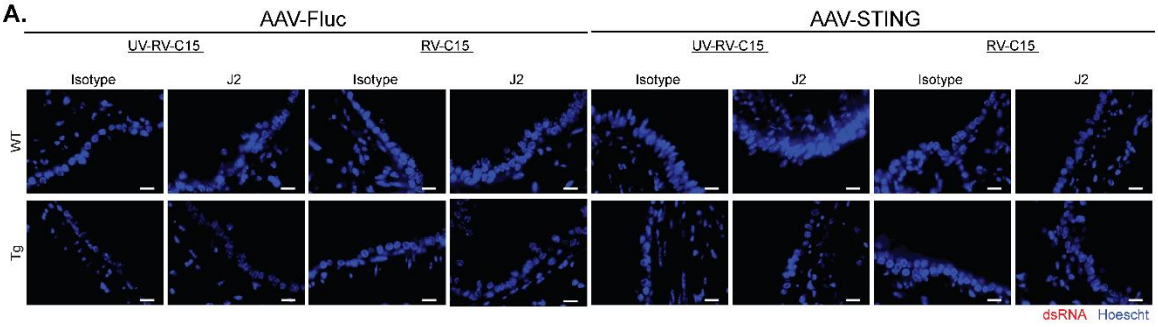

(**A**) Immunohistochemical detection of dsRNA (red) in RV-C15 infected paraffin-embedded mouse lung sections 12hpi. Nuclei (DAPI; blue). Scale bar = 20µm.

4.6.10 Figure S4.10: The addition of human STING does not impact RV=A1A infection of WT mice.

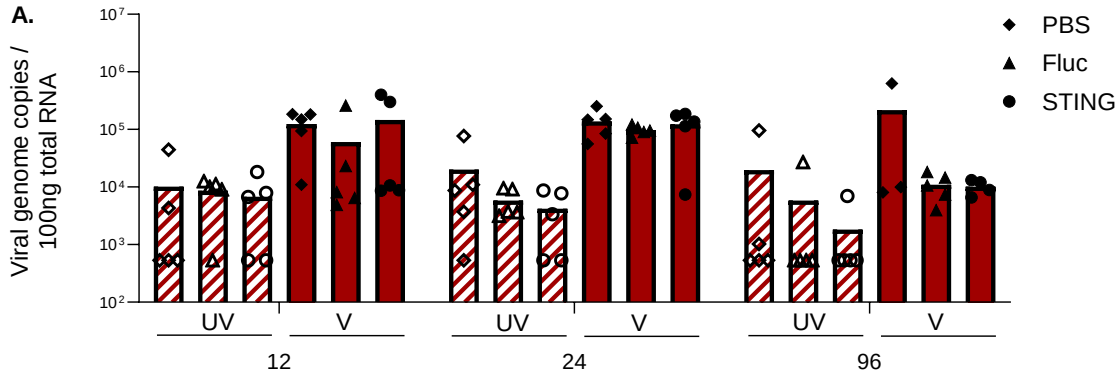

(**A**) WT mice were transduced with either human STING, or firefly luciferase (Fluc) via adeno-associated virus (AAV) or PBS control by intranasal inoculation. On day 10 post-AAV transduction, mice were then intransally inoculated with RV-A1A or UV-inactivated RV-A1A. Mice were then sacrificed and total lungs were collected at 12, 24 and 96 hpi for qPCR detection of RV genome copy numbers. Diamonds represent mice receiving PBS, triangles represent mice receiving AAV-Fluc, and circles represent mice receiving AAV-STING. Empty shapes represent UV-inactivated RV-A1A conditions while filled in shapes represent mice receiving infectious RV-A1A.

4.6.11 Figure S4.11: LET1 and LET1-expressing hCDHR3 cells are not susceptible to RV-C15 infection.

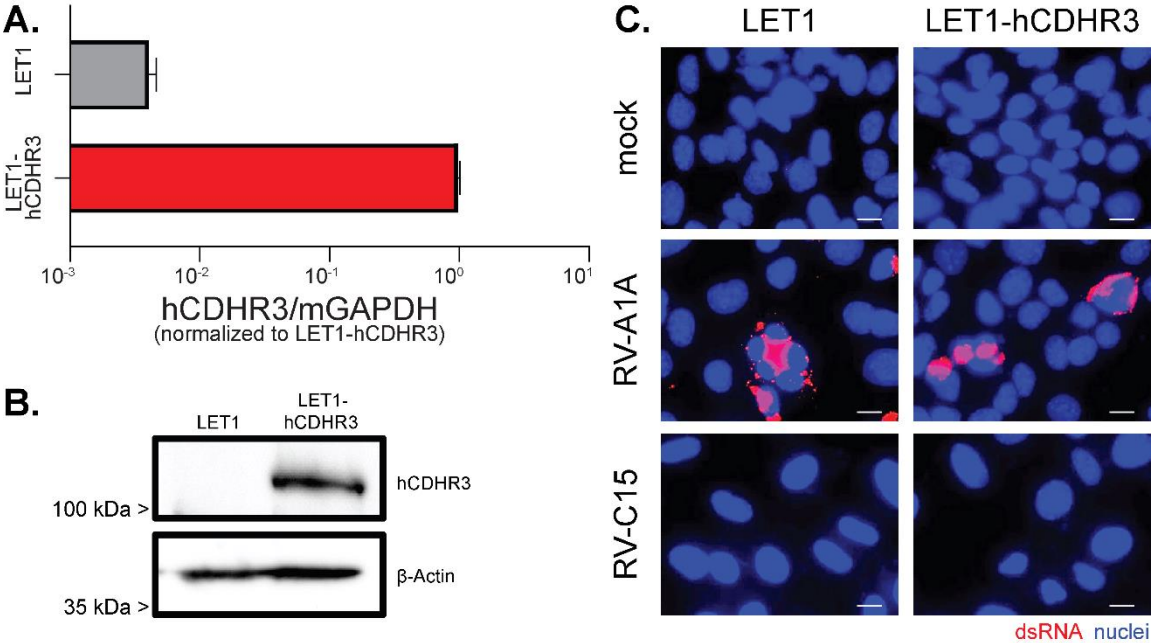

(**A**) hCDHR3 transcript expression relative to murine GAPDH expression in LET1 and LET1-hCDHR3, normalized to LET1-hCDHR3. (**B**) hCDHR3 protein expression in LET1-hCDHR3 compared to LET1 using a hCDHR3-specific antibody. β-Actin; loading control. (**C**) LET1 cells (left) or LET1-hCDHR3 cells (right) were either mock-infected or infected

with RV-A1A or RV-C15. 24 hpi cells were fixed and stained for dsRNA (red) and nuclei (blue). Scale bar = 20μm.

4.6.12 Figure S4.12: MAVS amino acid homology by species, highlighting the predicted RV-C 3C cleavage site in humans at Q|A.

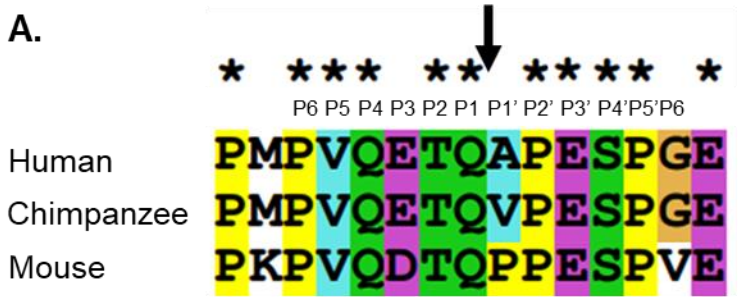

(**A**) MAVS amino acid homology surrounding cleavage site at Q|A. Note the conserved P1-6, but variability at P1' which is also a critical residue at the interface of the protease activity depicted with an arrow. Performed using ClustalX2.

4.7 Author Contributions

Conceptualization: Monty E. Goldstein, Margaret A. Scull.

Data curation: Monty E. Goldstein, Matthew R. Whorton, Yueh-Ming Loo

Formal analysis: Monty E. Goldstein, Maxinne A. Ignacio, Jeff M. Loube

Funding acquisition: Margaret A. Scull

Supervision: Margaret A. Scull.

Writing – original draft: Monty E. Goldstein

Writing – review & editing: Monty E. Goldstein, Margaret A. Scull.

4.8 Acknowledgements

We thank Drs. James Gern and Anne Palmenberg for providing rhinovirus plasmids. We additionally thank Drs. Yuri Bochkov and James Gern for proving HeLa-E8 cells. We thank Dr. Stanley Lemon for providing the inducible hSTING plasmid. We are grateful to directors and teams at the MPRI Flow Cytometry and Cell Sorting Facility, Imaging Core, and Department of Laboratory Animal Resources at the University of

Maryland, College Park, for their assistance. Additionally, we thank the team at the Experimental Pathology Research Core at New York University.

Chapter 5 : Development of Novel Cell Lines to Support Further Study of the Molecular Determinants of RV-C Infection in Mice

Monty E. Goldstein[1], and Margaret A. Scull[1]

1 Department of Cell Biology and Molecular Genetics, Maryland Pathogen Research Institute, 3134 Bioscience Research Building, University of Maryland, College Park, MD 20742, USA.

Previously we our data implicated human CDHR3 and human STING as necessary host factors toward the elevation of a mouse model. However, these mice have yet to be perfected, and here we design several novel cell lines which can provide the platform for identification of additional required host factors. Thus these newly-described factors can be then applied towards improving the current mouse model.

My contribution to this work includes performing all experiments and preparing this Chapter manuscript.

5.1 Abstract

Rhinovirus C (RV-C) is an important respiratory pathogen that has been linked to the development of childhood asthma. While many aspects of the RV-C life cycle remain unknown, prior studies have identified cadherin-related family member 3 (CDHR3) as the putative receptor mediating entry of RV-C. Notably, our previous work has identified differences in human and murine CDHR3 orthologs at the RV-C capsid-CDHR3 interface,

and demonstrated that mCDHR3 alone does not support robust RV-C infection *in vivo*. Further, we determined that deletion of mCDHR3 was embryonically lethal in mice. Still, the precise nature of RV-C interaction with murine CDHR3 is not clear, and the cellular function of CDHR3 has yet to be determined. To this extent, we developed a murine lung epithelial type1 (LET1) cell line, expressing both human CDHR3 and stimulator of interferon genes (STING) to provide an *in vitro* model system to further interrogate RV-C infection of murine epithelium. Then, to support further studies on the biological role of CDHR3 and further elucidate RV-C interactions with human and mouse CDHR3 orthologs, we developed and characterized LET1 and HeLa cell lines expressing and murine CDHR3.

5.2 Introduction

Rhinovirus-C (RV-C) infections have important clinical and economic impacts [28–35]. [430]. We and others have utilized pseudostratified human airway epithelium (HAE) cultures which support the entire RV-C life cycle to probe RV-C – host interactions, revealing key roles for both cadherin-related family member 3 (CDHR3) and stimulator of interferon genes (STING) [56,93,336]. More recently, our studies in mice confirmed the importance of expression of these two human orthologs for enhanced RV-C replication *in vivo*. Nonetheless, replication in this mouse model is still transient indicating additional improvements are necessary. Further, while our data indicate that mCDHR3 is not sufficient for infection, it remains unclear whether this is due to a lack of mCDHR3 expression on the cell surface, or specific residues in EC1 that preclude interaction with the RV-C15 capsid. Finally, while CDHR3 expression has been strongly associated with ciliated epithelial cells (in the lung and in extrapulmonary tissues) in both humans and mice, little is currently known about the canonical cellular role for CDHR3 in either species

[399,400,415]. This, together with the unexpected lethality of CDHR3 knockout in mice, indicate additional work on CDHR3 biology is warranted.

To address these outstanding questions, we establish several CDHR3-expressing cell lines which can be aid in the RV-C field. Further, these cells can also be applied to those primarily focused on cadherin biology and defining a cellular role for CDHR3.

5.3 Results

5.3.1 Establishment of LET1-hCDHR3 cells expressing hSTING: An *in vitro* platform to further interrogate the requirements of RV-C replication in a murine cell system

Our previous studies indicated hCDHR3 and hSTING expression enhance infection in mice. However, more work is needed as these infections did not induce any overt symptoms in infected mice and only moderate, albeit significant increases in viral titers were noted. Further supplementation with additional human factors, or depletion of mouse factors is likely necessary to garner prolonged replication *in vivo*. As exploration and genetic manipulations are difficult in a whole organism model, we took initial steps towards establishing an *in vitro* system to facilitate these future studies. Since we previously generated LET1-hCDHR3-expressing cells we now further modified these cells to express doxycycline-inducible hSTING, thereby providing an *in vitro* correlate to our *in vivo* model (**Figure 5.1A**).

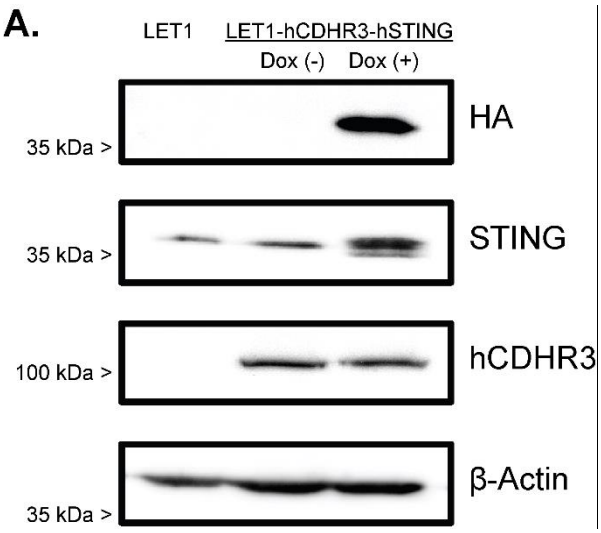

Figure 5.1: LET1 cells expressing hCDHR3 and inducible hSTING provide an *in vitro* alternative to transgenic mice. (**A**) Protein expression of HA-tagged inducible hSTING, total STING and hCDHR3 in LET1-hCDHR3-hSTING induced with doxycycline (Dox(+)) compared to LET1-hCDHR3-hSTING uninduced (Dox(-)) and LET1 cells. β-Actin; loading control.

These cells can be used to further assess the impact of hSTING expression on RV-C15 replication in a mouse background and as a platform for the addition of other human factors discovered to be important for RV-C infection.

5.3.2 Establishment and characterization of mCDHR3-expressing cell lines

Our previous results in Chapter 4 also highlighted differences between hCDHR3 and mCDHR3 at the extracellular domain 1 (EC1) - RV-C interface and at position 529. Still, further work is needed to understand the impact of the histidine at position 529 on the subcellular localization of mCDHR3 and the impact of specific mCDHR3 residues on RV capsid binding and subsequent uptake of viral particles. To this end, the expression of wild type (and mutant versions of) mCDHR3 in both mouse and human backgrounds could be informative. Notably, neither LET1 cells nor HeLa cells express endogenous CDHR3, providing a “clean slate” for such studies. Further, while HeLa cells are not naturally susceptible to RV-C infection, they are permissive, and can therefore be used to determine

the ability of ectopically-expressed CDHR3 proteins from different species, or harboring specific mutations, to support RV-C binding and entry. Thus, as an initial step, we engineered LET1 cells and HeLa cells line to express mCDHR3 (**Figure 5.2A**). These cell lines were generated by lentiviral transduction and subsequent fluorescence-associated cell sorting (FACS) to select for only those cells expressing the GFP, indicative of mCDHR3 expression.

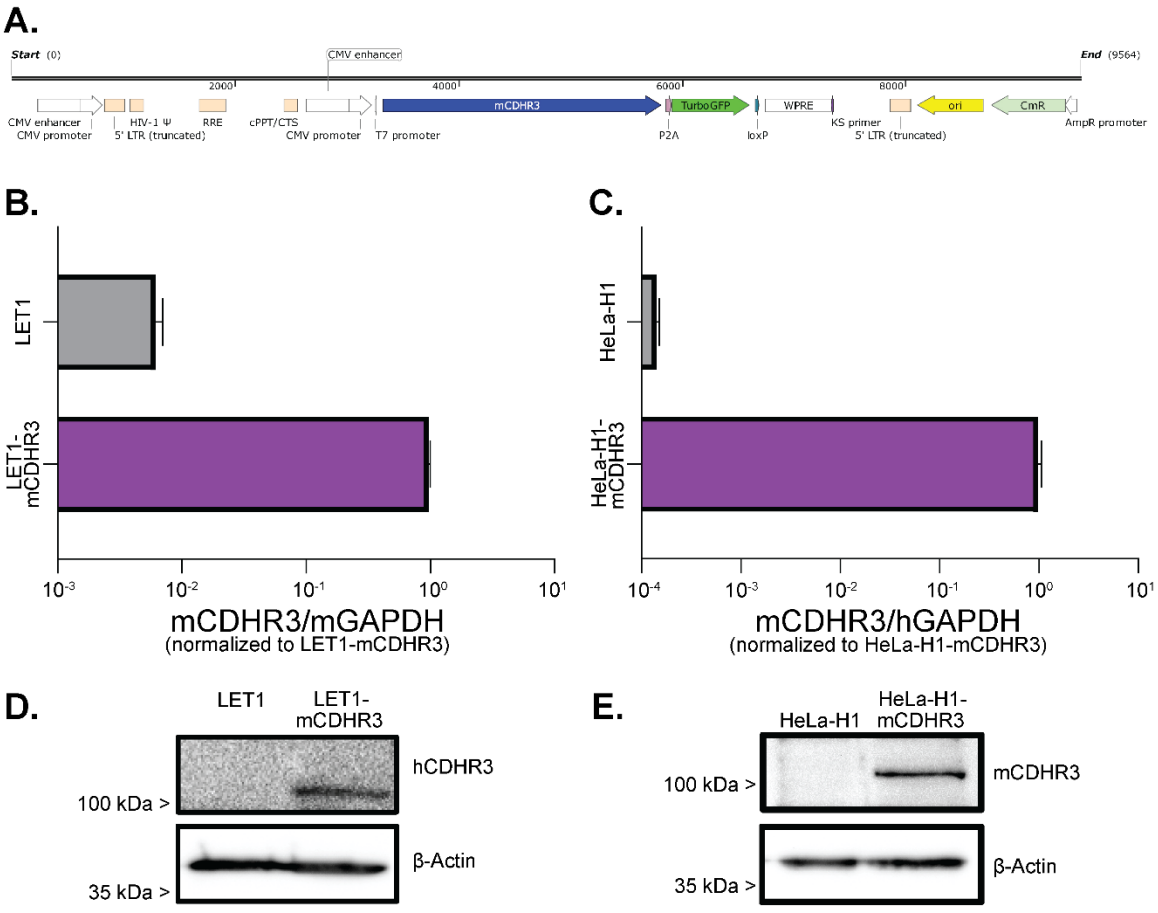

Figure 5.2: Development and characterization of human and murine CDHR3-expressing cell lines. (**A**) Plasmid map detailing mCDHR3 construct. (**B**) mCDHR3 transcript expression relative to murine GAPDH expression in LET1 and LET1-mCDHR3 and normalized to LET1-mCDHR3 cells. (**C**) mCDHR3 transcript expression relative to human GAPDH expression in HeLa-H1, and HeLa-mCDHR3 and normalized to HeLa-H1-mCDHR3 cells. (**D**) mCDHR3 protein expression in LET1-mCDHR3 compared to LET1 cells. β-Actin; loading control. (**E**) mCDHR3 protein expression in HeLa-mCDHR3 compared to HeLa-H1 cells. β-Actin; loading control.

We then quantified the relative mCDHR3 transcript abundance and mCDHR3 protein levels in the resulting bulk-sorted LET1-mCDHR3 (**Figure 5.2B and Figure 5.2C**) and similarly in HeLa-mCDHR3 cells (**Figure 5.2D and Figure 5.2E**), confirming successful generation of these lines.

5.3.3 Infection of hCDHR3-expressing HeLa cells highlights the need for further optimization.

We next sought to utilize the HeLa-mCDHR3 cells in parallel with previously-established HeLa-E8 cells (expressing hCDHR3) in a RV-C15 infection experiment. Following inoculation of HeLa-H1, HeLa-E8, and HeLa-mCDHR3 cells with RV-C15, we observed similar genome copy numbers 24 hpi in both HeLa-mCDHR3 cells and control HeLa-H1 cells, suggesting a lack of RV-C15 entry into HeLa-mCDHR3 cells (**Figure 5.3A**).

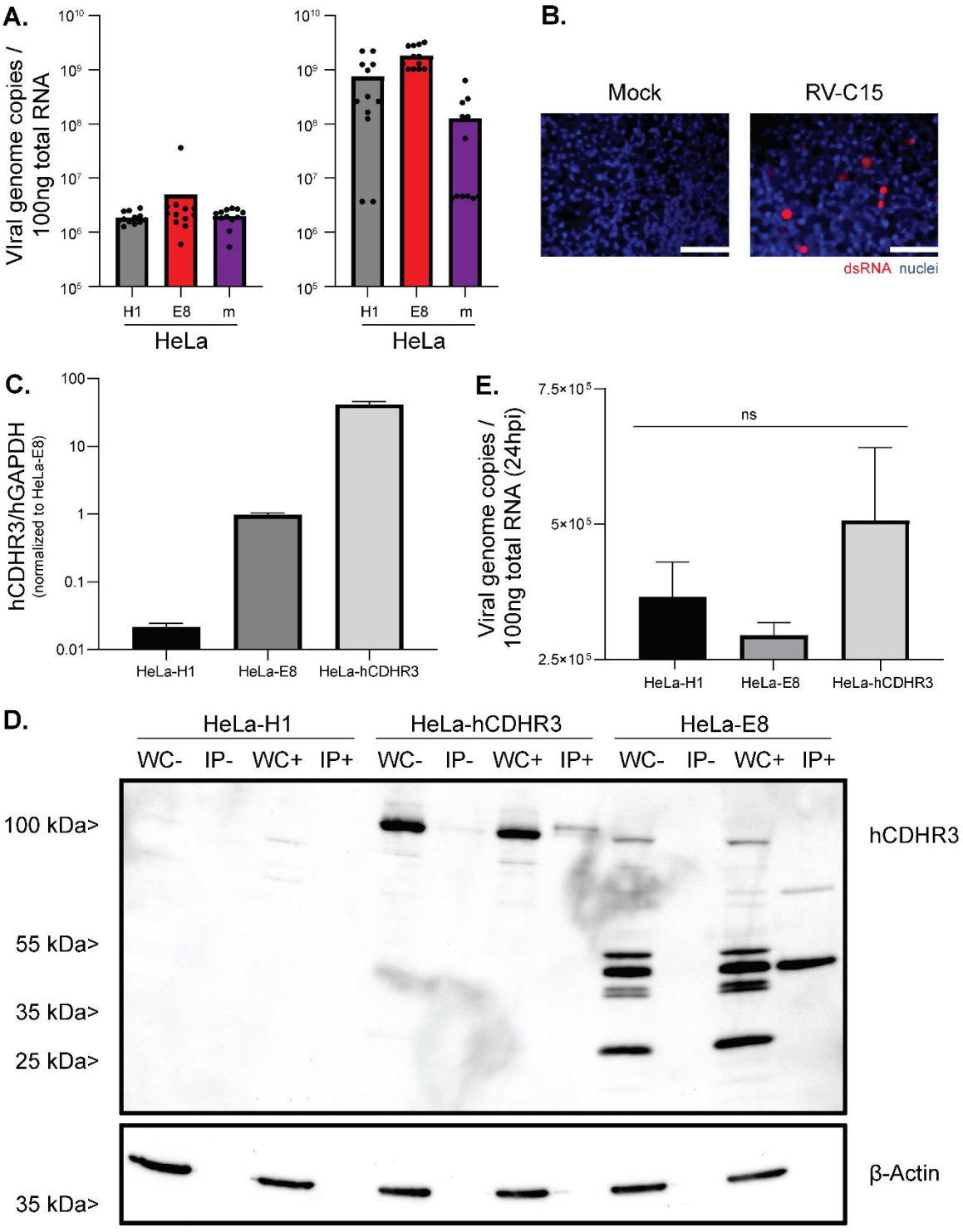

Figure 5.3: RV-C15 stock is infectious, yet does not replicate to significant levels in HeLa-E8 cells. (**A**) qPCR to detect RV RNA in HeLa-H1, HeLa-E8 and HeLa-mCDHr3 (m) and infected with RV-C15 (left) and RV-A1A (right) at 24 hpi. (**B**) Immunofluorescence-mediated detection of dsRNA (red) in HAE cultures infected with RV-C15 and fixed 12 hpi. Scale bar = 50um. (**C**) hCDHR3 transcript expression relative to human GAPDH expression in HeLa-H1 (black), HeLa-E8 (dark gray) and HeLa-hCDHR3

(light gray), and normalized to HeLa-E8. (**D**) Surface biotinlylation IP and subsequent western blot detection of hCDHR3 in HeLa-H1, HeLa-hCDHR3 and HeLa-E8 across whole cell lysate without biotin labeling (WC-), whole cell lysate with biotin labeling (WC+), IP fraction control without biotin labeling (IP-) and IP fraction with biotin labeling (IP+). β-Actin; loading control. (**E**) HeLa-H1 (black), HeLa-E8 (dark gray) and HeLa-hCDHR3 (light gray) were infected with RV-C15 and cell lysates were collected 24 hpi for qPCR detection of RV genomes.

However, we also noted that titers in HeLa-E8 cells were also not significantly different than HeLa-H1 cells. To rule out the possibility that the RV-C15 stock used in these experiments was compromised, we inoculated HAE cultures and probed for dsRNA by *en face* staining 12 hpi. Visualization of dsRNA staining by fluorescence microscopy then confirmed the presence of infectious particles (**Figure 5.3B**).

We next took a closer look at CDHR3 expression in the HeLa-E8 line. For comparison, we generated a new HeLa line using the same hCDHR3 construct that was bulk selected using blasticidin, but not clonally selected as previously done for the HeLa-E8 line (**Figure 5.3C**). Both HeLa-E8 and our HeLa-hCDHR3 cells express human CDHR3-529Y, where the tyrosine at position 529 has been shown to promote stabilization on the cell surface and interaction with RV-C [31,96,415]. Thus, we sought to confirm cell-surface expression using a biotin-labeling approach (**Figure 5.3D**). As anticipated, we detected surface-expressed hCDHR3 at the expected ~100kD molecular weight in HeLa-hCDHR3. While the band intensity was much lower in the IP fraction compared with whole-cell lysates, these bands cannot be compared directly, as it is indeterminate how much protein is successfully eluted during the IP. However, because input across all whole cell lysates conditions were normalized by total protein mass, and input IP fractions were also normalized by total protein mass, we can conclude that HeLa-hCDHR3 express hCDHR3 on the cell surface. However, this was not the case for HeLa-E8 cells, where we noted a multitude of lower molecular weight bands in the whole cell lysates that do not correspond

to any known CDHR3 presentations. Notably, two of these bands were detected in the IP lane, suggesting cell surface expression. Still, whether these potentially truncated forms can support interaction or entry of RV-C is unclear. Additional experiments to assess RV-C15 infection in our HeLa-hCDHR3 line demonstrated a marginal, non-significant increase in genome copy numbers over HeLa-E8 and HeLa-H1 control cells (**Figure 5.3E**). These data suggest that further selection of these cells to isolate a high hCDHR3-expressing clone that robustly supports replication is needed.

5.4 Discussion

Here we have generated several cell lines to further assess the requirements of RV-C15 replication in a mouse cell background and interrogate CDHR3 function and interaction with RV-C at the cell surface. Our previous data in Chapter 4 showed a lack of dsRNA in LET1 cells expressing hCDHR3, which correlated with a loss of RV-C15 titer between 12 and 24 hpi in Tg1 mice. We suspect this may not be due to a block at the level of entry in these cells; rather, these data could be the result of low amounts of virus that gain entry and thereby LET1-hCDHR3 cells lacks robust replication in the absence of hSTING. Indeed, the combination of hCDHR3 and hSTING was required to boost replication *in vivo*. Thus, we anticipate that RV-C15 replication in LET-hCDHR3 cells expressing hSTING will allow detection of infection and also provide a platform for further "host" manipulation – with the goal of applying additional knowledge gained about the molecular determinants of RV-C replication in mouse cell in vitro back to the *in vivo* model.

The discovery of CDHR3 as a host receptor for RV-C has proven critical to the study of RV-C. Prior to CDHR3's identification, groups were entirely reliant on RV-C infection in *ex vivo* tissues and primary cell culture systems [56,84,93,336]. Now, cells and tissues can be screened for CDHR3 expression, and allow for a more rapid determination

of RV-C susceptible cells and tissue systems. Further, previously Bochkov et. al demonstrated CDHR3 could be added into non-susceptible cells and tissues, rendering them susceptible to RV-C infection [15]. Thus here, we develop a LET1- and HeLa-mCDHR3-expressing cell lines towards understanding the role of mCDHR3 in the context of RV-C infection, as well as for further determination of the functional roles of individual residue differences between human and murine CDHR3 orthologs. Additionally, testing of novel RV-C host factors, can be initially assessed in the permissive HeLa cell context. Further, given the role for HeLa cells in the production of RVs, further modifications of these cells may provide a robust cell line for generating large quantities of infectious RV-C.

The lack of full-length CDHR3 on the cell surface in HeLa-E8 cells was surprising, but could explain the lack of infection observed in our preliminary experiments. Further, these data highlight the importance of passage-limited studies and suggest routine monitoring of CDHR3 surface expression may be critical in these cell lines to ensure consistent results.

Finally, and perhaps most importantly, in addition to the multifunctional role for the CDHR3-expressing cell lines characterized here, this study can be implemented towards studies aiming to determine the cellular function of CDHR3. Thus, once the molecular role for CDHR3 is elucidated, the results can directly impact and hopefully improve our understanding and prevention of RV-C-induced disease.

5.5 Methods

5.5.1 Plasmids

RV-A1A and RV-C15 cDNAs were previously described [84], and kindly provided by Drs. Anne Palmenberg and James Gern, respectively. hCDHR3 construct used initial

development of HeLa-E8 as well as later creation of HeLa-hCDHR3 was also provided by Dr. James Gern. mCDHR3 lentivirus construct was cloned into a pLenti-p2a-tGFP construct with a CMV promoter using NotI (#R0189S, New England Biolabs) and AsiSI (R0630S, New England Biolabs) restriction enzymes.

5.5.2 Tissue Culture

All HEK-293T cells (CRL-3216, ATTC), HeLa-H1 (CRL-1958, ATCC), HeLa-E8 [15] (Gern Lab), HeLa-mCDHR3, HeLa-hCDHR3, LET1 cells (NR-42941, BEI Resources), LET1-hCDHR3-hSTING, and LET1-mCDHR3 cells were grown in DMEM with 10% heat-inactivated fetal bovine serum (FBS), and maintained at 37^{o}C with 5% CO_2. All cell lines containing the hCDHR3 construct: HeLa-E8, and HeLa-hCDHR3 cell lines were supplemented with 5ug/mL Blasticidin S HCl (#A11139-03, Gibco) and LET1-hCDHR3-hSTING with 2.5ug/ mL Blasticidin S HCl. LET1-hCDHR3-hSTING media was further supplemented with 0.8ug/mL puromycin. To induce hSTING expression in LET1-hCDHR3-hSTING cells, 10ug/mL doxycycline was added three days prior to transfection.

Human airway tracheobronchial epithelial cells isolated from airway specimens from four unique donors without underlying lung disease were provided by Lonza, Inc. Primary cells derived from single patient sources were expanded on plastic and subsequently plated (5 x 10^4 cells/well) on rat-tail collagen type 1-coated permeable transwell membrane supports (6.5mm, #3470, Corning). HAE cultures were grown in Pneumacult-Ex Plus basal medium (#05040, StemCell Technologies), or Pneumacult-ALI medium (#05001, StemCell Technologies) with provision of an air-liquid interface for approximately 6 weeks to form differentiated, polarized cultures that resemble *in vivo* pseudostratified mucociliary epithelium.

5.5.3 *In vitro* transcription, rhinovirus rescue and amplification

RV-A1A was linearized using the XhoI restriction enzyme (#R0146S, New England Biolabs), and RV-C15 was linearized using the ClaI restriction enzyme (#R0197S, New England Biolabs). The linear plasmid was purified using either Monarch DNA Cleanup Kit (#T1030S, New England Biolabs) or QiaQuick Gel Extraction Kit (#28704, Qiagen) using the MinElute columns (#28004, Qiagen). *In vitro*-transcribed RV RNAs were synthesized using the MEGAscript T7 Kit (#AM1337, Invitrogen) following the manufacturer's protocol. Infectious virus stocks were then produced in HeLa-H1 cells by transfection of *in vitro*-transcribed RNA. For RV-A1A $7.0x10^5$ HeLa-H1 cells were seeded per well into a 24-well plate, while for RV-C15, HeLa-H1 were grown in a T75 until 90% confluence before transfecting using JetPrime (Polyplus), following the manufacturer's protocol. For RV-C15 rescue, double the amount of RNA and JetPrime reagent were used. Four hours post-transfection the media containing the transfection mix was removed and replenished with McCoy's media containing 2% FBS, 1% penicillin-streptomycin, 1% L-glutamine and 30 mM $MgCl_2$ and incubated at 34^{o}C. RV-C15 was collected 24 hpt, while RV-A1A was collected after observing robust cell death. For amplification, RV-A1A supernatants were then transferred to a T75 containing confluent HeLa-H1 monolayers. RV-A1A supernatants were collected upon observing cytopathic effects, typically 48-72 hpi, and RV-C15 supernatants were collected at 24hpt. These supernatants were then clarified by centrifugation at 1,000 x g for 10min. RV-A1A supernatants were titered by plaque assay, and the genome copy number of RV-C15 stocks were quantified by qPCR.

5.5.4 Plaque Assay

RV-A1A and RV-A16 stocks were titrated by plaque assay method using H1 HeLa cells plated in 24-well dishes and a published protocol with modifications [392]. Briefly,

90% confluent H1 HeLa monolayers were inoculated with ten-fold serial dilutions of the viral stock in McCoy's medium with 2% FBS and 30mM $MgCl_2$. After a 1hr incubation at room temperature, the inoculum was exchanged for a semi-solid overlay composed of 0.6% of bacteriological agar (#A5306; Sigma-Aldrich) in DMEM-F12 (#12500062; Gibco), supplemented with 1% FBS, 1% penicillin/streptomycin, 1% L-glutamine (#25030081; Gibco), and 30mM $MgCl_2$. The plate was incubated at 34^{o}C for 72 hours and the cells were fixed with 4% formaldehyde (#47608; Sigma-Aldrich; diluted in a 0.15 M saline solution). The fixing solution was removed together with the overlay after a 24-hour incubation at room-temperature and plaques visualized by staining the monolayer with 0.1% Crystal Violet (#C0775; Sigma-Aldrich) diluted in a 20% ethanol solution.

5.5.5 RV genome quantification by qPCR

Total RNA was extracted from cells using an RNeasy Mini Kit (#74104; Qiagen). To quantify viable RV genomes from an RV stock or experimental supernatant, 100µl sample was first treated with 1u RNase A (#EN053; Thermo) and 1u DNase I (#18047019; Invitrogen–Thermo Scientific) for 1hr at 37˚C and then inactivated at 70˚C for 15min. Viral RNA was then extracted using a QIAamp Viral RNA Mini Kit (#52904; Qiagen). For RNA extraction from whole tissues, tissues were homogenized using a TissueLyser (Qiagen) using 5mm stainless steel beads (#69989; Qiagen) for 15min at 50 oscillations/sec. Total RNA was then extracted from tissue using an RNeasy Universal Kit (#73404; Qiagen).

To reverse transcribe extracted RNA into cDNA, 100 ng of total cellular RNA was used in a reverse transcription reaction (High Capacity cDNA Reverse Transcriptase Kit; #4368814; Applied Biosystems), with random hexamer primers, as per the manufacturer's protocol. For cDNA synthesis after viral RNA extraction from supernatants, a fixed 10uL volume was used.

qPCR was done using 3µl of cDNA, 10pM HRVTF63 forward (5'–ACMGTGTYCTAGCCTGCGTGGC–3') and HRVTR reverse (5'–GAAACACGGACAC CCAAAGT GT–3') primers, 10pM HRVTF probe (5'–FAM/TCCTCCGGCCCCTGAAT/ BHQ1–3'), and LuminoCT Taqman Master Mix (#L6669; Sigma-Aldrich) according to the manufacturer's protocol. For absolute quantification, a standard curve was delineated using cDNA generated from ten-fold serial dilutions of *in vitro*-transcribed pRV-C15, pRV-A1A. This standard curve of RNA was used to calculate an exponential regression line based on the corresponding standard curve when plotted on a semi-log scale. This formula could then be used to input the cycle threshold (CT) value of interest to calculate the genome copy number from a particular well of a qPCR run.

5.5.6 Immortalized Cell Infection

For infection experiments, HeLa-H1 cells and all modified HeLa cells were seeded in 24well plates at $7.0x10^5$ cells/well. Following overnight incubation, cells were inoculated with an MOI =1 for RV-A1A and with 10^8 copies of RV-C15 and cells were incubated at 34^oC for 24hr.

5.5.7 Host gene quantification by qPCR

Total RNA was extracted and cDNA was prepared as detailed above. Relative gene expression was quantified using the two-step QuantiFast SYBR Green Kit (#204054; Qiagen) using a Roche LC480 thermocycler (Roche Life Sciences) according to the manufacturer's protocol. Primers were as follows: mCDHR3: 5'-AGGACCGAAAGCATTCGATTT-3' and 5'-AGGCTCGTTCACATCTGTCAC-3'; mGAPDH (endogenous control): 5'-AGGTCGGTGTGAACGGATTTG-3' and 5'-GGGGTCGTTGATGGCAACA-3'. For transduced cell line validation, total RNA was

extracted using the RNeasy Kit (#74104, Qiagen) prior to qRT-PCR analysis, as above. Human CDHR3 primers used were: 5'-TTACCTGCTACAGGCAATGTG-3' and 5'-CCTGACAGCCAATTCACCCTAA-3'.

5.5.8 Lentivirus Production

6-well plates were coated with Poly-L-lysine (3P8920, Sigma-Aldrich), washed with cell-grade H_2O (#A1287301, Gibco Laboratories), and allowed to dry prior to seeding HEK-293T cells ($4x10^5$ cells/well). Cells were grown overnight at 37°C / 5% CO_2 in Dulbecco's Modified Eagle Medium (DMEM; #25-500, Genesee Scientific) containing 10% FBS (GenClone) to achieve 80% confluency the next day. Cells were then washed with PBS and transfected with psPAX2 (a gift from Dr. Didier Trono (Addgene plasmid #12260), pCMV-VSV-G (a gift from Dr. Bob Weinberg (Addgene plasmid #8454) and murine or human CDHR3 expression plasmids using JetPrime (Polyplus) according to the manufacturer's protocol. 6 hours post-transfection (hpt), media was replaced with DMEM / 3% FBS and lentivirus-containing supernatant was collected at 48 and 72 hpt. Harvested supernatants were pooled, clarified by centrifugation (2000 *x* g, 10 min, 4°C) and filtered (0.2 micron). HEPES (#15630-080, Gibco Laboratories) and polybrene (#TR1003G, Fisher Scientific) were added to achieve final concentrations of 20mM and 4µg/mL, respectively, and lentiviral stocks were stored at -80°C prior to use.

5.5.9 Generation of human and mouse CDHR3 cell lines

HeLa-H1 and LET1 cells were seeded into 12 well plates at $7x10^4$ cells/well and incubated overnight at 37°C. The next day, cells were transduced with 400µL of lentivirus stock in a final volume of 2ml DMEM / 10% FBS containing 20mM HEPES and 4µg/mL polybrene via centrifugation (1000 *x* g) for 1 hr at 37°C). Following spinoculation, cells were returned to the incubator for 6-18hrs at which point the media was replaced with 1mL

DMEM / 2% FBS until the transduced phenotype was observed and / or cells were required to be split. hCDHR3-containing cells were selected using 5ug/mL Blasticidin S HCl. mCDHR3-containing cells were observed to be GFP+, an indicator of transduction, and then enriched using a FACS Aria cell sorter.

5.5.10 SDS-PAGE and Western Blot

Cell lysates were collected in RIPA buffer containing protease inhibitors (#N653-500mL, VWR) and total protein was quantified using a Pierce BCA assay (#23227, Thermo Fisher Scientific; Waltham, MA). Protein lysates (25µg) were denatured by heating (98^{o}C, 2min) and separated on a Novex^{TM} WedgeWell 4–20% Tris-Glycine gel (#XP04202BOX; Invitrogen-Thermo) under reducing conditions. Proteins were transferred to PVDF membranes (GE Healthcare Life Sciences; Marlborough, MA or using eBlot L1 (GenScript).

Membranes were blocked in 5% milk diluted in tris-buffered saline with 0.1% Tween-20 (TBS-T; #BP337-100, Fisher Scientific) for 1 hour at room temperature with rocking. Human and murine CDHR3 proteins were then detected using primary antibodies (#HPA011218, 1:2000; Sigma-Aldrich; #orb182906, 1:1000; Biorbyt) diluted in blocking buffer. STING was detected endogenously (66680-1-Ig, 1:1000; Proteintech) or by HA-tag (26183 1:1000, Invitrogen). Following incubation overnight at 4^{o}C membranes were washed 3X for 15 minutes each with TBS-T before incubation with HRP-conjugated donkey anti-Rabbit IgG (1:10,000; #A16035, Invitrogen). Anti-β-Actin-HRP conjugated antibody (#A3854, Sigma-Aldrich) was diluted 1:35000 in 5% TBS-T and incubated at room temperature for one hour. Western blots were visualized with SuperSignal West dura (#34075, Thermo Scientific), or femto (#35095, Thermo Scientific) reagent and imaged on either FujiFilm LAS-3000 or iBright FL15000 imagers.

5.5.11 Cell Surface Biotinylation and Immunoprecipitation Assay

The entire biotinylation and immunoprecipitation was performed using the Pierce Cell Surface Biotinylation and Isolation Kit (#A44390, Thermo Scientific) following the manufacturer's protocol. HeLa-H1, HeLa-E8 and HeLa-hCDHR3 cells were seeded in 15cm dishes (#25-203, Genesee Scientific) and allowed to proliferate until >85% confluency. Media was aspirated and cells were washed with 20mL PBS, prior to addition of 10mL Sulfo-NHS-SS-Biotin-containing or PBS-containing PBS for control samples. To prevent cells from detaching in the absence of media, cells were incubated for 30min at 4^{o}C. Cells were then carefully washed twice with 20mL of ice-cold TBS and all cells were scraped off of the 15cm dishes and into 10mL of TBS. TBS-containing cells, were centrifuged for 500 x g for 3min at 4^{o}C to pellet the biotinylated cells and supernatant was carefully aspirated. Protease inhibitors were added to 500µL of lysis buffer and added to the cell pellet. Cells were fully lysed by pipetting >20 times and transferred to 1.7mL Eppendorf tubes and incubated on ice for 30min. Prior to, and immediately following the 30min incubation on ice, lysates were vortexed for 5s to ensure full lysis. Lysates were then centrifuged at 15,000 x g for 5min and the clarified supernatant was transferred to a fresh Eppendorf tube. To ensure equivalent concentrations of protein in each sample, a BCA assay was performed on each sample. Then equal total amounts of protein were loaded for the immunoprecipitation portions of the assay detailed below.

NeutrAvidin Agarose was gently swirled to obtain an even suspension before adding 250µL to each column. Prior to centrifugation for 1min at 1000 x g, the cap was applied loosened one-quarter turn. Flow-through was discarded and the plug was applied. The lysates were applied to the column and sealed tightly before 30min incubation with ample rocking to ensure agarose would not settle. Columns were centrifuged for 1min at 1000 x g, with the cap was applied loosened one-quarter turn. Flow-through was discarded

and washed with 500mL Wash Buffer. Columns were inverted 3X prior to centrifugation at 1000 x g for 1min. Washing was repeated 2X, for a total of 3 washes. 225µL Elution Buffer was mixed with 25µL DTT to achieve a final concentration of 10mM DTT, and 200µL were added to each column. Columns were then capped and incubated for 30min with ample rocking. Lysates were eluted by centrifuging for 2min at 1000 x g and were then prepared for subsequent western blotting.

5.5.12 Immunofluorescence

24 hours post-infection, cells were fixed with 4% paraformaldehyde (Electron Microscopy Sciences; Hatfield, PA) for 15 minutes. Following fixation, cells were washed 2X with PBS and 3X with PBS++, then permeabilized with 0.2% Triton X-100 (Thermo Fisher Scientific; Waltham, MA) in PBS for 15 minutes. After permeabilization, cells were blocked in 10% donkey serum in PBS for 15min in a humidified chamber at room temperature. J2 antibody (#10010200, Scicons) was diluted 1:1000 in 1% BSA / PBS.). Following overnight incubation at 4^{o}C, cells were washed with PBS prior to secondary antibody staining. Secondary antibodies, AlexaFluor555 anti-mouse IgG2a 1:200 was applied for 1 hour at room temperature in a humidified chamber. Cells were washed with PBS and incubated with Hoescht (1:1000, 10 min; Thermo Fisher Scientific; Waltham, MA). Images were acquired with a Zeiss Axio Observer 3 Inverted fluorescence microscope (Cell Observer HS image system, Zeiss Axiocam 503 mono camera.

5.6 Acknowledgments

We thank Drs. James Gern and Anne Palmenberg for providing rhinovirus plasmids. We additionally thank Drs. Yuri Bochkov and James Gern for proving HeLa-E8 cells. We thank Dr. Stanley Lemon for providing the inducible hSTING plasmid. We are

grateful to directors and teams at the MPRI Flow Cytometry and Cell Sorting Facility and Imaging Core at the University of Maryland, College Park, for their assistance.

Chapter 6 : Discussion and Conclusion

Rhinovirus C (RV-C) was discovered over 15 years ago, but little remains known about this clinically-relevant pathogen due, in part, to the lack of *in vitro* and *in vivo* model systems that support the RV-C life cycle. In Chapter 2, we provide a detailed review highlighting of the importance of considering species, cell type, differentiation state, and microenvironmental context for studying virus-host interactions, and host immune responses in particular, in model systems. Building on these concepts, and with the goal of understanding the requirements of RV-C infection, we have engineered physiologically-relevant *in vitro* and *in vivo* model systems to better understand the requirement of specific host factors in human and mouse cells. Specifically, in Chapter 3 we utilized a physiologically-relevant *in vitro* model of human airway epithelium (HAE) to study RV-C replication, and applied CRISPR/Cas9 technology in these cultures to assess a specific role for stimulator of interferon genes (STING) in promoting viral replication. This was significant as HAE cultures are historically difficult to manipulate, and there remain few examples of genetic manipulation in the HAE model in the literature. Since RV-C has a restricted host range, we next sought to apply our knowledge of RV-C replication in HAE cultures to elevate the RV-C mouse model. As described in Chapter 4, we first characterize the ability of RV-C to replicate in mouse cells towards the development of a small animal model; second, we apply these *in vitro* findings to establish the first RV-C sustained infection in transgenic mice. While infection of these transgenic mice resulted in significantly enhanced viral titers, it also suggested that additional modifications are required to make mice more amenable to robust RV-C replication. Thus, to both provide an easy platform to better interrogate RV-C interactions with the murine CDHR3 ortholog and assay the impact of further modification in the mouse background, we generated additional cell lines which represent novel tools for further study described in Chapter 5.

HAE cultures represent a physiologically-relevant *in vitro* model that supports the replication of many respiratory viral infections, including RV-C, enabling us to describe RV-C replication dynamics and make direct comparisons to major and minor group RVs. Importantly, our work in this area has primarily utilized a microscopy-based approach and focused our analysis at 12 hour-post infection. Thus, future studies could attempt to synchronize infection in the HAE system and assay viral replication dynamics and the impacts of RV-C replication on host cells with greater kinetic resolution. These efforts, together with the detection of specific host factors or cellular organelles, may yield additional insights into the biogenesis of RV-C replication complexes and progression of cytopathic effects. By employing a larger panel of RV-C isolates, these studies would also allow for RV-C- (vs. RV-C15-) specific phenotypes to be determined.

Future investigation of RV-C utilizing the HAE culture system should also aim to define potential differences in host innate immune responses between RV groups which could provide mechanistic insights into the more severe disease outcomes associated with RV-C infections. The application of technologies such as single cell RNA-sequencing in this context would enable simultaneous detection of polyA-tailed RV genomes in HAE component cell types – further refining our understanding of RV cell tropism – and corresponding host transcriptome in infected and bystander cells. Further, only a single group to date has attempted to detail the mechanism through which RV-C evades the host immune response via 3C-mediated cleavage of RIG-I and MAVS [420]. Thus, additional studies are needed to identify other affected antiviral pathways. Assessing the ability and timing of RV-C protease-mediated degradation of innate immune sensors, in direct comparison to other RVs, may uncover unique characteristics of RV-C immune evasion. Ultimately, addressing these questions, will further the field's understanding of RV-C biology and host impact.

Notably, in 2020, work from Stanley Lemon's group identified STING as an essential host factor for RV-A replication in a genome-wide siRNA screen in HeLa cells [87]. Our work in STING knockout HAE cultures supports the findings of McKnight et. al, where we demonstrate a significant decrease in RV-C15 and RV-A16, but not RV-B14, replication in HAE lacking STING. However, a proviral role for STING during RV-B replication was subsequently implicated by Triantifilou et al. [91]. The underlying reason for the discrepancy in results across these papers with respect to RV-B14 remains unclear, still, these data suggest that the impacts of STING may extend to additional RVs.

While the underlying mechanism of STING's proviral function remains unknown, initial data [87,91] suggest a likely role for the use of STING positive membranes in the formation of replication organelles. Current hypotheses suggest STING interaction with phosphatidylinositol-4-phosphate (PI4P) lipids results in formation of viral replication complexes. Then, during later stages of the viral lifecycle, STING-positive membranes are repurposed to form autophagosome-like vesicles, which, prior to fusing with the lysosome, are co-opted for non-lytic release of viral progeny. Notably, many positive-sense RNA viruses alter cytosolic membranes to form replication complexes but do not appear to depend on STING for efficient replication. Therefore, future efforts investigating the proviral role for STING need to better incorporate the specificity towards RVs into the current hypothesis. Indeed, the experiments proposed above that seek to further characterize RV-C replication dynamics and replication organelle formation in HAE should also include evaluation of STING expression and localization. Such work will provide key insights into STING behavior at different stages of the viral life cycle in a pseudostratified epithelial model which may then inform on its proviral role(s). Interestingly, we were the first group to report an increase in total STING protein upon RV infection and Triantifilou et. al subsequently noted an increase in STING mRNA transcripts [91]. Both of these

findings are surprising given that RVs mediate host shut off. Currently, the means through which STING expression is elevated and the implications of elevated STING during RV replication has yet to be deciphered.

The potential involvement of STING in autophagy during RV infection is also notable given our data suggesting the induction of incomplete autophagy for RV-C15, and altered timing of viral release upon RV-A16 infection in HAE cultures depleted of STING. Still, an enhanced understanding of the role for autophagy during RV particle production in physiological context is needed. To what extent autophagy is utilized by RV-C15 (and other RV-Cs) as a means of egress, and whether direct manipulation of the autophagy pathway results in altered viral output will be important questions to address. Such studies could take advantage of autophagy inhibitors or the generation of HAE cultures depleted for autophagy-related genes using the same workflow we established to knock out STING. Still, it is important to acknowledge the RV strain-specific impacts on autophagy and assess the extent to which these same strains depend on STING for infection. Further, STING plays many functions in the cell, not related to antiviral signaling, and beyond autophagy, and thus may support RV replication via multiple pathways.

In mice, *in vivo*, we only observed significantly increased RV-C15 replication in transgenic mice expressing human cadherin-related family member 3 (hCDHR3) in the presence of human STING (hSTING), suggesting that transgenic expression of hCDHR3 is required for RV-C15 infection in mice to occur, and that efficient replication requires hSTING. Given our surprising results describing the embryonic lethality of CDHR3 knockout in mice, our transgenic model was engineered in the presence of endogenous murine CDHR3, and therefore expresses both endogenous and hCDHR3 orthologs. While the cellular function of CDHR3 has not yet been uncovered, other closely related cadherin proteins have been implicated in cell adhesion, epithelial polarity, cell-cell interaction and

cellular differentiation [96]. Additional studies probing CDHR3 biology have noted that CDHR3 genotype does not impact tight junction formation [413], yet complete knock out of CDHR3 results in a loss of TEER [415]. The impact of excess CDHR3 expression in our model would then be predicted to enhance epithelial barrier function *in vivo*. While the potential direct impact of this on viral replication is not obvious, we speculate this may have impacts on the activation of host immune responses, particularly with respect to the interaction of apical cytokines with receptors on the basolateral surface of epithelial cells, and infiltration of inflammatory cell types. Further examination of the hCDHR3-transgenic mouse airway would be needed to assess whether the additional CDHR3 present aberrantly restricts cell-cell junctions.

While ectopic expression of hCDHR3 in the mouse airway could feasibly limit immune responses, expression of hSTING in the murine airway has the potential to dysregulate antiviral sensing. Indeed, overexpression of STING *in vitro* is sufficient to induce NF-kB and IRF3 [431], leading to interferon production. Elevated levels of interferon in our mouse model would likely have had a negative impact on viral replication due to the establishment of an antiviral state prior to RV inoculation. Importantly, we did not obtain any evidence to suggest that interferon levels were altered, and most notably, observed the opposite impact on viral replication where titers were increased in transgenic mice that also received hSTING-expressing AAV.

In this dissertation we focused our efforts on studying RV-C without modifications, and thus our mouse model required transgenic expression of human proteins. With further characterization and optimization, our current mouse model may yield a suitable system for RV-C pathogenesis studies, and enable *in vivo* comparisons between the different RV species and groups. It could also be used in conjunction with current methods for inducing asthma phenotypes *in vivo*, which can possibly induce a more severe phenotype in mice

upon RV-C infection, and additionally provide deeper understanding of the role of RV-C in childhood development of asthma.

While the additional modifications required to further support RV-C replication in mice are currently not known, we hypothesize that RV replication is limited by murine immune responses. Studies in HAE cultures as noted earlier in this discussion will further detail how RV-C both activates and antagonizes critical antiviral signaling pathways in human cells which may provide insight into these interactions (or lack thereof) in mice. The cell lines developed in Chapter 5, especially LET1-hCDHR3-hSTING, and murine airway cultures derived from our hCDHR3 transgenic mice, can also be explored as additional platforms to modulate host factors. Importantly, while depletion of innate or adaptive components of host immunity in our current mouse model may further promote RV-C replication and simultaneously provide insights into host restriction, such a model may not be ideal for studying pathogenesis or testing vaccine candidates where presence of these immune responses is central to the work. Thus, it may be important to consider additional approaches, such as viral adaptation through passage in mouse tissues, in parallel.

Ultimately, future efforts toward improving and establishing both model systems (one which seeks to adapt the host and the other, the virus) have merit. Should our current mouse model be improved simply with inclusion of additional human factors and without needing to remove murine factors, this would be most optimal – as now pathogenesis and therapeutic studies can be advanced jointly and additional wild type RV-C isolates can be assayed. However, elevating a RV-C mouse model through the inclusion of RV-C mouse-adapted mutations to allow for infection of unmodified mice, would be highly beneficial should murine factors be discovered which preclude long-lasting RV-C infection. Overall, as further modifications are made to our existing *in vivo* platform or as alternative

approaches are pursued, organism-wide anti-RV-C immune responses can be better understood, and more effective treatments and preventative measures can be advanced.

In sum, from this dissertation, we have advanced knowledge of RV-C replication dynamics in human airway epithelium, and applied these results to explore the limitations of RV species tropism. To this effect, we developed a RV-C infection model in mice, which can serve as a basis for understanding RV-C pathogenesis and immune response, interplay with asthma, and development of therapeutics. While these mice are not without limitations, they do represent the first substantiated RV-C infection in a non-primate host. Likewise, the previously established major and minor group RV mouse models [108], are also not completely perfected models of infection. Thus, ultimately, as more required host factors are described for RV-C, these can then be applied to improve the mice detailed here.

References

1. Taylor-Robinson D, Tyrrell DA. Serotypes of viruses (rhinoviruses) isolated from common colds. Lancet. 1962 Mar 3;1(7227):452–4.

2. Lamson D, Renwick N, Kapoor V, Liu Z, Palacios G, Ju J, et al. MassTag polymerase-chain-reaction detection of respiratory pathogens, including a new rhinovirus genotype, that caused influenza-like illness in New York State during 2004-2005. J Infect Dis. 2006 Nov 15;194(10):1398–402.

3. Genus: Enterovirus | ICTV [Internet]. [cited 2023 Jul 14]. Available from: https://ictv.global/report/chapter/picornaviridae/picornaviridae/enterovirus

4. McIntyre CL, Knowles NJ, Simmonds P. Proposals for the classification of human rhinovirus species A, B and C into genotypically assigned types. J Gen Virol. 2013 Aug;94(Pt 8):1791–806.

5. Palmenberg AC, Gern JE. Classification and Evolution of Human Rhinoviruses. Methods Mol Biol. 2015;1221:1–10.

6. Palmenberg AC, Spiro D, Kuzmickas R, Wang S, Djikeng A, Rathe JA, et al. Sequencing and Analyses of All Known Human Rhinovirus Genomes Reveal Structure and Evolution. Science. 2009 Apr 3;324(5923):55–9.

7. Simmonds P, McIntyre C, Savolainen-Kopra C, Tapparel C, Mackay IM, Hovi T. Proposals for the classification of human rhinovirus species C into genotypically assigned types. J Gen Virol. 2010 Oct;91(Pt 10):2409–19.

8. McIntyre CL, Knowles NJ, Simmonds P. Proposals for the classification of human rhinovirus species A, B and C into genotypically assigned types. J Gen Virol. 2013 Aug;94(Pt 8):1791–806.

9. Palmenberg AC, Gern JE. Classification and Evolution of Human Rhinoviruses. In: Jans DA, Ghildyal R, editors. Rhinoviruses: Methods and Protocols [Internet]. New York, NY: Springer; 2015 [cited 2023 Jul 10]. p. 1–10. (Methods in Molecular Biology). Available from: https://doi.org/10.1007/978-1-4939-1571-2_1

10. Palmenberg AC, Spiro D, Kuzmickas R, Wang S, Djikeng A, Rathe JA, et al. Sequencing and analyses of all known human rhinovirus genomes reveal structure and evolution. Science. 2009 Apr 3;324(5923):55–9.

11. Greve JM, Davis G, Meyer AM, Forte CP, Yost SC, Marlor CW, et al. The major human rhinovirus receptor is ICAM-1. Cell. 1989 Mar 10;56(5):839–47.

12. Staunton DE, Merluzzi VJ, Rothlein R, Barton R, Marlin SD, Springer TA. A cell adhesion molecule, ICAM-1, is the major surface receptor for rhinoviruses. Cell. 1989 Mar 10;56(5):849–53.

13. Tomassini JE, Graham D, DeWitt CM, Lineberger DW, Rodkey JA, Colonno RJ. cDNA cloning reveals that the major group rhinovirus receptor on HeLa cells is

intercellular adhesion molecule 1. Proc Natl Acad Sci USA. 1989 Jul;86(13):4907–11.

14. Hofer F, Gruenberger M, Kowalski H, Machat H, Huettinger M, Kuechler E, et al. Members of the low density lipoprotein receptor family mediate cell entry of a minor-group common cold virus. Proc Natl Acad Sci U S A. 1994 Mar 1;91(5):1839–42.

15. Bochkov YA, Watters K, Ashraf S, Griggs TF, Devries MK, Jackson DJ, et al. Cadherin-related family member 3, a childhood asthma susceptibility gene product, mediates rhinovirus C binding and replication. Proc Natl Acad Sci U S A. 2015 Apr 28;112(17):5485–90.

16. Arruda E, Boyle TR, Winther B, Pevear DC, Gwaltney JM, Hayden FG. Localization of Human Rhinovirus Replication in the Upper Respiratory Tract by in situ Hybridization. The Journal of Infectious Diseases. 1995;171(5):1329–33.

17. Mäkelä MJ, Puhakka T, Ruuskanen O, Leinonen M, Saikku P, Kimpimäki M, et al. Viruses and Bacteria in the Etiology of the Common Cold. Journal of Clinical Microbiology. 1998 Feb 1;36(2):539–42.

18. Gern JE. The ABCs of Rhinoviruses, Wheezing, and Asthma. Journal of Virology. 2010 Aug 1;84(15):7418–26.

19. Arruda E, Pitkäranta A, Witek TJ, Doyle CA, Hayden FG. Frequency and natural history of rhinovirus infections in adults during autumn. J Clin Microbiol. 1997 Nov;35(11):2864–8.

20. Lee WM, Robert F. Lemanske J, Evans MD, Vang F, Pappas T, Gangnon R, et al. Human Rhinovirus Species and Season of Infection Determine Illness Severity. American Journal of Respiratory and Critical Care Medicine. 2012 Nov 11;186(9):886.

21. Corne JM, Marshall C, Smith S, Schreiber J, Sanderson G, Holgate ST, et al. Frequency, severity, and duration of rhinovirus infections in asthmatic and non-asthmatic individuals: a longitudinal cohort study. Lancet. 2002 Mar 9;359(9309):831–4.

22. Bizzintino J, Lee WM, Laing IA, Vang F, Pappas T, Zhang G, et al. Association between human rhinovirus C and severity of acute asthma in children. Eur Respir J. 2011 May;37(5):1037–42.

23. Zhu J, Message SD, Qiu Y, Mallia P, Kebadze T, Contoli M, et al. Airway inflammation and illness severity in response to experimental rhinovirus infection in asthma. Chest. 2014 Jun;145(6):1219–29.

24. Turunen R, Jartti T, Bochkov YA, Gern JE, Vuorinen T. Rhinovirus species and clinical characteristics in the first wheezing episode in children. J Med Virol. 2016 Dec;88(12):2059–68.

25. Fendrick AM, Monto AS, Nightengale B, Sarnes M. The Economic Burden of Non–Influenza-Related Viral Respiratory Tract Infection in the United States. Archives of Internal Medicine. 2003 Feb 24;163(4):487–94.

26. Avolio M, Venturini S, De Rosa R, Crapis M, Basaglia G. Epidemiology of respiratory virus before and during COVID-19 pandemic. Infez Med. 2022 Mar 1;30(1):104–8.

27. Arden KE, Greer RM, Wang CYT, Mackay IM. Genotypic diversity, circulation patterns and co-detections among rhinoviruses in Queensland, 2001. Access Microbiology. 2020;2(1):e000075.

28. Nakagome K, Bochkov YA, Ashraf S, Brockman-Schneider RA, Evans MD, Pasic TR, et al. Effects of rhinovirus species on viral replication and cytokine production. Journal of Allergy and Clinical Immunology. 2014 Aug 1;134(2):332-341.e10.

29. Lee WM, Lemanske RF Jr, Evans MD, Vang F, Pappas T, Gangnon R, et al. Human rhinovirus species and season of infection determine illness severity. Am J Respir Crit Care Med. 2012 Nov 1;186(9):886–91.

30. Essaidi-Laziosi M, Brito F, Benaoudia S, Royston L, Cagno V, Fernandes-Rocha M, et al. Propagation of respiratory viruses in human airway epithelia reveals persistent virus-specific signatures. J Allergy Clin Immunol. 2018 Jun;141(6):2074–84.

31. Palmenberg AC. Rhinovirus C, Asthma, and Cell Surface Expression of Virus Receptor CDHR3. J Virol [Internet]. 2017 Apr 1;91(7). Available from: https://www.ncbi.nlm.nih.gov/pubmed/28100615 https://www.ncbi.nlm.nih.gov/pmc/articles/PMC5355607/pdf/e00072-17.pdf

32. Matsuno AK, Gagliardi TB, Paula FE, Luna LKS, Jesus BLS, Stein RT, et al. Human coronavirus alone or in co-infection with rhinovirus C is a risk factor for severe respiratory disease and admission to the pediatric intensive care unit: A one-year study in Southeast Brazil. PLoS One. 2019;14(6):e0217744.

33. Chen WJ, Arnold JC, Fairchok MP, Danaher PJ, McDonough EA, Blair PJ, et al. Epidemiologic, clinical, and virologic characteristics of human rhinovirus infection among otherwise healthy children and adults: rhinovirus among adults and children. J Clin Virol. 2015 Mar;64:74–82.

34. Miller EK, Linder J, Kraft D, Johnson M, Lu P, Saville BR, et al. Hospitalizations and outpatient visits for rhinovirus-associated acute respiratory illness in adults. J Allergy Clin Immunol. 2016 Mar;137(3):734-743.e1.

35. Bønnelykke K, Coleman AT, Evans MD, Thorsen J, Waage J, Vissing NH, et al. Cadherin-related Family Member 3 Genetics and Rhinovirus C Respiratory Illnesses. Am J Respir Crit Care Med. 2017 Nov 9;197(5):589–94.

36. O'Neill MB, Laval G, Teixeira JC, Palmenberg AC, Pepperell CS. A Complex Evolutionary History for the Disease Susceptibility CDHR3 Locus. bioRxiv. 2018 Nov 15;186031.

37. Palmenberg AC. American Society for Virology. Annual meeting 2020. Keynote Address. Available from: https://asv.org/asv2020/events-and-meeting-details/

38. Royston L, Tapparel C. Rhinoviruses and Respiratory Enteroviruses: Not as Simple as ABC. Viruses. 2016 Jan;8(1):16.

39. Doggett JE, Bynoe ML, Tyrrell DAJ. Some Attempts to Produce an Experimental Vaccine with Rhinoviruses. BMJ. 1963 Jan 5;1(5322):34–6.

40. Glanville N, Johnston SL. Challenges in developing a cross-serotype rhinovirus vaccine. Current Opinion in Virology. 2015 Apr 1;11:83–8.

41. Lee S, Nguyen MT, Currier MG, Jenkins JB, Strobert EA, Kajon AE, et al. A polyvalent inactivated rhinovirus vaccine is broadly immunogenic in rhesus macaques. Nat Commun. 2016 Sep 22;7(1):12838.

42. Esneau C, Duff AC, Bartlett NW. Understanding Rhinovirus Circulation and Impact on Illness. Viruses. 2022 Jan 13;14(1):141.

43. McLean GR. Developing a vaccine for human rhinoviruses. J Vaccines Immun. 2014 Oct 1;2(3):16–20.

44. Palmenberg A. A vaccine for the common cold? Nature. 1987 Oct;329(6141):668–9.

45. Hamory BH, Hamparian VV, Conant RM, Gwaltney JM. Human Responses to Two Decavalent Rhinovims Vaccines. Journal of Infectious Diseases. 1975 Dec 1;132(6):623–9.

46. Rossmann MG. The canyon hypothesis. Hiding the host cell receptor attachment site on a viral surface from immune surveillance. J Biol Chem. 1989 Sep 5;264(25):14587–90.

47. Hayden FG, Herrington DT, Coats TL, Kim K, Cooper EC, Villano SA, et al. Efficacy and Safety of Oral Pleconaril for Treatment of Colds Due to Picornaviruses in Adults: Results of 2 Double-Blind, Randomized, Placebo-Controlled Trials. Clinical Infectious Diseases. 2003 Jun 15;36(12):1523–32.

48. Senior K. FDA panel rejects common cold treatment. The Lancet Infectious Diseases. 2002 May 1;2(5):264.

49. Hao W, Bernard K, Patel N, Ulbrandt N, Feng H, Svabek C, et al. Infection and propagation of human rhinovirus C in human airway epithelial cells. J Virol. 2012 Dec;86(24):13524–32.

50. Dick EC. Experimental infections of chimpanzees with human rhinovirus types 14 and 43. Proc Soc Exp Biol Med. 1968 Apr;127(4):1079–81.

51. Shipkowitz NL, Bower RR, Schleicher JB, Aquino F, Appell RN, Roderick WR. Antiviral activity of a bis-benzimidazole against experimental rhinovirus infections in chimpanzees. Appl Microbiol. 1972 Jan;23(1):117–22.

52. Pinto CA, Haff RF. Experimental infection of gibbons with rhinovirus. Nature. 1969 Dec 27;224(5226):1310–1.

53. Scully EJ, Basnet S, Wrangham RW, Muller MN, Otali E, Hyeroba D, et al. Lethal Respiratory Disease Associated with Human Rhinovirus C in Wild Chimpanzees, Uganda, 2013. Emerg Infect Dis. 2018 Feb;24(2):267–74.

54. Jakiela B, Gielicz A, Plutecka H, Hubalewska-Mazgaj M, Mastalerz L, Bochenek G, et al. Th2-Type Cytokine–Induced Mucus Metaplasia Decreases Susceptibility of Human Bronchial Epithelium to Rhinovirus Infection. Am J Respir Cell Mol Biol. 2014 Mar 3;51(2):229–41.

55. Griggs TF, Bochkov YA, Basnet S, Pasic TR, Brockman-Schneider RA, Palmenberg AC, et al. Rhinovirus C targets ciliated airway epithelial cells. Respir Res. 2017 May 4;18(1):84.

56. Tapparel C, Sobo K, Constant S, Huang S, Van Belle S, Kaiser L. Growth and characterization of different human rhinovirus C types in three-dimensional human airway epithelia reconstituted in vitro. Virology. 2013 Nov;446(1–2):1–8.

57. Fuchs R, Blaas D. Uncoating of human rhinoviruses. Rev Med Virol. 2010 Sep;20(5):281–97.

58. Royston L, Tapparel C. Rhinoviruses and Respiratory Enteroviruses: Not as Simple as ABC. Viruses. 2016 Jan;8(1):16.

59. Feng Q, Langereis MA, Lork M, Nguyen M, Hato SV, Lanke K, et al. Enterovirus 2Apro Targets MDA5 and MAVS in Infected Cells. J Virol. 2014 Mar;88(6):3369–78.

60. Castelló A, Izquierdo JM, Welnowska E, Carrasco L. RNA nuclear export is blocked by poliovirus 2A protease and is concomitant with nucleoporin cleavage. Journal of Cell Science. 2009 Oct 15;122(20):3799–809.

61. de Breyne S, Bonderoff JM, Chumakov KM, Lloyd RE, Hellen CUT. Cleavage of eukaryotic initiation factor eIF5B by enterovirus 3C proteases. Virology. 2008 Aug 15;378(1):118–22.

62. Bonderoff JM, LaRey JL, Lloyd RE. Cleavage of Poly(A)-Binding Protein by Poliovirus 3C Proteinase Inhibits Viral Internal Ribosome Entry Site-Mediated Translation. J Virol. 2008 Oct;82(19):9389–99.

63. Ventoso I, MacMillan SE, Hershey JWB, Carrasco L. Poliovirus 2A proteinase cleaves directly the eIF-4G subunit of eIF-4F complex. FEBS Letters. 1998;435(1):79–83.

64. Kean KM, Howell MT, Grünert S, Girard M, Jackson RJ. Substitution Mutations at the Putative Catalytic Triad of the Poliovirus 3C Protease Have Differential Effects on Cleavage at Different Sites. Virology. 1993 May 1;194(1):360–4.

65. Hellen CU, Fäcke M, Kräusslich HG, Lee CK, Wimmer E. Characterization of poliovirus 2A proteinase by mutational analysis: residues required for autocatalytic

activity are essential for induction of cleavage of eukaryotic initiation factor 4F polypeptide p220. J Virol. 1991 Aug;65(8):4226–31.

66. Martínez-Gil L, Bañó-Polo M, Redondo N, Sánchez-Martínez S, Nieva JL, Carrasco L, et al. Membrane integration of poliovirus 2B viroporin. J Virol. 2011 Nov;85(21):11315–24.

67. Horova V, Lyoo H, Różycki B, Chalupska D, Smola M, Humpolickova J, et al. Convergent evolution in the mechanisms of ACBD3 recruitment to picornavirus replication sites. PLoS Pathog. 2019 Aug;15(8):e1007962.

68. Choe SS, Dodd DA, Kirkegaard K. Inhibition of cellular protein secretion by picornaviral 3A proteins. Virology. 2005 Jun 20;337(1):18–29.

69. Belov GA, Altan-Bonnet N, Kovtunovych G, Jackson CL, Lippincott-Schwartz J, Ehrenfeld E. Hijacking components of the cellular secretory pathway for replication of poliovirus RNA. J Virol. 2007 Jan;81(2):558–67.

70. Rodríguez PL, Carrasco L. Poliovirus protein 2C has ATPase and GTPase activities. J Biol Chem. 1993 Apr 15;268(11):8105–10.

71. Adams P, Kandiah E, Effantin G, Steven AC, Ehrenfeld E. Poliovirus 2C protein forms homo-oligomeric structures required for ATPase activity. J Biol Chem. 2009 Aug 14;284(33):22012–21.

72. Ambros V, Baltimore D. Protein is linked to the 5’ end of poliovirus RNA by a phosphodiester linkage to tyrosine. J Biol Chem. 1978 Aug 10;253(15):5263–6.

73. Kitamura N, Adler CJ, Rothberg PG, Martinko J, Nathenson SG, Wimmer E. The genome-linked protein of picornaviruses. VII. Genetic mapping of poliovirus VPg by protein and RNA sequence studies. Cell. 1980 Aug;21(1):295–302.

74. Paul AV, Peters J, Mugavero J, Yin J, van Boom JH, Wimmer E. Biochemical and genetic studies of the VPg uridylylation reaction catalyzed by the RNA polymerase of poliovirus. J Virol. 2003 Jan;77(2):891–904.

75. Plotch SJ, Palant O, Gluzman Y. Purification and properties of poliovirus RNA polymerase expressed in Escherichia coli. J Virol. 1989 Jan;63(1):216–25.

76. Teterina NL, Zhou WD, Cho MW, Ehrenfeld E. Inefficient complementation activity of poliovirus 2C and 3D proteins for rescue of lethal mutations. J Virol. 1995 Jul;69(7):4245–54.

77. Aldabe R, Carrasco L. Induction of membrane proliferation by poliovirus proteins 2C and 2BC. Biochem Biophys Res Commun. 1995 Jan 5;206(1):64–76.

78. Barco A, Carrasco L. A human virus protein, poliovirus protein 2BC, induces membrane proliferation and blocks the exocytic pathway in the yeast Saccharomyces cerevisiae. The EMBO Journal. 1995 Jul 7;14(14):3349.

79. Harris JR, Racaniello VR. Amino acid changes in proteins 2B and 3A mediate rhinovirus type 39 growth in mouse cells. J Virol. 2005 May;79(9):5363–73.

80. Li X, Wang M, Cheng A, Wen X, Ou X, Mao S, et al. Enterovirus Replication Organelles and Inhibitors of Their Formation. Frontiers in Microbiology [Internet]. 2020 [cited 2023 Jul 26];11. Available from: https://www.frontiersin.org/articles/10.3389/fmicb.2020.01817

81. Belov GA, van Kuppeveld FJ. (+)RNA viruses rewire cellular pathways to build replication organelles. Current Opinion in Virology. 2012 Dec 1;2(6):740–7.

82. Roulin PS, Lötzerich M, Torta F, Tanner LB, van Kuppeveld FJM, Wenk MR, et al. Rhinovirus uses a phosphatidylinositol 4-phosphate/cholesterol counter-current for the formation of replication compartments at the ER-Golgi interface. Cell Host Microbe. 2014 Nov 12;16(5):677–90.

83. Baggen J, Thibaut HJ, Strating JRPM, van Kuppeveld FJM. The life cycle of non-polio enteroviruses and how to target it. Nat Rev Microbiol. 2018 Jun;16(6):368–81.

84. Bochkov YA, Palmenberg AC, Lee WM, Rathe JA, Amineva SP, Sun X, et al. Molecular modeling, organ culture and reverse genetics for a newly identified human rhinovirus C. Nat Med. 2011;17(5):627–32.

85. Lai JKF, Sam IC, Chan YF. The Autophagic Machinery in Enterovirus Infection. Viruses. 2016 Feb;8(2):32.

86. Kerr SL, Mathew C, Ghildyal R. Rhinovirus and Cell Death. Viruses. 2021 Apr 7;13(4):629.

87. McKnight KL, Swanson KV, Austgen K, Richards C, Mitchell JK, McGivern DR, et al. Stimulator of interferon genes (STING) is an essential proviral host factor for human rhinovirus species A and C. PNAS [Internet]. 2020 Oct 15 [cited 2020 Oct 19]; Available from: https://www.pnas.org/content/early/2020/10/14/2014940117

88. Sun L, Wu J, Du F, Chen X, Chen ZJ. Cyclic GMP-AMP synthase is a cytosolic DNA sensor that activates the type I interferon pathway. Science. 2013 Feb 15;339(6121):786–91.

89. Amurri L, Horvat B, Iampietro M. Interplay between RNA viruses and cGAS/STING axis in innate immunity. Frontiers in Cellular and Infection Microbiology [Internet]. 2023 [cited 2023 Jul 21];13. Available from: https://www.frontiersin.org/articles/10.3389/fcimb.2023.1172739

90. Chen C, Xu P. Cellular functions of cGAS-STING signaling. Trends in Cell Biology. 2023 Aug 1;33(8):630–48.

91. Triantafilou M, Ramanjulu J, Booty LM, Jimenez-Duran G, Keles H, Saunders K, et al. Human rhinovirus promotes STING trafficking to replication organelles to promote viral replication. Nat Commun. 2022 Mar 17;13(1):1406.

92. Lee WM, Wang W, Bochkov YA, Lee I. Reverse genetics system for studying human rhinovirus infections. Methods Mol Biol. 2015;1221:149–70.

93. Hao W, Bernard K, Patel N, Ulbrandt N, Feng H, Svabek C, et al. Infection and propagation of human rhinovirus C in human airway epithelial cells. J Virol. 2012 Dec;86(24):13524–32.

94. Basnet S, Mohanty C, Bochkov YA, Brockman-Schneider RA, Kendziorski C, Gern JE. Rhinovirus C causes heterogeneous infection and gene expression in airway epithelial cell subsets. Mucosal Immunol. 2023 Feb 14;S1933-0219(23)00009-0.

95. Essaidi-Laziosi M, Brito F, Benaoudia S, Royston L, Cagno V, Fernandes-Rocha M, et al. Propagation of respiratory viruses in human airway epithelia reveals persistent virus-specific signatures. J Allergy Clin Immunol. 2018 Jun;141(6):2074–84.

96. Bonnelykke K, Sleiman P, Nielsen K, Kreiner-Moller E, Mercader JM, Belgrave D, et al. A genome-wide association study identifies CDHR3 as a susceptibility locus for early childhood asthma with severe exacerbations. Nat Genet. 2014 Jan;46(1):51–5.

97. Yin FH, Lomax NB. Host range mutants of human rhinovirus in which nonstructural proteins are altered. J Virol. 1983 Nov;48(2):410–8.

98. Yin FH, Lomax NB. Establishment of a mouse model for human rhinovirus infection. J Gen Virol. 1986 Nov;67 (Pt 11):2335–40.

99. Harris JR, Racaniello VR. Changes in rhinovirus protein 2C allow efficient replication in mouse cells. J Virol. 2003 Apr;77(8):4773–80.

100. Reithmayer M, Reischl A, Snyers L, Blaas D. Species-specific receptor recognition by a minor-group human rhinovirus (HRV): HRV serotype 1A distinguishes between the murine and the human low-density lipoprotein receptor. J Virol. 2002 Jul;76(14):6957–65.

101. Tuthill TJ, Papadopoulos NG, Jourdan P, Challinor LJ, Sharp NA, Plumpton C, et al. Mouse respiratory epithelial cells support efficient replication of human rhinovirus. J Gen Virol. 2003 Oct;84(Pt 10):2829–36.

102. Bartlett NW, Walton RP, Edwards MR, Aniscenko J, Caramori G, Zhu J, et al. Mouse models of rhinovirus-induced disease and exacerbation of allergic airway inflammation. Nat Med. 2008 Feb;14(2):199–204.

103. Lee SB, Song JA, Choi GE, Kim HS, Jang YJ. Rhinovirus infection in murine chronic allergic rhinosinusitis model. Int Forum Allergy Rhinol. 2016 Nov;6(11):1131–8.

104. Singanayagam A, Glanville N, Walton RP, Aniscenko J, Pearson RM, Pinkerton JW, et al. A short-term mouse model that reproduces the immunopathological features of rhinovirus-induced exacerbation of COPD. Clin Sci (Lond). 2015 Aug;129(3):245–58.

105. Lomax NB, Yin FH. Evidence for the role of the P2 protein of human rhinovirus in its host range change. Journal of Virology. 1989 May 1;63(5):2396–9.

106. Bella J, Rossmann MG. Review: rhinoviruses and their ICAM receptors. J Struct Biol. 1999 Dec 1;128(1):69–74.

107. Xatzipsalti M, Papadopoulos NG. Cellular and Animals Models for Rhinovirus Infection in Asthma. Models of Exacerbations in Asthma and COPD. 2007;14:33–41.

108. Bartlett NW, Singanayagam A, Johnston SL. Mouse models of rhinovirus infection and airways disease. Methods Mol Biol. 2015;1221:181–8.

109. Grunert HP, Wolf KU, Langner KD, Sawitzky D, Habermehl KO, Zeichhardt H. Internalization of human rhinovirus 14 into HeLa and ICAM-1-transfected BHK cells. Med Microbiol Immunol. 1997 Jun;186(1):1–9.

110. Arden KE, Mackay IM. Newly identified human rhinoviruses: molecular methods heat up the cold viruses. Rev Med Virol. 2010 May;20(3):156–76.

111. Rajput C, Han M, Ishikawa T, Lei J, Goldsmith AM, Jazaeri S, et al. Rhinovirus C Infection Induces Type 2 Innate Lymphoid Cell Expansion and Eosinophilic Airway Inflammation. Frontiers in Immunology [Internet]. 2021 [cited 2023 Jan 30];12. Available from: https://www.frontiersin.org/articles/10.3389/fimmu.2021.649520

112. Goldstein ME, Scull MA. Modeling Innate Antiviral Immunity in Physiological Context. Journal of Molecular Biology. 2021 Dec 1;167374.

113. Meyts I, Casanova JL. Viral infections in humans and mice with genetic deficiencies of the type I IFN response pathway. Eur J Immunol. 2021 May;51(5):1039–61.

114. Bastard P, Rosen LB, Zhang Q, Michailidis E, Hoffmann HH, Zhang Y, et al. Autoantibodies against type I IFNs in patients with life-threatening COVID-19. Science. 2020 Oct;370(6515).

115. Zhang Q, Bastard P, Liu Z, Le Pen J, Moncada-Velez M, Chen J, et al. Inborn errors of type I IFN immunity in patients with life-threatening COVID-19. Science. 2020 Oct;370(6515).

116. Ku CL, Chen IT, Lai MZ. Infection-induced inflammation from specific inborn errors of immunity to COVID-19. FEBS J. 2021 May;

117. Isaacs A, Lindenmann J. Virus interference. I. The interferon. Proc R Soc Lond B Biol Sci. 1957 Sep;147(927):258–67.

118. Isaacs A, Lindenmann J, Valentine RC. Virus interference. II. Some properties of interferon. Proc R Soc Lond B Biol Sci. 1957 Sep;147(927):268–73.

119. Janeway CA Jr. Approaching the asymptote? Evolution and revolution in immunology. Cold Spring Harb Symp Quant Biol. 1989;54 Pt 1:1–13.

120. Rojas JM, Alejo A, Martín V, Sevilla N. Viral pathogen-induced mechanisms to antagonize mammalian interferon (IFN) signaling pathway. Cell Mol Life Sci. 2021 Feb;78(4):1423–44.

121. Mesev EV, LeDesma RA, Ploss A. Decoding type I and III interferon signalling during viral infection. Nat Microbiol. 2019 Jun;4(6):914–24.

122. Hoffmann HH, Schneider WM, Rice CM. Interferons and viruses: an evolutionary arms race of molecular interactions. Trends Immunol. 2015 Mar;36(3):124–38.

123. Medzhitov R, Preston-Hurlburt P, Janeway CA Jr. A human homologue of the Drosophila Toll protein signals activation of adaptive immunity. Nature. 1997 Jul;388(6640):394–7.

124. Rock FL, Hardiman G, Timans JC, Kastelein RA, Bazan JF. A family of human receptors structurally related to Drosophila Toll. Proc Natl Acad Sci U S A. 1998 Jan;95(2):588–93.

125. Chaudhary PM, Ferguson C, Nguyen V, Nguyen O, Massa HF, Eby M, et al. Cloning and characterization of two Toll/Interleukin-1 receptor-like genes TIL3 and TIL4: evidence for a multi-gene receptor family in humans. Blood. 1998 Jun;91(11):4020–7.

126. Singh H, Koury J, Kaul M. Innate Immune Sensing of Viruses and Its Consequences for the Central Nervous System. Viruses. 2021 Jan;13(2).

127. Zheng M, Karki R, Williams EP, Yang D, Fitzpatrick E, Vogel P, et al. TLR2 senses the SARS-CoV-2 envelope protein to produce inflammatory cytokines. Nat Immunol. 2021 Jul;22(7):829–38.

128. Olejnik J, Hume AJ, Mühlberger E. Toll-like receptor 4 in acute viral infection: Too much of a good thing. PLoS Pathog. 2018 Dec;14(12):e1007390.

129. Alexopoulou L, Holt AC, Medzhitov R, Flavell RA. Recognition of double-stranded RNA and activation of NF-kappaB by Toll-like receptor 3. Nature. 2001 Oct;413(6857):732–8.

130. Diebold SS, Kaisho T, Hemmi H, Akira S, Reis e Sousa C. Innate antiviral responses by means of TLR7-mediated recognition of single-stranded RNA. Science. 2004 Mar;303(5663):1529–31.

131. Heil F, Hemmi H, Hochrein H, Ampenberger F, Kirschning C, Akira S, et al. Species-specific recognition of single-stranded RNA via toll-like receptor 7 and 8. Science. 2004 Mar;303(5663):1526–9.

132. Lund J, Sato A, Akira S, Medzhitov R, Iwasaki A. Toll-like receptor 9-mediated recognition of Herpes simplex virus-2 by plasmacytoid dendritic cells. J Exp Med. 2003 Aug;198(3):513–20.

133. Monteiro JT, Lepenies B. Myeloid C-Type Lectin Receptors in Viral Recognition and Antiviral Immunity. Viruses. 2017 Mar;9(3).

134. Geijtenbeek TB, Kwon DS, Torensma R, van Vliet SJ, van Duijnhoven GC, Middel J, et al. DC-SIGN, a dendritic cell-specific HIV-1-binding protein that enhances trans-infection of T cells. Cell. 2000 Mar;100(5):587–97.

135. Tassaneetrithep B, Burgess TH, Granelli-Piperno A, Trumpfheller C, Finke J, Sun W, et al. DC-SIGN (CD209) mediates dengue virus infection of human dendritic cells. J Exp Med. 2003 Apr;197(7):823–9.

136. Hornung V, Ellegast J, Kim S, Brzózka K, Jung A, Kato H, et al. 5'-Triphosphate RNA is the ligand for RIG-I. Science. 2006 Nov;314(5801):994–7.

137. Baum A, Sachidanandam R, García-Sastre A. Preference of RIG-I for short viral RNA molecules in infected cells revealed by next-generation sequencing. Proc Natl Acad Sci U S A. 2010 Sep;107(37):16303–8.

138. Kato H, Takeuchi O, Mikamo-Satoh E, Hirai R, Kawai T, Matsushita K, et al. Length-dependent recognition of double-stranded ribonucleic acids by retinoic acid–inducible gene-I and melanoma differentiation–associated gene 5. Vol. 205, Journal of Experimental Medicine. 2008. p. 1601–10.

139. Rehwinkel J, Gack MU. RIG-I-like receptors: their regulation and roles in RNA sensing. Nat Rev Immunol. 2020 Sep;20(9):537–51.

140. Ablasser A, Bauernfeind F, Hartmann G, Latz E, Fitzgerald KA, Hornung V. RIG-I-dependent sensing of poly(dA:dT) through the induction of an RNA polymerase III-transcribed RNA intermediate. Nat Immunol. 2009 Oct;10(10):1065–72.

141. Chiu YH, MacMillan JB, Chen ZJ. RNA Polymerase III Detects Cytosolic DNA and Induces Type I Interferons through the RIG-I Pathway. Vol. 138, Cell. 2009. p. 576–91.

142. Yoneyama M, Kikuchi M, Matsumoto K, Imaizumi T, Miyagishi M, Taira K, et al. Shared and Unique Functions of the DExD/H-Box Helicases RIG-I, MDA5, and LGP2 in Antiviral Innate Immunity. The Journal of Immunology. 2005 Sep;175(5):2851–8.

143. Takaoka A, Wang Z, Choi MK, Yanai H, Negishi H, Ban T, et al. DAI (DLM-1/ZBP1) is a cytosolic DNA sensor and an activator of innate immune response. Nature. 2007 Jul;448(7152):501–5.

144. Zhang Z, Yuan B, Bao M, Lu N, Kim T, Liu YJ. The helicase DDX41 senses intracellular DNA mediated by the adaptor STING in dendritic cells. Nat Immunol. 2011 Sep;12(10):959–65.

145. Unterholzner L, Keating SE, Baran M, Horan KA, Jensen SB, Sharma S, et al. IFI16 is an innate immune sensor for intracellular DNA. Nat Immunol. 2010 Nov;11(11):997–1004.

146. Hornung V, Ablasser A, Charrel-Dennis M, Bauernfeind F, Horvath G, Caffrey DR, et al. AIM2 recognizes cytosolic dsDNA and forms a caspase-1-activating inflammasome with ASC. Nature. 2009 Mar;458(7237):514–8.

147. Sun L, Wu J, Du F, Chen X, Chen ZJ. Cyclic GMP-AMP synthase is a cytosolic DNA sensor that activates the type I interferon pathway. Science. 2013 Feb;339(6121):786–91.

148. Yang P, An H, Liu X, Wen M, Zheng Y, Rui Y, et al. The cytosolic nucleic acid sensor LRRFIP1 mediates the production of type I interferon via a beta-catenin-dependent pathway. Nat Immunol. 2010 Jun;11(6):487–94.

149. Kienes I, Weidl T, Mirza N, Chamaillard M, Kufer TA. Role of NLRs in the Regulation of Type I Interferon Signaling, Host Defense and Tolerance to Inflammation. Int J Mol Sci. 2021 Jan;22(3):1301.

150. Havell EA, Berman B, Ogburn CA, Berg K, Paucker K, Vilcek J. Two antigenically distinct species of human interferon. Proc Natl Acad Sci U S A. 1975 Jun;72(6):2185–7.

151. LaFleur DW, Nardelli B, Tsareva T, Mather D, Feng P, Semenuk M, et al. Interferon-kappa, a novel type I interferon expressed in human keratinocytes. J Biol Chem. 2001 Oct;276(43):39765–71.

152. Hauptmann R, Swetly P. A novel class of human type I interferons. Nucleic Acids Res. 1985 Jul;13(13):4739–49.

153. Hardy MP, Owczarek CM, Jermiin LS, Ejdebäck M, Hertzog PJ. Characterization of the type I interferon locus and identification of novel genes. Genomics. 2004 Aug;84(2):331–45.

154. Wheelock EF. Interferon-Like Virus-Inhibitor Induced in Human Leukocytes by Phytohemagglutinin. Science. 1965 Jul;149(3681):310–1.

155. Kotenko SV, Gallagher G, Baurin VV, Lewis-Antes A, Shen M, Shah NK, et al. IFN-lambdas mediate antiviral protection through a distinct class II cytokine receptor complex. Nat Immunol. 2003 Jan;4(1):69–77.

156. Sheppard P, Kindsvogel W, Xu W, Henderson K, Schlutsmeyer S, Whitmore TE, et al. IL-28, IL-29 and their class II cytokine receptor IL-28R. Nat Immunol. 2003 Jan;4(1):63–8.

157. Prokunina-Olsson L, Muchmore B, Tang W, Pfeiffer RM, Park H, Dickensheets H, et al. A variant upstream of IFNL3 (IL28B) creating a new interferon gene IFNL4 is associated with impaired clearance of hepatitis C virus. Nat Genet. 2013 Feb;45(2):164–71.

158. Uzé G, Lutfalla G, Gresser I. Genetic transfer of a functional human interferon alpha receptor into mouse cells: cloning and expression of its cDNA. Cell. 1990 Jan;60(2):225–34.

159. Novick D, Cohen B, Rubinstein M. The human interferon alpha/beta receptor: characterization and molecular cloning. Cell. 1994 May;77(3):391–400.

160. Platanias LC. Mechanisms of type-I- and type-II-interferon-mediated signalling. Nat Rev Immunol. 2005 May;5(5):375–86.

161. Pokrovskaja K, Panaretakis T, Grandér D. Alternative signaling pathways regulating type I interferon-induced apoptosis. J Interferon Cytokine Res. 2005 Dec;25(12):799–810.

162. Rusinova I, Forster S, Yu S, Kannan A, Masse M, Cumming H, et al. Interferome v2.0: an updated database of annotated interferon-regulated genes. Nucleic Acids Res. 2013 Jan;41(Database issue):D1040-6.

163. Schneider WM, Chevillotte MD, Rice CM. Interferon-stimulated genes: a complex web of host defenses. Annu Rev Immunol. 2014 Feb;32:513–45.

164. Golding A, Rosen A, Petri M, Akhter E, Andrade F. Interferon-alpha regulates the dynamic balance between human activated regulatory and effector T cells: implications for antiviral and autoimmune responses. Immunology. 2010 Sep;131(1):107–17.

165. Srivastava S, Koch MA, Pepper M, Campbell DJ. Type I interferons directly inhibit regulatory T cells to allow optimal antiviral T cell responses during acute LCMV infection. J Exp Med. 2014 May;211(5):961–74.

166. Schreiber G. The molecular basis for differential type I interferon signaling. J Biol Chem. 2017 May;292(18):7285–94.

167. Zheng H, Qian J, Varghese B, Baker DP, Fuchs S. Ligand-stimulated downregulation of the alpha interferon receptor: role of protein kinase D2. Mol Cell Biol. 2011 Feb;31(4):710–20.

168. Malakhova OA, Kim KI, Luo JK, Zou W, Kumar KGS, Fuchs SY, et al. UBP43 is a novel regulator of interferon signaling independent of its ISG15 isopeptidase activity. EMBO J. 2006 Jun;25(11):2358–67.

169. Huang S, Liu K, Cheng A, Wang M, Cui M, Huang J, et al. SOCS Proteins Participate in the Regulation of Innate Immune Response Caused by Viruses. Front Immunol. 2020 Sep;11:558341.

170. Bryant CE, Monie TP. Mice, men and the relatives: cross-species studies underpin innate immunity. Open Biol. 2012 Apr;2(4):120015.

171. Riera Romo M, Pérez-Martínez D, Castillo Ferrer C. Innate immunity in vertebrates: an overview. Immunology. 2016 Jun;148(2):125–39.

172. Buchmann K. Evolution of Innate Immunity: Clues from Invertebrates via Fish to Mammals. Front Immunol. 2014 Sep;5:459.

173. Sang Y, Miller LC, Nelli RK, Giménez-Lirola LG. Harness Organoid Models for Virological Studies in Animals: A Cross-Species Perspective. Front Microbiol. 2021 Sep;12:725074.

174. Seok J, Warren HS, Cuenca AG, Mindrinos MN, Baker HV, Xu W, et al. Genomic responses in mouse models poorly mimic human inflammatory diseases. Proc Natl Acad Sci U S A. 2013 Feb;110(9):3507–12.

175. Bolker J. Model organisms: There's more to life than rats and flies. Nature. 2012 Nov;491(7422):31–3.

176. Warren HS, Tompkins RG, Moldawer LL, Seok J, Xu W, Mindrinos MN, et al. Mice are not men. Proc Natl Acad Sci U S A. 2015 Jan;112(4):E345.

177. Martić-Kehl MI, Schibli R, Schubiger PA. Can animal data predict human outcome? Problems and pitfalls of translational animal research. Eur J Nucl Med Mol Imaging. 2012 Sep;39(9):1492–6.

178. Zschaler J, Schlorke D, Arnhold J. Differences in innate immune response between man and mouse. Crit Rev Immunol. 2014;34(5):433–54.

179. Hagai T, Chen X, Miragaia RJ, Rostom R, Gomes T, Kunowska N, et al. Gene expression variability across cells and species shapes innate immunity. Nature. 2018 Nov;563(7730):197–202.

180. Enard D, Cai L, Gwennap C, Petrov DA. Viruses are a dominant driver of protein adaptation in mammals. 2016 May;

181. Barreiro LB, Quintana-Murci L. From evolutionary genetics to human immunology: how selection shapes host defence genes. Nat Rev Genet. 2010 Jan;11(1):17–30.

182. Fore F, Indriputri C, Mamutse J, Nugraha J. TLR10 and Its Unique Anti-Inflammatory Properties and Potential Use as a Target in Therapeutics. Immune Netw. 2020 Jun;20(3):e21.

183. Tian X, Pascal G, Monget P. Evolution and functional divergence of NLRP genes in mammalian reproductive systems. BMC Evol Biol. 2009 Aug;9:202.

184. Zarember KA, Godowski PJ. Tissue expression of human Toll-like receptors and differential regulation of Toll-like receptor mRNAs in leukocytes in response to microbes, their products, and cytokines. J Immunol. 2002 Jan;168(2):554–61.

185. Qureshi ST, Larivière L, Leveque G, Clermont S, Moore KJ, Gros P, et al. Endotoxin-tolerant mice have mutations in Toll-like receptor 4 (Tlr4). J Exp Med. 1999 Feb;189(4):615–25.

186. Rehli M. Of mice and men: species variations of Toll-like receptor expression. Trends Immunol. 2002 Aug;23(8):375–8.

187. Heinz S, Haehnel V, Karaghiosoff M, Schwarzfischer L, Müller M, Krause SW, et al. Species-specific regulation of Toll-like receptor 3 genes in men and mice. J Biol Chem. 2003 Jun;278(24):21502–9.

188. Bauer S, Kirschning CJ, Häcker H, Redecke V, Hausmann S, Akira S, et al. Human TLR9 confers responsiveness to bacterial DNA via species-specific CpG motif recognition. Proc Natl Acad Sci U S A. 2001 Jul;98(16):9237–42.

189. Lund JM, Alexopoulou L, Sato A, Karow M, Adams NC, Gale NW, et al. Recognition of single-stranded RNA viruses by Toll-like receptor 7. Vol. 101, Proceedings of the National Academy of Sciences. 2004. p. 5598–603.

190. Oldenburg M, Kruger A, Ferstl R, Kaufmann A, Nees G, Sigmund A, et al. TLR13 Recognizes Bacterial 23S rRNA Devoid of Erythromycin Resistance-Forming Modification. Vol. 337, Science. 2012. p. 1111–5.

191. Gorden KKB, Qiu XX, Binsfeld CCA, Vasilakos JP, Alkan SS. Cutting Edge: Activation of Murine TLR8 by a Combination of Imidazoquinoline Immune Response Modifiers and PolyT Oligodeoxynucleotides. Vol. 177, The Journal of Immunology. 2006. p. 6584–7.

192. Zhang ZJ, Guo JS, Li SS, Wu XB, Cao DL, Jiang BC, et al. TLR8 and its endogenous ligand miR-21 contribute to neuropathic pain in murine DRG. J Exp Med. 2018 Dec;215(12):3019–37.

193. Hirai-Yuki A, Hensley L, McGivern DR, González-López O, Das A, Feng H, et al. MAVS-dependent host species range and pathogenicity of human hepatitis A virus. Science. 2016 Sep;353(6307):1541–5.

194. Aguirre S, Maestre AM, Pagni S, Patel JR, Savage T, Gutman D, et al. DENV Inhibits Type I IFN Production in Infected Cells by Cleaving Human STING. Vol. 8, PLoS Pathogens. 2012. p. e1002934.

195. Ding Q, Gaska JM, Douam F, Wei L, Kim D, Balev M, et al. Species-specific disruption of STING-dependent antiviral cellular defenses by the Zika virus NS2B3 protease. Vol. 115, Proceedings of the National Academy of Sciences. 2018. p. E6310–8.

196. Grant A, Ponia SS, Tripathi S, Balasubramaniam V, Miorin L, Sourisseau M, et al. Zika Virus Targets Human STAT2 to Inhibit Type I Interferon Signaling. Cell Host Microbe. 2016 Jun;19(6):882–90.

197. Ashour J, Morrison J, Laurent-Rolle M, Belicha-Villanueva A, Plumlee CR, Bernal-Rubio D, et al. Mouse STAT2 restricts early dengue virus replication. Cell Host Microbe. 2010 Nov;8(5):410–21.

198. Manry J, Laval G, Patin E, Fornarino S, Itan Y, Fumagalli M, et al. Evolutionary genetic dissection of human interferons. J Exp Med. 2011 Dec;208(13):2747–59.

199. Harari D, Abramovich R, Zozulya A, Smith P, Pouly S, Köster M, et al. Bridging the species divide: transgenic mice humanized for type-I interferon response. PLoS One. 2014 Jan;9(1):e84259.

200. Staeheli P, Grob R, Meier E, Sutcliffe JG, Haller O. Influenza virus-susceptible mice carry Mx genes with a large deletion or a nonsense mutation. Mol Cell Biol. 1988 Oct;8(10):4518–23.

201. Lindenmann J. Inheritance of Resistance to Influenza Virus in Mice. Vol. 116, Experimental Biology and Medicine. 1964. p. 506–9.

202. Hémont C, Neel A, Heslan M, Braudeau C, Josien R. Human blood mDC subsets exhibit distinct TLR repertoire and responsiveness. J Leukoc Biol. 2013 Apr;93(4):599–609.

203. Price AE, Shamardani K, Lugo KA, Deguine J, Roberts AW, Lee BL, et al. A Map of Toll-like Receptor Expression in the Intestinal Epithelium Reveals Distinct Spatial, Cell Type-Specific, and Temporal Patterns. Immunity. 2018 Sep;49(3):560-575.e6.

204. Ioannidis I, Ye F, McNally B, Willette M, Flaño E. Toll-like receptor expression and induction of type I and type III interferons in primary airway epithelial cells. J Virol. 2013 Mar;87(6):3261–70.

205. Wu X, Kwong AC, Rice CM. Antiviral resistance of stem cells. Curr Opin Immunol. 2019 Feb;56:50–9.

206. Burke DC, Graham CF, Lehman JM. Appearance of interferon inducibility and sensitivity during differentiation of murine teratocarcinoma cells in vitro. Cell. 1978 Feb;13(2):243–8.

207. Hong XX, Carmichael GG. Innate immunity in pluripotent human cells: attenuated response to interferon-β. J Biol Chem. 2013 May;288(22):16196–205.

208. Maillard PV, Ciaudo C, Marchais A, Li Y, Jay F, Ding SW, et al. Antiviral RNA interference in mammalian cells. Science. 2013 Oct;342(6155):235–8.

209. Wu X, Dao Thi VL, Huang Y, Billerbeck E, Saha D, Hoffmann HH, et al. Intrinsic Immunity Shapes Viral Resistance of Stem Cells. Cell. 2018 Jan;172(3):423-438.e25.

210. Wilmanski JM, Petnicki-Ocwieja T, Kobayashi KS. NLR proteins: integral members of innate immunity and mediators of inflammatory diseases. J Leukoc Biol. 2008 Jan;83(1):13–30.

211. Huhta H, Helminen O, Kauppila JH, Salo T, Porvari K, Saarnio J, et al. The Expression of Toll-like Receptors in Normal Human and Murine Gastrointestinal Organs and the Effect of Microbiome and Cancer. J Histochem Cytochem. 2016 Aug;64(8):470–82.

212. Heyl KA, Klassert TE, Heinrich A, Müller MM, Klaile E, Dienemann H, et al. Dectin-1 is expressed in human lung and mediates the proinflammatory immune response to nontypeable Haemophilus influenzae. MBio. 2014 Aug;5(5):e01492-14.

213. Cohen-Kedar S, Baram L, Elad H, Brazowski E, Guzner-Gur H, Dotan I. Human intestinal epithelial cells respond to β-glucans via Dectin-1 and Syk. Eur J Immunol. 2014 Dec;44(12):3729–40.

214. Stappers MHT, Clark AE, Aimanianda V, Bidula S, Reid DM, Asamaphan P, et al. Recognition of DHN-melanin by a C-type lectin receptor is required for immunity to Aspergillus. Nature. 2018 Mar;555(7696):382–6.

215. Faure-Dupuy S, Vegna S, Aillot L, Dimier L, Esser K, Broxtermann M, et al. Characterization of Pattern Recognition Receptor Expression and Functionality in Liver Primary Cells and Derived Cell Lines. J Innate Immun. 2018 Jul;10(4):339–48.

216. Izaguirre A, Barnes BJ, Amrute S, Yeow WS, Megjugorac N, Dai J, et al. Comparative analysis of IRF and IFN-alpha expression in human plasmacytoid and monocyte-derived dendritic cells. J Leukoc Biol. 2003 Dec;74(6):1125–38.

217. Siegal FP. The Nature of the Principal Type 1 Interferon-Producing Cells in Human Blood. Vol. 284, Science. 1999. p. 1835–7.

218. Cantell K, Hirvonen S, Kauppinen HL, Myllylä G. Production of interferon in human leukocytes from normal donors with the use of Sendai virus. Methods Enzymol. 1981;78(Pt A):29–38.

219. Fung KY, Mangan NE, Cumming H, Horvat JC, Mayall JR, Stifter SA, et al. Interferon-ϵ protects the female reproductive tract from viral and bacterial infection. Science. 2013 Mar;339(6123):1088–92.

220. Xi Y, Day SL, Jackson RJ, Ranasinghe C. Role of novel type I interferon epsilon in viral infection and mucosal immunity. Mucosal Immunol. 2012 Nov;5(6):610–22.

221. Sommereyns C, Paul S, Staeheli P, Michiels T. IFN-Lambda (IFN-λ) Is Expressed in a Tissue-Dependent Fashion and Primarily Acts on Epithelial Cells In Vivo. Vol. 4, PLoS Pathogens. 2008. p. e1000017.

222. Aso H, Ito J, Koyanagi Y, Sato K. Comparative Description of the Expression Profile of Interferon-Stimulated Genes in Multiple Cell Lineages Targeted by HIV-1 Infection. Front Microbiol. 2019 Mar;10:429.

223. van Boxel-Dezaire AHH, Rani MRS, Stark GR. Complex modulation of cell type-specific signaling in response to type I interferons. Immunity. 2006 Sep;25(3):361–72.

224. Chen HM, Tanaka N, Mitani Y, Oda E, Nozawa H, Chen JZ, et al. Critical role for constitutive type I interferon signaling in the prevention of cellular transformation. Cancer Sci. 2009 Mar;100(3):449–56.

225. Kuilman T, Michaloglou C, Vredeveld LCW, Douma S, van Doorn R, Desmet CJ, et al. Oncogene-induced senescence relayed by an interleukin-dependent inflammatory network. Cell. 2008 Jun;133(6):1019–31.

226. Moiseeva O, Mallette FA, Mukhopadhyay UK, Moores A, Ferbeyre G. DNA damage signaling and p53-dependent senescence after prolonged beta-interferon stimulation. Mol Biol Cell. 2006 Apr;17(4):1583–92.

227. Reddel RR. Senescence: an antiviral defense that is tumor suppressive? Carcinogenesis. 2010 Jan;31(1):19–26.

228. Munoz-Fontela C, Garcia MA, Garcia-Cao I, Collado M, Arroyo J, Esteban M, et al. Resistance to viral infection of super p53 mice. Oncogene. 2005 Apr;24(18):3059–62.

229. Ma-Lauer Y, Carbajo-Lozoya J, Hein MY, Müller MA, Deng W, Lei J, et al. p53 down-regulates SARS coronavirus replication and is targeted by the SARS-unique domain and PLpro via E3 ubiquitin ligase RCHY1. Proc Natl Acad Sci U S A. 2016 Aug;113(35):E5192-201.

230. Critchley-Thorne RJ, Simons DL, Yan N, Miyahira AK, Dirbas FM, Johnson DL, et al. Impaired interferon signaling is a common immune defect in human cancer. Proc Natl Acad Sci U S A. 2009 Jun;106(22):9010–5.

231. Hare D, Collins S, Cuddington B, Mossman K. The Importance of Physiologically Relevant Cell Lines for Studying Virus-Host Interactions. Viruses. 2016 Nov;8(11).

232. Blight KJ, McKeating JA, Rice CM. Highly permissive cell lines for subgenomic and genomic hepatitis C virus RNA replication. J Virol. 2002 Dec;76(24):13001–14.

233. Desmyter J, Melnick JL, Rawls WE. Defectiveness of interferon production and of rubella virus interference in a line of African green monkey kidney cells (Vero). J Virol. 1968 Oct;2(10):955–61.

234. Mosca JD, Pitha PM. Transcriptional and posttranscriptional regulation of exogenous human beta interferon gene in simian cells defective in interferon synthesis. Mol Cell Biol. 1986 Jun;6(6):2279–83.

235. Bianchi F, Pretto S, Tagliabue E, Balsari A, Sfondrini L. Exploiting poly(I:C) to induce cancer cell apoptosis. Cancer Biol Ther. 2017 Oct;18(10):747–56.

236. Hata N, Sato M, Takaoka A, Asagiri M, Tanaka N, Taniguchi T. Constitutive IFN-alpha/beta signal for efficient IFN-alpha/beta gene induction by virus. Biochem Biophys Res Commun. 2001 Jul;285(2):518–25.

237. Smith MC, Goddard ET, Perusina Lanfranca M, Davido DJ. hTERT extends the life of human fibroblasts without compromising type I interferon signaling. PLoS One. 2013 Mar;8(3):e58233.

238. Kumar A, Kim JH, Ranjan P, Metcalfe MG, Cao W, Mishina M, et al. Influenza virus exploits tunneling nanotubes for cell-to-cell spread. Sci Rep. 2017 Jan;7:40360.

239. Sowinski S, Jolly C, Berninghausen O, Purbhoo MA, Chauveau A, Köhler K, et al. Membrane nanotubes physically connect T cells over long distances presenting a novel route for HIV-1 transmission. Nat Cell Biol. 2008 Feb;10(2):211–9.

240. Roberts KL, Manicassamy B, Lamb RA. Influenza A virus uses intercellular connections to spread to neighboring cells. J Virol. 2015 Feb;89(3):1537–49.

241. Cifuentes-Munoz N, El Najjar F, Dutch RE. Viral cell-to-cell spread: Conventional and non-conventional ways. Adv Virus Res. 2020 Sep;108:85–125.

242. Jolly C, Booth NJ, Neil SJD. Cell-cell spread of human immunodeficiency virus type 1 overcomes tetherin/BST-2-mediated restriction in T cells. J Virol. 2010 Dec;84(23):12185–99.

243. Richardson MW, Carroll RG, Stremlau M, Korokhov N, Humeau LM, Silvestri G, et al. Mode of transmission affects the sensitivity of human immunodeficiency virus type 1 to restriction by rhesus TRIM5alpha. J Virol. 2008 Nov;82(22):11117–28.

244. Murrell I, Bedford C, Ladell K, Miners KL, Price DA, Tomasec P, et al. The pentameric complex drives immunologically covert cell–cell transmission of wild-type human cytomegalovirus. Vol. 114, Proceedings of the National Academy of Sciences. 2017. p. 6104–9.

245. Jansens RJJ, Tishchenko A, Favoreel HW. Bridging the Gap: Virus Long-Distance Spread via Tunneling Nanotubes. J Virol. 2020 Mar;94(8).

246. Ablasser A, Schmid-Burgk JL, Hemmerling I, Horvath GL, Schmidt T, Latz E, et al. Cell intrinsic immunity spreads to bystander cells via the intercellular transfer of cGAMP. Nature. 2013 Nov;503(7477):530–4.

247. Chen Q, Boire A, Jin X, Valiente M, Er EE, Lopez-Soto A, et al. Carcinoma-astrocyte gap junctions promote brain metastasis by cGAMP transfer. Nature. 2016 May;533(7604):493–8.

248. Pépin G, De Nardo D, Rootes CL, Ullah TR, Al-Asmari SS, Balka KR, et al. Connexin-Dependent Transfer of cGAMP to Phagocytes Modulates Antiviral Responses. MBio. 2020 Jan;11(1).

249. Assil S, Webster B, Dreux M. Regulation of the Host Antiviral State by Intercellular Communications. Vol. 7, Viruses. 2015. p. 4707–33.

250. Décembre E, Assil S, Hillaire MLB, Dejnirattisai W, Mongkolsapaya J, Screaton GR, et al. Sensing of immature particles produced by dengue virus infected cells induces an antiviral response by plasmacytoid dendritic cells. PLoS Pathog. 2014 Oct;10(10):e1004434.

251. Hynes RO, Naba A. Overview of the matrisome–an inventory of extracellular matrix constituents and functions. Cold Spring Harb Perspect Biol. 2012 Jan;4(1):a004903.

252. Tomlin H, Piccinini AM. A complex interplay between the extracellular matrix and the innate immune response to microbial pathogens. Immunology. 2018 Oct;155(2):186–201.

253. Hynes RO. The Extracellular Matrix: Not Just Pretty Fibrils. Vol. 326, Science. 2009. p. 1216–9.

254. Busch SM, Lorenzana Z, Ryan AL. Implications for Extracellular Matrix Interactions With Human Lung Basal Stem Cells in Lung Development, Disease, and Airway Modeling. Front Pharmacol. 2021 May;12:645858.

255. Stylianopoulos T, Diop-Frimpong B, Munn LL, Jain RK. Diffusion anisotropy in collagen gels and tumors: the effect of fiber network orientation. Biophys J. 2010 Nov;99(10):3119–28.

256. Ramanujan S, Pluen A, McKee TD, Brown EB, Boucher Y, Jain RK. Diffusion and convection in collagen gels: implications for transport in the tumor interstitium. Biophys J. 2002 Sep;83(3):1650–60.

257. Baker BM, Chen CS. Deconstructing the third dimension – how 3D culture microenvironments alter cellular cues. Journal of Cell Science. 2012.

258. Macri L, Silverstein D, Clark RAF. Growth factor binding to the pericellular matrix and its importance in tissue engineering. Adv Drug Deliv Rev. 2007 Nov;59(13):1366–81.

259. Yoshida K, Kondoh A, Narumi K, Yoshida T, Aoki K. Extracellular matrix interacts with interferon alpha protein: retention and display of cytotoxicity. Biochem Biophys Res Commun. 2008 Nov;376(2):299–304.

260. Kuwashiro T, Iwane S, Jinghe X, Matsuhashi S, Eguchi Y, Anzai K, et al. Regulation of interferon signaling and HCV-RNA replication by extracellular matrix. International Journal of Molecular Medicine. 2018.

261. Fouda GG, Jaeger FH, Amos JD, Ho C, Kunz EL, Anasti K, et al. Tenascin-C is an innate broad-spectrum, HIV-1-neutralizing protein in breast milk. Proc Natl Acad Sci U S A. 2013 Nov;110(45):18220–5.

262. Jia W, Li H, He YW. Pattern recognition molecule mindin promotes intranasal clearance of influenza viruses. J Immunol. 2008 May;180(9):6255–61.

263. Kono H, Rock KL. How dying cells alert the immune system to danger. Nat Rev Immunol. 2008 Apr;8(4):279–89.

264. Marchant DJ, Bellac CL, Moraes TJ, Wadsworth SJ, Dufour A, Butler GS, et al. A new transcriptional role for matrix metalloproteinase-12 in antiviral immunity. Nat Med. 2014 May;20(5):493–502.

265. Zhang L, Bukreyev A, Thompson CI, Watson B, Peeples ME, Collins PL, et al. Infection of ciliated cells by human parainfluenza virus type 3 in an in vitro model of human airway epithelium. J Virol. 2005 Jan;79(2):1113–24.

266. Sinn PL, Williams G, Vongpunsawad S, Cattaneo R, McCray PB Jr. Measles virus preferentially transduces the basolateral surface of well-differentiated human airway epithelia. J Virol. 2002 Mar;76(5):2403–9.

267. Ciencewicki JM, Brighton LE, Jaspers I. Localization of type I interferon receptor limits interferon-induced TLR3 in epithelial cells. J Interferon Cytokine Res. 2009 May;29(5):289–97.

268. Stanifer ML, Mukenhirn M, Muenchau S, Pervolaraki K, Kanaya T, Albrecht D, et al. Asymmetric distribution of TLR3 leads to a polarized immune response in human intestinal epithelial cells. Nat Microbiol. 2020 Jan;5(1):181–91.

269. Muir A, Soong G, Sokol S, Reddy B, Gomez MI, Van Heeckeren A, et al. Toll-like receptors in normal and cystic fibrosis airway epithelial cells. Am J Respir Cell Mol Biol. 2004 Jun;30(6):777–83.

270. Gewirtz AT, Navas TA, Lyons S, Godowski PJ, Madara JL. Cutting edge: bacterial flagellin activates basolaterally expressed TLR5 to induce epithelial proinflammatory gene expression. J Immunol. 2001 Aug;167(4):1882–5.

271. Schaap-Nutt A, Liesman R, Bartlett EJ, Scull MA, Collins PL, Pickles RJ, et al. Human parainfluenza virus serotypes differ in their kinetics of replication and cytokine secretion in human tracheobronchial airway epithelium. Virology. 2012 Nov;433(2):320–8.

272. Vanderheiden A, Ralfs P, Chirkova T, Upadhyay AA, Zimmerman MG, Bedoya S, et al. Type I and Type III Interferons Restrict SARS-CoV-2 Infection of Human Airway Epithelial Cultures. J Virol. 2020 Sep;94(19).

273. Kolb P, Schundner A, Frick M, Gottschalk KE. In Vitro Measurements of Cellular Forces and their Importance in the Lung—From the Sub- to the Multicellular Scale. Vol. 11, Life. 2021. p. 691.

274. Kılıç A, Ameli A, Park JA, Kho AT, Tantisira K, Santolini M, et al. Mechanical forces induce an asthma gene signature in healthy airway epithelial cells. Vol. 10, Scientific Reports. 2020.

275. Solis AG, Bielecki P, Steach HR, Sharma L, Harman CCD, Yun S, et al. Mechanosensation of cyclical force by PIEZO1 is essential for innate immunity. Nature. 2019 Sep;573(7772):69–74.

276. Huse M. Mechanical forces in the immune system. Nat Rev Immunol. 2017 Nov;17(11):679–90.

277. Garcia-Cardeña G, Comander J, Anderson KR, Blackman BR, Gimbrone MA Jr. Biomechanical activation of vascular endothelium as a determinant of its functional phenotype. Proc Natl Acad Sci U S A. 2001 Apr;98(8):4478–85.

278. Brooks AR, Lelkes PI, Rubanyi GM. Gene expression profiling of human aortic endothelial cells exposed to disturbed flow and steady laminar flow. Physiol Genomics. 2002;9(1):27–41.

279. Tsai YC, Hsieh HJ, Liao F, Ni CW, Chao YJ, Hsieh CY, et al. Laminar flow attenuates interferon-induced inflammatory responses in endothelial cells. Cardiovasc Res. 2007 Jun;74(3):497–505.

280. Brooks AR, Lelkes PI, Rubanyi GM. Gene expression profiling of vascular endothelial cells exposed to fluid mechanical forces: relevance for focal susceptibility to atherosclerosis. Endothelium. 2004 Jan;11(1):45–57.

281. Lancaster MA, Knoblich JA. Generation of cerebral organoids from human pluripotent stem cells. Nat Protoc. 2014 Oct;9(10):2329–40.

282. Kim J, Sullivan GJ, Park IH. How well do brain organoids capture your brain? iScience. 2021 Feb;24(2):102063.

283. van der Vaart J, Lamers MM, Haagmans BL, Clevers H. Advancing lung organoids for COVID-19 research. Dis Model Mech. 2021 Jun;14(6).

284. Iverson E, Kaler L, Agostino EL, Song D, Duncan GA, Scull MA. Leveraging 3D Model Systems to Understand Viral Interactions with the Respiratory Mucosa. Viruses. 2020 Dec;12(12).

285. García-Rodríguez I, Sridhar A, Pajkrt D, Wolthers KC. Put Some Guts into It: Intestinal Organoid Models to Study Viral Infection. Viruses. 2020 Nov;12(11).

286. Blutt SE, Crawford SE, Ramani S, Zou WY, Estes MK. Engineered Human Gastrointestinal Cultures to Study the Microbiome and Infectious Diseases. Cell Mol Gastroenterol Hepatol. 2018 Mar;5(3):241–51.

287. Turco MY, Gardner L, Kay RG, Hamilton RS, Prater M, Hollinshead MS, et al. Trophoblast organoids as a model for maternal-fetal interactions during human placentation. Nature. 2018 Dec;564(7735):263–7.

288. Sheridan MA, Fernando RC, Gardner L, Hollinshead MS, Burton GJ, Moffett A, et al. Establishment and differentiation of long-term trophoblast organoid cultures from the human placenta. Nat Protoc. 2020 Oct;15(10):3441–63.

289. Prior N, Inacio P, Huch M. Liver organoids: from basic research to therapeutic applications. Gut. 2019 Dec;68(12):2228–37.

290. Zhu X, Zhang B, He Y, Bao J. Liver Organoids: Formation Strategies and Biomedical Applications. Tissue Eng Regen Med. 2021 Aug;18(4):573–85.

291. de Dios-Figueroa GT, Aguilera-Marquez JDR, Camacho-Villegas TA, Lugo-Fabres PH. 3D Cell Culture Models in COVID-19 Times: A Review of 3D Technologies to Understand and Accelerate Therapeutic Drug Discovery. Biomedicines. 2021 May;9(6).

292. Ramani S, Crawford SE, Blutt SE, Estes MK. Human organoid cultures: transformative new tools for human virus studies. Curr Opin Virol. 2018 Apr;29:79–86.

293. Clevers H. Modeling Development and Disease with Organoids. Cell. 2016 Jun;165(7):1586–97.

294. Henjakovic M, Sewald K, Switalla S, Kaiser D, Müller M, Veres TZ, et al. Ex vivo testing of immune responses in precision-cut lung slices. Toxicol Appl Pharmacol. 2008 Aug;231(1):68–76.

295. Temann A, Golovina T, Neuhaus V, Thompson C, Chichester JA, Braun A, et al. Evaluation of inflammatory and immune responses in long-term cultured human precision-cut lung slices. Hum Vaccin Immunother. 2017 Feb;13(2):351–8.

296. Neuhaus V, Schwarz K, Klee A, Seehase S, Förster C, Pfennig O, et al. Functional testing of an inhalable nanoparticle based influenza vaccine using a human precision cut lung slice technique. PLoS One. 2013 Aug;8(8):e71728.

297. Neuhaus V, Chichester JA, Ebensen T, Schwarz K, Hartman CE, Shoji Y, et al. A new adjuvanted nanoparticle-based H1N1 influenza vaccine induced antigen-specific local mucosal and systemic immune responses after administration into the lung. Vaccine. 2014 May;32(26):3216–22.

298. Pezzulo AA, Starner TD, Scheetz TE, Traver GL, Tilley AE, Harvey BG, et al. The air-liquid interface and use of primary cell cultures are important to recapitulate the transcriptional profile of in vivo airway epithelia. Am J Physiol Lung Cell Mol Physiol. 2011 Jan;300(1):L25-31.

299. Hui KPY, Ching RHH, Chan SKH, Nicholls JM, Sachs N, Clevers H, et al. Tropism, replication competence, and innate immune responses of influenza virus: an analysis of human airway organoids and ex-vivo bronchus cultures. Lancet Respir Med. 2018 Nov;6(11):846–54.

300. Cheemarla NR, Watkins TA, Mihaylova VT, Wang B, Zhao D, Wang G, et al. Dynamic innate immune response determines susceptibility to SARS-CoV-2 infection and early replication kinetics. J Exp Med. 2021 Aug;218(8).

301. Wu A, Mihaylova VT, Landry ML, Foxman EF. Interference between rhinovirus and influenza A virus: a clinical data analysis and experimental infection study. Lancet Microbe. 2020 Oct;1(6):e254–62.

302. Cho HJ, Verbridge SS, Davalos RV, Lee YW. Development of an In Vitro 3D Brain Tissue Model Mimicking In Vivo-Like Pro-inflammatory and Pro-oxidative Responses. Ann Biomed Eng. 2018 Jun;46(6):877–87.

303. Haw RTY, Tong CK, Yew A, Lee HC, Phillips JB, Vidyadaran S. A three-dimensional collagen construct to model lipopolysaccharide-induced activation of BV2 microglia. J Neuroinflammation. 2014 Jul;11:134.

304. Pöttler M, Zierler S, Kerschbaum HH. An artificial three-dimensional matrix promotes ramification in the microglial cell-line, BV-2. Neurosci Lett. 2006 Dec;410(2):137–40.

305. Song Q, Jiang Z, Li N, Liu P, Liu L, Tang M, et al. Anti-inflammatory effects of three-dimensional graphene foams cultured with microglial cells. Biomaterials. 2014 Aug;35(25):6930–40.

306. Abreu CM, Gama L, Krasemann S, Chesnut M, Odwin-Dacosta S, Hogberg HT, et al. Microglia Increase Inflammatory Responses in iPSC-Derived Human BrainSpheres. Front Microbiol. 2018 Dec;9:2766.

307. Watanabe M, Buth JE, Vishlaghi N, de la Torre-Ubieta L, Taxidis J, Khakh BS, et al. Self-Organized Cerebral Organoids with Human-Specific Features Predict Effective Drugs to Combat Zika Virus Infection. Cell Rep. 2017 Oct;21(2):517–32.

308. Ortega-Prieto AM, Skelton JK, Wai SN, Large E, Lussignol M, Vizcay-Barrena G, et al. 3D microfluidic liver cultures as a physiological preclinical tool for hepatitis B virus infection. Nat Commun. 2018 Feb;9(1):682.

309. Bayer A, Lennemann NJ, Ouyang Y, Bramley JC, Morosky S, Marques ETDA Jr, et al. Type III Interferons Produced by Human Placental Trophoblasts Confer Protection against Zika Virus Infection. Cell Host Microbe. 2016 May;19(5):705–12.

310. Corry J, Arora N, Good CA, Sadovsky Y, Coyne CB. Organotypic models of type III interferon-mediated protection from Zika virus infections at the maternal-fetal interface. Proc Natl Acad Sci U S A. 2017 Aug;114(35):9433–8.

311. Sheridan MA, Yunusov D, Balaraman V, Alexenko AP, Yabe S, Verjovski-Almeida S, et al. Vulnerability of primitive human placental trophoblast to Zika virus. Proc Natl Acad Sci U S A. 2017 Feb;114(9):E1587–96.

312. Dang J, Tiwari SK, Lichinchi G, Qin Y, Patil VS, Eroshkin AM, et al. Zika Virus Depletes Neural Progenitors in Human Cerebral Organoids through Activation of the Innate Immune Receptor TLR3. Cell Stem Cell. 2016 Aug;19(2):258–65.

313. D'Aiuto L, Bloom DC, Naciri JN, Smith A, Edwards TG, McClain L, et al. Modeling Herpes Simplex Virus 1 Infections in Human Central Nervous System Neuronal Cells Using Two- and Three-Dimensional Cultures Derived from Induced Pluripotent Stem Cells. J Virol. 2019 May;93(9).

314. Brown RM, Rana PSJB, Jaeger HK, O'Dowd JM, Balemba OB, Fortunato EA. Human Cytomegalovirus Compromises Development of Cerebral Organoids. J Virol. 2019 Sep;93(17).

315. Jackson R, Eade S, Zehbe I. An epithelial organoid model with Langerhans cells for assessing virus-host interactions. Philos Trans R Soc Lond B Biol Sci. 2019 May;374(1773):20180288.

316. Helms HC, Abbott NJ, Burek M, Cecchelli R, Couraud PO, Deli MA, et al. In vitro models of the blood-brain barrier: An overview of commonly used brain endothelial cell culture models and guidelines for their use. J Cereb Blood Flow Metab. 2016 May;36(5):862–90.

317. Cucullo L, Hossain M, Puvenna V, Marchi N, Janigro D. The role of shear stress in Blood-Brain Barrier endothelial physiology. BMC Neurosci. 2011 May;12:40.

318. Bramley JC, Drummond CG, Lennemann NJ, Good CA, Kim KS, Coyne CB. A Three-Dimensional Cell Culture System To Model RNA Virus Infections at the Blood-Brain Barrier. mSphere. 2017 May;2(3).

319. Stifter SA, Bhattacharyya N, Sawyer AJ, Cootes TA, Stambas J, Doyle SE, et al. Visualizing the Selectivity and Dynamics of Interferon Signaling In Vivo. Cell Rep. 2019 Dec;29(11):3539-3550.e4.

320. Pulverer JE, Rand U, Lienenklaus S, Kugel D, Zietara N, Kochs G, et al. Temporal and spatial resolution of type I and III interferon responses in vivo. J Virol. 2010 Sep;84(17):8626–38.

321. Zhao X, Li C, Liu X, Chiu MC, Wang D, Wei Y, et al. Human Intestinal Organoids Recapitulate Enteric Infections of Enterovirus and Coronavirus. Stem Cell Reports. 2021 Mar;16(3):493–504.

322. Drummond CG, Bolock AM, Ma C, Luke CJ, Good M, Coyne CB. Enteroviruses infect human enteroids and induce antiviral signaling in a cell lineage-specific manner. Proc Natl Acad Sci U S A. 2017 Feb;114(7):1672–7.

323. Triana S, Metz-Zumaran C, Ramirez C, Kee C, Doldan P, Shahraz M, et al. Single-cell analyses reveal SARS-CoV-2 interference with intrinsic immune response in the human gut. Mol Syst Biol. 2021 Apr;17(4):e10232.

324. Hammel JH, Cook SR, Belanger MC, Munson JM, Pompano RR. Modeling Immunity In Vitro: Slices, Chips, and Engineered Tissues. Annu Rev Biomed Eng. 2021 Jul;23:461–91.

325. Villenave R, Wales SQ, Hamkins-Indik T, Papafragkou E, Weaver JC, Ferrante TC, et al. Human Gut-On-A-Chip Supports Polarized Infection of Coxsackie B1 Virus In Vitro. PLoS One. 2017 Feb;12(2):e0169412.

326. Junaid A, Tang H, van Reeuwijk A, Abouleila Y, Wuelfroth P, van Duinen V, et al. Ebola Hemorrhagic Shock Syndrome-on-a-Chip. iScience. 2020 Jan;23(1):100765.

327. Ojo BA, VanDussen KL, Rosen MJ. The Promise of Patient-Derived Colon Organoids to Model Ulcerative Colitis. Inflamm Bowel Dis. 2021 Jul;

328. Strikoudis A, Cieślak A, Loffredo L, Chen YW, Patel N, Saqi A, et al. Modeling of Fibrotic Lung Disease Using 3D Organoids Derived from Human Pluripotent Stem Cells. Cell Rep. 2019 Jun;27(12):3709-3723.e5.

329. Vaidyanathan S, Salahudeen AA, Sellers ZM, Bravo DT, Choi SS, Batish A, et al. High-Efficiency, Selection-free Gene Repair in Airway Stem Cells from Cystic Fibrosis Patients Rescues CFTR Function in Differentiated Epithelia. Cell Stem Cell. 2020 Feb;26(2):161-171.e4.

330. Liu X, Ory V, Chapman S, Yuan H, Albanese C, Kallakury B, et al. ROCK inhibitor and feeder cells induce the conditional reprogramming of epithelial cells. Am J Pathol. 2012 Feb;180(2):599–607.

331. Suprynowicz FA, Upadhyay G, Krawczyk E, Kramer SC, Hebert JD, Liu X, et al. Conditionally reprogrammed cells represent a stem-like state of adult epithelial cells. Proc Natl Acad Sci U S A. 2012 Dec;109(49):20035–40.

332. Everman JL, Sajuthi S, Saef B, Rios C, Stoner AM, Numata M, et al. Functional genomics of CDHR3 confirms its role in HRV-C infection and childhood asthma exacerbations. J Allergy Clin Immunol. 2019 Oct;144(4):962–71.

333. Chu HW, Rios C, Huang C, Wesolowska-Andersen A, Burchard EG, O'Connor BP, et al. CRISPR-Cas9-mediated gene knockout in primary human airway epithelial cells reveals a proinflammatory role for MUC18. Gene Ther. 2015 Oct;22(10):822–9.

334. Schwank G, Koo BK, Sasselli V, Dekkers JF, Heo I, Demircan T, et al. Functional repair of CFTR by CRISPR/Cas9 in intestinal stem cell organoids of cystic fibrosis patients. Cell Stem Cell. 2013 Dec;13(6):653–8.

335. Haga K, Ettayebi K, Tenge VR, Karandikar UC, Lewis MA, Lin SC, et al. Genetic Manipulation of Human Intestinal Enteroids Demonstrates the Necessity of a Functional Fucosyltransferase 2 Gene for Secretor-Dependent Human Norovirus Infection. MBio. 2020 Mar;11(2).

336. Gagliardi TB, Goldstein ME, Song D, Gray KM, Jung JW, Ignacio MA, et al. Rhinovirus C replication is associated with the endoplasmic reticulum and triggers cytopathic effects in an in vitro model of human airway epithelium. PLOS Pathogens. 2022 Jan 7;18(1):e1010159.

337. Ng KT, Oong XY, Lim SH, Chook JB, Takebe Y, Chan YF, et al. Viral Load and Sequence Analysis Reveal the Symptom Severity, Diversity, and Transmission Clusters of Rhinovirus Infections. Clin Infect Dis. 2018 Jul 2;67(2):261–8.

338. Lemanske RF, Jackson DJ, Gangnon RE, Evans MD, Li Z, Shult PA, et al. Rhinovirus illnesses during infancy predict subsequent childhood wheezing. J Allergy Clin Immunol. 2005 Sep;116(3):571–7.

339. Stenberg-Hammar K, Hedlin G, Söderhäll C. Rhinovirus and preschool wheeze. Pediatr Allergy Immunol. 2017 Sep;28(6):513–20.

340. Lamson D, Renwick N, Kapoor V, Liu Z, Palacios G, Ju J, et al. MassTag polymerase-chain-reaction detection of respiratory pathogens, including a new rhinovirus genotype, that caused influenza-like illness in New York State during 2004-2005. J Infect Dis. 2006 Nov 15;194(10):1398–402.

341. Palmenberg AC, Spiro D, Kuzmickas R, Wang S, Djikeng A, Rathe JA, et al. Sequencing and analyses of all known human rhinovirus genomes reveal structure and evolution. Science. 2009 Apr 3;324(5923):55–9.

342. Liu Y, Hill MG, Klose T, Chen Z, Watters K, Bochkov YA, et al. Atomic structure of a rhinovirus C, a virus species linked to severe childhood asthma. Proc Natl Acad Sci U S A. 2016 Aug 9;113(32):8997–9002.

343. Royston L, Tapparel C. Rhinoviruses and Respiratory Enteroviruses: Not as Simple as ABC. Viruses. 2016 Jan 11;8(1):16.

344. Bochkov YA, Watters K, Ashraf S, Griggs TF, Devries MK, Jackson DJ, et al. Cadherin-related family member 3, a childhood asthma susceptibility gene product, mediates rhinovirus C binding and replication. Proc Natl Acad Sci U S A. 2015 Apr 28;112(17):5485–90.

345. Bønnelykke K, Sleiman P, Nielsen K, Kreiner-Møller E, Mercader JM, Belgrave D, et al. A genome-wide association study identifies CDHR3 as a susceptibility locus for early childhood asthma with severe exacerbations. Nat Genet. 2014 Jan;46(1):51–5.

346. Bønnelykke K, Coleman AT, Evans MD, Thorsen J, Waage J, Vissing NH, et al. Cadherin-related Family Member 3 Genetics and Rhinovirus C Respiratory Illnesses. Am J Respir Crit Care Med. 2018 Mar 1;197(5):589–94.

347. Bochkov YA, Palmenberg AC, Lee WM, Rathe JA, Amineva SP, Sun X, et al. Molecular modeling, organ culture and reverse genetics for a newly identified human rhinovirus C. Nat Med. 2011 May;17(5):627–32.

348. Everman JL, Sajuthi S, Saef B, Rios C, Stoner AM, Numata M, et al. Functional genomics of CDHR3 confirms its role in HRV-C infection and childhood asthma exacerbations. J Allergy Clin Immunol. 2019 Oct;144(4):962–71.

349. McKnight KL, Swanson KV, Austgen K, Richards C, Mitchell JK, McGivern DR, et al. Stimulator of interferon genes (STING) is an essential proviral host factor for human rhinovirus species A and C. Proc Natl Acad Sci U S A. 2020 Nov 3;117(44):27598–607.

350. Ashraf S, Brockman-Schneider R, Bochkov YA, Pasic TR, Gern JE. Biological characteristics and propagation of human rhinovirus-C in differentiated sinus epithelial cells. Virology. 2013 Feb 5;436(1):143–9.

351. Hao W, Bernard K, Patel N, Ulbrandt N, Feng H, Svabek C, et al. Infection and propagation of human rhinovirus C in human airway epithelial cells. J Virol. 2012 Dec;86(24):13524–32.

352. Belov GA, Nair V, Hansen BT, Hoyt FH, Fischer ER, Ehrenfeld E. Complex dynamic development of poliovirus membranous replication complexes. J Virol. 2012 Jan;86(1):302–12.

353. Oh HS, Banerjee S, Aponte-Diaz D, Sharma SD, Aligo J, Lodeiro MF, et al. Multiple poliovirus-induced organelles suggested by comparison of spatiotemporal dynamics of membranous structures and phosphoinositides. PLoS Pathog. 2018 Apr;14(4):e1007036.

354. Banerjee S, Aponte-Diaz D, Yeager C, Sharma SD, Ning G, Oh HS, et al. Hijacking of multiple phospholipid biosynthetic pathways and induction of membrane biogenesis by a picornaviral 3CD protein. PLoS Pathog. 2018 May;14(5):e1007086.

355. Dourmashkin RR, Dunn G, Castano V, McCall SA. Evidence for an enterovirus as the cause of encephalitis lethargica. BMC Infect Dis. 2012 Jun 20;12:136.

356. CDC CSG and YZ. English: This photo shows an electron micrograph of a thin section of numerous, spherical EV-D68 viral particles. Note that some of the viral particles appear as if they are “empty,” missing their contents of single-stranded RNA. [Internet]. 2014 [cited 2023 Jul 24]. Available from: https://commons.wikimedia.org/wiki/File:Ev-d68-photo-1.jpg

357. Banerjee S, Aponte-Diaz D, Yeager C, Sharma SD, Ning G, Oh HS, et al. Hijacking of multiple phospholipid biosynthetic pathways and induction of membrane biogenesis by a picornaviral 3CD protein. PLoS Pathog. 2018 May;14(5):e1007086.

358. Quiner CA, Jackson WT. Fragmentation of the Golgi apparatus provides replication membranes for human rhinovirus 1A. Virology. 2010 Nov 25;407(2):185–95.

359. Mousnier A, Swieboda D, Pinto A, Guedán A, Rogers AV, Walton R, et al. Human rhinovirus 16 causes Golgi apparatus fragmentation without blocking protein secretion. J Virol. 2014 Oct;88(20):11671–85.

360. Wessels E, Duijsings D, Lanke KHW, van Dooren SHJ, Jackson CL, Melchers WJG, et al. Effects of picornavirus 3A Proteins on Protein Transport and GBF1-dependent COP-I recruitment. J Virol. 2006 Dec;80(23):11852–60.

361. Chen YH, Du W, Hagemeijer MC, Takvorian PM, Pau C, Cali A, et al. Phosphatidylserine vesicles enable efficient en bloc transmission of enteroviruses. Cell. 2015 Feb 12;160(4):619–30.

362. Jackson WT, Giddings TH, Taylor MP, Mulinyawe S, Rabinovitch M, Kopito RR, et al. Subversion of cellular autophagosomal machinery by RNA viruses. PLoS Biol. 2005 May;3(5):e156.

363. Klein KA, Jackson WT. Human rhinovirus 2 induces the autophagic pathway and replicates more efficiently in autophagic cells. J Virol. 2011 Sep;85(18):9651–4.

364. Corona AK, Saulsbery HM, Corona Velazquez AF, Jackson WT. Enteroviruses Remodel Autophagic Trafficking through Regulation of Host SNARE Proteins to Promote Virus Replication and Cell Exit. Cell Rep. 2018 Mar 20;22(12):3304–14.

365. Zhu Q, Hu H, Liu H, Shen H, Yan Z, Gao L. A synthetic STING agonist inhibits the replication of human parainfluenza virus 3 and rhinovirus 16 through distinct mechanisms. Antiviral Res. 2020 Nov;183:104933.

366. Walters MS, Gomi K, Ashbridge B, Moore MAS, Arbelaez V, Heldrich J, et al. Generation of a human airway epithelium derived basal cell line with multipotent differentiation capacity. Respir Res. 2013 Dec 3;14(1):135.

367. Colegio OR, Van Itallie C, Rahner C, Anderson JM. Claudin extracellular domains determine paracellular charge selectivity and resistance but not tight junction fibril architecture. Am J Physiol Cell Physiol. 2003 Jun;284(6):C1346-1354.

368. Gray KM, Katz DB, Brown EG, Stroka KM. Quantitative Phenotyping of Cell-Cell Junctions to Evaluate ZO-1 Presentation in Brain Endothelial Cells. Ann Biomed Eng. 2019 Jul;47(7):1675–87.

369. Pranda MA, Gray KM, DeCastro AJL, Dawson GM, Jung JW, Stroka KM. Tumor Cell Mechanosensing During Incorporation into the Brain Microvascular Endothelium. Cell Mol Bioeng. 2019 Oct;12(5):455–80.

370. Gray KM, Jung JW, Inglut CT, Huang HC, Stroka KM. Quantitatively relating brain endothelial cell-cell junction phenotype to global and local barrier properties under varied culture conditions via the Junction Analyzer Program. Fluids Barriers CNS. 2020 Feb 11;17(1):16.

371. Fuchs R, Blaas D. Uncoating of human rhinoviruses. Rev Med Virol. 2010 Sep;20(5):281–97.

372. Suhy DA, Giddings TH, Kirkegaard K. Remodeling the endoplasmic reticulum by poliovirus infection and by individual viral proteins: an autophagy-like origin for virus-induced vesicles. J Virol. 2000 Oct;74(19):8953–65.

373. Egger D, Bienz K. Intracellular location and translocation of silent and active poliovirus replication complexes. J Gen Virol. 2005 Mar;86(Pt 3):707–18.

374. Schögler A, Caliaro O, Brügger M, Oliveira Esteves BI, Nita I, Gazdhar A, et al. Modulation of the unfolded protein response pathway as an antiviral approach in airway epithelial cells. Antiviral Res. 2019 Feb;162:44–50.

375. Song J, Chi M, Luo X, Song Q, Xia D, Shi B, et al. Non-Structural Protein 2B of Human Rhinovirus 16 Activates Both PERK and ATF6 Rather Than IRE1 to Trigger ER Stress. Viruses. 2019 Feb 1;11(2):133.

376. van Kuppeveld FJ, Hoenderop JG, Smeets RL, Willems PH, Dijkman HB, Galama JM, et al. Coxsackievirus protein 2B modifies endoplasmic reticulum membrane and plasma membrane permeability and facilitates virus release. EMBO J. 1997 Jun 16;16(12):3519–32.

377. Wu J, Chen YJ, Dobbs N, Sakai T, Liou J, Miner JJ, et al. STING-mediated disruption of calcium homeostasis chronically activates ER stress and primes T cell death. J Exp Med. 2019 Apr 1;216(4):867–83.

378. Wan D, Jiang W, Hao J. Research Advances in How the cGAS-STING Pathway Controls the Cellular Inflammatory Response. Front Immunol. 2020;11:615.

379. Sajjan U, Wang Q, Zhao Y, Gruenert DC, Hershenson MB. Rhinovirus disrupts the barrier function of polarized airway epithelial cells. Am J Respir Crit Care Med. 2008 Dec 15;178(12):1271–81.

380. Coyne CB, Gambling TM, Boucher RC, Carson JL, Johnson LG. Role of claudin interactions in airway tight junctional permeability. Am J Physiol Lung Cell Mol Physiol. 2003 Nov;285(5):L1166-1178.

381. Coyne CB, Vanhook MK, Gambling TM, Carson JL, Boucher RC, Johnson LG. Regulation of airway tight junctions by proinflammatory cytokines. Mol Biol Cell. 2002 Sep;13(9):3218–34.

382. Zihni C, Mills C, Matter K, Balda MS. Tight junctions: from simple barriers to multifunctional molecular gates. Nat Rev Mol Cell Biol. 2016 Sep;17(9):564–80.

383. Michi AN, Yipp BG, Dufour A, Lopes F, Proud D. PGC-1α mediates a metabolic host defense response in human airway epithelium during rhinovirus infections. Nat Commun. 2021 Jun 16;12(1):3669.

384. Bustamante-Marin XM, Ostrowski LE. Cilia and Mucociliary Clearance. Cold Spring Harb Perspect Biol. 2017 Apr 3;9(4):a028241.

385. Lachowicz-Scroggins ME, Boushey HA, Finkbeiner WE, Widdicombe JH. Interleukin-13-induced mucous metaplasia increases susceptibility of human airway epithelium to rhinovirus infection. Am J Respir Cell Mol Biol. 2010 Dec;43(6):652–61.

386. Laoukili J, Perret E, Willems T, Minty A, Parthoens E, Houcine O, et al. IL-13 alters mucociliary differentiation and ciliary beating of human respiratory epithelial cells. J Clin Invest. 2001 Dec;108(12):1817–24.

387. Yuta A, Doyle WJ, Gaumond E, Ali M, Tamarkin L, Baraniuk JN, et al. Rhinovirus infection induces mucus hypersecretion. Am J Physiol. 1998 Jun;274(6):L1017-1023.

388. He SH, Zheng J, Duan MK. Induction of mucin secretion from human bronchial tissue and epithelial cells by rhinovirus and lipopolysaccharide. Acta Pharmacol Sin. 2004 Sep;25(9):1176–81.

389. Griggs TF, Bochkov YA, Nakagome K, Palmenberg AC, Gern JE. Production, purification, and capsid stability of rhinovirus C types. J Virol Methods. 2015 Jun 1;217:18–23.

390. Sanjana NE, Shalem O, Zhang F. Improved vectors and genome-wide libraries for CRISPR screening. Nat Methods. 2014 Aug;11(8):783–4.

391. Stewart SA, Dykxhoorn DM, Palliser D, Mizuno H, Yu EY, An DS, et al. Lentivirus-delivered stable gene silencing by RNAi in primary cells. RNA. 2003 Apr;9(4):493–501.

392. Fiala M. Plaque formation by 55 rhinovirus serotypes. Appl Microbiol. 1968 Oct;16(10):1445–50.

393. Schindelin J, Arganda-Carreras I, Frise E, Kaynig V, Longair M, Pietzsch T, et al. Fiji: an open-source platform for biological-image analysis. Nat Methods. 2012 Jun 28;9(7):676–82.

394. Measuring cell fluorescence using ImageJ — The Open Lab Book v1.0 [Internet]. [cited 2023 Jul 24]. Available from:

https://theolb.readthedocs.io/en/latest/imaging/measuring-cell-fluorescence-using-imagej.html

395. Bolte S, Cordelières FP. A guided tour into subcellular colocalization analysis in light microscopy. J Microsc. 2006 Dec;224(Pt 3):213–32.

396. Watters K, Palmenberg AC. CDHR3 extracellular domains EC1-3 mediate rhinovirus C interaction with cells and as recombinant derivatives, are inhibitory to virus infection. PLoS Pathog. 2018 Dec 10;14(12):e1007477.

397. Taylor-Robinson D, Tyrrell DAJ. SEROTYPES OF VIRUSES (RHINOVIRUSES) ISOLATED FROM COMMON COLDS. The Lancet. 1962 Mar 3;279(7227):452–4.

398. Rosenberger CM, Podyminogin RL, Askovich PS, Navarro G, Kaiser SM, Sanders CJ, et al. Characterization of innate responses to influenza virus infection in a novel lung type I epithelial cell model. J Gen Virol. 2014 Feb;95(Pt 2):350–62.

399. Montoro DT, Haber AL, Biton M, Vinarsky V, Lin B, Birket SE, et al. A revised airway epithelial hierarchy includes CFTR-expressing ionocytes. Nature. 2018 Aug;560(7718):319–24.

400. Plasschaert LW, Žilionis R, Choo-Wing R, Savova V, Knehr J, Roma G, et al. A single-cell atlas of the airway epithelium reveals the CFTR-rich pulmonary ionocyte. Nature. 2018 Aug;560(7718):377–81.

401. Koonin EV. The phylogeny of RNA-dependent RNA polymerases of positive-strand RNA viruses. J Gen Virol. 1991 Sep;72 (Pt 9):2197–206.

402. Stirling DR, Swain-Bowden MJ, Lucas AM, Carpenter AE, Cimini BA, Goodman A. CellProfiler 4: improvements in speed, utility and usability. BMC Bioinformatics. 2021 Dec;22(1):433.

403. Rajput C, Han M, Ishikawa T, Lei J, Goldsmith AM, Jazaeri S, et al. Rhinovirus C Infection Induces Type 2 Innate Lymphoid Cell Expansion and Eosinophilic Airway Inflammation. Front Immunol. 2021;12:649520.

404. Foxman EF, Storer JA, Fitzgerald ME, Wasik BR, Hou L, Zhao H, et al. Temperature-dependent innate defense against the common cold virus limits viral replication at warm temperature in mouse airway cells. Proc Natl Acad Sci U S A. 2015 Jan 20;112(3):827–32.

405. Hong JY, Chung Y, Steenrod J, Chen Q, Lei J, Comstock AT, et al. Macrophage activation state determines the response to rhinovirus infection in a mouse model of allergic asthma. Respir Res. 2014 Jun 7;15:63.

406. Rasmussen AL, Racaniello VR. Selection of rhinovirus 1A variants adapted for growth in mouse lung epithelial cells. Virology. 2011 Nov 25;420(2):82–8.

407. Newcomb DC, Sajjan US, Nagarkar DR, Wang Q, Nanua S, Zhou Y, et al. Human Rhinovirus 1B Exposure Induces Phosphatidylinositol 3-Kinase–dependent

Airway Inflammation in Mice. Am J Respir Crit Care Med. 2008 May 15;177(10):1111–21.

408. Kuss SK, Etheredge CA, Pfeiffer JK. Multiple host barriers restrict poliovirus trafficking in mice. PLoS Pathog. 2008 Jun 6;4(6):e1000082.

409. Han M, Ishikawa T, Stroupe CC, Breckenridge HA, Bentley JK, Hershenson MB. Deficient inflammasome activation permits an exaggerated asthma phenotype in rhinovirus C-infected immature mice. Mucosal Immunol. 2021 Nov;14(6):1369–80.

410. CDHR3 protein expression summary - The Human Protein Atlas [Internet]. [cited 2023 Sep 22]. Available from: https://www.proteinatlas.org/ENSG00000128536-CDHR3

411. Sun Y, Watters K, Hill MG, Fang Q, Liu Y, Kuhn RJ, et al. Cryo-EM structure of rhinovirus C15a bound to its cadherin-related protein 3 receptor. PNAS [Internet]. 2020 Mar 5 [cited 2020 Mar 11]; Available from: https://www.pnas.org/content/early/2020/03/04/1921640117

412. Watters K, Palmenberg AC. CDHR3 extracellular domains EC1-3 mediate rhinovirus C interaction with cells and as recombinant derivatives, are inhibitory to virus infection. Belov GA, editor. PLOS Pathogens. 2018 Dec 10;14(12):e1007477.

413. Basnet S, Bochkov YA, Brockman-Schneider RA, Kuipers I, Aesif SW, Jackson DJ, et al. CDHR3 Asthma-Risk Genotype Affects Susceptibility of Airway Epithelium to Rhinovirus C Infections. American Journal of Respiratory Cell and Molecular Biology [Internet]. 2019 Mar 27 [cited 2019 Apr 1]; Available from: https://www.atsjournals.org/doi/10.1165/rcmb.2018-0220OC

414. Çalışkan M, Bochkov YA, Kreiner-Møller E, Bønnelykke K, Stein MM, Du G, et al. Rhinovirus Wheezing Illness and Genetic Risk of Childhood-Onset Asthma. N Engl J Med. 2013 Apr 11;368(15):1398–407.

415. Everman JL, Sajuthi S, Saef B, Rios C, Stoner AM, Numata M, et al. Functional genomics of CDHR3 confirms its role in HRV-C infection and childhood asthma exacerbations. Journal of Allergy and Clinical Immunology [Internet]. 2019 Mar 29 [cited 2019 Jun 20]; Available from: http://www.sciencedirect.com/science/article/pii/S009167491930418X

416. Petersen JF, Cherney MM, Liebig HD, Skern T, Kuechler E, James MN. The structure of the 2A proteinase from a common cold virus: a proteinase responsible for the shut-off of host-cell protein synthesis. EMBO J. 1999 Oct 15;18(20):5463–75.

417. Barral PM, Sarkar D, Fisher PB, Racaniello VR. RIG-I is cleaved during picornavirus infection. Virology. 2009 Sep 1;391(2):171–6.

418. Barral PM, Morrison JM, Drahos J, Gupta P, Sarkar D, Fisher PB, et al. MDA-5 is cleaved in poliovirus-infected cells. J Virol. 2007 Apr;81(8):3677–84.

419. Drahos J, Racaniello VR. Cleavage of IPS-1 in cells infected with human rhinovirus. J Virol. 2009 Nov;83(22):11581–7.

420. Pang LL, Yuan XH, Shao CS, Li MZ, Wang Y, Wang HM, et al. The suppression of innate immune response by human rhinovirus C. Biochem Biophys Res Commun. 2017 Aug 12;490(1):22–8.

421. Her Z, Teng TS, Tan JJL, Teo TH, Kam YW, Lum FM, et al. Loss of TLR3 aggravates CHIKV replication and pathology due to an altered virus-specific neutralizing antibody response. EMBO Mol Med. 2015 Jan;7(1):24–41.

422. Gardner J, Anraku I, Le TT, Larcher T, Major L, Roques P, et al. Chikungunya virus arthritis in adult wild-type mice. J Virol. 2010 Aug;84(16):8021–32.

423. Rossi SL, Tesh RB, Azar SR, Muruato AE, Hanley KA, Auguste AJ, et al. Characterization of a Novel Murine Model to Study Zika Virus. Am J Trop Med Hyg. 2016 Jun 1;94(6):1362–9.

424. Shresta S, Sharar KL, Prigozhin DM, Beatty PR, Harris E. Murine model for dengue virus-induced lethal disease with increased vascular permeability. J Virol. 2006 Oct;80(20):10208–17.

425. Frieman MB, Chen J, Morrison TE, Whitmore A, Funkhouser W, Ward JM, et al. SARS-CoV pathogenesis is regulated by a STAT1 dependent but a type I, II and III interferon receptor independent mechanism. PLoS Pathog. 2010 Apr 8;6(4):e1000849.

426. Zhao J, Li K, Wohlford-Lenane C, Agnihothram SS, Fett C, Zhao J, et al. Rapid generation of a mouse model for Middle East respiratory syndrome. Proc Natl Acad Sci U S A. 2014 Apr 1;111(13):4970–5.

427. Nelemans T, Kikkert M. Viral Innate Immune Evasion and the Pathogenesis of Emerging RNA Virus Infections. Viruses. 2019 Oct 18;11(10):961.

428. Waterhouse A, Bertoni M, Bienert S, Studer G, Tauriello G, Gumienny R, et al. SWISS-MODEL: homology modelling of protein structures and complexes. Nucleic Acids Res. 2018 02;46(W1):W296–303.

429. Sun Y, Watters K, Hill MG, Fang Q, Liu Y, Kuhn RJ, et al. Cryo-EM structure of rhinovirus C15a bound to its cadherin-related protein 3 receptor. Proc Natl Acad Sci U S A. 2020 Mar 24;117(12):6784–91.

430. Bønnelykke K, Coleman AT, Evans MD, Thorsen J, Waage J, Vissing NH, et al. Cadherin-related Family Member 3 Genetics and Rhinovirus C Respiratory Illnesses. Am J Respir Crit Care Med. 2018 Mar 1;197(5):589–94.

431. Ishikawa H, Barber GN. STING is an endoplasmic reticulum adaptor that facilitates innate immune signalling. Nature. 2008 Oct 2;455(7213):674–8.